THE EFFECTS OF PASSIVE WALL POROSITY ON THE LINEAR STABILITY OF BOUNDARY LAYERS

LEE J. PORTER

B.Eng.(Hons)

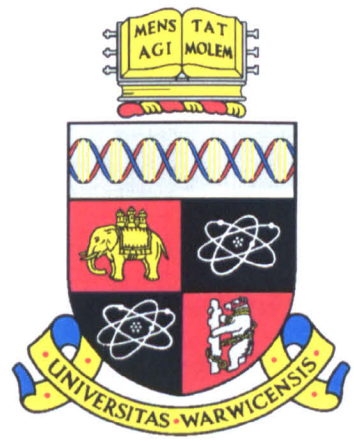

Department of Engineering
The University of Warwick

Thesis submitted to the University of Warwick for the degree of Doctor of Philosophy

November 1998

SYNOPSIS

A two-dimensional and quasi three-dimensional model has been developed which enables the stability characteristics of laminar boundary layer flows over porous surfaces to be evaluated. The theory assumes the porosity to be continuous over a fixed portion of the computational domain. The chosen configuration also assumes a continuous plenum chamber, of variable depth, beneath the thin porous boundary. It has been suggested that surfaces of this type may be of use in the delay of a laminar boundary-layer's transition to turbulence. Hence, a program of study, involving both simulation and experimentation, was initiated to catalogue the effects of porosity.

The numerical model consists of two sets of coupled solutions; one describing the cavity dynamics and the other describing the flow above the porous surface. The two systems are coupled together using their common wall boundary condition. This is defined in terms of a complex function which attempts to model the effects of the viscous and inertial stresses within the fluid as it periodically flows through the wall into the cavity. Essentially, the function defines the magnitude and phase relationship between the pressure across the porous boundary and the flow through it.

The cavity dynamics are determined by an analytical solution to the Orr-Sommerfeld equation in the absence of a mean flow field. The upper boundary condition for this flow is provided by the admittance function of the porous surface. The Orr-Sommerfeld equation is then solved again for the boundary layer flow - with the mean flow provided by solutions to the Falkner-Skan (or Falkner-Skan-Cooke) group of similarity profiles. This solution uses the admittance function to define its lower boundary condition. A high accuracy spectral technique, using Chebyshev polynomials, is used for the integration of the Orr-Sommerfeld equation.

Numerical simulations suggest that the appropriate selection of cavity depth and porosity fraction can lead to a complete suppression of the Tollmien-Schlichting instability for the case of zero pressure gradient. The model also suggests that

further suppression is possible (above that which would occur anyway) for the case of accelerating flows (advantageous pressure gradients). However, the theory predicts a worsening in the stability characteristics if passive porous surfaces are applied to either decelerating flows or flows with a crossflow component.

Attempts were made to verify the above findings through experimentation. It seems that a practical application of such porous surfaces relies heavily upon the assumption that there is no net inflow/outflow of fluid into/from the cavity. This requires each faceted porous segment to have a zero pressure gradient across its span. The experiment was initially set up for zero pressure gradient (Blasius flow). However, the streamwise and spanwise variation in pressure was still too large to avoid problems with bulk fluid flow. The use of staggered streamwise baffles helped alleviate the problem but ultimately failed to remove it altogether. Pressure differentials of only two or three Pascals over the porous surface seem sufficient to cause outflows large enough to render the wall ineffectual.

Two porous surfaces were tested in the wind tunnel: one of 6% porosity and one of 10%. Both failed to suppress the growth of Tollmien Schlichting waves within the boundary layer. The 6% porous surface failed due to the blowing mechanism outlined above. The 10% porous surface behaved rather differently. This surface produced a self-sustained cavity oscillation whose magnitude could be up to 40% of the free-stream flow speed. These oscillations were found to be caused by a shear layer instability, self-excited by the feedback of disturbances caused by the shear layer's own impingement on the downstream cavity edge. A theoretical model for the instability has been developed which gives qualitative agreement with the experimental results. However, various cavity baffle configurations ultimately failed to remove the instability. Hence, linear experiments on the 10% porous surface were not possible.

The final two chapters of the thesis concern the stability of a general three-dimensional boundary layer when the PPW boundary condition is applied. Flows with varying degrees of streamwise pressure gradient and sweep were considered.

It was noted, for the zero sweep case, that flows which exhibited viscous instability with decelerating fluid (tending towards inviscid instability) performed rather poorly when influenced by the PPW boundary condition. Furthermore, a wholly inviscid mechanism, such as that exhibited by the crossflow instability, was seen to have massively increased growth rates under the action of passive wall porosity. These two observations where seen as independent evidence in support of the prediction that the PPW boudary-condition is only theoretically of use when instabilities are wholly viscous.

Contents

List of Tables

List of Figures

Acknowledgments

This work was supported by the EPSRC under grant GR/G/22795. The research was carried out jointly at the Department of Engineering, University of Warwick and the Department of Aeronautical Engineering, Queen Mary and Westfield College, London. The author gratefully acknowledges the support of both departments.

The author wishes to convey his special thanks to Professor Peter Carpenter for his guidance and unfailing support. Particular gratitude is due to Peter for the provision of such a clearly defined, well planned and well resourced project.

Thanks are extended to Professor Mike Gaster and Dr. Jimmy Shaikh, at QMC London, for giving the author the benefit of their experimental expertise and the use of an excellent wind tunnel facility. Special thanks are due to Mr. Iain Bater and the other technical staff at QMC for their commitment to the timely commissioning and smooth running of the tunnel. The author is particularly grateful to Iain for his practical suggestions and technical assistance.

Finally ,this author wishes to thank the staff at British Aerospace's Sowerby Research Center for their support throughout the research program. Particularly thanks to the staff of the Laser Applications Group, Optics and Lasers Dept., for their assistance in the manufacture of the porous surfaces used in the experimental studies.

Declaration

The author declares the work presented herein to be the product of his own individual effort. Contributions and citations from others are clearly marked and acknowledged in the text. None of this thesis' contents have been used or published before the study period for this degree began. None of this work has been submitted for any other degree.

Chapter 1

Introduction

1.1 Overview - Transition control for drag reduction

The study of boundary-layer transition was initiated nearly a century ago. It was Prandtl who first drew attention to the connection between a body's drag and the transition from a laminar to a turbulent boundary layer. Prandtl's famous experiments went on to inspire a generation of scientists. The first real breakthroughs occurred some years later when Tollmien successfully computed the critical Reynolds number for transition over a flat plate. The experimental verification of Tollmien's work then followed (Schubauer and Skramstad (1949)) and this lead to the birth of boundary-layer stability theory as it is today.

Since those early days, there has been a phenomenal amount of work on transition. The stability theory is now fully developed and many of the key stages of transition are well understood, particularly in the linear regime. The theory now represents one of the largest and most important topics in fluid dynamics. It has been used in conjunction with experiments to produce firm engineering design practices which have produced technologies of real commercial value. While the development of techniques that ultimately reduce skin friction drag have an obvious commercial use, it must also be remembered that the accurate prediction

of the point of transition is also of interest to industry. For example, the physics of combustion process is critically depended upon where transition has occurred within internal flows.

Current methods for drag reduction by delayed boundary layer transition can be broadly divided into one of two categories: *Profile Modification* and *Wave Cancellation.* The first technique aims to modify mean velocity profiles such that disturbance amplification is attenuated. Avoidance of inviscid inflectional (or Rayleigh) type instability is the prime concern with these methods. Techniques such as shaping, suction, surface cooling in air and heating in water, all fall into this category. Essentially, these methods either make the profile curvature at the wall $(\partial^2 u/\partial y^2)_w$ more negative or directly alter the local fluid viscosity thereby reducing surface shear stresses.

Shaping is simply the term used to describe a technique of wing design which exploits the favorable pressure gradient effect. The aim is to ensure the boundary layers remains both non-inflectional and stable to the viscous Tollmien-Schlichting type instability. It led to the development of the NACA 6-series airfoils. The objective of this design method is to create a favorable pressure gradient for as much of the wing as possible. Once within the adverse pressure gradient region, the shaping methodology then focuses on ensuring the boundary-layer remains attached.

Suction techniques represent the brute force approach to Laminar Flow Control (LFC). This technique literally removes the stagnated region of the boundary-layer, creating fuller, more stable, profiles. Suction techniques have also been applied to turbulent boundary layers, where they are of particular use in the prevention of flow separation. Distributed suction has been used in a variety of locations on practical aircraft. Such techniques can remove leading-edge contamination, caused by turbulence from the fuselage, leading to the relaminarisation and stabilization of the flow down the attachment line. Suction is also particularly effective on both the Tollmien-Schlichting (T-S) and crossflow instabilities within the mid-chord regions of swept-wings.

Wave cancellation methods have only recently started to attract the attention of the industrial and academic community. Such methods are unique in that they attempt to modify the velocity perturbations directly, rather than changing the stability characteristics of the carrier boundary-layer. These cancellation methods can be both passive and active. Active cancellation of the T-S instability is a very challenging proposition which is currently attracting a huge amount of interest. Micro Electro-mechanical Systems Engineering (MEMS) might well enable the practical application of active control in the years to come. Passive cancellation methods have been developed, to a large extent, already. In particular wall compliance or boundary flexibility has been shown to be effective in postponing transition in marine applications. A desire to develop an equivalent surface which could be applied in aerospace applications was one of the motivations behind the current research into passive porous walls.

1.2 Motivation and origins of research into Passive Porous Walls (PPW's)

The discussion of the previous section would lead one to believe that some of the technologies of LFC have reached maturity. In fact, this is not the case in most instances. Indeed, there is a lack in the application of LFC throughout industry. None of the regional or trans-continental commercial airlines currently use laminar flow devices on any of their aircraft. The same is true for all the other sectors of engineering which could benefit. The reason for this shortfall is clear; it is difficult to engineer these technologies to be sufficiently robust for everyday service. Nevertheless, the aircraft industry has recently shown a renewed interest in suction techniques used in conjunction with appropriately shaped airfoils. Furthermore, the drivers for this technology are becoming ever stronger. Modern commercial aircraft have a skin friction which accounts for around 50% of the total drag. As such, long-haul airlines can expect to make dramatic reductions in their direct

operating costs if they can reduce this figure. Thomas (1985) estimates that a 10% drag reduction on a large transport aircraft could save up to 13 million gallons of fuel over the lifetime of the aircraft.

The question to be answered is this; how could a passive laminar flow device succeed where existing technologies have failed, or received little commercial interest? Practical aircraft are required to operate in very harsh environments. Aircraft are exposed to a variety of surface contaminants such as airborne particulates, insects and icing deposits. In addition to this, everyday service exposes aircraft to a significant amount of panel damage due to the careless manoeuvres of service vehicles, bird strikes and even poor takeoffs and landings. As such, any LFC device must be robust enough to operate under such conditions. LFC is intended to extend the range of aircraft or to reduce the fuel payload. As such, the failure of such devices may leave insufficient fuel for the mission. For this reason, even when used in cruise conditions, LFC devices are safety critical and their failure is unacceptable. Furthermore, the use of such devices when the aircraft is at incidence presents further safety problems because their failure may lead to flow separation and ultimately to wing stall.

Distributed suction techniques seem most likely to find practical application in the near future. Indeed, the A3XX aircraft, of AIRBUS Industries, has been flagged as a possible recipient of such systems. However, the installation and maintenance of distributed suction ducting and associated control systems is a complex and very costly procedure. It requires the complete redesign of the wing spar and control surface actuators. Retro-fitting of such a system is not practical. In addition to this, the suction required to stabilize the boundary layer must be generated from auxiliary compressors. This additional power requirement reduces the overall benefit gained. However, low-pressure venting may provide some of the suction requirement at no additional cost.

The above discussion illustrates where opportunities lie in the field of Laminar-Flow-Control. There is a clear willingness for industry to use these technologies

if only they could be made robust. It can be inferred that a device of minimum complexity is likely to succeed where others have failed provided it performs well given the operational environment. This is essentially where the concept of passive wall porosity may triumph, since it requires none of the systems and ducting required of distributed suction.

1.3 Preliminary discussion of the presumed physics of the PPW effect

The current work focuses on the transition-delaying potential of a surface covered with an array of cylindrical pores or slots connecting the boundary layer to a common cavity. A general admittance theory is used to study the effect of porosity on the evolution of Tollmien-Schlichting waves within a transitional boundary layer.

The following chapters will strive to produce both theoretical and experimental evidence in support of the T-S wave suppression characteristics of PPW's. However, at this early stage, it is useful to postulate a possible physical mechanism by which such suppression may occur. The physics of the inviscid instability are well documented following the theorems of Rayleigh and Tollmien. When considering viscous stability, most researchers tend to bypass any physical discussion, preferring instead to address the mathematics of the linear stability theory. Lighthill (1963) is a notable exception to this rule. Figure (1.1) is instructive in illustrating Lighthill's *freight-train* analogy to transition.

Each carriage on the train is loaded with alternate packets of vorticity (+ve followed by -ve) and thus can be said to represent the T-S wave centered at the critical layer. Carriage doors being left open, each carriage sheds its vorticity to the boundary layer. Each packet of vorticity dissipates itself through the boundary layer. Some of the vorticity will convect down through the boundary layer where it encounters the wall. As the packet hits the wall it induces a vorticity of oppo-

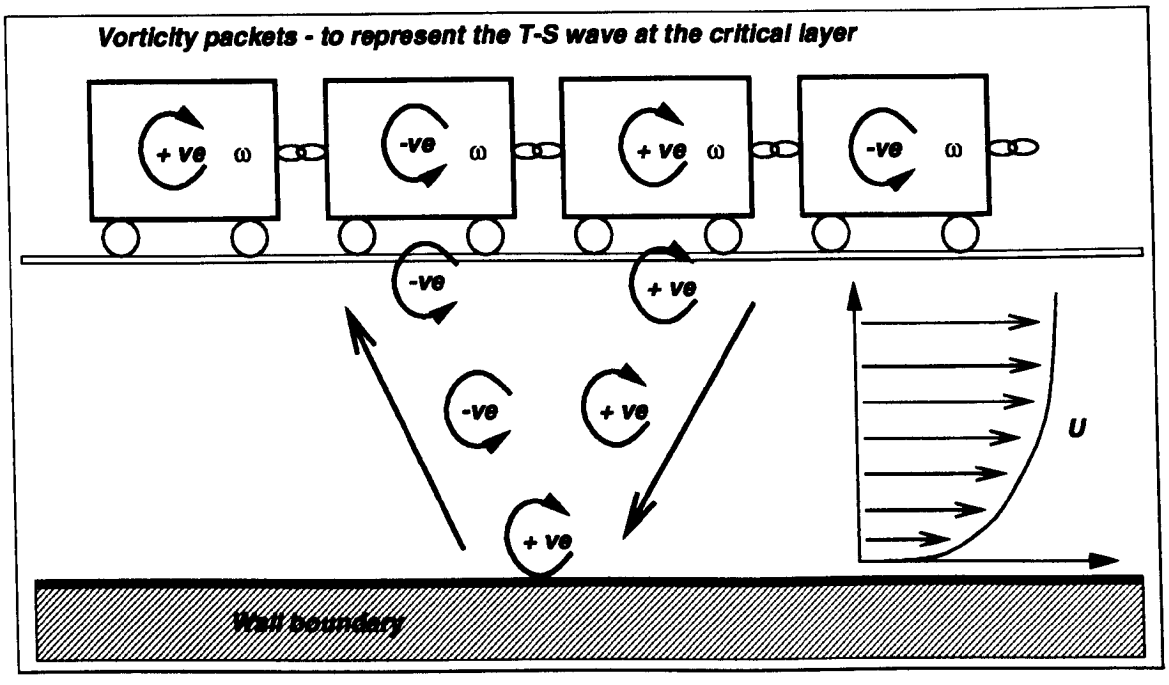

Figure 1.1: Freight-Train analogy of Lighthill (1963).

site sign. This induced vorticity of inverted sign can then convect back through the boundary layer and hop on to the next carriage. This next carriage, being of opposite vorticity to the one ahead of it, is therefore reinforced by the induced vorticity that has just boarded. Hence, by this mechanism, each carriage can increase its net vorticity and therefore, by analogy, the T-S wave will grow.

1.3.1 Conjectures on the Passive Porous Wall (PPW) effect

Following the analogy described in § 1.3 it is now possible to see a mechanism by which passive porosity can suppress viscous instability. Figure (1.2) illustrates the PPW configuration and mode of operation. The arrows indicate minute inflows/outflows of fluid which have resulted from the pressure perturbations of a Tollmien-Schlichting wave. It is conceivable that the porous surface and cavity can interrupt the generation of vorticity at the wall. The wall could do this in one of two ways. It could either alter the phase of the generated vorticity feedback such that, in the context of the analogy, it misses the carriage behind that from which it originated. If this were the case, vorticity reinforcement would not occur and the T-S wave could not grow. Another suppression mechanism is that in

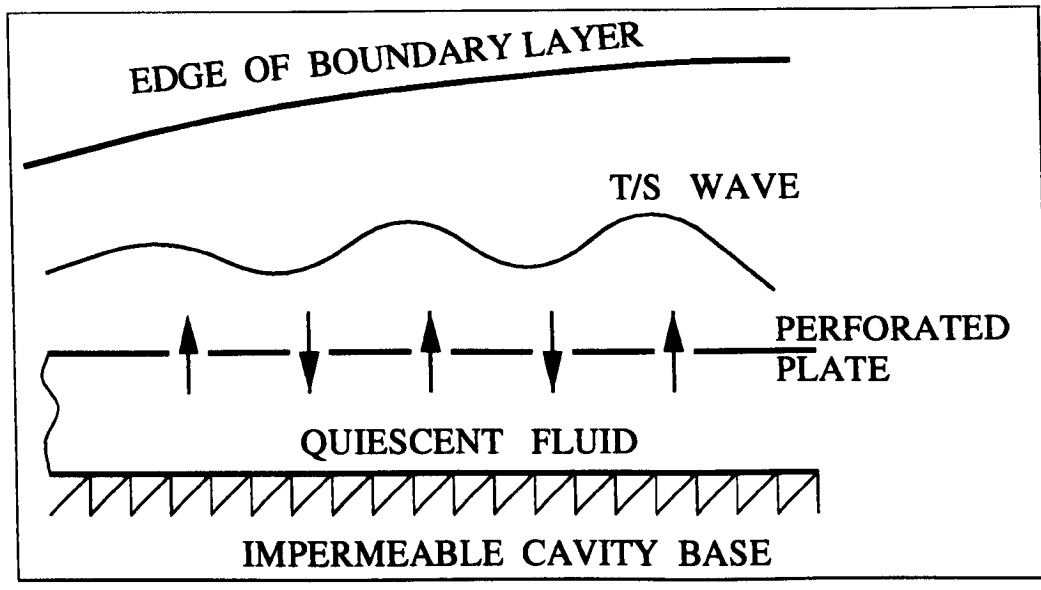

Figure 1.2: Physical representation of the PPW mechanism

which the wall and cavity absorb the incoming vorticity and disperse it within the quiescent fluid contained within the cavity.

1.4 Aims of the research and assumptions made at its outset

The primary aim of this research is to discover whether porous aerodynamic surfaces, of the type described previously, can be used to delay the onset of turbulence. To this end, the research aims to construct an appropriate numerical model to simulate the behavior of such surfaces. One would then seek to verify this model with experimental data and, assuming satisfactory verification, use the model to optimize the performance of such surfaces.

Following the suppositions of § 1.3 it is clear even at this early stage that the parameters of interest when prototyping passive porous surfaces are porosity fraction, cavity depth and porosity geometry (holes/slots). Hence, we can identify the key aim of this work as the optimization of the above parameters such that maximum transition delay can be realized.

The chosen method of modeling the flow over a porous surface will determine the assumptions made. At the most fundamental level, the choices are to either model each individual pore discretely, or to model the porous surface as a continuum. The problem with the former method is that if the model is to be verified against data from the proposed experiment, the model must involve the inclusion of many hundreds of thousands of individual pores. This would clearly involve the use of numerical schemes which discretize the domain using an extremely fine mesh. Such a model would be very computationally expensive and may not even be possible owing to the expected size of individual pores ($\approx 50\mu$ m).

The extent of research into PPW's, prior to the current work, was very rudimentary. As such, early studies such as the one carried out here do not warrant a full numerical simulation (of the DNS type) in which the geometry of individual pores is modeled. A far easier and probably more rewarding approach is to model the PPW boundary condition as if it were a continuum. This can be most easily done using techniques developed from the science of acoustics in which the boundary condition is defined by a complex admittance. This method allowed the production of meaningful results with the least complication. Indeed, it is likely to be practically impossible to model the porosity discretely, and as such, we must default to the admittance method through necessity. For these reasons it was the admittance approach which was chosen for further development.

The admittance technique seeks to mathematically model the viscous and inertial stresses which effect the unsteady (periodic) flow though a pore simply by defining a magnitude and phase relationship between the pressure across the porous boundary and the flow through it. Essentially this approach liberates us from considering the fluid mechanics which occur within individual pores. Clearly, if we choose to ignore something that fundamental then we must expect the model to be deficient in some way. It turns out that using this approach makes it impossible to predict the geometry of the pore which is most likely to give a beneficial result. For example, distinctions between holed and slotted configurations can-

not be made. Furthermore, the model cannot provide information concerning the effects of finite wall thickness. Some progress has, however, been made in this respect. Carpenter (1996) has made additions to the current model using the assumption of a fully developed unsteady pipe flow within the pore. This enables the effect of wall thickness to be taken into account. However, it is unlikely, given the typically aspect ratio of a pore, that the flow within a pore can be considered fully developed. Such flows are only considered fully developed once the flow has reach a downstream position of several times the pipe diameter. The typical aspect ratios used here are unity, making fully developed flow impossible. Nevertheless, the pipe flow assumption must be an improvement upon the current model which assumes an infinitely thin foil.

Clearly the two major assumptions applicable to the admittance theory are that the wall is infinitely thin and that the porosity is continuously distributed. However, such characteristics have no physical realization and so compromises have to be made. Therefore, for no better reason than to match the theory, one would choose a minimal foil thickness for the porous surface (say 50μm). Section 6.1.1 discusses this aspect in more detail. Similarly, the size and shape of individual pores is selected to match the theory. Admittance theory implies continuity and homogeneity across the surface. Very small equi-spaced holes seem to be a good approximation to this. However, these arguments only represent intuitive thought and their origins are not wholly scientific. For this reason they will only be used as guide-lines. The prototyping stage will involve the manufacture of foils with a range of geometric configurations so that all the possibilities can be explored.

Chapter 2

Literature Review

2.1 Work specific to the effects of passive wall porosity

A cursory glance at the literature reveals some obvious shortfalls. To date, much of the work has focused upon turbulence modification rather than transition delay. Suction techniques through porous panels have proven useful in reducing skin friction. Indeed, such techniques may soon be used within the aerospace industry. *Passive porous walls* have also been considered for turbulence modification, but much of the work reviewed herein concludes that such walls have a detrimental effect on drag. However, these experimental studies frequently show little evidence of theoretical guidance, especially concerning porous wall parameter selection. This is perhaps, not surprising since analytical studies are only applicable to the small disturbances found during transition and do not apply to fully turbulent boundary layers. Therefore, a far more logical starting point would be to consider the transition problem both analytically (using linear stability theory) and experimentally. The few analytical studies which do exist often fall short of providing practical guide-lines to the selection of optimum wall parameters. The topic is, therefore, in dire need of a combined theoretical and experimental investigation.

For clarity, those walls which have porosity but no other external energy sources (such as suction) will be termed *passive porous walls* (PPW's).

Passive porous walls are a relatively new area of research. As such, the depth of literature available is limited. A few configurations have been investigated in recent years, but the majority of the research has been focused upon the control of either subsonic, already turbulent, flows or on the control of shock waves in transonic flow over aerofoils.

Suction techniques using pores have also been studied in connection with transition delay and with reduction of the momentum thickness of already turbulent boundary layers. The mechanics of this technique are somewhat different from that of the proposed method currently under consideration. Essentially, these techniques are intended to remove the slow-moving fluid at the wall of an already turbulent boundary layer - hence reducing the effective displacement thickness, reducing drag and delaying separation. These techniques have particular application in the adverse pressure gradients found downstream of the apex of aerofoil sections. This mechanism has very little in common with PPW's other than that pores are used. Hence, the topic will be given no further consideration, and is mentioned only to avoid any confusion with the use of pores in aerofoil sections.

The extent of literature available on PPW's for laminar flow stabilization has been confined to an initial feasibility study by Carpenter (1996) and some analytical/numerical work by Lekoudis (1978) and Gaponov (1971, 1975a,b).

Carpenter (1996) focuses on the transition-delaying potential of a surface covered with an array of cylindrical pores or slots connecting the boundary layer to a common cavity. A general admittance theory is used to study the effect of porosity on the evolution of Tollmien-Schlichting waves within a transitional boundary layer. The theory used herein is essentially the same as that used in Carpenter and Morris (1990), only the formulation of the kinematic boundary conditions are

slightly different. This initial investigation has yielded a modicum of optimism in the practical application of PPW's for transition delay. Carpenter has shown that boundary layer stabilization is possible for a restricted range of values of admittance phase angle. Furthermore, the theory suggests that pores aligned with oblique flow entry angles may be more effective than those having pores aligned normal to the surface[†]. However, the practical application of oblique pores is questionable. This is primarily because Carpenter's most successful models were those of comparatively small wall thicknesses. As such, it is unlikely that the pore aspect ratio is sufficient to allow the flow to align itself with the pore.

Carpenter also compares PPW's with their compliant wall counterparts. Here some important distinctions have been made. His work shows that for sub-resonant behavior* PPW's are less effective than compliant walls simply because compliant walls move in response to pressure perturbations. This movement creates an additional viscous dissipation term in the coupled wall-flow system that is not available in the PPW case. However, whereas compliant walls cannot be used effectively at super-resonant frequencies it has been shown that PPW's can. Indeed, Carpenter considers super-resonant walls to have a greater chance of practical realization.

The work of Gaponov (1971) (part 1), which was both numerical and analytical, was important in that it was the first to recognize that the previously used boundary conditions at the wall, for porous surfaces with suction, were incorrect. Previous work, Ulrich (1944) (as cited by Gaponov), had assumed that while the steady-state normal velocity components at the wall were obviously non-zero, the disturbance normal velocities at the wall could also be taken as zero. Gaponov shows that this was not a valid approximation. Although suction techniques are not of primary interest in the current study, the kinematic boundary conditions

[†]For the super-resonant case only. No such benefits are predicted for the sub-resonant case.

*Sub-resonant walls are those whose natural frequencies of oscillation are below the frequencies of the most dominant Tollmien-Schlichting waves. Super-resonant behavior has the converse meaning.

for porous walls with suction are essentially the same as those for PPW. This more complete description of the passive porous "law of the wall" paved the way for a range of additional analytical investigations, particularly in studies of compliant walls. Gaponov obtained preliminary results for the reformulated stability problem using the asymptotic theory developed by Landahl (1962). The link between the boundary layer and cavity dynamics was made by assuming a periodic pipe flow solution within the cylindrical pore, the cavity dynamics were represented in a similar manner to those of the boundary layer (using the Orr-Sommerfeld equation) except that the mean flow was set to zero. The final part of the paper focuses upon the identification of neutral stability curves. Gaponov illustrates two neutral stability curves for his PPW construction. The class-A type (Tollmien-Schlichting) instability is also plotted for the rigid-wall case for comparison. The plots clearly show that the region of instability for the T-S mode has been considerably reduced with the use of porosity. This is therefore some cause for encouragement. However, this paper (Gaponov's first on this topic) gives little explanation of the mechanisms involved.

Gaponov (1975a) continues his work with an investigation into the potential of a transverse slotted surface for boundary layer stability. The current *state of the art* analysis when this paper was written assumed a spatially evolving disturbance. Gaponov discarded the previously used asymptotic approach and choose to use Floquet's theorem (using Fourier series expansions) to represent the semi-infinite boundary value problem. A spatially evolving complex exponential form of disturbance was used in accordance with the work of Gaster (1965).

Lekoudis (1978) performed an investigation which had a similar structure to the one proposed in the current research. He studied the stability of boundary layers over permeable surfaces using linear stability theory. Since this theory is only applicable to laminar and transitional flows it can be assumed that these were the areas of interest, but this is not stated explicitly. His work focuses upon two cases. The first is that of a porous wall with a continuous plenum chamber allow-

ing traveling waves to develop underneath the wall. The other case considered is that of closely spaced pores each with its own small chamber (honeycomb-type structure). Gaponov (1975b) had already shown the importance of compressibility for such a construction. The second case will not, however, be reviewed in detail because it turns out that such a wall construction has little potential for transition delay. Lekoudis's work did, however, recognize Gaponov's contributions to the subject and indeed used his revised boundary conditions. The use of neutral stability curves is also questioned in this paper. The author recognizes that such curves only provide absolute bounds on the Reynolds number, and tells us nothing about the transition process. Lekoudis therefore chose a mixture of numerical techniques which enabled him to evaluate the growth rate of disturbances. His techniques enabled him to optimize wall parameters by varying each in turn. Indeed, Lekoudis's work has been extremely useful in that it outlines the effect of varying each parameter, thereby providing an excellent basis upon which to design PPW prototypes. It was concluded that the continuous plenum chamber configuration provides conditions for stabilization if it is optimized, while the other configuration was found to have no beneficial effect.

Schetz and Kong (1981) carried out experiments on the practical application of PPW's for turbulence modification. They obtained direct measurements of skin friction, turbulence intensity and Reynolds stress profiles in the boundary layer. This work makes the initial assumption that porous walls cannot be made with a relative roughness[†] of less than 5. To account for this, they chose to compare a porous wall with a solid wall of equivalent roughness. Their most significant result was that all turbulence quantities and skin friction measurements show a marked increase for the porous wall case. This disappointing conclusion should, however, be expected. Kong and Schetz have presented little evidence of a considered approach towards the selection of an appropriate pore construction. Carpenter

[†]A relative roughness, k^+, of less than 5 corresponds to a hydraulically smooth surface. $k^+ = U_\tau k/\nu$ where k is the roughness height, U_τ is the friction velocity ($U_\tau = \sqrt{\tau_w/p}$) and ν is the kinematic viscosity.

(1996) has shown, for transition only, that only specific pore designs can yield a favourable result. Hence, it would seem likely that pore design would be equally critical for fully developed turbulent boundary layers.

Schetz and Kong experimented on sintered metal porous walls. They did not, however, focus on obtaining minimal roughness. Strictly speaking, the surface roughness of their walls was such that they could be considered hydrodynamically smooth. However, it is conceivable that the definition of hydrodynamic smoothness for a solid wall may need to be redefined for a porous wall. It is likely that the materials and processes they used could not provide a more hydrodynamically smooth porous wall. Hence, in the current research we will strive to achieve minimal roughness. Laser-drilling techniques are expected to be invaluable in achieving this goal. The roughness incurred is expected to be vastly reduced although the quality of finish will be largely dependent on the material used.†

Wilkinson (1983) provides an experimental investigation similar to that of Schetz and Kong (1981). However, a more complete range of wall configurations is considered. Again, turbulence reduction was the proposed mechanism. The conclusions drawn were that the PPW's exhibited increased drag over their non-porous counterparts. This is in agreement with all previous investigations. Wilkinson attempts to provide a physical explanation for the results obtained. He suggests that a local region of reduced pressure over the wall causes a local adverse pressure gradient and instantaneous "wall blowing", both of which are known to be de-stabilizing. For a local high-pressure region, a favorable pressure gradient and "wall suction" occur which are know to be stabilizing. He argues that the de-stabilizing effect of the local blowing is, however, longer lasting and the overall effect of the porosity is de-stabilizing. The basis for this reasoning is not made clear in his paper. A low-pressure fluctuation in time can be viewed as a spatially moving adverse pressure gradient which locally de-stabilized the flow. This

† § 6.1.1 outlines the selection of the porous foil used in the current study.

process is augmented by injection of fluid through the wall (due to the low pressure) and may result in more violent bursting than in the impermeable wall case and, hence, higher skin friction. Other possible mechanisms which he considered worthy of investigation were: the effect of porosity on coherent structures in the turbulent boundary layer and the effect of pressure drag on the hole edges. Wilkinson mentions in passing that no pressure distribution data was available for the small pores. He recognized the obvious benefit of such data, particularly in quantifying the pressure drag which inevitably occurs at the edges of each pore. This pressure drag may partly explain why increased porosity for a given roughness led to increased drag.

Collier and Schetz (1983) performed another experimental study of skin friction and turbulence intensity over a porous wall with and without blowing. Again wholly turbulent boundary layers were under investigation. The results for the test case, without blowing, were in agreement with the work mentioned above. However, they report substantial reductions in skin friction once a considerable amount of blowing was applied. The amount of blowing required illustrated that this method was not viable for conventional drag reduction purposes. Nevertheless, this work is of particular use in the design of blade cooling systems within gas turbines. Unfortunately no mention is made of the physical mechanisms by which blowing proves successful in reducing turbulence intensity and hence heat transfer.

2.2 Review of formulations of the viscous stability problem for the Blasius profile - theoretical & numerical developments

The starting point for most formulations is the linearized stability equation known as the *Orr-Sommerfeld* equation. This equation is obtained by the substitution of

a complex exponential mathematical representation of a wave-like disturbance (temporal or spatial) into the linearized viscous Navier-Stokes equations. The resultant equation, together with the three boundary conditions of the Blasius profile, can be arranged into a system of three equations which together form the eigenvalue problem. It should be noted that, for the spatial case, the resulting characteristic equation is nonlinear with respect to the complex eigenvalue (α). By contrast, the temporal formulation is linear with respect to the eigenvalue (ω or c). The theory under discussion applies strictly to parallel flows, but it has been shown by Pretsch (1941) (as reported by Schlichting (1987)), that the solutions can also be applied to boundary layers provided the Reynolds number is sufficiently large.

The literature available on this topic is too extensive to review in the current work. Only the most significant or the more recent developments in the theory will be reviewed herein. Lin (1945) provides a complete review of much of the early work. He discusses both the inviscid and viscous formulations used in the early works of Rayleigh, Prandtl, Tollmien and Heisenberg amongst others. Lin's work is invaluable in the clarification of the result of these previous investigations.

Tollmien can be credited with the first successful treatment of the Blasius profile. He used Frobenius expansions to resolve the two inviscid solutions for a velocity profile composed of a straight line inner section joined to a parabolic outer region. Schlichting continued this line of development and managed to construct a neutral stability curve.

Gaster (1962) did some influential studies into the hydrodynamic stability problem. This paper investigates the role of spatially growing T-S waves. He illustrates that his revised mathematical representation of small disturbances provides a more realistic model of convective instabilities. The results of Schubauer and Skramstad (1949), who's experimental studies used a vibrating ribbon to generate T-S waves, concluded that these spatially evolving disturbances could exist. Gaster, realizing that existing theory did not model such disturbances properly,

then developed the now widely used spatial mathematical representation of a convective disturbance. This formulation used a complex wavenumber rather than complex frequency as shown below:

$$v(y,x,t) = \hat{v}(y)\exp[i(\alpha x - \omega t)] \qquad \alpha = \alpha_r + i\alpha_i \tag{2.1}$$

where α_r is the wavenumber, $-\alpha_i$ is the spatial growth rate, ω is real frequency and the phase velocity is given by $c = \omega/\alpha_r$.

Gaster notes that the ribbon generated T-S waves of Schubauer were not of the form used in previous theoretical treatments, where α is real and ω complex. Instead, he shows that the opposite is the case. In most real flows, the disturbances are periodic in time (real ω) and space but also grow or decay exponentially with distance (complex α). The previously used form is incorrect because it corresponds to a disturbance which is periodic in x and grows or decays with time. Gaster postulates that there is a general form of disturbance, giving additional solutions to the eigenvalue problem, which result from a mathematical form in which both α and ω can be complex. However, for comparison with generated disturbance experiments, Gaster shows that his revised form of disturbance equation is a better representation. However, it should be noted that neutral stability curves calculated on the basis of a temporally growing wave system are still applicable since the neutral conditions for the two systems are identical when α and ω are both real.

A class of frequently used direct solutions to the aforementioned eigenvalue [†] problem are based upon approximating the disturbance amplitude by orthogonal polynomial expansions. Orszag (1971) made a significant contribution in the use of such techniques. He proposed the use of Chebyshev polynomials and argued that they offered substantial increases in accuracy while expending little additional computational power. This particular paper considers plane Poiseuille

[†] Approximate solutions can be derived from the asymptotic theory of Tollmien. Such theory is not expected to be of use in the current work and will not be reviewed herein.

flow only, but Orszag demonstrated that his technique is universal and can easily be applied to the semi-infinite boundary value problem given by the Blasius profile. Orszag's spectral method can be broken down into three basic steps.

- The equations for the expansion coefficients are found by formally substituting the Chebyshev polynomial approximation series into the Orr-Sommerfeld equation, re-expanding it in terms of Chebyshev polynomials and equating coefficients of each order of the polynomial to zero.

- The expansion coefficient are then derived from the above equations using Lanczos (1956) tau method. These are then substituted back into the equations for the expansion coefficients previously calculated. The resultant is a set of linear equations which can be solved to deduce the various eigenvalues.

- The final step is the solution of the eigenvalues. Orszag postulated two possible methods. The first is a simple iterative method which relies upon an initial guess at the eigenvalue. The second is a global search using the *QR* matrix technique pioneered by Wilkinson (1965). Orszag recommends the *QR* method be used only when no reasonable approximations to the eigenvalues are available. This is primarily because the global scheme requires a number of floating point operations which is a power of three greater than that of the simple iterative method. Later numerical investigations by Bridges and Morris (1984) used this *QR* algorithm along with Chebyshev polynomials to study the stability of the Blasius profile.

For the current research into PPW's, it is significant that no global search of instability modes has yet been done. Although it is unlikely that additional forms of absolute[†] or convective instability will be discovered, this supposition still requires numerical justification.

[†]PPW's cannot experience absolute instabilities of the divergence type, shown by compliant walls, because the wall structure is rigid.

For comparison with experimental studies, for which the frequency and Reynolds number are held constant (using an acoustic source in a wind tunnel), the *QR* matrix method is particularly useful because we can use its results to filter out a group of the most unstable modes. These will be the modes which will grow in preference to others in the physical situation. Indeed, the most unstable modes could theoretically be used to identify the critical Reynolds number Re_c (based on plate length). However, it is notable that the onset of turbulent spots will occur downstream of a location at which linear stability would predict instability. This is not surprising since the mode of instability which leads to transition will necessarily travel through a non-linear transition region before becoming fully turbulent. The use of values of Re_c obtained numerically is therefore questionable since they have no physical significance. It does, however provide a good reference value by which the various numerical and analytical methods can be compared.

Orszag's spectral method can be extended to a more general case. The method allows arbitrary forms of nearly parallel flows to be represented. Indeed, Orszag presented the formulation which is applicable to the Blasius profile and showed that its structure is identical to that used for the symmetrical Poiseuille profile.

The primary drawback of Orszag's method is that it is only applicable to the temporally evolving disturbance. Following the work of Gaster (1965), Bridges and Morris (1984) constructed a solution to the global eigenvalue formulation which assumes a spatially evolving disturbance. The complexity of this formulation is considerably increased. The use of a complex wavenumber produces a nonlinear characteristic equation for α. Gaster achieved an approximate solution by using his temporal-spatial transformations. However, Bridges and Morris attempted to solve the problem directly using finite Chebyshev series. The detail of this paper is too complex to be reviewed here. Essentially the formulation they constructed was equivalent to the *QR* global matrix method for the spatial modes.

Chapter 3

The Linear Theory

3.1 The Orr-Sommerfeld equation

The starting point for the majority of linear stability formulations is the *Orr-Sommerfeld* equation. This equation is obtained by the substitution of a complex exponential mathematical representation of a wave-like disturbance (temporal or spatial) into the Navier-Stokes equation given below:

$$\frac{\partial \vec{q}}{\partial t} + \vec{q} \cdot \nabla \vec{q} = -\frac{\nabla p}{\rho} + \nu \nabla^2 \vec{q} \tag{3.1}$$

where $\vec{q}$ is the velocity vector of the flow field, ∇p defines the pressure field, ρ is the fluid density and ν is the kinematic viscosity. The following paragraphs only give a general description of the formation of the Orr-Sommerfeld equation. The reader should consult Schlichting (1987) for a complete discussion of the approximations and linearizations made.

Equation (3.1) can be interpreted physically as follows. Reading from left to right we are reminded that unsteady and convective fluid motions are related to pressure gradients (i.e. normal stresses) and viscous shear stresses. The current research is confined to flows over a flat surface. The resultant equation, together with the three boundary conditions of the Blasius profile, can be arranged into

a system of equations which together form an eigenvalue problem. It should be noted that the equations appear non-linearly in the complex wave number, α, when spatial disturbances are considered.

The theory under discussion applies strictly to parallel flows such as channel flow. However, it is also possible to apply it to so-called nearly-parallel flows, such as boundary layer flows, provided the Reynolds number is sufficiently large. The parallel-flow assumption, which implies constant Reynolds number, considerably reduces the complexity of the problem by allowing the equation of motion to take a separable form. Since the problem is linear, the disturbances can be decomposed into their Fourier components and the behavior of a single component analyzed.

Upon the superposition of perturbed velocity components onto the mean flow $\vec{q} = (U+u', v')$ and neglecting second-order terms and higher, we obtain eqn.(3.2) for the x-component of velocity, where U is the profile of the unperturbed flow field (the Blasius profile in this case).

$$\frac{\partial u'}{\partial t} + U\frac{\partial u'}{\partial x} + v'\frac{\partial U}{\partial y} + \frac{1}{\rho}(\frac{dp}{dx} + \frac{\partial p'}{\partial x}) \equiv \nu \bigtriangledown^2 u' + \nu\frac{\partial^2 U}{\partial y^2} \tag{3.2}$$

where primed variables indicate perturbation velocity components.

This equation decomposes into the following equation for the undisturbed and perturbed components of the flow respectively:

$$\frac{1}{\rho}\frac{dp}{\partial x} = \nu\frac{\partial^2 U}{\partial y^2} \tag{3.3}$$

$$\frac{\partial u'}{\partial t} + U\frac{\partial u'}{\partial x} + v'\frac{\partial U}{\partial y} + \frac{1}{\rho}\frac{dp'}{dx} = \nu \bigtriangledown^2 u' \tag{3.4}$$

Velocity and pressure disturbances can be written in terms of the following traveling-wave form:

$$(u', v', p') = (\hat{u}, \hat{v}, \hat{p})e^{i(\alpha x - \omega t)} \tag{3.5}$$

where $\alpha = \alpha_r + i\alpha_i$, α_r = wavenumber, c = phase velocity $(\partial\omega/\partial\alpha)$, α_i = spatial growth rate exponent and ω = real frequency (a prescribed parameter). Hats denote the amplitudes of their respective variables.

Amplitudes of disturbances in physical space can only be obtained if the real part of eqn.(3.5) is found as follows.

$$\Re(\hat{u}, \hat{v}, \hat{p})e^{i(\alpha x - \omega t)} = (\hat{u}, \hat{v}, \hat{p})e^{i(\alpha x - \omega t)} + \text{c.c} \tag{3.6}$$

where **c.c.** denotes the complex conjugate, or;

$$\Re(\hat{u}, \hat{v}, \hat{p})e^{i(\alpha x - \omega t)} = (\hat{u}_r, \hat{v}_r, \hat{p}_r)e^{-\alpha_i x}\sin(\alpha_r x - \omega t) \tag{3.7}$$

The 'r' subscripts denote the real parts of the various quantities. Thus, it can be seen from the above that α_i has a special significance since it is the exponent which governs the spatial growth of a disturbance. This parameter is the essential marker used in much of the numerical studies that are to follow. A decrease in the negative value of α_i or even the attainment of a positive value will generally constitute a favorable result.

The usual boundary conditions, requiring exponential decay of the disturbance velocity, are assumed at the outer edge of the boundary layer. Using the linearized Navier-Stokes equation for both x and y components, it can be shown that the pressure terms can be eliminated by cross differentiation to give:

$$\frac{\partial}{\partial t}(\frac{\partial v'}{\partial x} - \frac{\partial u'}{\partial y}) + U\frac{\partial}{\partial x}(\frac{\partial v'}{\partial x} - \frac{\partial u'}{\partial y}) - v'\frac{\partial^2 v'}{\partial y^2} = \nu \bigtriangledown^2 (\frac{\partial v'}{\partial x} - \frac{\partial u'}{\partial y}) \tag{3.8}$$

After non-dimensionalising, the substitution of the expression for the spatially evolving disturbance (3.5) into (3.8) gives the familiar Orr-Sommerfeld equation:

$$v'''' - 2\alpha^2 v'' + \alpha^4 - \frac{\alpha}{Re}i[(U - c)(v'' - \alpha^2 v) - vU''] = 0 \tag{3.9}$$

This is the equation upon which the subsequent numerical predictions are based. The derivation of eqn.(3.9) is shown fully in Appendix A.1.

3.2 Shortcomings in the use of the Orr-Sommerfeld equation

The use of the Orr-Sommerfeld stability equation is slowly going out of favor with the CFD community. This is primarily due to the development of new, efficient methods of solving the complete (non-linear) Navier-Stokes equations. The ever-increasing speeds of digital computers have made the use of 'Direct Numerical Simulation' codes (DNS) more appealing. These DNS codes do, however, require considerably more computational power, and should only be applied when necessary. Furthermore, the use of such techniques has dangers in itself because it can temp one to loose touch with the physics of the problem.

There are two principal objections to the use of the Orr-Sommerfeld equation. These stem from the fact that the Navier-Stokes equations have been linearized and that a local parallel-flow approximation has been used. To assess the implications of these approximations, it is essential that we consider the physics of the flow. In particular, it is vital that one understands when these non-parallel and non-linear effects become important.

The true physical problem involves disturbances made up of many modes which interact in a non-linear manner only in the later stages of transition. This implies that the Orr-Sommerfeld equation should only be used to predict the behaviour of a disturbance in the early stages of transition. Furthermore, because the equations have been manipulated to form an eigenvalue problem, there can be no account of the amplitude of the ingested disturbance. It has, however, become common practice for engineers to use a semi-empirical method known as the e^n method of Smith and Gamberoni (1956). This method uses predictions from the linear theory to obtain an approximation to the transitional Reynolds number. This technique is explained in more detail in § 4.4.3.

For the current research programme, the primary aim is to ascertain whether

PPW's can achieve transition delay. For this purpose, we are not particularly interested in the later stages of transition. Hence, the use of the linearized equations (and the Orr-Sommerfeld equation) represents a more appropriate use of computational resources. Additional complications such as the effect of curvature or compressibility can be accounted for, but the current study considers neither.

Section 6.5.1 outlines how to circumvent the problem of arbitrary disturbance amplitude which is inherent in the eigenvalue problem. By scaling numerical results from values obtained by experiment, it is possible to map the evolution of a disturbance. Furthermore, linearity tests taken from experimental results provide a valuable tool in assessing at what point non-linear effects become important, and when computational results from the linear code can no longer be relied upon.

Most boundary layers grow in the downstream direction. Furthermore, even for a wave of constant frequency, the wavenumber and perturbation quantities $(\alpha, \hat{u}, \hat{v}, \hat{p})$ of the 2D boundary layer are all functions of x. Therefore, the problem of boundary layer stability is essentially a wave propagation problem in a nonuniform medium. Furthermore, the linearized Navier- Stokes equations are not separable in this form and therefore a normal mode solution is not available. The situation can be simplified greatly by using the so called *quasi parallel* stability theory. This theory essentially sets the non-parallel terms in the stability equations, to zero (as shown in § 7.3.1). This is equivalent to the assumption that the growth of the boundary layer is negligible over the distance of a single wavelength. The method retains the parallel-flow normal modes as local solutions, but it does represent an additional approximation over that of linearisation. Clearly these effects will become more important at lower Reynolds numbers, or when one considers the propagation of waves over many wavelengths. However, in view of the infancy of the current research and the relatively high Reynolds numbers envisaged, the quasi parallel theory is adequate. Extensions of this PPW theory to include non-parallel effects are best left for future development.

3.3 The passive porous wall boundary condition

The following work relies on the concept of admittance used in the field of acoustics. The theory was essential the product of an initial feasibility study by Carpenter (1996). The beauty of the admittance approach is that one can specify a range of wall configurations with one complex admittance value. Hence, the parameter space searched by stability codes when seeking to optimize PPW's is very much reduced. This technique allows the selection of the appropriate wall admittance values which seem likely to produce T-S suppression. Once the beneficial admittance parameter space is defined, it is then possible to apply physical wall parameters to determine if these admittances are achievable in practice. Furthermore, the complexity of the model used to define the wall admittance can be increased without the need to recompute the ranges of beneficial admittance.

The general complex admittance function for a wall can be defined as follows;

$$Y_b \equiv \frac{\text{Fluctuating flow rate per unit area through wall}}{\text{Fluctuating effective pressure at wall}} \tag{3.10}$$

or in a succinct mathematical form:

$$Y_b = \frac{\hat{q}_w}{\hat{p}_w} \tag{3.11}$$

where $\hat{q}_w$ is the fluctuating flow rate per unit area entering the wall and $\hat{p}_w$ is the fluctuating driving pressure at the wall's upper surface. Using the sign conventions shown in fig.(3.1) it is clear that for unit area, $\hat{q}_w = -\hat{v}_w$.

For continuity, the admittance calculated at the boundary-layer side, eqn.(3.11) must be equal to the admittance of the wall itself, Y_w. Hence:

$$Y_b = Y_w \tag{3.12}$$

or

$$Y_w \cdot \hat{p}_w + \hat{v}_w = 0 \tag{3.13}$$

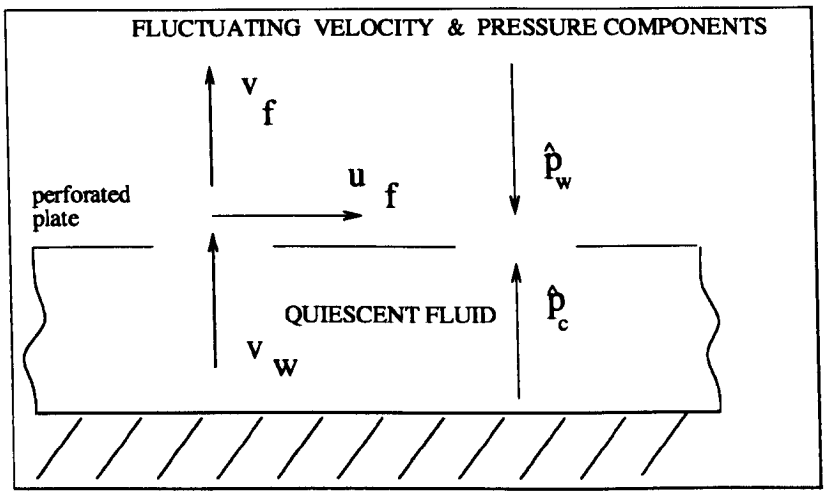

Figure 3.1: Sign conventions used for the pressure and velocity perturbations through the porous surface

To date the admittance of the wall has been taken to be the collective admittances of both the perforated plate and the cavity fluid beneath it. However, if the wall and common cavity are treated separately, it is possible to define their individual admittances as follows:

For the pores themselves;

$$Y_p = \frac{\hat{q}_w}{\hat{p}_w - \hat{p}_c} \tag{3.14}$$

where Y_p is the admittance afforded to the pores within the wall and $(\hat{p}_w - \hat{p}_c)$ is the fluctuating pressure differential across a pore.

For the cavity fluid;

$$Y_s = \frac{\hat{q}_w}{\hat{p}_c} \tag{3.15}$$

where $\hat{p}_c$ is the effective driving pressure at the wall's lower surface and Y_s is the admittance of the fluid in the cavity.

It can be seen that the elimination of all pressure and flow rate terms in eqns. (3.14), (3.15) and (3.13) reveals the following relationship for the overall admittance of the wall (note $\hat{q}_w = -\hat{v}_w$):

$$\frac{1}{Y_w} = \frac{1}{Y_p} + \frac{1}{Y_s} \tag{3.16}$$

The current theory is constrained to infinitely thin walls. As such we can say that the pores have an infinite admittance ($Y_p = \infty$). In practice this means that there can be no losses due to shear stresses on the sides of the pore, which seems reasonable for infinitely thin walls with a continuous distribution of porosity. Hence:

$$\frac{1}{Y_w} = \frac{1}{Y_s} + \frac{1}{Y_p} \approx \frac{1}{Y_s}$$

The above simplification allow us to revert to the use of eqn.(3.13) for the remainder of this chapter. However, the exercise illustrates that the theory does have the capacity to be expanded to include features (which may reduce overall admittances) such as finite wall thickness, provided one can create a model which appropriately accounts for this.

3.3.1 Forming the PPW boundary conditions for the Blasius boundary layer

The admittance function used in the remainder of this chapter will only account for the admittance of the cavity fluid. Clearly, only a fraction of the fluid is exposed to the boundary layer (this fraction being the porosity). Admittance factors must therefore be multiplied by the porosity factor σ. Hence:

$$Y_w = \sigma(Y_w)_{\sigma=1} \tag{3.17}$$

where σ is defined as:

$$\sigma = \left[\frac{\text{Area of a single pore} \times \#\text{ of pores}}{\text{Total porous area}}\right] \tag{3.18}$$

The linear stability characteristics of flows over PPW's can be determined by the solution of the Orr-Sommerfeld equation as discussed in § 3.1. The current

section deals with the mathematics of casting the PPW boundary conditions in a form suitable for the numerical solution of eqn.(3.9).

The basic strategy for solving the Orr-Sommerfeld equation for the PPW boundary condition is to specify the admittance from both sides of the wall. The stability characteristics of the boundary layer flow are modeled conventionally, using the Orr-Sommerfeld equation. The only difference here is that the wall boundary conditions are modified to account for the admittance (or porosity). The cavity flow is also modeled using the Orr-Sommerfeld equation, but setting the mean flow component to zero. Again, an admittance is defined for the velocity and pressure perturbations into the wall from the cavity side. The existence of a zero mean cavity flow is convenient because it greatly simplifies the solution to the equation. Indeed, an analytical solution can be derived for the cavity dynamics. The solution to the whole system is completed by demanding that the admittance from the boundary layer side be equal to that of the cavity side.

The pressure term of eqn.(3.13) can be eliminated by using the un-steady Navier-Stokes equations. For the x-component of the perturbation velocity and pressure, the following equation is derived:

$$\frac{\partial \hat{u}}{\partial t} + U\frac{\partial \hat{u}}{\partial x} + \hat{v}\frac{\partial U}{\partial y} + \frac{1}{\rho}\frac{\partial \hat{p}}{\partial x} = \nu \nabla^2 \hat{u} \tag{3.19}$$

The non-dimensional forms of the variables are defined as follows:

$$\bar{\hat{p}} = \frac{\hat{p}}{\rho U_\infty^2} \tag{3.20}$$

$$\bar{t} = \frac{tU_\infty}{\delta^*} \tag{3.21}$$

$$\bar{u} = \frac{\hat{u}}{\hat{U_\infty}} \tag{3.22}$$

The hats refer to the magnitudes of the relevant quantities and the over-bars refer to non-dimensional quantities. Using these non-dimensional quantities,

eqn.(3.19) can be written as follows:

$$\frac{\partial \bar{\hat{u}}}{\partial \bar{t}} + \bar{U}\frac{\partial \bar{\hat{u}}}{\partial \bar{x}} + \bar{\hat{v}}\frac{\partial \bar{U}}{\partial \bar{y}} + \frac{\partial \bar{\hat{p}}}{\partial \bar{x}} = \frac{1}{Re}\nabla^2 \bar{\hat{u}} \tag{3.23}$$

Assuming a disturbance of the form:

$$\bar{u} = \bar{\hat{u}}e^{i(\alpha x - \bar{\omega}\bar{t})} \tag{3.24}$$

therefore:
$$\frac{\partial \bar{\hat{u}}}{\partial \bar{x}} = i\alpha \bar{\hat{u}}e^{i(\alpha x - \bar{\omega}\bar{t})} \tag{3.25}$$

But, from the continuity equation:

$$\bar{\hat{u}} = \frac{iD\bar{\hat{v}}}{\alpha} \tag{3.26}$$

The 'D' denotes differentiation with respect to the non-dimensional y co-ordinate. Hence, all quantities can be expressed in terms of the non-dimensional y perturbation, $\bar{\hat{v}}$:

$$\frac{\partial \bar{\hat{u}}}{\partial \bar{x}} = -D\bar{\hat{v}} \tag{3.27}$$

$$\frac{\partial \bar{\hat{u}}}{\partial \bar{t}} = \frac{\omega D\bar{\hat{v}}}{\alpha} \tag{3.28}$$

The calculation of wall admittance requires all the relevant quantities be evaluated at the wall. Therefore the non-dimensional, unsteady Navier-Stokes eqn.(3.23) becomes:

$$\frac{\partial \bar{\hat{u}}_w}{\partial \bar{t}} + \bar{U}_w\frac{\partial \bar{\hat{u}}_w}{\partial \bar{x}} + \bar{\hat{v}}_w\frac{\partial U_w}{\partial \bar{y}} + \frac{\partial \bar{\hat{p}}_w}{\partial \bar{x}} = \frac{1}{Re}\nabla^2 \bar{\hat{u}}_w \tag{3.29}$$

The 'w' subscript refers to quantities evaluated at the wall. The second term is discounted because of the no-slip condition. After the substitution of expressions (3.26), (3.27), and (3.28) the following equation is obtained for the perturbation pressure:

$$\bar{\hat{p}}_w = \frac{1}{\alpha^2 Re}[(D^3\bar{\hat{v}}_w - \alpha^2 D\bar{\hat{v}}_w) + iRe(\omega D\bar{\hat{v}}_w + \alpha\bar{\hat{v}}_w + \alpha\bar{\hat{v}}_w DU_w)] \tag{3.30}$$

From eqn.(3.13) we have $Y_w\bar{\hat{p}}_w+\bar{\hat{v}}_w = 0$. Substituting for the perturbation pressure gives the following equation defining the wall's admittance from the boundary layer side:

$$\frac{Y_w D^3\bar{\hat{v}}_w}{Re} - \frac{\alpha^2 Y_w D\bar{\hat{v}}_w}{Re} + Y_w i\omega D\bar{\hat{v}}_w + Y_w i\alpha\bar{\hat{v}}_w DU_w + \alpha^2\bar{\hat{v}}_w = 0 \tag{3.31}$$

But,

$$\bar{\hat{u}}_w = D\bar{\hat{v}}_w = 0 \tag{3.32}$$

therefore:

$$\frac{Y_w D^3\bar{\hat{v}}_w}{Re} + Y_w i\alpha\bar{\hat{v}}_w DU_w + \alpha^2\bar{\hat{v}}_w = 0 \tag{3.33}$$

Equations (3.33) and (3.32) above stipulate two of the four real boundary conditions. The other two are implemented at the outer edge of the boundary layer. The outer boundary conditions ensure that disturbances will fall exponentially to zero at the outer edge.

Note that we require the wall boundary condition to perform as if it were a non-porous wall when the admittance is set to zero. For this to be the case, we require the u_w perturbation to be zero at the wall (the no-slip condition) and the v_w perturbation to be zero also (the no-penetration condition). It follows that if $u_w = 0$ then, using eqn.(3.32), $dv_w/dy = 0$ and hence $du_w/dx = 0$ by continuity. The constraints on the u_w perturbation and its derivative apply to both porous and non-porous walls equally provided normally aligned pores are assumed; only the penetration condition is altered by porosity. Indeed, if Y_w were set to zero then eqn.(3.33) would satisfy the no-penetration condition without any problem. However, the porous wall boundary condition fails to implement the no-slip condition, so this must be specified separately. Equation (3.31) refers to the general case where inclined pores can exist and for which the no-slip condition would not apply. For normal pores the no-slip condition is applicable, and all terms containing Dv_w and its higher derivatives in eqn. (3.31) may be neglected, resulting in eqn.(3.33).

3.3.2 Note on formulation of the PPW boundary condition for general 3D boundary layers

The derivation of the required boundary condition for general 3D boundary layers follows a pattern much the same as that followed in the previous section. The full derivation is presented in § 7.5. However, the equation is also included here for comparison with the 2D result of eqn.(3.33).

$$\frac{Y_w D^3 \bar{\hat{v}}_w}{Re} + Y_w i\bar{\hat{v}}_w \left[\alpha D\overline{U}_w + \beta D\overline{W}_w\right] + (\alpha^2 + \beta^2)\bar{\hat{v}}_w = 0 \tag{3.34}$$

It is apparent that the two equations are of a very similar form. The 3D boundary layer has a complex wavenumber of two components; one streamwise α and one spanwise wavenumber β. There are also two mean profile components, U and W. The use of this boundary condition will be discussed in detail in chapter 7.

3.4 Evaluation of wall admittance $Y_w = -\hat{v}_w/\hat{p}_c$ - solving the cavity dynamics

The cavity dynamics are described using the familiar Orr-Sommerfeld equation (3.9) with the mean flow set to zero:

$$\omega(D^2 - \alpha^2)\hat{v}_s = i\nu(D^2 - \alpha^2)^2\hat{v}_s \tag{3.35}$$

'D' denotes differentiation with respect to the non-dimensional y co-ordinate. The 's' subscript refers to the cavity flow below the passive porous plate.

Equation (3.35) is a 4^{th} order ordinary differential equation and has fundamental solutions of the form $e^{\lambda y}$. Its solution reduces to the following quartic equation:

$$-i\hat{v}_s[\lambda^4 - (2\alpha^2 + \frac{\omega}{i\nu})\lambda^2 + (\alpha^4 + \frac{\alpha^2\omega}{i\nu})] = 0 \tag{3.36}$$

The general solution to this equation takes the following form (as shown by Carpenter and Garrad (1985)):

$$\lambda_{1,2} = \pm\alpha, \quad \lambda_{3,4} = \pm\Omega \tag{3.37}$$

where

$$\Omega^2 = \alpha^2 - \frac{i\omega}{\nu} \tag{3.38}$$

giving:

$$\hat{v}_s = A_1 e^{\alpha y} + A_2 e^{-\alpha y} + A_3 e^{\Omega y} + A_4 e^{-\Omega y} \tag{3.39}$$

Using the same co-ordinate system as used on the boundary layer side of the wall, i.e. $y = 0$ corresponds to the top of the cavity next to the porous plate and $y = -H$ corresponds to the bottom of the cavity. The following boundary conditions apply to the cavity flow through a surface with normal pore alignment:

$$\hat{u}_s = \hat{v}_s = 0 \quad \text{at} \quad y = -H \tag{3.40}$$

$$\hat{v}_s = -\hat{v}_w, \quad \hat{u}_s = 0 \quad \text{at} \quad y = 0 \tag{3.41}$$

where the w subscript refers to values evaluated at the boundary layer side of the wall.

A symbolic algebra computation package (*MAPLE*) was used to evaluate the coefficients $A_1 \cdots A_4$ using the boundary conditions (3.40) and (3.41). The pressure term, required for the evaluation of the wall's admittance, was also computed using the technique outlined above.

3.4.1 Detailed solution of $\hat{v}_s$: cavity-normal perturbation velocity

First the system of equations, as defined by eqns.(3.39), (3.40) and (3.41), are written in matrix form:

$$\begin{bmatrix} e^{-\alpha H} & e^{\alpha H} & e^{-\Omega H} & e^{\Omega H} \\ \alpha e^{-\alpha H} & -\alpha e^{\alpha H} & \Omega e^{-\Omega H} & -\Omega e^{\Omega H} \\ 1 & 1 & 1 & 1 \\ \alpha & -\alpha & \Omega & -\Omega \end{bmatrix} \cdot \begin{bmatrix} A_1 \\ A_2 \\ A_3 \\ A_4 \end{bmatrix} = \begin{bmatrix} 0 \\ 0 \\ -q_w \\ 0 \end{bmatrix} \tag{3.42}$$

The matrix on the LHS in then inverted, using *MAPLE*, to give the required coefficients:

$$\begin{bmatrix} A_1 \\ A_2 \\ A_3 \\ A_4 \end{bmatrix} = \frac{1}{\Delta} \cdot \begin{bmatrix} \Omega \left(e^{\alpha H} \Omega e^{-\Omega H} - e^{\alpha H} \Omega e^{\Omega H} + \alpha e^{\alpha H} e^{-\Omega H} + \alpha e^{\alpha H} e^{\Omega H} - 2\alpha e^{-\Omega H} e^{\Omega H} \right) q_w \\ \Omega \left(-e^{-\alpha H} \Omega e^{-\Omega H} + e^{-\alpha H} \Omega e^{\Omega H} + \alpha e^{-\alpha H} e^{-\Omega H} + \alpha e^{-\alpha H} e^{\Omega H} - 2\alpha e^{-\Omega H} e^{\Omega H} \right) q_w \\ \alpha \left(-2e^{-\alpha H} e^{\alpha H} \Omega + e^{-\alpha H} \Omega e^{\Omega H} + \alpha e^{-\alpha H} e^{\Omega H} + e^{\alpha H} \Omega e^{\Omega H} - \alpha e^{\alpha H} e^{\Omega H} \right) q_w \\ -\alpha \left(2e^{-\alpha H} e^{\alpha H} \Omega - e^{-\alpha H} \Omega e^{-\Omega H} + \alpha e^{-\alpha H} e^{-\Omega H} - e^{\alpha H} \Omega e^{-\Omega H} - \alpha e^{\alpha H} e^{-\Omega H} \right) q_w \end{bmatrix} \tag{3.43}$$

where $\triangle$, the determinant of the matrix, is given as:

$$\triangle = 8\,\alpha\,\Omega + 2\,(\alpha - \Omega)^2 \cosh(H\,(\alpha + \Omega)) - 2\,(\alpha + \Omega)^2 \cosh(H\,(\alpha - \Omega)) \quad (3.44)$$

At the porous surface, from the cavity side, eqns.(3.39) and 3.41

define $\hat{v}_{s_{y=0}} = \hat{v}_w$ as:

$$\hat{v}_w = A_1 + A_2 + A_3 + A_4 \quad (3.45)$$

hence, the wall normal perturbation from within the cavity is computed simply by a summation of the coefficients given by matrix eqn.(3.43).

3.4.2 Detailed solution of $\hat{p}_c$ - perturbation pressure beneath porous boundary

The substitution of the boundary conditions of eqn.(3.41) into a version of the equation for perturbation pressure eqn.(3.30) with $DU_w = 0$ gives the following expression for $\hat{p}_c$ (the pressure at the underside of the porous surface) in the absence of a mean flow (details given Appendix A.4):

$$\hat{p}_c = \frac{\mu(D^3\hat{v}_s)_{y=0}}{\alpha^2} \quad (3.46)$$

This equation is made non-dimensional in the usual way, with $\hat{p} = \bar{\hat{p}}\rho U_\infty^2$, $\alpha = \overline{\alpha}/\delta^*$ and $\omega = \frac{\overline{\omega} U_\infty}{\delta^*}$:

$$\overline{p}_c = \frac{\nu(\overline{D}^3\hat{v}_s)_{y=0}}{\overline{\alpha}^2\delta^* U_\infty} = \frac{(\overline{D}^3\hat{v}_s)_{y=0}}{\overline{\alpha}^2 Re} \quad (3.47)$$

Recalling eqn.(3.39), the normal velocity perturbations within the cavity are:

$$\hat{v}_s = A_1 e^{\alpha y} + A_2 e^{-\alpha y} + A_3 e^{\Omega y} + A_4 e^{-\Omega y} \quad (3.48)$$

The third derivative of this, when evaluated at the wall gives:

$$(D^3\hat{v}_s)_{y=0} = \alpha^3 A_1 - \alpha^3 A_2 + \Omega^3 A_3 - \Omega^3 A_4 \quad (3.49)$$

while the no slip condition ($D\hat{v}_s = 0$) gives:

$$\alpha[A_1 - A_2] = -\Omega[A_3 - A_4] \tag{3.50}$$

Hence, after non-dimensionalising, $D^3\hat{v}_s$ simplifies to:

$$(D^3\overline{\hat{v}_s})_{y=0} = \overline{\alpha}[\overline{\alpha}^2 - \overline{\Omega}^2][A_1 - A_2] \tag{3.51}$$

However:

$$\Omega^2 = \alpha^2 - \frac{i\omega}{\nu} \qquad \text{implying:} \qquad \overline{\Omega}^2 = \overline{\alpha}^2 - i\overline{\omega}Re \tag{3.52}$$

so:

$$(D^3\overline{\hat{v}_s})_{y=0} = i\overline{\alpha}\overline{\omega}Re[A_1 - A_2] \tag{3.53}$$

and eqn.(3.47) becomes:

$$\overline{\hat{p}}_c = \frac{i\overline{\omega}}{\overline{\alpha}}[A_1 - A_2] \tag{3.54}$$

This indicates that the pressure at the cavity wall (or underside of the porous surface) is not directly affected by the viscous part of the solution.

The resultant expression for Y_s (the admittance from the cavity side) is given below:

$$Y_s \equiv -\sigma\frac{\hat{v}_w}{\hat{p}_c} = \sigma\frac{\overline{\alpha}}{\overline{\omega}}\left[\frac{A_1 + A_2 + A_3 + A_4}{A_1 - A_2}\right] = \sigma\frac{\overline{\alpha}}{\overline{\omega}}\frac{\Delta}{N_1} \tag{3.55}$$

where:

$$\Delta = 8\overline{\alpha}\overline{\Omega} + 2\left(\overline{\alpha} - \overline{\Omega}\right)^2\cosh(H\left(\overline{\alpha} + \overline{\Omega}\right)) - 2\left(\overline{\alpha} + \overline{\Omega}\right)^2\cosh(H\left(\overline{\alpha} - \overline{\Omega}\right)) \tag{3.56}$$

and

$$N_1 = \left[\overline{\Omega}(\overline{\alpha} + \overline{\Omega})(e^{(\overline{\alpha}-\overline{\Omega})H} - e^{-(\overline{\alpha}-\overline{\Omega})H}) + \overline{\Omega}(\overline{\alpha} - \overline{\Omega})(e^{(\overline{\alpha}+\overline{\Omega})H} - e^{-(\overline{\alpha}+\overline{\Omega})H})\right] \tag{3.57}$$

Note that the above expressions contain physical wall parameters such as cavity depth h (or $H = h/\delta^*$), substrate fluid viscosity ν and wall porosity σ. These

represent the three primary variables. It is notable that this analysis does not rely up the fluid substrate having the same viscosity as the fluid within the boundary layer. Indeed, the use of *aerogels* and other cavity damping materials permits the fluid substrate viscosity to be increased to achieve an optimum value of admittance. However, the effect of varying this parameter will not be assessed at this early stage.

When reference is made to sub/super-resonant operation, the following is implied. If we define a general admittance function as:

$$Y = \frac{-v}{p} \qquad p = \hat{p}e^{i\theta} \qquad v = \hat{v}e^{i\phi} \qquad \frac{-v}{p} = e^{i\pi/2}$$

where v is a fluctuating velocity and p a pressure. The phase relationship between these two quantities is given as:

$$\hat{p}e^{i(\theta+\pi/2)} = (-\hat{v})e^{i\phi}$$

Hence, if the phase of the driving pressure leads the flow into wall by $\leq \pi/2$, then the admittance is said to be in Super-Resonant mode. Sub-Resonance is defined by the phase relationship of $\geq -pi/2$. The results of § 5.1.3 indicate that, theoretically, the beneficial effects of PPW's occur due to super-resonant operation. This is in contrast to compliant walls which, as shown by Carpenter and Morris (1990), exhibit sub-resonant behavior.

3.4.2.1 Note on the evaluation of Y_s for a general three-dimensional boundary layer

The three-dimensional Orr-Sommerfeld equation takes the form;

$$\hat{v}'''' - 2\hat{v}''(\alpha^2+\beta^2) + (\alpha^2+\beta^2)^2\hat{v} = \frac{i}{\nu}\left[\overline{Q}(\hat{v}'' - \hat{v}(\alpha^2+\beta^2)) - \overline{Q''}\hat{v}\right] \qquad (3.58)$$

where $\overline{Q} = \alpha\overline{U} + \beta\overline{W} - \omega$.

For the cavity flow, the mean velocities U and W are set to zero. Thus $\overline{Q} = -\omega$. The resultant Orr-Sommerfeld equation for the cavity is:

$$\hat{v}'''' - 2\hat{v}''(\alpha^2 + \beta^2) + (\alpha^2 + \beta^2)^2\hat{v} = \frac{i}{\nu}\left[\overline{\omega}(\hat{v}'' - \hat{v}(\alpha^2 + \beta^2))\right] \tag{3.59}$$

If the definition $k^2 = [\alpha^2 + \beta^2]$ is used, the equation takes a form which is exactly the same as the two-dimensional equation (3.35), namely:

$$\omega(D^2 - k^2)\hat{v}_s = i\nu(D^2 - k^2)^2\hat{v}_s \tag{3.60}$$

The pressure at the upper wall of the cavity is given as:

$$\hat{p}_c = \frac{\mu D^3 \hat{v}_w}{k^2} \tag{3.61}$$

Therefore, the expression for the admittance Y_s is given as:

$$\frac{1}{\overline{Y_s}} = \frac{1}{\Delta_{3D}} \cdot \frac{i\overline{\omega}\overline{\Omega}}{\overline{k}} \cdot \left[2(\overline{k} + \overline{\Omega})\sinh(H(\overline{k} - \overline{\Omega})) + 2(\overline{k} - \overline{\Omega})\sinh(H(\overline{k} + \overline{\Omega}))\right] \tag{3.62}$$

$$\Delta_{3D} = 8\overline{k}\,\overline{\Omega} + 2\left(\overline{k} - \overline{\Omega}\right)^2\cosh(H\left(\overline{k} + \overline{\Omega}\right)) - 2\left(\overline{k} + \overline{\Omega}\right)^2\cosh(H\left(\overline{k} - \overline{\Omega}\right)) \tag{3.63}$$

So, it is apparent that the expressions for the cavity's admittance for the three-dimensional case is exactly the same as that for the two-dimensional case. All that is required is a simple substitution of the wavenumber $\overline{k} = \sqrt{\overline{\alpha}^2 + \overline{\beta}^2}$ where $\overline{\alpha}$ appeared previously.

Chapter 4

Solution Procedure - Spectral Method

4.1 Outline of the spectral method

A spectral discretisation method was chosen in preference to finite difference techniques for two main reasons. In the first instance, it has been shown that the use of Chebyshev polynomials is particularly suited to hydrodynamic stability problems because they require less storage and CPU time while still achieving high levels of accuracy. Orszag (1971) gives a detailed appraisal of such spectral techniques and their benefits. However, developments in computing over the past 15 years have made the comments of Orszag seem rather dated. The computation of the eigenvalues of the Orr-Sommerfeld equation is rather a trivial computational task by today's standards. Although one would still prefer to use efficient codes, the increased complexity and loss of transparency that accompany spectral codes makes their use unwarranted for reasons of speed and memory alone. There is, however, a far more compelling reason for using spectral techniques. As is shown in the proceeding section, the spectral formulation produces sets of linear equations cast in a manner which lend themselves well to solution

using the QR algorithm (details given by Press *et al.* (1992)). The QR algorithm has the particular advantage that it can provide every solution to the eigensystem without the requirement for an initial guess. Such schemes are termed *globally convergent.* A code with these capabilities has a two-fold use. The first is the instant identification (with a trained eye) of the expected T-S eigenvalue. This value can then be entered into the local code where one can study the effects of parameter variations, i.e. identification of neutral curves or growth curves. Hence, any local eigenvalue scheme would no longer require a clumsy initial guess at the T-S eigenvalue. The second benefit of a globally convergent scheme is that one can examine the likelihood of any additional modes of instability which result from a modified wall boundary condition. Work on compliant walls, Lucey and Carpenter (1995), reveals that additional wall-bound instabilities can exist which can themselves lead to transition. Global codes such as those envisaged here have been invaluable in predicting such instabilities. Although one would obviously not expect PPW's to exhibit an instability akin to divergence in compliant walls , it is nonetheless important that a global search is done to ensure that no other, as yet unknown, instabilities can exist.

The Orr-Sommerfeld equation (3.9) is expressed, in operator form, in eqn.4.1 below where L_i is a linear differential operator, ϕ is a complex function and α is a complex eigenvalue.

$$\sum_{i=0}^{4} \alpha^{4-i} L_i \phi = 0 \tag{4.1}$$

The semi-infinite fluid domain $y \in [0, \infty]$ is mapped to the finite spectral interval $z \in [-1, 1]$ using the following algebraic mapping:

$$z = \frac{y-2}{y+2} \tag{4.2}$$

The derivative of the physical variable, y, is related to the derivative of the mapped variable z, by the metric $(m(z))$:

$$\frac{d}{dy} = m(z)\frac{d}{dz} \qquad \text{where} \qquad m(z) = \frac{(1-z)^2}{4}$$

Higher order derivatives are obtained in a similar manner and are shown in Appendix A.2.

Using the non-dimensional form of the Orr-Sommerfeld equation given by eqn.(3.9). The mapped variable (z) transforms this equation into the following form:

$$A\hat{v}''''(z) + B\hat{v}'''(z) + C\hat{v}''(z) + D\hat{v}'(z) + E\hat{v}(z) = 0 \tag{4.3}$$

The values of the coefficients A ... E are given as follows, where A represents the coefficients of the 4^{th} order derivative, B the 3^{rd} order ... and E the $\hat{v}$ coefficients.

$$\begin{aligned}
A &= im^4 \\
B &= 6im^3m' \\
C &= 7im^2m'^2 + 4im^3m'' - 2i\alpha^2m^2 - Re\, m^2(\omega - \alpha\overline{U}) \\
D &= 4im^2m'm'' + im^3m'' + imm'^3 - 2i\alpha^2mm' \\
&\quad -Re\, mm'(\omega - \alpha\overline{U}) \\
E &= i\alpha^4 - Re\,\alpha^3\overline{U} + Re\,\alpha^2\omega - Re\,\alpha\left[mm'\overline{U}' + m^2\overline{U}''\right]
\end{aligned} \tag{4.4}$$

where m' etc. are the derivatives of the metric (as defined by eqn.(4.3)) with respect to the mapped co-ordinate z.

As outlined by Bridges and Morris (1984), it is much easier to use integrals of Chebyshev polynomials rather than derivatives. Accordingly, eqn.(4.3) is integrated four times to yield the following;

$$\begin{aligned}
A\hat{v} + \int(-4A' + B)\hat{v}dz + \int\int(6A'' - 3B' + C)\hat{v}dz + \int\int\int(-4A''' + 3B'' - 2C' + D)\hat{v}dz \\
+ \int\int\int\int(A'''' - B''' + C'' - D' + E)\hat{v}dz = d_0 + d_1z + d_2z^2 + d_3z^3
\end{aligned} \tag{4.5}$$

where $d_0 \ldots d_4$ are constants of integration.

The transformed variable $\hat{v}(z)$ is then expressed as a finite Chebyshev series expansion:

$$\hat{v}(z) = \sum_{n=0}^{N} a_n T_n(z) \tag{4.6}$$

where $T_n(z) = \cos n\theta$ and $\theta = \cos^{-1}(z), \quad n = 0, 1, 2, 3, \ldots$

and $z_j = \cos \frac{\pi j}{N} \qquad j = 0, \ldots, N$

Equation (4.5) is now discretised using the series expansion of equation (4.6) and the following recurrent integral relations:

$$\int T_n(z)dz = \begin{cases} \frac{T_{n+1}(z)}{2(n+1)} - \frac{T_{n-1}(z)}{2(n-1)} & \text{n} \geq 2 \\ \frac{1}{4}\{T_0(z) + T_2(z)\} & \text{n} = 1 \\ T_1(z) & \text{n=0} \end{cases} \tag{4.7}$$

The derivations of these relations are given by Fox and Parker (1968). The following Chebyshev product formula is also required:

$$2T_m(z)T_n(z) = T_{m+n}(z) + T_{m-n}(z) \tag{4.8}$$

A set of discretised equations can now be obtained by equating the coefficients of T_n for $n = 4, \ldots, N$. This provides $(N - 4)$ equations in terms of the unknowns $a_4, \ldots, a_N$. The MAPLE symbolic algebra package was used to compute the required coefficients. The detailed form of the resulting equations is far too complicated to be presented here. However, a simplified view of the discretised equation is given as follows:

$$D_4(\alpha) = C_4\alpha^4 + C_3\alpha^3 + C_2\alpha^2 + C_1\alpha + C_0 = 0 \tag{4.9}$$

Here, each equation is separated into powers of the eigenvalue α. $C_4 \ldots C_0$ are complex matrices of order $(N + 1)$.

The equations for $n = 0, \ldots, 3$ can be used to determine the constants of integration, $d_0, \ldots, d_3$. However, the solution of these is not important for the eigenvalue problem. Instead, the four boundary conditions can be inserted into the system in their place.

The lambda matrix $D_4(\alpha)$ may also be cast in companion matrix form. This is simply a linearisation of the lambda matrix (Lancaster (1964)), with order $4(N+1)$. Equation (4.10) below illustrates how the companion matrix is formed:

$$\left\{ \left| \begin{array}{cccc} -C_1 & -C_2 & -C_3 & -C_4 \\ I & 0 & 0 & 0 \\ 0 & I & 0 & 0 \\ 0 & 0 & I & 0 \end{array} \right| - \alpha \left| \begin{array}{cccc} C_0 & 0 & 0 & 0 \\ 0 & I & 0 & 0 \\ 0 & 0 & I & 0 \\ 0 & 0 & 0 & I \end{array} \right| \right\} \left\{ \begin{array}{c} \alpha^3 \mathrm{a} \\ \alpha^2 \mathrm{a} \\ \alpha \mathrm{a} \\ \mathrm{a} \end{array} \right\} = \left\{ \begin{array}{c} 0 \\ 0 \\ 0 \\ 0 \end{array} \right\} \tag{4.10}$$

where 'a' is the right latent vector of $D_4(\alpha)$.

4.1.1 Spectral representation of PPW boundary conditions

The system of equations defined in the previous section must now be closed using the 4 boundary conditions (2 wall conditions and 2 far field conditions). The discretisation is done as follows:

Both the no-slip condition and the outer boundary condition remain unchanged for the PPW case. These constraints, together with the PPW wall admittance boundary condition are shown below. Note that the wall coordinate is represented by $z = -1$ in the mapping, while the free stream corresponds to $z = 1$. Primes denote derivative with respect to the mapped variable (z).

$$\bar{\hat{v}}'(-1) = 0 \tag{4.11}$$

$$\frac{Y_w \bar{\hat{v}}'''(-1)}{Re} + Y_w i\alpha \bar{\hat{v}}(-1) U_w' + \alpha^2 \bar{\hat{v}}(-1) = 0 \tag{4.12}$$

$$\bar{\hat{v}}(1) = 0 \tag{4.13}$$

$$\bar{\hat{v}}'(1) = 0 \tag{4.14}$$

The various terms evaluated at the boundary are given as :

$$\bar{\hat{v}}(-1) = \sum_{n=1}^{N} a_n T_n(-1) \tag{4.15}$$

$$\bar{\hat{v}}'(-1) = \sum_{n=0}^{N} a_n T_n'(-1) \tag{4.16}$$

etc ...

The derivatives T_n' etc., are given by (remembering $z = \cos\theta$):

$$\frac{d}{d\theta}(T_n(z)) = \frac{d}{dz}T_n(z)\frac{dz}{d\theta} = -T_n'(z)\sin\theta = -n\sin n\theta \tag{4.17}$$

Giving:

$$T_n'(z) = T_n'(\cos\theta) = \frac{n\sin n\theta}{\sin\theta} \tag{4.18}$$

At the wall boundary $z = -1$. Hence, $\theta = \cos^{-1}(-1) = \pm\pi$ and $T_n(-1) = \cos(\pm n\pi) = (-1)^n$.

Higher order derivatives (evaluated at the wall) are evaluated in a similar manner. A few are given below:

$$\begin{aligned} T_n'(-1) &= (-1)^{n-1}n^2 \\ T_n''(-1) &= \frac{1}{3}n^2(n^2-1)(-1)^n \\ T_n'''(-1) &= \frac{1}{15}(-1)^n(-n^6+5n^4-4n^2) \end{aligned} \tag{4.19}$$

The following equation defines the admittance boundary condition. This requires the computation of the third order mapped spatial derivative,

$$\frac{Y_w \bar{\hat{v}}_w'''(y)}{Re} + Y_w i\alpha \bar{\hat{v}}_w(y) U_w'(y) + \alpha^2 \bar{\hat{v}}_w(y) = 0 \tag{4.20}$$

where

$$\frac{d^3\bar{\tilde{v}}(y)}{dy^3} = m^3 \frac{d^3\bar{\tilde{v}}}{dz^3} + 3m^2 \frac{dm}{dz}\frac{d^2\bar{\tilde{v}}}{dz^2} + (m^2 \frac{d^2m}{dz^2} + m\frac{dm}{dz}^2)\frac{d\bar{\tilde{v}}}{dz} \tag{4.21}$$

But at $z = -1$, $m(-1) = 1/4[1-(-1)]^2 = 1$. Similarly, $m'(-1) = -1$ and $m''(-1) = 1/2$

Therefore, the third derivative evaluated at the wall, can be simplified to give the following:

$$\bar{\tilde{v}}_w''' = \bar{\tilde{v}}'''(-1) - 3\bar{\tilde{v}}''(-1) + \frac{3}{2}\bar{\tilde{v}}'(-1) \tag{4.22}$$

Upon substitution of the Chebyshev series:

$$\bar{\tilde{v}}_w''' = \frac{1}{30}\sum_{n=0}^{N}(-1)^n[-2n^6 - 20n^4 - 23^2] \tag{4.23}$$

The transformations used on the $\bar{\tilde{v}}$ derivatives also apply to the mean flow derivatives. However, since $U_w' = m(-1)U'(-1)$ and $m(-1) = 1$, the result remains unchanged.

In summary, the discretised wall boundary conditions take the follow form:

$$\begin{aligned}
\bar{\tilde{v}}(-1) &= \sum_{n=0}^{N}\left[\frac{Y_w(-1)^n[-2n^6 - 20n^4 - 23^2]}{30Re} + (-1)^n\left(Y_w i\alpha U_w' + \alpha^2\right)\right]a_n = 0 \\
\bar{\tilde{v}}'(-1) &= \sum_{n=0}^{N}(-1)^{n-1}n^2 a_n = 0
\end{aligned} \tag{4.24}$$

The outer boundary conditions are unchanged for the PPW and are discretised as follows:

$$\bar{\tilde{v}}(1) = \sum_{n=0}^{N} a_n = 0$$

$$\bar{\hat{v}}'(1) \quad = \quad \sum_{n=0}^{N} n^2 a_n = 0 \tag{4.25}$$

4.2 The globally convergent scheme

The benefits of a globally convergent scheme have already been outlined at the beginning of this chapter. This section briefly outlines how the linear equations must be formulated for such a scheme. Globally convergent schemes can only be applied to the system of equations (4.9) once the matrix equation has been transformed into companion matrix form eqn.(4.10). Details of this transformation are given in Appendix A. Equation (4.26) below gives the final form of the Frobenius companion matrix.

$$A = \begin{bmatrix} -C_0^{-1}C_1 & -C_0^{-1}C_2 & -C_0^{-1}C_3 & -C_0^{-1}C_4 \\ I & 0 & 0 & 0 \\ 0 & I & 0 & 0 \\ 0 & 0 & I & 0 \end{bmatrix} \tag{4.26}$$

This equation has increased the order of the eigensystems fourfold, making its solution much more computationally expensive. In particular, the application of the QR algorithm to this equation will require computational times of order $(4m)^3$. However, as previously explained, the global code is not intended to be the 'work horse' of the current numerical investigation. Its role is to feed local eigenvalue schemes with starting values and to provide a means of searching for additional modes of instability. The speed of the code is, therefore, not of primary concern.

The QR algorithm uses QR decomposition to transform the matrix into a form whereby it can be solved through back substitution.

For a given matrix A, QR decomposition is defined as:

$$A = Q \cdot R \tag{4.27}$$

where Q is an orthogonal and R is an upper triangular matrix.

Therefore, to solve a system of equations given by:

$$Ax = b \tag{4.28}$$

we must first form $(Q^T b)$ and then seek the solution to eqn.(4.29) below by back substitution.

$$Rx = Q^T b \tag{4.29}$$

This is a fairly simple computation since R is upper triangular. The majority of the algorithm's work involves the initial formation of the Q & R matrices. This is normally done using successive Householder transformations. In the current investigation, once the companion matrix has been formed, the Nag^{TM} FORTRAN library subroutine $F02GJF$ is used as a ***black box*** implementation of the QR algorithm.

4.3 Local iteration of eigenvalues

The global method of § 4.2 is not suitable for the eigenvalue codes which require continuous parameter variation. The computation of disturbance growth curves (e^n methods), neutral curves and alike need efficient numerical schemes because they require many concurrent solutions to the eigensystem. Such schemes should aim to locally track the path of a eigenvalue, given a reasonable initial guess, while one or more parameters is continuously perturbed. The initial guess could simply be the eigenvalue computed at the previous parameter value, or a better guess could be extrapolated from a series of previous solutions. The extrapolation technique would be preferred because this would allow larger parameters steps without loss of convergence.

Bridges and Morris (1984) provide details of an appropriate numerical technique which suits our purpose. The scheme uses the lambda matrix, eqn.(4.30) given below, of order $(N + 1)$ rather than the companion matrix which is four times larger. As such, this scheme has the potential to be very much faster.

$$D = +\alpha^4 \left[C_4 \right] +\alpha^3 \left[C_3 \right] +\alpha^2 \left[C_2 \right] +\alpha \left[C_1 \right] + \left[C_0 \right] \qquad (4.30)$$

The eigenvalues of the lambda matrix are deduced using the local iteration scheme of Lancaster (1964). The cubicly convergent iterative formula is given as:

$$a_{k+1} = \frac{a_k - 2f(a_k)}{\{[f(a_k)]^2 - f^{(1)}(a_k)\}} \qquad (4.31)$$

where $f(a_k)$ if given by:

$$f(a_k) = T_r\{D^{-1}(a_k)D^{(1)}(a_k)\}. \qquad (4.32)$$

D^{-1} is the inverse of the D matrix eqn.(4.9), D^1 is the derivative with respect to α,

$$f^{(1)} = T_r\{D^{-1}D^{(2)} - [D^{-1}D^{(1)}]^2\} \qquad (4.33)$$

and $T_r\{A\}$ denotes the trace of A, which is the sum of the main diagonal elements $a_{ii}, i = 1, 2, \ldots, n$.

In the majority of codes used in the current work, the eigenvalue used at the start of each iterative step is given using extrapolation routines. This is necessary because the equations to be solved are coupled by the wavenumber α which appears in the boundary condition. Therefore, solutions must be of an iterative nature. This feature is explained in more detail in § 4.3.1. However, the codes used here predict the next eigenvalue by using a polynomial curve fit to past solutions along the parameter/eigenvalue path. Cubic polynomials are used in most instances together with an adaptive step size routine which ensures stability. For example, the computation of neutral curves uses the past values of Reynolds number for the ordinate of the curve fit, and the eigenvalue for the abscissa. Two extrapolations can be used in this case, one for $\Re(\alpha)$ vs. *Re* (which speeds up local eigenvalue iteration) and the other for ω vs. *Re* (which speeds up the iteration routine used to identify the neutral eigenvalue § 4.4.2).

4.3.1 Solution of the coupled equations

The eigenvalue problem described above is complicated because the boundary conditions themselves change depending upon the solution to the equation, i.e. the boundary conditions are coupled to the complex wavenumber (α).

Having discretised the Orr-Sommerfeld equation (using a spectral technique) into a series of linear equations, it becomes evident that the resulting equations have the parameter α appearing non-linearly. This has particular relevance when specifying the boundary conditions. If the discretisation technique outlined by Bridges and Morris (1984) is used, then the boundary conditions are contained within the first four rows of the resulting matrix. The first row in particular, contains the wall boundary condition which is dependent upon the wall admittance. Since the value of admittance is dependent upon the complex eigenvalue, it is evident that the matrix is coupled and cannot be solved directly using global techniques such as the QR algorithm (Press *et al.* (1992)). Iterative schemes must

therefore be used.

The above complication was overcome in initial numerical simulations by decoupling the problem as follows. First an assumed complex value for the wall admittance was specified, and then the boundary layer eigenvalue problem was solved to yield the corresponding complex wavenumber (α). This admittance and wavenumber were then checked with the analytical expression for the cavity flow to see if they were achievable in practice (using physical wall parameters). However, the prototyping of passive porous walls requires the specification of the optimum wall porosity σ, cavity depth h and wall thickness. As such, the computation outlined above, while being of considerable academic interest, is of little practical value because is does not attempt to solve the coupled problem. In essence, only the solution of the coupled problem will enable individual physical wall parameters to be varied such that the wall's performance can be optimized.

It would, of course, be possible to specify a complex admittance and then calculate the resulting corresponding value of α. This value of α could then be used to calculate an updated value of admittance and the process could be repeated in an iterative manner until the assumed admittance and the calculated value converge. This technique is the simplest way of decoupling the equations and gaining some meaningful results. However, its implementation is rather clumsy and slow; thus a search for a more elegant method was initiated.

A quick and easy way to solve the problem was to use extrapolation techniques. Essentially, as the parameter space is mapped out, the solution wavenumbers tend to follow smooth loci. This could be exploited to provide accurate initial estimates to the eigenvalue at the next step of a particular parameter. This technique is not without its problems. At the start of the computation there are no previous values upon which to base the extrapolation. As such, the local eigenvalue scheme has difficulty is searching for solutions, and convergence is slow. This can be overcome by making only small steps in parameter space. Once three of four values are available for extrapolation, the search scheme becomes much

quicker. In general, the initial guess is good enough so that the first two iterations were within a tolerance limit of 1×10^{-6}. The scheme used in the current study had adaptive step size control. This allowed the step size to be either increased or decreased depending on the speed and degree of convergence.

4.4 Techniques to illustrate the effects of porosity

There are many different ways in which the results of the numerical simulations can be presented. All such schemes use the same basic code. The following sections present the basic principles behind each of these schemes and give an insight into how their results can be interpreted.

From a practical point of view, the primary goal of these methods is to illustrate whether PPW's can have a favorable effect upon transition. However, having proven PPW's to either work or fail, the challenge is then to find out why. Once the basic mechanism has been understood, the engineer is better equipped to optimize the wall's properties to achieve more beneficial results. To this end, some of the schemes presented here have been specifically designed to uncover the fundamental mechanisms behind any possible transition-delaying properties.

The numerical methods used herein have been used extensively in previous investigations, e.g. Carpenter and Morris (1990). As such, a validation of the theory is not explicitly required. However, this particular application of the Chebyshev–Tau method is rather complex and prone to coding error. Furthermore, research into compliant walls using a similar spectral technique has shown that a finer computational resolution is required for such walls to achieve accuracies equivalent to those of the non-porous wall. i.e. higher order Chebyshev polynomials are required. The order of Chebyshev polynomial used is expected to be critically dependent upon the degree of porosity of a particular porous wall. If the order is too low the results will not be of the required accuracy, too high and the code will be needlessly slow and some floating point operations may exceed machine pre-

cision (since the higher order terms become extremely small). For these reasons, it is important to compare the spectral code's performance with other techniques. Section 5.2.1 details the selection of an appropriate polynomial order based upon the degree of wall porosity.

4.4.1 Eigenfunctions

The eigenfunctions given by the numerical simulations are the solution vectors to the Orr-Sommerfeld equation. Provided the Tollmien-Schlichting instability is the only instability responsible for the early stages of transition for PPW's, we will only be interested in the eigenfunction (or solution vector) which corresponds to this mode.

The computation of eigenvectors is done within the framework of the locally convergent scheme § 4.3. The method outlined here is the same as that used by Bridges and Morris (1984) whereby a set of linear equations (of a form given by eqn.(4.34) below) are solved using a cubically convergent iterative scheme. The computation of the $D(\alpha)$ matrix is achieved efficiently using the aforementioned scheme. However, the computation of the inverse $(D(\alpha)^{-1})$ is also a fortunate byproduct of the numerical scheme which can be put to good use in the computation of eigenvectors. A simple inverse iteration of the solution vectors provides a very robust method for deducing the eigenfunctions. The iterative steps are defined as follows:

$$D_4(\alpha_i)x_i = 0 \tag{4.34}$$

$$D_4(\alpha)x^{k+1} = \sigma x^k \tag{4.35}$$

The vectors x^{k+1} and x^k are consecutive approximations to the eigenvector and σ is a scaling factor (set to unity in this case). Using an initial guess of $x_0 = [1, 1, \ldots, 1]^T$, convergence is generally achieved within two iterations.

The eigenfunctions of the T-S mode have a physical significance. If the function is plotted through the boundary layer, it can be interpreted as the normal-

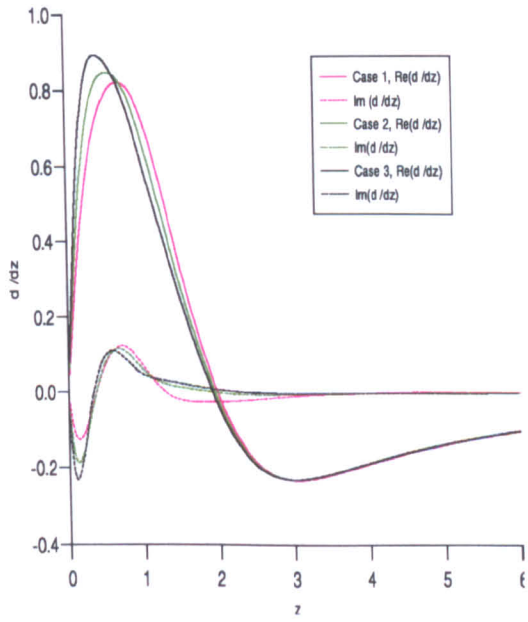

4.1.1: Spectral code computation of the eigenfunction components, corresponding to the same parameters as used in 4.1.2

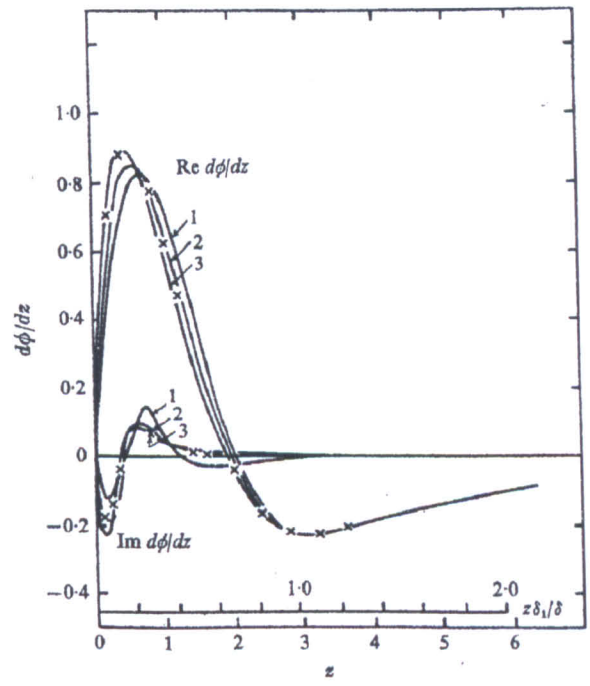

4.1.2: Results of Jordinson (1970) - Eigenfunctions Case 1, *Re*= 336, $\beta = 0.1297$, $\alpha_r = 0.3084$, $\alpha_i = 0.0079$. Case2, *Re*= 598, $\beta = 0.1201$ $\alpha_r = 0.3079$, $\alpha_i = 0.0019$. Case 3, *Re*= 998, $\beta = 0.1122$, $\alpha_r = 0.3086$, $\alpha_i = -0.0057$.

Figure 4.1: Validation of spectral code's eigenfunction computation by comparison with the published results of Jordinson (1970)

ized variation in the normal component of the perturbation velocity which corresponds to a Tollmien-Schlichting wave. It must be remembered that no amplitude information is provided, so that one can only deduce how the function varies through the boundary layer.

The computations of Jordinson (1970) are used to validate current computations. Figure (4.1.1) plots the eigenfunctions generated using the method described in this section. These results can be compared directly with those of Jordinson, fig.(4.1.2). In both cases the amplitudes of the eigenfunctions are normalized. There is excellent agreement between the two plots for all of the cases shown. It can therefore be concluded that the codes used to generate eigenfunc-

tions are free from error.

4.4.2 Neutral curves

The production of neutral curves requires the computation of both ω and α_r such that $\alpha_i = 0$ for a given Reynolds number. Again, the work of Bridges and Morris (1984) details a suitable technique for the identification of such points. The technique they use is outlined as follows.

At a given Reynolds number, a simple Newton-Raphson method is used to calculate the step in frequency required to find the root ($\alpha_i = 0$). The following step ($\Delta\omega$) is used:

$$\Delta\omega = -(\alpha_i)_k / \Im\left[\frac{\partial\alpha}{\partial\omega}\right]_k \tag{4.36}$$

$\Im$ denotes the imaginary part of the relevent argument. Similarly, $\Re$ represents the real part. The k represents the current iteration cycle. The step in frequency, given above, must be accompanied by a step in wavenumber (α_r) using $\Re\left[\delta\alpha/\delta\omega\right]$:

$$(\alpha_r)_{k+1} = (\alpha_r)_k + \Delta\omega\Re\left[\frac{\partial\alpha}{\partial\omega}\right]_k \tag{4.37}$$

with

$$\omega_{k+1} = \omega_k + \Delta\omega \tag{4.38}$$

The right eigenvector a is defined by:

$$D_4(\alpha)a = 0 \tag{4.39}$$

The left eigenvector b is also required such that:

$$b^H D_4(\alpha) = 0 \tag{4.40}$$

where H denotes the complex conjugate transpose. However, b also satisfies:

$$D_4^H(\alpha)b = 0 \tag{4.41}$$

The computation of $\delta\alpha/\delta\omega$ is achieved as follows.

First, the right eigenvector, b_i, is computed using the inverse iteration technique of eqn.(4.35). Then, differentiating eqn.(4.39) with respect to ω to get:

$$\frac{\partial D_4}{\partial \omega} a + D_4 \frac{\partial a}{\partial \omega} = 0 \tag{4.42}$$

Multiplying through by b_i^H cancels the second term in the above (see eqn.(4.40)), to give:

$$b^H \frac{\partial D_4}{\partial \omega} a = 0 \tag{4.43}$$

Note from eqn.(4.4) that the coefficients of ω are only those terms containing α^2 and α^0 terms. Hence, only C_2 and C_4 are required for the computation of $(\partial\alpha/\partial\omega)$:

$$\frac{\partial D_4}{\partial \omega} = \alpha^2 \frac{\partial C_2}{\partial \omega} + \frac{\partial C_4}{\partial \omega} + \frac{\partial D_4}{\partial \alpha} \frac{\partial \alpha}{\partial \omega} \tag{4.44}$$

Equation (4.43) becomes:

$$b_i \left[\alpha^2 \frac{\partial C_2}{\partial \omega} + \frac{\partial C_4}{\partial \omega} + D_4^{(1)} \frac{\partial \alpha}{\partial \omega} \right] a_i = 0 \tag{4.45}$$

The derivative can thus be computed:

$$\frac{\partial \alpha}{\partial \omega} = \frac{-b^H (\partial C_2/\partial \omega)\alpha^2 + (\partial C_4/\partial \omega) a}{b^H D_4^{(1)}(\alpha) a} \tag{4.46}$$

the $D_4^{(1)}$ derivative is available from the local iteration algorithm shown in § 4.3.

Therefore, the derivatives required for the search scheme defined by equation (4.36) and (4.37), are obtained simply by computing the real and imaginary parts of eqn.(4.46).

Figure (4.2) plots the paths of neutral stability for the Blasius boundary layer, derived using the techniques outline above. Here, the regions enclosed by the curves denote areas of instability. This plot also illustrates the neutral curves obtained by the solution of the coupled equations - for both 6% and 12% porous walls. Note how the critical Reynolds number increases from $Re_{cr}^{0\%} = 520$ to $Re_{cr}^{12\%} = 790$. It can also be seen that the application of the PPW boundary-condition tends to reduce the span of unstable frequencies. Furthermore, those frequencies which are unstable tend to be slightly higher than those for the non-porous control case.

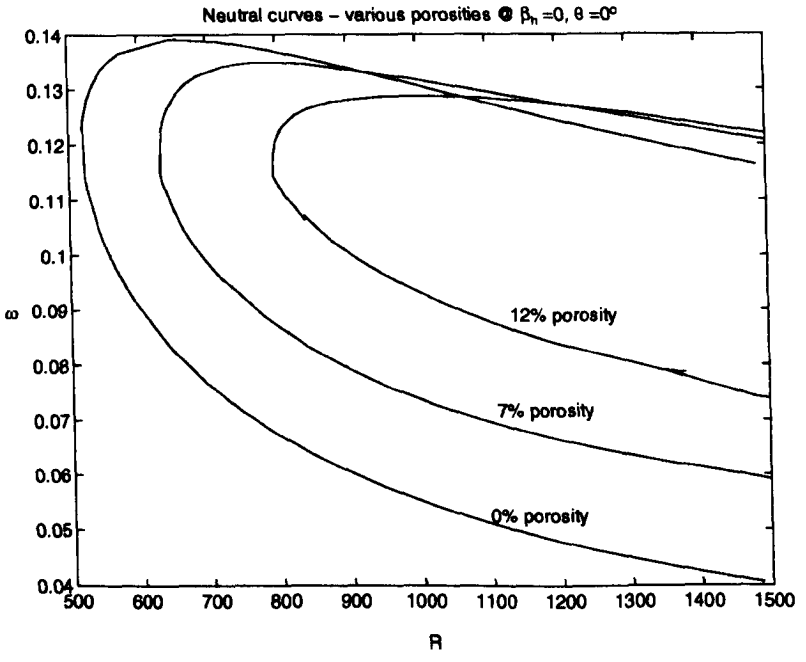

Figure 4.2: Neutral curves for the Blasius boundary layer for porosities of 0% ($Re_{cr} = 520$), 7% ($Re_{cr} = 635$) and 12% ($Re_{cr} = 790$).

4.4.3 Growth curves - e^n calculations

The theory presented herein allows the computation of the linear growth of a sinusoidal disturbance as it propagates downstream. From eqn.(3.7), we can deduce the following relation for the amplitude of a parallel harmonic disturbance as a function of x:

$$A(x) = A_0 e^{-\alpha_i x} \tag{4.47}$$

where A_0 is a constant. For a weakly non-parallel flow, α_i may be assumed to be a slow function of x - i.e. $d\alpha/dx \approx 0$. Therefore:

$$\frac{dA}{A} = -\alpha_i dx \tag{4.48}$$

Upon integration, we obtain:

$$\ln\left(\frac{A(x)}{A(x_0)}\right) = -\int_{x_0}^{x} \alpha_i(x)\, dx \tag{4.49}$$

where $\alpha_i(x)$ is evaluated assuming a locally parallel flow. Changing the variable of integration from the x co-ordinate to the equivalent streamwise Reynolds number

and non-dimensionalising all quantities gives:

$$\frac{\hat{v}_x}{\hat{v}_i} = \exp[\frac{-2}{(1.7204)^2} \int_{Re_i}^{Re} \bar{\alpha}_i^* \, dRe] \tag{4.50}$$

The value of the exponent in eqn.(4.50) is the so called n *exponent* in e^n calculations. As explained in § 3.2, the e^n method is a semi-empirical method used to predict transition. Generally, when the exponent reaches a value close to 9, a Blasius boundary layer is on the verge of transition to turbulence. There is no fundamental physical basis for this use of 9 as the critical exponent, it is merely a consequence of an extrapolation of the linear theory into the non-linear region apparent in the later stages of transition. The value of 9 has simply been derived by comparison with experimental results.

The use of the e^n method is, in itself, a very crude prediction of transition. However, its use is still very useful as a benchmark by which the performance of different wall configurations can be compared. For this reason, § 5.2.5 shows plots of how the n exponent varies down the length of the plate for a variety of wall porosities.

4.4.3.1 e^n code validation

The integration required for the computation of n factors was achieved using the FORTRAN numerical algorithm (Nag^{TM}), routine $D01GAF$. It is convenient at this stage to validate the implementation of this routine, together with the computation of eigenvalues. The e^n computation involves the summation of many eigenvalues and is useful for checking the accuracy of the code used herein. Comparisons are made with the published results of Yeo (1986) as follows: The non-dimensional frequency, F, is defined as:

$$F = \frac{\omega}{Re} \times 10^6 \tag{4.51}$$

$$\text{But} \quad \omega = \frac{\overline{\omega} U_\infty}{\delta^*} \quad \text{therefore:} \quad F = \frac{\overline{\omega}}{Re_{\delta^*}} = \frac{\omega \delta^*}{U_\infty Re_{\delta^*}} = \frac{\omega \nu}{U_\infty^2} \tag{4.52}$$

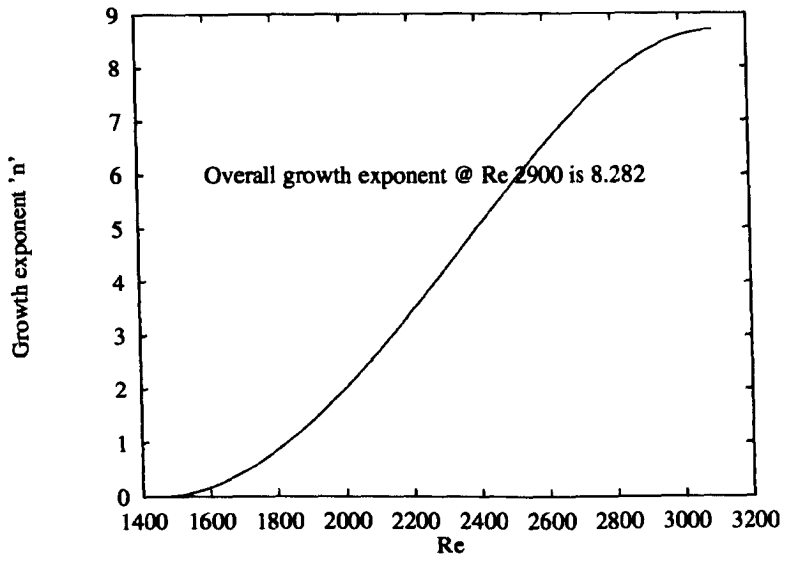

Figure 4.3: Growth curve for non-porous plate, $F = 28.5$, $Re = 1400$ to 2900 and overall exponent $n = 8.282$

Figure (4.3) corresponds to a disturbance of non-dimensional frequency 28.5×10^{-6}, which propagates down the length of a flat plate from a Reynolds number of 1400 to 2900. Such a disturbance has a overall growth exponent (at $Re = 2900$) of 8.282. This value is in agreement with Yeo (1986). It is thus concluded that the growth code is free from error.

4.4.4 Energy production by the Reynolds shear stress

The production of energy by the Reynolds stresses is the main mechanism by which the T-S instability is destabilized in rigid walls. Since our proposed wall is passive and non-evasive to the boundary layer, this is also likely to be the case for the PPW. For this reason, efforts have been made to ascertain what effect wall porosity can have on the Reynolds stress variation across the boundary layer. The component of Reynolds stress of interest is $-\rho\overline{uv}$, which interacts with the mean velocity gradient $d\overline{U}/dy$ to increase the energy of the perturbation. Thus, if $-\rho\overline{uv}$ and $d\overline{U}/dy$ are of the same sign over a dominant part of the flow, the perturbation grows in amplitude.

The Reynolds shear stress averaged over a cycle is given by:

$$\overline{\rho u' v'} = \frac{1}{T} \int_0^T \rho u' v' \, dt \tag{4.53}$$

where u' and v' are the instantaneous components of the perturbation velocity, parallel and perpendicular to the flat plate, and T is the period $2\pi/\omega$ of one oscillation of a T-S wave.

The Reynolds stress can now be formulated, using only the v' eigenfunction, as follows:

$$-\overline{\rho u' v'} = -\rho U_\infty^2 (\hat{u}\hat{v}^\dagger + \hat{u}^\dagger \hat{v}) \tag{4.54}$$

From the continuity equation, $\bar{\hat{u}} = iD\bar{\hat{v}}/\alpha$.

Therefore,

$$-\overline{\rho u' v'} = \frac{i\rho U_\infty^2}{\alpha} (\hat{v}^\dagger D\hat{v} - \hat{v} D\hat{v}^\dagger) \tag{4.55}$$

where $()^\dagger$ denotes the complex conjugate.

4.4.4.1 Validation of the Reynolds stress computation

The Reynolds stress computation will be validated by comparison with the published results of Jordinson (1970). Note the amplitude scaling is arbitrary since the eigenfunctions used to calculate the Reynolds stress are themselves arbitrarily scaled. The shape of the function, and the positions of maxima and minima are the only criteria by which comparisons can be made. Figure (4.4.1) plots the variation in Reynolds stress through the boundary layer for a $Re = 998$, $\beta = 0.1122$, $\alpha_r = 0.3086$ and $\alpha_i = -0.0057$. Figure (4.4.2) plots the results of Jordinson (1970) for the same range of parameters. Comparison between figures (4.4.1) and (4.4.2) shows excellent agreement. It is thus concluded that the Reynolds stress computation is free from error.

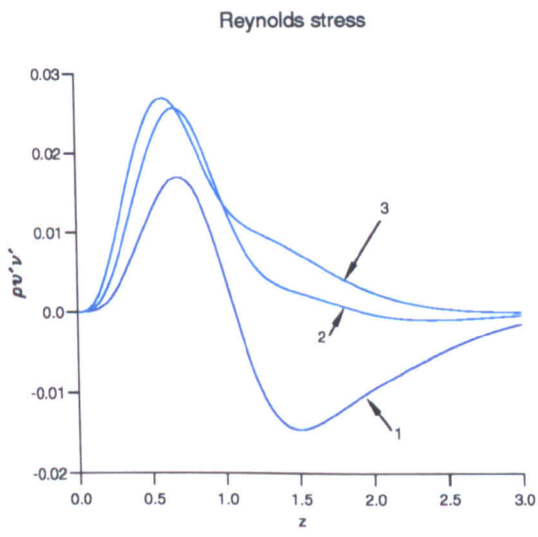

4.4.1: Spectral code computation of Reynolds stress distribution, corresponding to the same parameters as used in 4.4.2

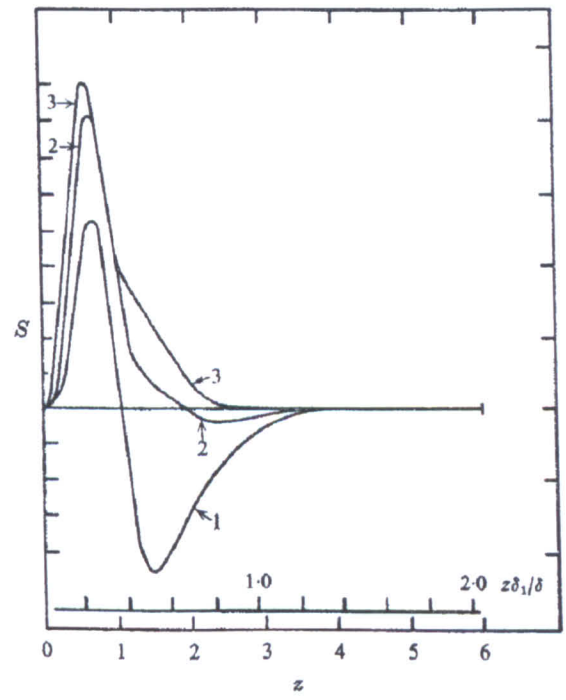

4.4.2: Results of Jordinson (1970), Reynolds stress distributions. Case 1, *Re*= 336, $\beta = 0.1297$, $\alpha_r = 0.3084$, $\alpha_i = 0.0079$. Case2, *Re*= 598, $\beta = 0.1201$ $\alpha_r = 0.3079$, $\alpha_i = 0.0019$. Case 3, *Re*= 998, $\beta = 0.1122$, $\alpha_r = 0.3086$, $\alpha_i = -0.0057$.

Figure 4.4: Validation of spectral code's Reynolds stress computation by comparison with the published results of Jordinson (1970)

4.4.5 The energy balance computation

As mentioned previously, it is critical that we understand the underlying mechanisms by which transition delay can occur. The energy balance technique is a very useful tool for this purpose.

For a linear spatially evolving disturbance, the energy balance can be computed as follows. First, the u' component of the linearized N/S equation is added

to the v' component to yield:

$$\frac{1}{2}\frac{\partial(q'^2)}{\partial t}+\frac{\overline{U}}{2}\frac{\partial(q'^2)}{\partial x}+(v'u')\frac{\partial\overline{U}}{\partial y}+\frac{\partial(u'p')}{\partial x}+\frac{\partial(v'p')}{\partial y}=\frac{1}{R}(\frac{\partial(v'\omega')}{\partial x}-\frac{\partial(u'w')}{\partial y}-\omega'^2) \tag{4.56}$$

where ω' is the perturbed component of vorticity defined below and q' is the total perturbation velocity $(u'^2+v'^2)^{1/2}$, and

$$\omega'=\frac{\partial v'}{\partial x}-\frac{\partial u'}{\partial y} \tag{4.57}$$

Note that the Laplacian operators are eliminated because $\nabla^2 u' = -\partial\omega'/\partial y$ and $\nabla^2 v' = \partial\omega'/\partial x$.

Next, the whole equation is integrated through the thickness of the boundary layer (with respect to y), the give:

$$\frac{\partial}{\partial x}[\int_0^\delta \frac{\overline{U}}{2}(\overline{u'^2}+\overline{v'^2})dy+\int_0^\delta(\overline{u'p'})dy+\frac{1}{R}\int_0^\delta(\overline{v'\omega'})dy]=-\int_0^\delta(\overline{u'v'})\frac{\partial\overline{u}}{\partial y}dy$$
$$-\frac{1}{R}\overline{u'_w\omega'_w}-\frac{1}{R}\int_0^\delta\overline{\omega'^2}dy+\overline{v'_w p'_w} \tag{4.58}$$

The overbars refer to time-averaged quantities. The no-slip condition, which applies to normal pores and slots, ensures that the 2^{nd} term on the RHS is zero. In addition to this, the 3^{rd} term on the LHS has been found to be negligible, as shown by Morris (1976) with his work the stability of axisymmetric jets and by a number of other researchers.

The various terms in eqn.(4.58) have the following physical interpretations. The 1^{st} term on the LHS is the total kinetic energy which is being convected past a given location. The 2^{nd} and 3^{rd} terms are flow work terms, they quantify the rates of work done by the disturbances against the perturbation stresses across an imaginary boundary at a given streamwise location.

The first term on the RHS of (4.58) is the rate of energy production by the Reynolds stress, the third term is the rate of viscous energy dissipation and the fourth term is the rate of irreversible work done to the wall by the disturbance pressure.

The pressure perturbations are evaluated below from the x-component of the N/S equation using the same method as that used above, giving

$$\hat{p} = \frac{1}{R}(\frac{D^3v'}{\alpha^2} - Dv') + iDv'(\frac{\omega}{\alpha^2} - \frac{\overline{U}}{\alpha}) + \frac{iv'}{\alpha}\frac{\partial \overline{u}}{\partial y} \tag{4.59}$$

4.4.5.1 Validation of energy balance computation

Validation of the energy balance computation is done simply by a method of *energy accounting*. Essentially, if the various terms on the RHS sum to give the total mechanical energy flux (the sum of the LHS) then the code can be assumed to be free of error. The results presented in § 5.2.6 include such accounting details. All computations to date have performed well in this respect.

4.4.6 Growth of oblique modes in the Blasius boundary layer

According the theorem of Squire (1933), provided no forcing is applied, it is the two-dimensional wave that will be the first to become unstable. However, the theorem only applies to the minimum critical Reynolds number and not the critical Reynolds number of a particular frequency, for which the most unstable mode may well be that of an oblique wave. Therefore, it is vital that one is aware of parameter ranges over which forced oblique waves become dominant.

Figure (4.5) illustrates some preliminary results gained from the three dimensional stability code presented in chapter 7. These results are presented here because they have specific relevance to the following chapter on the experimental investigation.

It can thus be deduced from fig.(4.5) that for the forced Blasius boundary layer there is a critical frequency below which an oblique wave will become dominant. This frequency is dependent on Reynolds number. In this case, for a Reynolds number of 1100, (corresponding to the central experimental region on the flat plate) the critical non-dimensional frequency is $F = 60$. Essentially, if acoustically

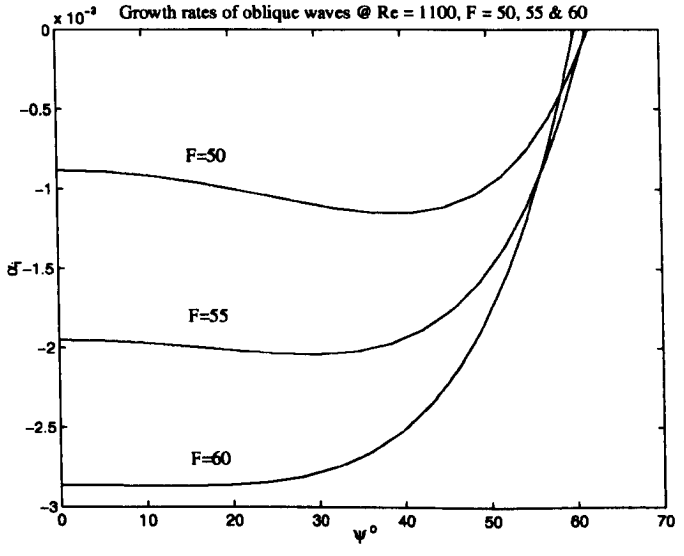

Figure 4.5: Disturbance amplification rate as a function of wave angle for $Re = 1100$ and $F = 50, 55, 60$ and 30.

driven T/S waves wave were forced below this frequency (equivalent to $160Hz$ using eqn. 4.52) then oblique waves would have the higher growth rate. This feature has practical implications during the experiments because the boundary layer's strongest response would no longer lie in the center of the plate thus making experimental measurements problematic.

Chapter 5

Numerical Results - Blasius Flow

5.1 Methods which specify an admittance value

5.1.1 Surveying for unexpected unstable modes

The globally convergent eigenvalue search scheme outlined in § 4.2 provides a complete range of possible solutions to a given eigensystem. However, porous walls offer a large number of possible parameter combinations. As such, even with this scheme, it is a daunting task to establish for certain that no previously unidentified unstable eigenvalues exist for a particular porous wall. In spite of this, the global technique has been used to survey a limited range of ω and Re.

Figure (5.1) contains sample plots of eigenvalues for the case of $Y_w = 0.46\angle 88.88^o$[†], $F = 75$ and $Re = 1105$. These parameters are typical of those found in experiments and the admittance values used are what might be expected from a wall of 12% porosity. The choice of a 12% porosity wall is explained in § 5.2.3. The plots shown in (5.1) (a) and (b) were created using identical parameters but different orders of Chebyshev polynomial. The majority of the eigenvalues shown are part

[†] Y_w is the complex admittance function defined in § 3.4. It is used to represent the properties of a particular porous wall by defining the relationship between the driving pressure at the wall surface and the flow through it.

of the continuous spectrum and are identified as such by altering the order of Chebyshev polynomial. Essentially, only those values which remain stationary with different orders of Chebyshev polynomial are identified as discrete eigenvalues of physical significance. For published values of eigenvalues spectrums, see Jordinson (1971) or Morris (1987)

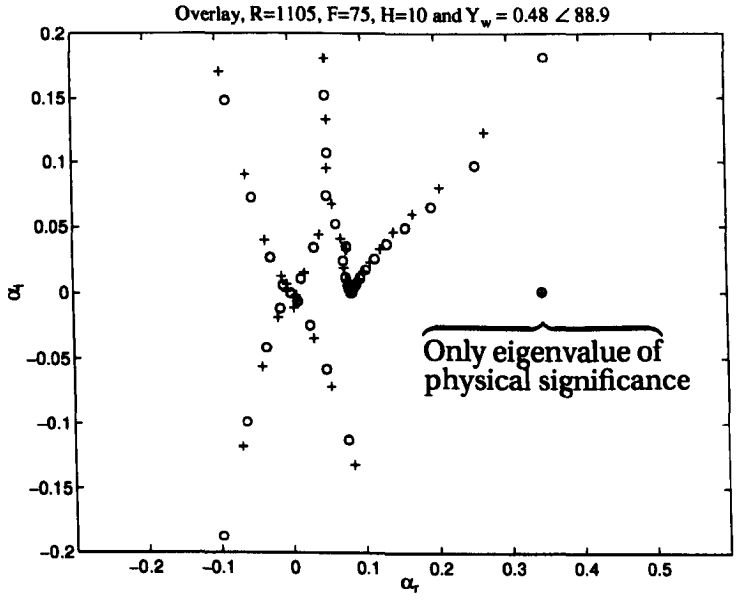

Figure 5.1: Global eigenvalue plots for Re= 1105, $F = 75$ and $Y_w = 0.48 < 88^o$. Plots show 2 different orders of Chebyshev polynomial used - (+ n = 60) and (o $n = 65$).

The isolated eigenvalue at $\alpha_r = 0.3443$, $\alpha_i = 0.0014$, as highlighted in fig.(5.1), was noted as being of particular interest. This was the only value to remain stationary for Chebyshev orders of 60 and 65 respectively. This is seen clearly when the two set of data are plotted together as in fig.(5.1). The real part of the eigenvalue corresponds to the non-dimensional wavenumber of the particular instability. It can be used to identify the physical significance of a given mode. The imaginary part of the eigenvalue determines the growth rate of that particular mode. If α_i is negative and the propagation direction as determined by the group velocity is downstream, the mode is unstable and the growth rate is given by its

magnitude.

The global eigenvalue search scheme does not facilitate the computation of group velocities. To overcome this, the local search scheme outlined in § 4.3 was employed to compute c_g for the above parameters. For the spatial formulation of the Orr-Sommerfeld equation, the group velocity is defined as $c_g = d\omega/d\alpha_r$. The phase velocity of a particular disturbance is given by $\overline{c}$.†

The non-dimensional frequency of the discrete mode of interest is given thus:

$$F = \frac{\overline{\omega}\nu}{U_\infty \delta^*} \qquad \text{and} \qquad \overline{\omega} = \overline{c}\,\overline{\alpha} \qquad \text{therefore} \quad F = \frac{\overline{c}_g \overline{\alpha}_r}{Re} \tag{5.1}$$

The dimensionless phase velocity was computed to be $\overline{c} = 0.293$. According to eqn.(5.1), this represents a non-dimensional frequency of $F = 92.3 \times 10^{-6}$. This is slightly higher than the frequency used to force the system ($F = 75 \times 10^{-6}$) and suggests that the action of passive wall porosity tends to force the most unstable waves to higher frequencies.

Searches of the type shown above were carried out for a very wide range of frequencies and Reynolds numbers. In all cases the conclusions drawn were consistent; the theory to date predicts that there are no additional modes of instability other than the expected forced T-S mode.

The flow parameters used above would ordinarily have generated instability. Indeed, for the rigid wall boundary condition, a forcing frequency of $F = 75$ would have produced the most rapidly growing mode at this Reynolds number. Instead, the appropriate selection of wall admittance has moved the eigenvalue up into the upper-half-plane of wavenumber space. As such this particular T-S mode has been completely stabilized. This is not to say that a wall with these

†When considering superposed waves, the **phase velocity** is the speed with which a crest having the average wavenumber would move. The **group velocity** is the speed at which the modulating envelope moves. It is called the group velocity because the envelope encloses a group of shorter wavelengths.

qualities could suppress the T-S instability altogether. It is likely that instability still exists and that the most unstable mode has simply shifted to a different frequency.

The preceding discussion has outlined an important point. Simply investigating the effects of the new boundary condition on a single mode is of little use. The most rigorous test of the virtues of PPW's would be to compare the reductions in growth rates which apply to the *most unstable modes* for a variety of flow conditions. The following sections aim to achieve such comparisons.

5.1.2 Verification of the assumption of continuous porosity

Gaponov (1975a) detailed the conditions for which arrays of holes can be assumed to approximate a continuous distribution. Gaponov showed that provided $d << \lambda$ the assumption is valid. Figure (5.2) details the nomenclature used.

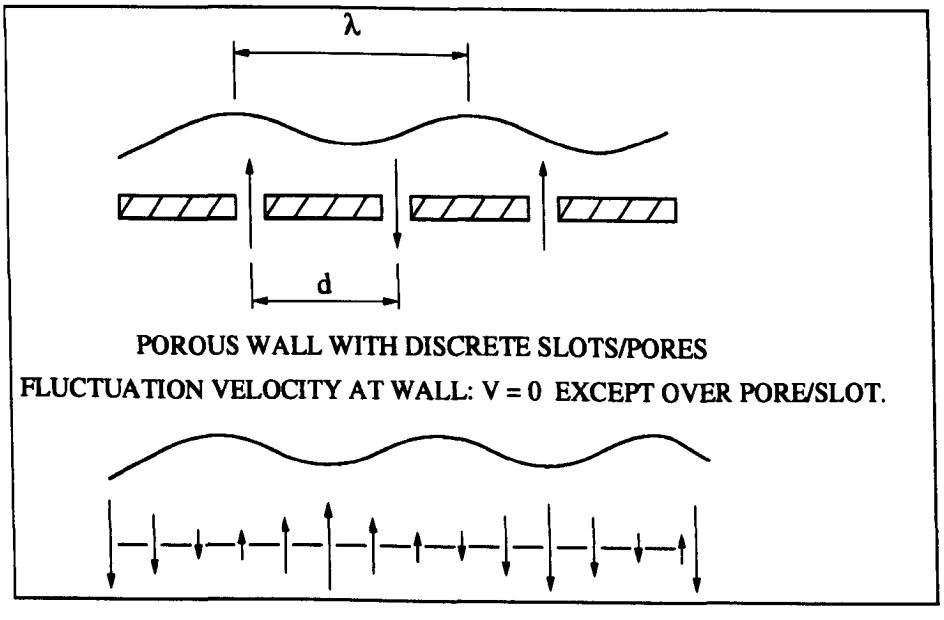

Figure 5.2: Continuous distribution of porosity - a valid assumption

Taking the case of a T-S wave generated in a typical transition experiment with $Re = 1100$, $U_\infty = 17\ \mathrm{m\,s^{-1}}$, $F = 75 \times 10^{-6}$ $\overline{\alpha} = 0.241$, giving $\alpha = \frac{\overline{\alpha}}{\delta^*}$, $\alpha = 243\ \mathrm{m^{-1}}$, $\lambda \approx 26mm$.

Y_w	**Beneficial ϕ range**
0.20	87.2^o to 90^o
0.50	86.1^o to 90^o
0.75	87.5^o to 90^o
0.10	88.6^o to 90^o

Table 5.1: Super-resonant regions of effective PPW operation, $F = 30$ and $R = 2240$. Results taken from Carpenter (1993).

For a 12% wall with 100μm holes - the pitch spacing of the pores is 275μm ($d << lambda$). It can therefore be concluded that the pore dimensions of $50\mu m$ are much smaller than the wavelength of the T-S waves apparent for these flow conditions. Accordingly, the continuous distribution of porosity is a valid assumption.

5.1.3 An illustration of the effect of a Passive Porous Wall

As explained in § 4.3.1, initial computations were done using an assumed value of complex admittance Y_w. The code used to generate the following results does not solve the coupled problem. Hence, these results can only be used to illustrate which values of admittance can yield a favorable result. The higher values of admittance phase angle may not be attainable in practice.

Carpenter (1993) solves the uncoupled problem for $Re = 2240$ and $F = 30 \times 10^{-6}$. The parameter space explored in his work will also be presented in the following results so that direct comparisons can be made. Carpenter used a Runge-Kutta finite-differencing technique combined with orthonormalization to discretise the Orr-Sommerfeld equation. Hence, if the same results can be reproduced using the spectral technique, one can be certain that the effect is not simply a coding error or a quirk in the discretisation technique.

The results of Carpenter (1993) are summarized in table (5.1) while fig.(5.3) presents the results generated by the spectral code. Figure (5.3) shows the vari-

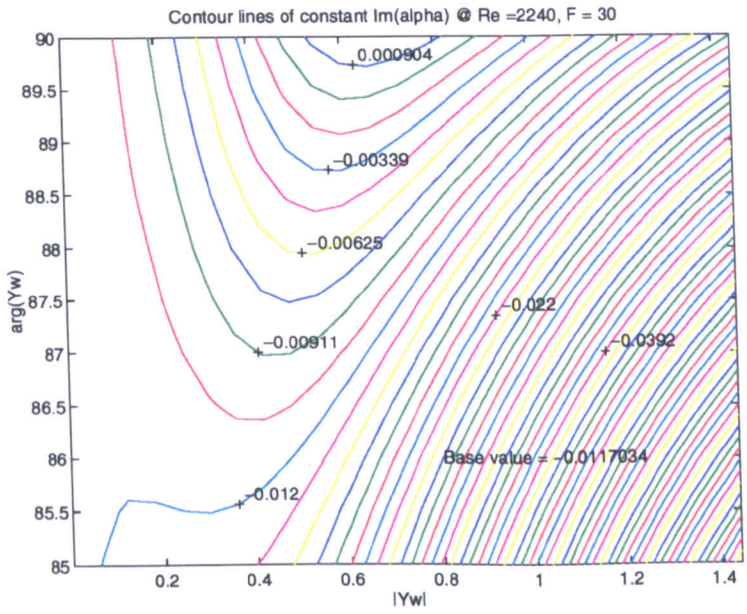

5.3.1: Contours of constant α_i

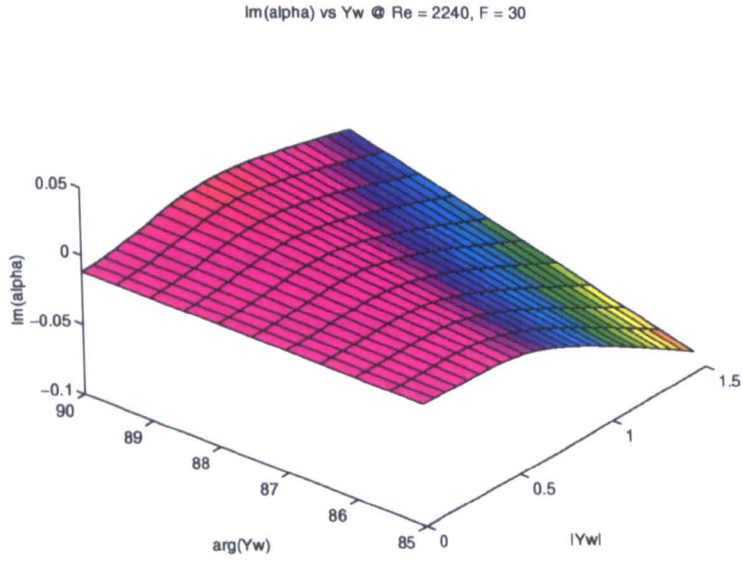

5.3.2: 3-D surface plot of α_i

Figure 5.3: Variation of α_i with admittance magnitude and phase - $Re = 2240$ and $F = 30$.

ation in α_i with $|Y_w|$ for a range of super-resonant phase angles. The base value for the disturbance growth rate is around $\alpha_i = -0.00117$. This is the value that would result from a non-porous wall. Close inspection of the contour plot in fig-

ure (5.3,a) reveals that there are no significant discrepancies between the two sets of results. Perhaps a more surprising result is that there is a optimum admittance value of $0.65 \angle 90°$. An admittance magnitude which exceeds this value will lead to a decline in T-S wave suppression.

The apparent similarity in the results of the current study and that of Carpenter would suggest that both codes are free from gross errors. While such comparisons obviously do not validate the theory itself, one can at least have confidence in the integrity of the computations.

Figure (5.4) represents the conditions which might be expected in the wind tunnel. Here, the contour pattern which emerges is much the same as that for the previous parameter set, this plot therefore warrants no further discussion.

5.2 Results from models which solve the coupled boundary condition problem

The results presented in the following section were generated using codes which attempt to solve the Orr-Sommerfeld equation with a coupled wall boundary condition defined by eqn.(3.33) with the admittance $\mathbf{Y_w}(\alpha, \omega, Re)$ itself being dependent upon the eigensolution α. The local iterative solver described in § 4.3 is used for this purpose. The results from this section can be used to identify optimum values of parameters such as porosity or cavity depth. The findings of this section therefore play an important role in the prototyping of PPW's. The use of terms such as *optimum parameter value* is perhaps unwarranted at this stage of investigation. It should be remembered that the model used here is quite crude in that it takes no account of the wall's finite thickness or of the particular geometry of individual pores. In addition to this, the theory assumes the boundary layer to be locally parallel. Therefore, the parameters selected in the proceeding sections are merely estimations of the optimum values, arrived at using a model which is

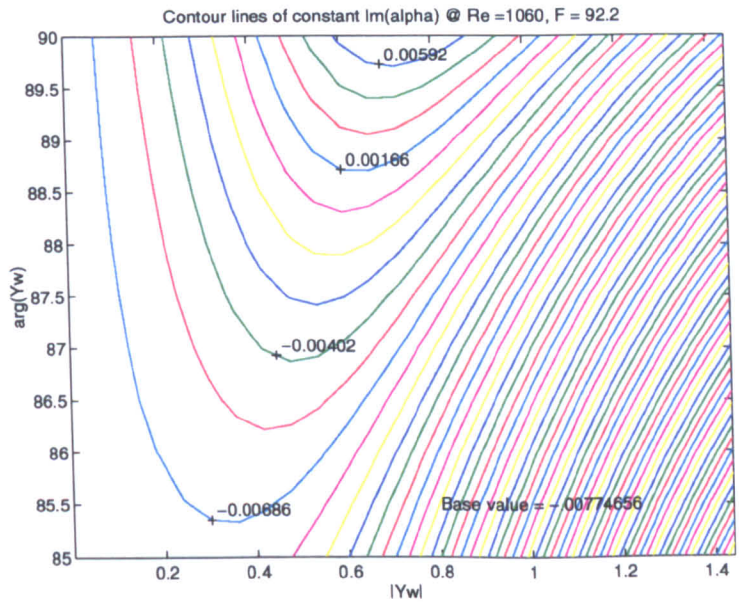

5.4.1: Contours of constant α_i

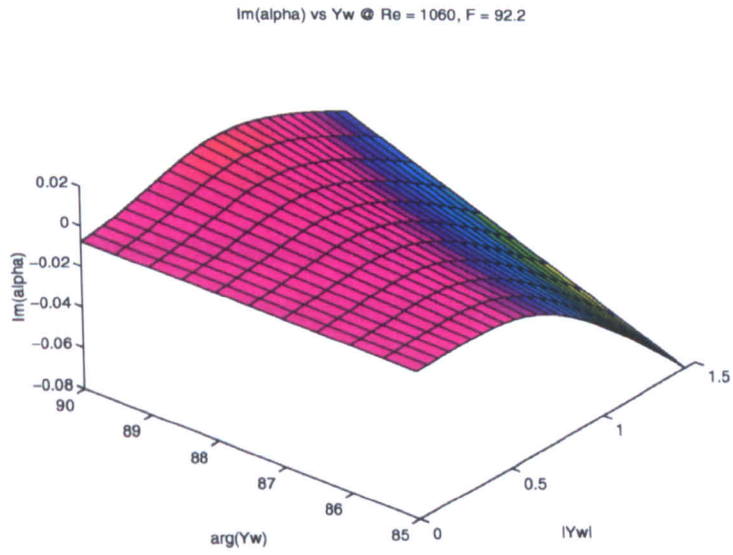

5.4.2: 3-D surface plot of α_i

Figure 5.4: Variation of α_i with admittance magnitude and phase - Re= 1060, F = 85.

somewhat limited. Section 1.4 gives a detailed discussion of the limitations of the current model.

The focus of the current section is the presentation of results from the so-

lution of the coupled boundary condition problem. Such coupling arises because the boundary conditions required by the numerical scheme depend on the wavenumber of the flow instability itself. This requires that the flow and its boundary condition be solved in an iterative manner until some convergence criterion is met. Section (4.3.1) gives a detailed description of the numerical techniques employed for this purpose. Since the local solver is iterative by design, and the coupled problem is solved through iteration also, the codes used to generate the following results require two levels of iteration. This makes the codes rather cumbersome. However, considerable improvement in the efficiency of these codes has been achieved using extrapolation subroutines which provide better initial guesses at the final solution for each step in a particular parameter. The steps taken in a given parameter space can also be larger. This approach enables the dynamic computation of parameters such as optimal porosity or cavity depth for a range of flow and disturbance parameters.

The tolerances, required for the convergence of the coupled boundary condition problem, can be estimated by a simple sensitivity analysis. A study of variation in admittance to perturbations of wavenumber gives an idea of the sensitivity of the admittance function. Table (5.3) and (5.2) present the results of such a sensitivity analysis for parameters typical of those expected in wind tunnel tests.

α_r	α_i	$\lvert Y_w \rvert$	ϕ_{Y_w}	% change in α_i	% change in ϕ	% change in $\lvert Y_w \rvert$
0.34241	0.00228	0.48039	88.88	0.00	0.00	0.00
0.34241	0.00248	0.48040	88.91	8.77	0.04	0.00
0.34241	0.00268	0.48041	88.95	17.54	0.07	0.00
0.34241	0.00288	0.48042	88.98	26.32	0.11	0.01
0.34241	0.00308	0.48043	89.01	35.09	0.15	0.01

Table 5.2: Sensitivity of Y_w to variations in α_i for $F = 75$, $R = 1105$

Tables (5.3) and (5.2) clearly show that the admittance phase angle ϕ_{Y_w} is not sensitive to large changes in either α_r or α_i. It is also noticed that the admittance

α_r	α_i	$\lvert Y_w \rvert$	ϕ_{Y_w}	% change in α_r	% change in ϕ	% change in $\lvert Y_w \rvert$
0.34241	0.00228	0.48039	88.88	0.00	0.00	0.00
0.37241	0.00228	0.52186	88.72	8.76	-0.18	8.63
0.40241	0.00228	0.56296	88.56	17.52	-0.36	17.19
0.43241	0.00228	0.60378	88.40	26.28	-0.54	25.68
0.46241	0.00228	0.64435	88.25	35.05	-0.71	34.13

Table 5.3: Sensitivity of Y_w to variations in α_r for $F = 75$, $R = 1105$

magnitude $|Y_w|$ is not affected by large variations in α_i. However, perhaps the most important result is that the magnitude of $|Y_w|$ varies roughly in proportion to α_r. Put simply, the wall's admittance varies in direct proportion to the wavenumber of the perturbations within the boundary layer (and hence the cavity).

The above analysis has revealed that, in solving the coupled boundary condition problem, the area of critical interest is the convergence of the non-dimensional wavenumber α_r. This is the parameter for which tight tolerances must be set. Furthermore, if solutions are to be extrapolated, α_r would be an appropriate choice of abscissa. In practice, the boundary condition was found to give satisfactory convergence provided that consecutive real and imaginary components of the admittance function were within 2% percent of each other. However, a typical convergence of less than 0.2% was achieved with only one iterative step.

5.2.1 Choosing accurate orders of Chebyshev polynomial

As outlined in § 4.4, the degree of Chebyshev polynomial should be selected such that high accuracy is achieved without too much computational expense. The results of this section correspond to solutions of the coupled boundary condition problem (Blasius boundary layer) for porosities of 0% and 6% for a range Chebyshev orders from n=35 to n=85.

n	α_r	α_i	% change in α_r	% change in α_i
35	0.2415290	-0.0079110	N/A	N/A
40	0.2415272	-0.0079100	-0.001	-0.013
45	0.2415288	-0.0079086	0.001	-0.018
50	0.2415281	-0.0079090	0.000	0.005
55	0.2415272	-0.0079084	0.000	-0.008
60	0.2415275	-0.0079108	0.000	0.031
65	0.2415277	-0.0079081	0.000	-0.034
70	0.2415281	-0.0079078	0.000	-0.004
75	0.2415296	-0.0079083	0.001	0.006
80	0.2415280	-0.0079094	-0.001	0.014
85	0.2415309	-0.0079103	0.001	0.012

Table 5.4: Accuracy of computed eigenvalues for various orders of Chebyshev polynomial (n) - 0% porosity - Blasius boundary layer, Re= 1105, $F = 75 \times 10^{-6}$.

Table (5.4) corresponds to a non-porous surface ($\sigma = 0$). In this case, the relative error between $n = 35$ and $n = 40$ is less than 1% for both the real and imaginary wavenumber components. Hence, computations for $\sigma = 0$ would not benefit from a Chebyshev order of $n > 35$.

Table (5.5) illustrates the results for a 6% porous surface. Here, relative errors do not reduce to within 1% until n=60 (indicating that n=55 will suffice). The reason for this higher order requirement is probably because the eigenfunctions

n	α_r	α_i	% change in α_r	% change in α_i
35	0.2708539	-0.0072008	N/A	N/A
40	0.2691941	-0.0081904	-0.617	12.082
45	0.2717770	-0.0064979	0.950	-26.047
50	0.2715350	-0.0054714	-0.089	-18.761
55	0.2711387	-0.0056734	-0.146	3.561
60	0.2711862	-0.0057106	0.018	0.651
65	0.2711435	-0.0054647	-0.016	-4.500
70	0.2710077	-0.0050878	-0.050	-7.409
75	0.2708277	-0.0047635	-0.066	-6.808
80	0.2706996	-0.0047299	-0.047	-0.709
85	0.2703984	-0.0040294	-0.111	-17.387

Table 5.5: Accuracy of computed eigenvalues for various orders of Chebyshev polynomial (n) - 6% porosity - Blasius boundary layer, Re= 1105, $F = 75 \times 10^{-6}$.

for surfaces with porosity vary very rapidly near the wall and thus require more spectral resolution. Further inspection of this table reveals an increase in relative error once n exceeds 55. The reason for this is, as yet, unclear. However, it is entirely possible that the use of such high polynomial orders has led to significant error due to machine precision (round-off errors).

5.2.2 Optimum cavity depth

The PPW concept relies upon the communication of disturbances within a common continuous cavity. For structural reasons, it would be impossible for a practical PPW to have a continuous cavity without some additional ribbing to give the thin porous surface the required mechanical stiffness. Clearly, structural ribbing would no longer render the cavity continuous, even if the ribbing itself was porous. Therefore, perhaps the most important question to ask is over what stream-

wise span should cavity waves be able to freely communicate. Intuitively, one might think that one T-S wavelength represents the limit below which any beneficial effects might be lost. However, since this has yet to be proved, the experimental set-up has been designed such that no stiffeners are required. Tensioning of the porous foil itself provides the stiffness required to avoid problems of aerodynamic flutter or vibration. Also, since the experimental setup had a cavity which was truly continuous, theoretical predictions of optimal cavity depth could be applied to the experimental prototype with the knowledge that the cavity dynamics were as close as possible to those modeled by the theory.

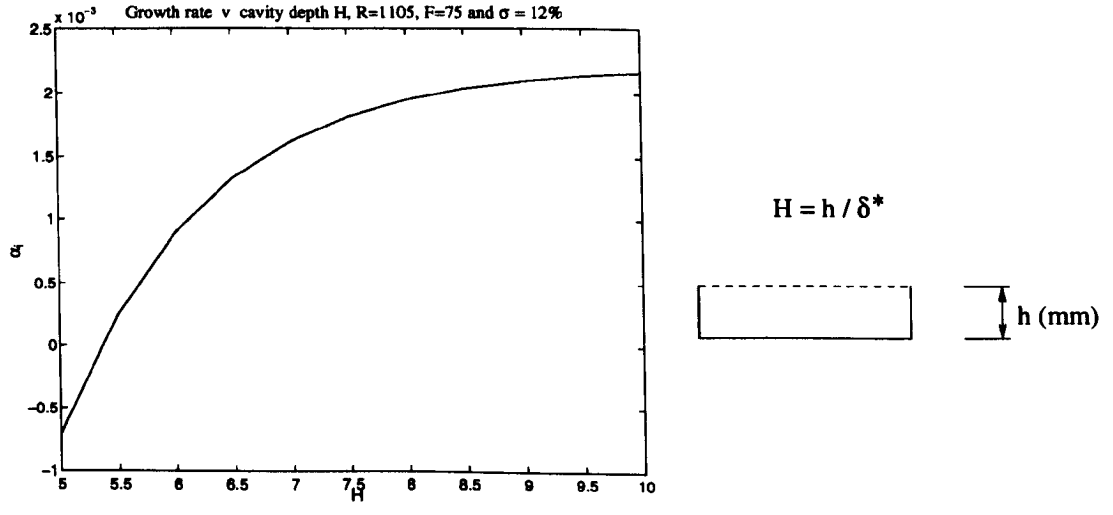

Figure 5.5: Variation of growth exponent with non-dimensional cavity depth H. $F = 75$, $R = 1105$ and $\sigma = 12\%$.

Early work by Lekoudis (1978) has hinted that increasing the depth has a stabilizing influence but that the trend is reversed for larger values of H at which the flow can become unstable. Inspection of figure (5.5) illustrates that the current model is not in complete agreement with the findings of Lekoudis. These results suggest that wave suppression continues to intensify with increasing cavity depth up to about $H = 10$. Little further improvement is achieved for $H > 10$. The current model does not predict a reversal in the trend for larger values of cavity depth. Lekoudis offers no explanation for this peculiarity in the wall's behaviour.

Certainly, if one refers to the physics of the PPW mechanism (outlined § 1.3), then the trends displayed by the current theory seems much more plausible.

In summary, these results suggest that a non-dimensional cavity depth of $H = 10$ would be suitable for prototype design. For a Reynolds Number of 1105, the typical displacement thickness would be 0.94 mm thus making the optimum physical dimension of the cavity 10.6 mm or greater.

5.2.3 Optimal porosity

Figure (5.6) illustrates the variation in the growth exponent with the porosity fraction σ for the range of Reynolds numbers corresponding to the span of the porous surface used in the experiment. Figures (5.6.2) and (5.6.4) are merely three dimen-

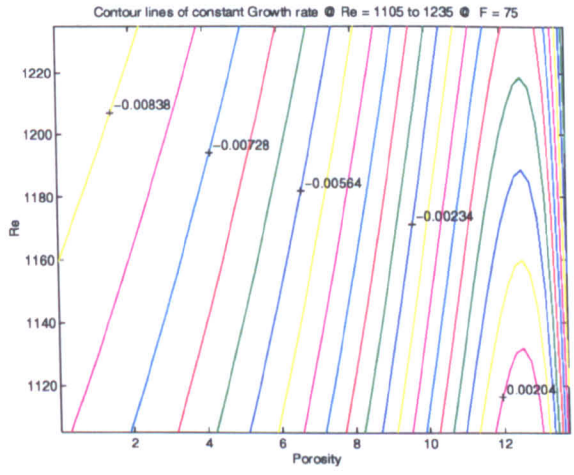

5.6.1: Contour plots - using solidity σ vs. *Re* with constant α_i defining contours. F=75

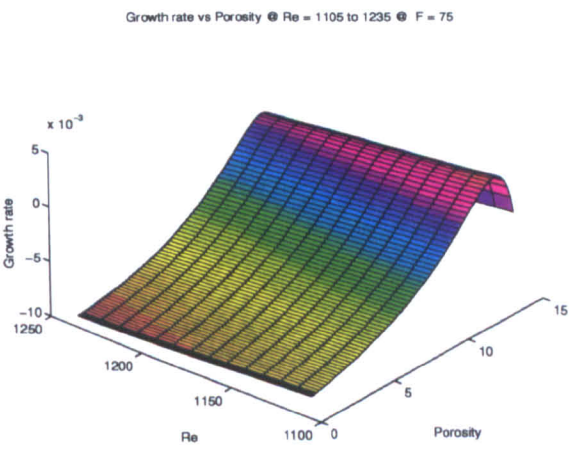

5.6.2: 3D surface plot of 5.6.1

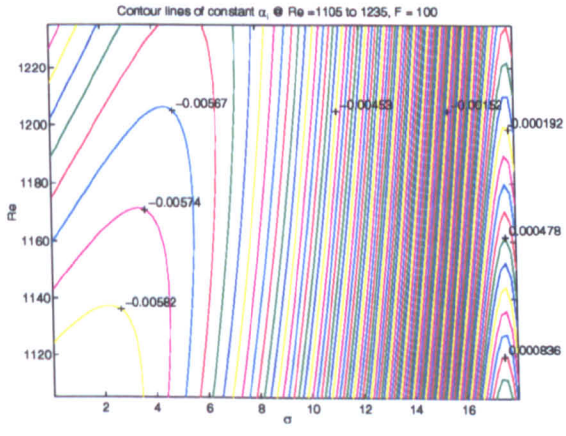

5.6.3: Contour plots - using solidity σ vs. *Re* with constant α_i defining contours. F=100

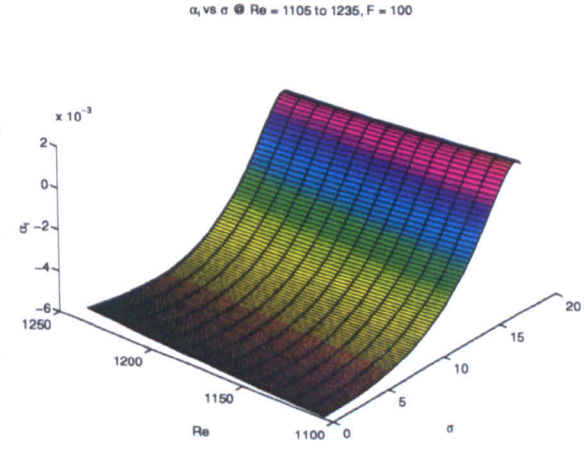

5.6.4: 3D surface plot of 5.6.3

Figure 5.6: Contour and surface plots illustrating the effects that changes in porosity and streamwise Reynolds number have on the growth exponent α_i for the Blasius boundary layer.

sional representations of the data shown in the contour plots (5.6.1) and (5.6.3). The marked values on the contour plots correspond to the growth exponent (α_i) in that region of parameter space.

For the Reynolds number range used during the experiments, the most unstable T-S modes for the case of a non-porous wall are around $F = 75$. The results for this frequency are shown in fig. (5.6.1, & 5.6.2). These plots show that such frequencies are completely suppressed by the PPW boundary condition, with the most effective suppression achieved for a porosity $\sigma = 13\%$. However, porosities in excess of this value rapidly lead to instability. The reasons for this are not immediately obvious and will therefore be investigated in further detail in § 5.2.6.

Figures (5.6.3, & 5.6.4) show that waves of higher non-dimensional frequency ($F = 100$ in this case) are not completely suppressed until much higher values of porosity. Indeed, the current theory seems to suggest that total suppression is not achieved until porosities of 16.5% are reached, with the optimum being at around 17.5%. This is particularly unfortunate because the design point for these high frequencies is such that the lower frequencies become rapidly unstable because the porosities are too high.

5.2.3.1 Estimation of optimum porosity for natural transition

During experiments it is easy to test the performance of the porous surface for one specific frequency; the forced frequency. However, a practical application of PPW's requires the wall to suppress T-S waves over a wide band of unstable frequencies. Particular attention should be given to the most unstable frequency as this is the mode which will physically appear within the flow.

The key question to ask concerning optimization of PPW's for natural transition is what value of porosity provides the maximum suppression for the most unstable frequency. Such information is presented in figure (5.7). Figure (5.7.1) shows the variation in the growth exponent α_i corresponding to the most unsta-

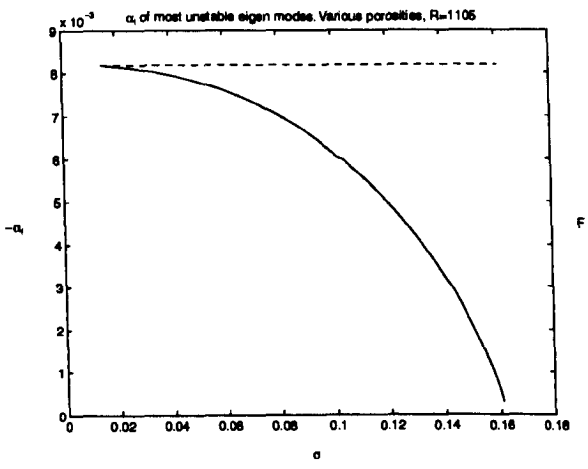

5.7.1: α_i vs. σ for most unstable mode.

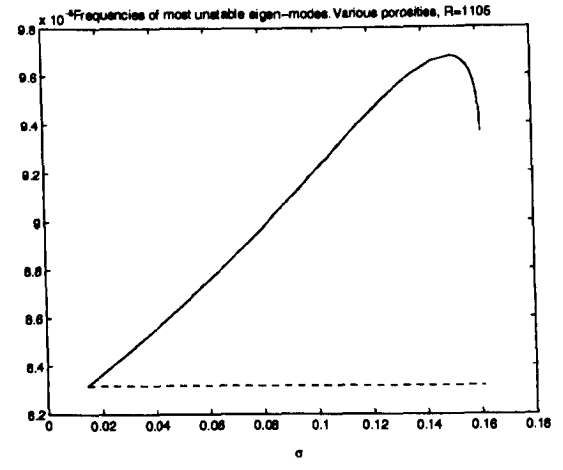

5.7.2: F vs. σ for most unstable mode.

Figure 5.7: Locus of must unstable eigenmode (in streamwise direction) as a function of surface porosity σ @ $Re = 1105$

ble frequency for a range of porosities while figure (5.7.2) shows the variation in the most unstable frequency.

The most unstable frequencies for PPW's are altogether different from those of non-porous walls. Indeed, these results suggest that increasing the porosity of the surface tends to shift the must unstable modes to higher frequencies. There seems to be a maximum in the most unstable frequency of $F = 96.5 \times 10^{-6}$ which occurs for 15% porosity. Figure (5.7.1) would also suggest that a porosity of 16.25% would provide total suppression of the T-S wave. A code designed to compute the most unstable modes will not converge when the T-S wave becomes stable. For this reason, no results are given for porosities in excess 16.25%. However, one can predict, by extrapolation of the results of figure (5.6), that porosities in excess of 17.25% will again lead to instability.

5.2.4 Reynolds stress computations

Section (4.4.4) explains, in some detail, the implications of the Reynolds stress on the stability of the T-S waves. A brief explanation is also given here for clarity. Essentially the Reynolds stress is a measure of the amount of energy imparted to T-S type disturbances from the mean flow. It is thought to be the primary cause of disturbance growth. If the production of disturbance energy by the Reynolds stress exceeds the viscous energy dissipation, then instability results. One is particularly interested in the product of the Reynolds stress $-\rho\overline{uv}$ with the mean velocity gradient $d\overline{U}/dy$. If these two quantities are of the same sign, over the dominant part of the flow, then T-S type instabilities will grow. The degree of instability can also be deduced by these two quantities. Fuller velocity profiles, like those found in accelerating flows, have values of $d\overline{U}/dy$, throughout the boundary layer, which are greater that those of Blasius flows. Such flows are known to be more stable. However PPW's, which are not invasive to the boundary layer, cannot produce changes in the shape of the mean velocity profile. Therefore, the only way such walls can produce stability is to reduce the magnitude the Reynolds stress, or even change its sign.

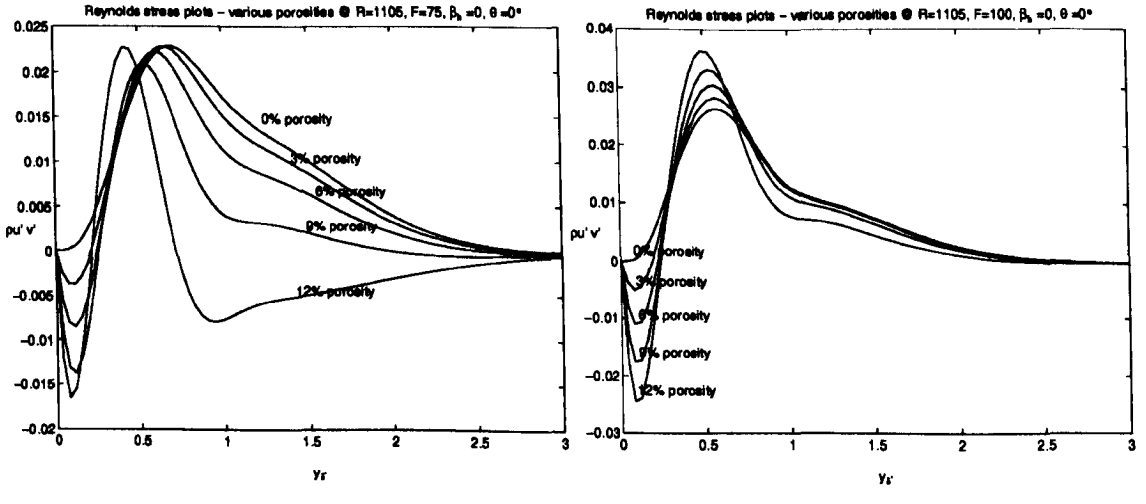

5.8.1: $F = 75$ 5.8.2: $F = 100$

Figure 5.8: Reynolds stress plots for various porosities @ Re= 1105.

Figure 5.8 illustrates how the Reynolds stresses are distributed through the boundary layer for the non-dimensional frequencies of $F = 75$ and $F = 100$. Five different porosities are shown, ranging from a non-porous wall to a wall of 12% porosity. The Reynolds stress approaches zero, in all cases, after approximately 3 displacement thicknesses. All plots exhibit a characteristic negative peak in Reynolds stress in the near-wall region. The magnitude of this peak varies in direct proportion to porosity. In addition to this, the wall's porosity has a marked effect further out in the boundary layer, beyond the critical layer. In these regions there is a significant reduction in $-\rho\overline{uv}$ over large portions of the flow. Indeed, the results of the proceeding section will illustrate that there is in fact a zero integrated Reynolds stress for the 12% surface at $F = 75$.

5.2.5 e^n computations using the porous boundary condition

The parameters used in the following computations have been chosen to match those which will exist in the wind tunnel. Growth curves are the primary tool used to compare theory with experiment, because computed values of e^n can be compared directly with experimentally measured gain in growth amplitudes A/A_o.

The results presented in the figure (5.9) only incorporate the PPW boundary condition for a small portion of the whole Reynolds number range; the non-porous boundary condition is applied everywhere except for a 90 mm porous patch centered at $x = 400$ mm from the leading edge. This patch has a porosity of 12%.

These results were generated simply by switching the porous boundary condition on and off at the appropriate Reynolds numbers. This corresponds to a discrete jump in the eigenfunction; something which would not occur in practice. The physical situation would involve a smearing of the eigenfunctions (or disturbance profiles) resulting in a degree of upstream influence. The current numerical method is unable to take account of such factors. Davies and Carpenter (1997) have recently developed a novel numerical formulation which can ac-

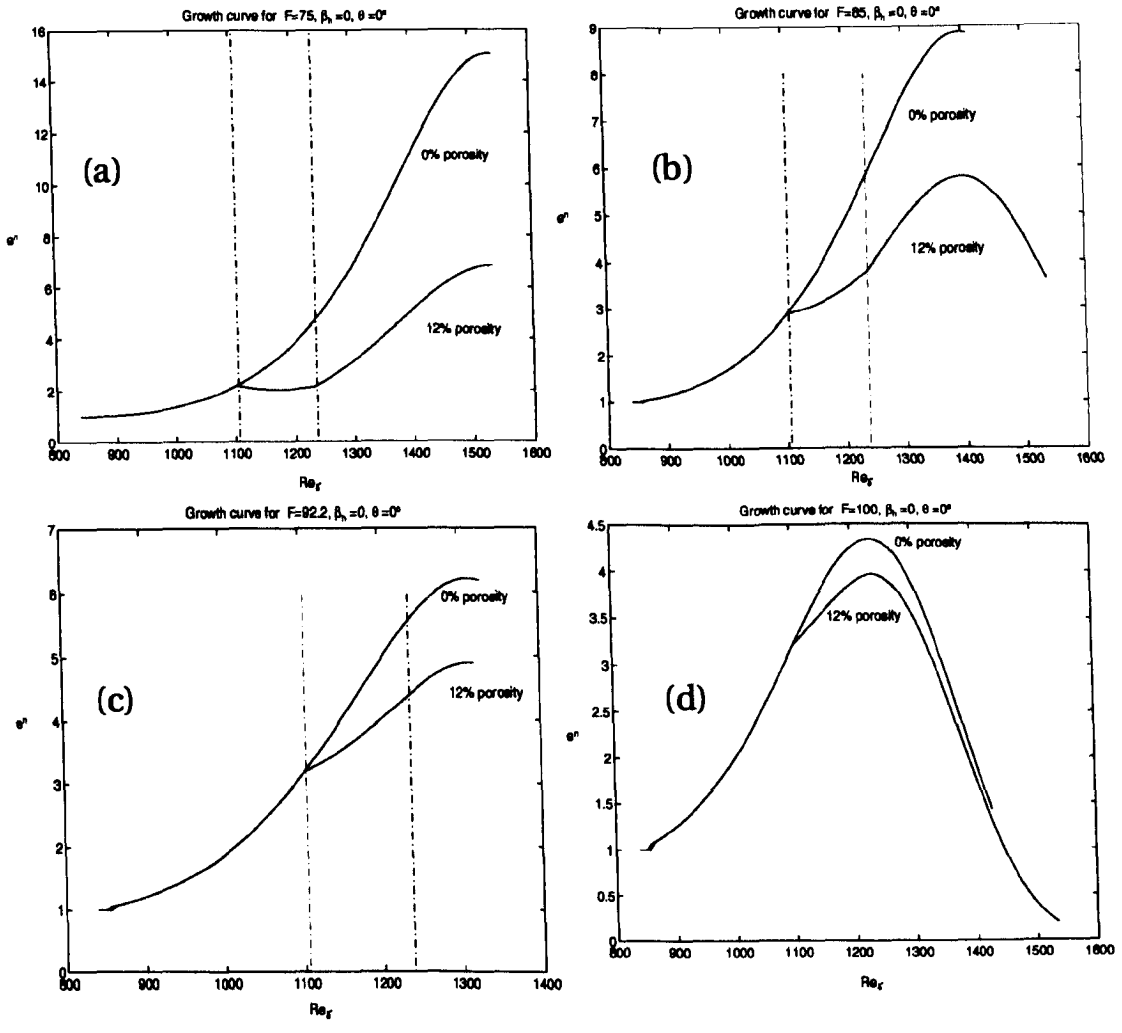

Figure 5.9: Growth curves for Re= 840 to $\approx$ 1600 comparing a 12% porous wall with a non-porous wall. (a) $F = 75$, (b) $F = 85$, (c) $F = 92.2$ and (d) $F = 100$. Porous boundary condition only applied between parallel lines.

count for upstream influence. They use a novel velocity-vorticity formulation of the Navier Stokes equations and apply their method to numerical simulations of the evolution of perturbations over compliant surfaces. The application of this numerical scheme to PPW's is a possible topic for future work.

In the wind tunnel, the location of the source-like wave-generator corresponds to a streamwise Reynolds number of 800 for a tunnel speed of 18.8 $\mathrm{m\,s^{-1}}$, while the end of the traversed section corresponds to $Re = 1600$. This was also the

range of Reynolds numbers in the current e^n computations. Inspection of figure (5.9) reveals some very encouraging results. In particular, the final growth exponent, for the surface of 12% porosity at a forcing frequency of $F = 75$ (shown in figure 5.9,c), is half that of the equivalent non-porous surface. This frequency is close to the most unstable frequency of a non-porous wall and therefore explains why the effect is so marked. The results of § 5.2.3 indicate that porous walls are particularly effective at suppressing these lower frequencies. † Forcing at $F < 75$ is less suitable because, as shown in § 4.4.6, the most unstable modes for such low frequencies tend to be oblique waves.

† The experimental investigation would benefit from forcing at these lower frequencies simply because the measured effect is likely to be more pronounced.

5.2.6 Energy balance computations - porous wall boundary condition

The following computations are crucial to the understanding of the basic mechanisms behind the passive porous effect. The following comparisons are useful in determining which energy transfer mechanisms are responsible for the theoretically beneficial effects given by passive porous walls.

The energy balance equation (4.58) , first derived in § 4.4.5, is shown again below.

$$\frac{\partial}{\partial x}[\int_0^\infty \frac{\overline{U}}{2}(\overline{u'^2}+\overline{v'^2})dy + \int_0^\infty (\overline{u'p'})dy + \frac{1}{R}\int_0^\infty (\overline{v'\omega'})dy] = -\int_0^\infty (\overline{u'v'})\frac{\partial \overline{u}}{\partial y}dy - \frac{1}{R}\overline{u'_w\omega'_w} - \frac{1}{R}\int_0^\infty \overline{\omega'^2}dy + \overline{v'_w p'_w}$$

Differentiating the LHS and normalizing by the integrated mechanical energy flux, i.e. $\int_0^\infty \frac{\overline{U}}{2}(\overline{u'^2}+\overline{v'^2})dy$ gives:

$$-2\alpha_i = \underbrace{-\int_0^\infty (\overline{u'p'})dy - \frac{1}{R}\int_0^\infty (\overline{v'\omega'})dy]}_{\widehat{\text{TME}}} \underbrace{-\int_0^\infty (\overline{u'v'})\frac{\partial \overline{u}}{\partial y}dy}_{\widehat{\text{EPRS}}} \underbrace{-\frac{1}{R}\overline{u'_w\omega'_w} - \frac{1}{R}\int_0^\infty \overline{\omega'^2}dy}_{\widehat{\text{EDAV}}} + \underbrace{\overline{v'_w p'_w}}_{\widehat{\text{IETW}}} \quad (5.2)$$

The labeled terms in eqn.(5.2) have the following definitions. TME relates to the Total Mechanical Energy of a given disturbance. The term EPRS is the Energy Production due to the Reynolds Stresses. This integral term is generated by the temporal averaging of the terms involved, i.e. $\overline{uv} = u^*v + v^*u$. The * superscript denotes the complex conjugate. EDAV is the integral term which corresponds to Energy Disipation through the Action of Viscosity. It accounts for the dissipation of vorticity, the breakdown of vortical structures and the eventual generation of heat. IETW, or $\overline{v'_w p'_w}$, accounts for the work done by the perturbation pressure across any given boundary. Negative values of this quantity account

for Irreversible Energy Transfer *into* the Wall and therefore a reduction in disturbance energy.

Figure (5.10) illustrates the magnitudes of the various terms in the energy equation. It compares the energy balances of non-porous surfaces (shown in black) with their porous counterparts (shown in grey). Figure (5.10.1) & (5.10.2) give balances for porosities of 6% and 12% respectively for $F = 100$. Figures (5.10.3) & (5.10.4) present results in the same format, but for $F = 85$. Finally, figs.(5.10.5) & (5.10.6) are for $F = 75$. In all the cases shown, the two sides of the energy equation were found to balance to at least 3 significant figures, thus validating the energy balance code.

All of the plots shown in figure (5.10) illustrate that the application of wall porosity will have three principal effects which will lead to an *overall* drop in the total mechanical energy of a disturbance. The first effect is a significant drop in the energy production term due to Reynolds stresses (EPRS). The second effect, which is destabilizing, is a drop in energy removal due to viscous dissipation (EDAV). However, this reduction in dissipation is almost wholly compensated by the third effect, which is the removal of disturbance energy due to pressure work at the wall (IETW).

Figure (5.10.4) compares the results of a non-porous wall with those of 12% porosity. Here, the sum of the dissipation terms (EDAV + IETW) are nearly equal to the production term (EPRS). This has resulted in total mechanical energy which is approaching zero, indicating that the disturbance has almost been totally suppressed. The 12% surface can even reduce the integrated Reynolds stress to zero for selected modes, as shown in figure (5.10.6). This plot indicates that at the lower frequencies of $F \approx 75$, the T-S wave becomes highly damped.

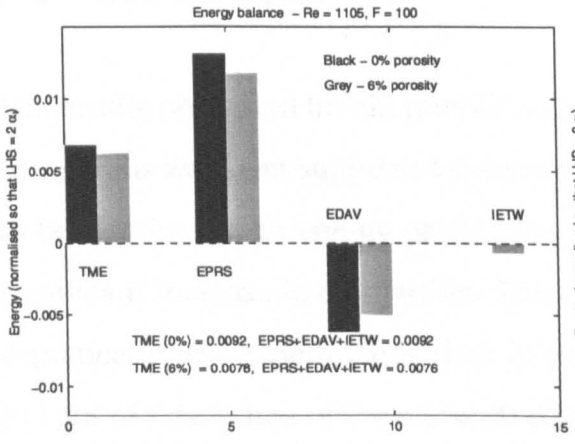

5.10.1: $F = 100, \sigma = 6\%$

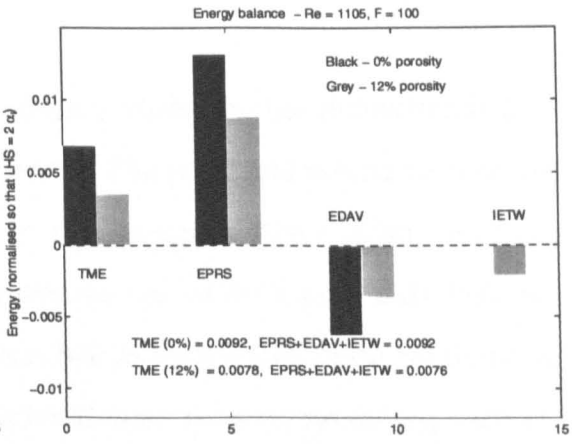

5.10.2: $F = 100, \sigma = 12\%$

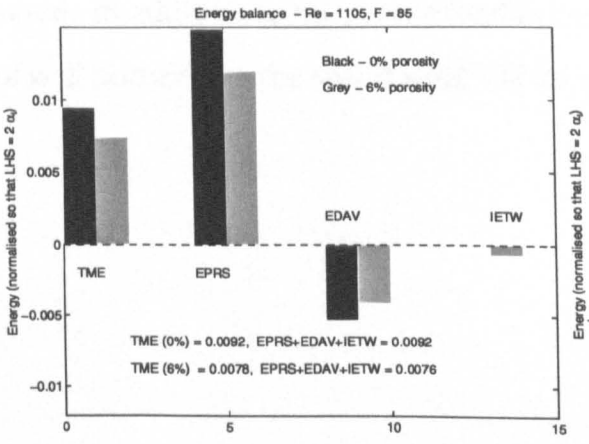

5.10.3: $F = 85, \sigma = 6\%$

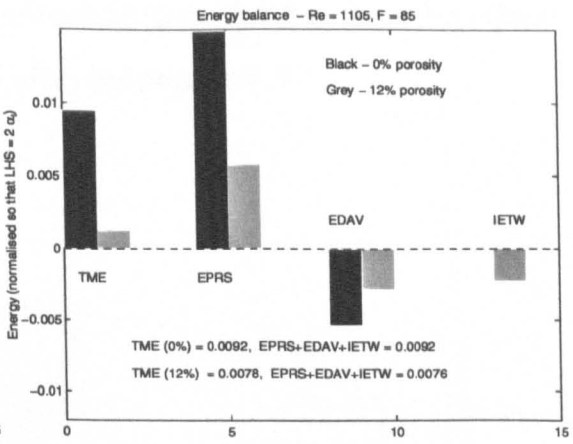

5.10.4: $F = 85, \sigma = 12\%$

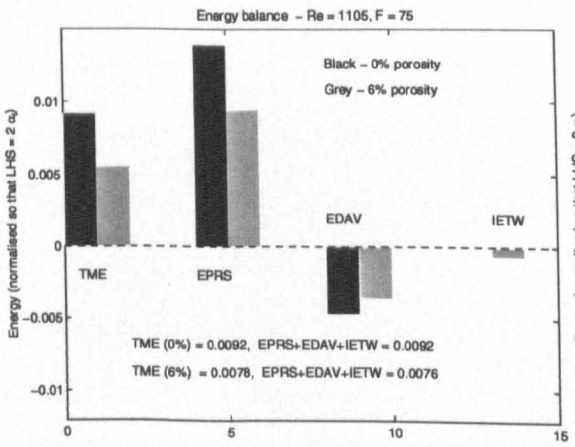

5.10.5: $F = 75, \sigma = 6\%$

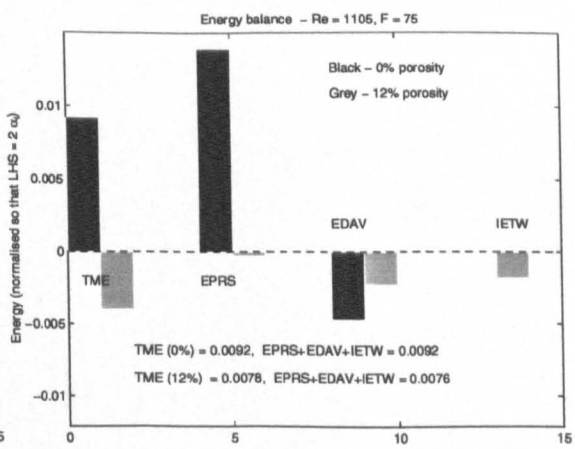

5.10.6: $F = 75, \sigma = 12\%$

Figure 5.10: Energy balances @ *Re*= 1105: Effect of porosity on energy terms (Blasius flow).

5.3 Conclusions

The results presented herein provide convincing evidence that theoretically passive porous walls can suppress T-S wave growth. The principal mechanism seems to be a reduction in energy production by the Reynolds stress rather than any significant increase in dissipation. However, the use of PPW's will gain little acceptance unless experimental data is provided in support of these predictions. In light of this, much of the research effort will now focus on providing such evidence. In the short term, attention must be given to the design of appropriate experimental apparatus such that the relevant admittance quantities can be measured. In addition to this, some further numerical investigations into the effects of wall porosity on the swept wing will be reported later in § 7.

Chapter 6

The Experimental Investigation

6.1 Experimental apparatus

6.1.1 Porous material selection

In accordance with the findings of § 5.1.3 it would appear that a porous surface, consisting in part of an infinitely thin porous plate, is likely to produce the most desirable results. In practice, this points towards the use of a foil-type material whose properties must be specially selected for our purpose. A nominal foil thickness of $50\mu m$ was assumed at the outset, primarily because this is a commonly available stock thickness for a large range of metal foils.

To produce a continuous distribution of porosity it is desirable to produce a surface covered with an array of small, closely spaced holes. It was suggested that hole diameters ranging from $50\mu m$ to $200\mu m$ should be used. Large numbers of such holes can only be practically manufactured using CNC laser drilling equipment with appropriate optics. A low intensity Yag laser (type T28 929) is available for this purpose[†]. The instantaneous surface temperature caused by the plasma beam needs to be sufficiently high to locally melt the material. Such a process

[†]The laser drilling was carried out by British Aerospace's Sowerby research centre, Bristol.

has the potential to cause significant surface deformation and alteration of the material's micro-structure. An obvious way to avoid such damage would be to increase the thermal mass of the drilled material. However, we are constrained in this respect because the foil material must be as thin as possible (of the order of $50\mu m$). Clamping the material with large thermal masses is unlikely to be of benefit, since the domain of heat conduction is extremely small. In general, the material properties that can be relied upon to minimize heat damage are those of high thermal conductivity and low melting point. A low melting point minimizes the dwell time the laser spends on each hole, thereby reducing heat damage. In addition to this, high thermal conductivity ensures efficient heat dissipation.

The foil material needs to be tensioned to ensure an even surface. Tensioning will also alleviate potential problems such as panel flutter caused either by tunnel vibration or the freestream flow. The degree of tensioning required was unknown at the outset and was never directly measured during preliminary testing; the foil was simply tensioned until the surface was flush and rigid to touch. However, in terms of material selection, it is reasonable to assume that yield strength, toughness, and tear strength are critical properties. Indeed, many blank foils were destroyed owing to incorrect material selection or over-tensioning.

The combination of properties outlined above would represent the ideal. However, some of them are clearly contradictory. For example, materials of high tensile strength will in general have a higher melting temperature. Therefore, an engineering judgment will need to be made in selecting the material which has acceptable properties in all the key areas.

The mechanical properties of the chosen foil are as important as the thermal properties. A high Youngs Modulus is required to allow a degree of elastic dilation so the foil lies flush with the top surface even around regions of rapid stress variation. Scope for plastic deformation is also required to prevent brittle fracture at the various stress raiser locations. Finally, a degree of hardness is needed to avoid pitting in areas of high contact stress. Figure (6.1) illustrates the various sources

Material	Thermal coeff. of expan. K^{-1}	Elastic modulus GPa	Tensile strength MPa	Dilat-ation (@ U.T.S) %
Stainless Steel 17-7PH Fe/Cr17/Ni 7	16.15×10^{-6}	214	$1020 - 1550$	$< 25\%$
Stainless Steel 15-7PH Fe/Cr15/Ni 7/Mo 2.25	14.4×10^{-6}	N/A	1020	$< 30\%$
Stainless Steel AISI 316 Fe/Cr18/Ni10/Mo 3	$16 - 18 \times 10^{-6}$	$190 - 210$	$460 - 860$	$< 60\%$
Titanium/Aluminium/Vanadium Ti90/Al 6/V 4	8.0×10^{-6}	$106 - 114$	$1035 - 1410$	$< 10\%$

Table 6.1: Material properties of the various foils considered for laser drilling.

of mechanical stress.

All of the materials listed in table (6.1) were considered because each of them have some of the properties which are desirable in this particular application. Discussions, with the Laser Applications Group at British Aerospace's Sowerby Research Centre, revealed that most of the selected foils could be laser drilled without any problems, with the possible exception of the Titanium alloy. In view of this, and the comparative expense of the Ti alloy, it was decided to disregard

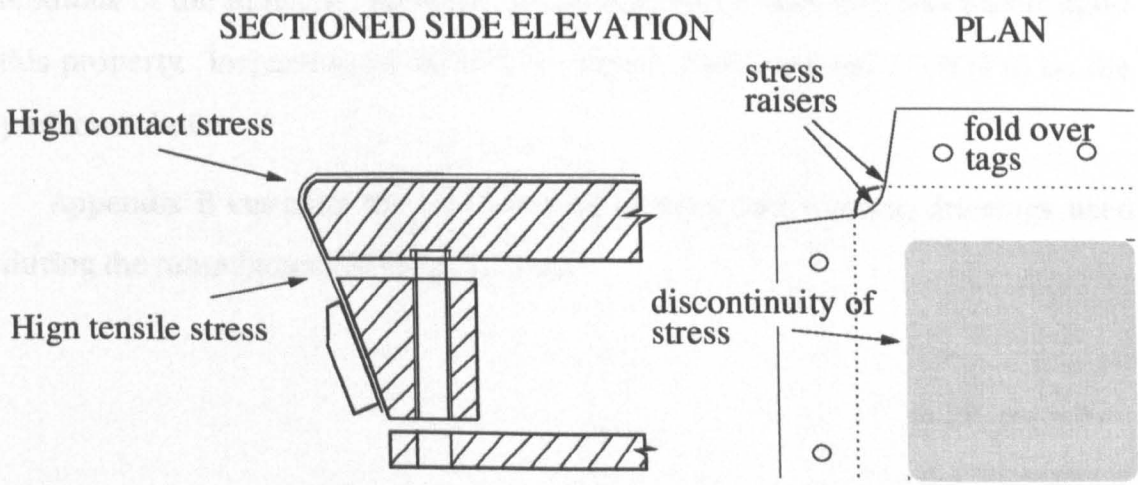

Figure 6.1: Stresses caused by the tensioning mechanism.

this material at the outset. Selection from the remaining materials was somewhat more difficult. The eventual choice could only be made through testing, so a sample of each material was tested to destruction in the disk-insert tensioning rig shown in fig.(6.2).

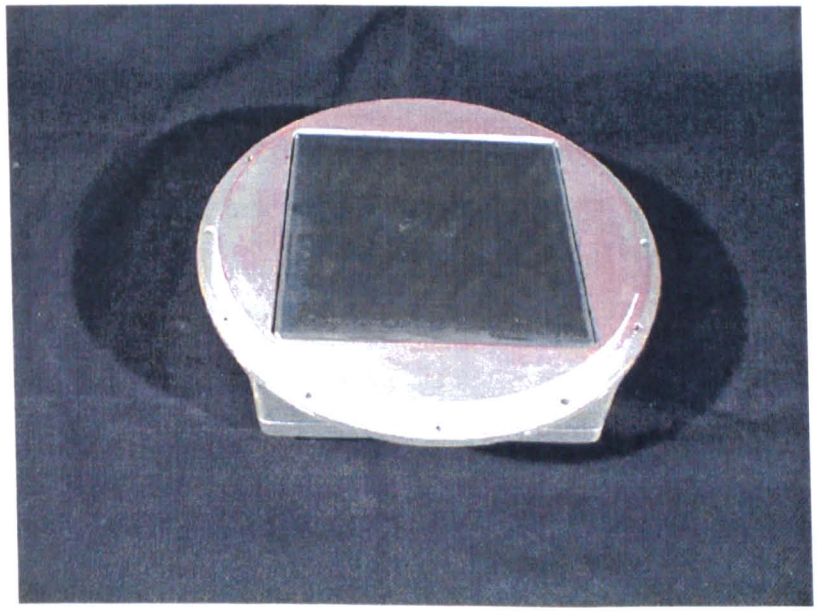

Figure 6.2: Photograph of finished tensioning mechanism and disk insert.

Testing revealed that the critical material property was tear strength. The corners between adjacent fold-over flaps proved particularly prone to failure. Tear strength is a material property which is dependent primarily upon the Young's modulus of the material. As such, the final material selection was based upon this property. Inspection of table (6.1), reveals stainless steel 17-7PH to be the preferred choice.

Appendix B contains the general arrangement and working drawings used during the manufacture of the disk-insert.

6.1.2 Design specifications for prototype porous surfaces

The foil drilling specifications, shown in table (6.2), were given to BAe (Sowerby Research Centre) for manufacture by their laser technologies department. Detailed drawings of the foil construction can be found in Appendix B, figure (B.8).

Foil #	Porosity %	Foil thickness (μm)	Hole diameter (μm)
1	6%	50	50
2	12%	50	50
3	12%	50	100
4	12%	50	200

Table 6.2: Specifications for the laser drilling of 17-7PH stainless steel foil.

Each foil was to have a $90 \times 90mm^2$ porous patch at its centre. However, problems were encountered during the drilling of certain foils. Marsdon (1996) advised that it would not be possible to produce foils 1 and 2 given the technology currently available. Essentially the laser optics could not be set up to produce holes of $50\mu m$ diameter. It was therefore decided not to pursue the manufacture of foils 1 and 2 any further. Consequently, only 2 foils were initially available for tunnel tests both of which were 12% porous. However, a 6% foil was later manufactured at the $100\mu m$ hole diameter and was received during the tunnel testing period.

6.2 The low turbulence wind tunnel and flat plate

The experiments on the PPW's were performed in the Low Turbulence Wind Tunnel at Queen Mary and Westfield College, London, under the supervision of Prof. Gaster. The tunnel is of the closed-return type, with a contraction ratio of 9:1, powered by a 25-hp DC-motor. The working section is 3 ft x 3 ft and is interchangeable. The turbulence intensity in the free stream is of the order 0.01%. The

test section houses an aluminium flat plate (figure 6.4) over which a boundary layer is formed. The plate has a flap and a trim tab which allow for the adjustment of the pressure gradient and the position of the stagnation line. Sixteen pressure taps are arranged in the streamwise direction along the front of the plate and two on the back of the plate, and are connected to an alcohol manometer bank.

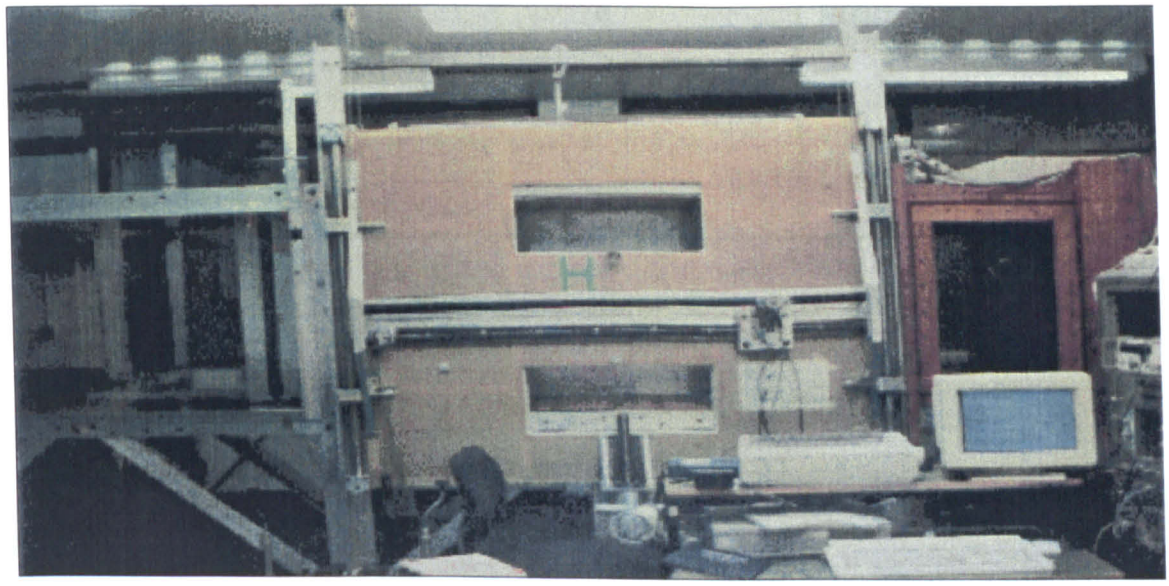

Figure 6.3: Photograph of the working section of the low-turbulence wind tunnel at QMW, London.

The hot-wire probe's traversing mechanism, shown in figure (6.3), uses the standard Cartesian coordinate system with the following reference points: $x = 0$ at the leading edge increasing in the streamwise direction, $y = 0$ at the surface of the plate increasing in the outward direction and $z = 0$ at the centerline of the plate in the spanwise direction. As the plate is mounted at a slight angle to the test section, the physical position of the surface with respect to the traverse gear's y coordinate changes with the streamwise co-ordinate.

The tunnel's aluminium flat plate has two interchangeable disc inserts with centers located (on the centerline) at $x = 400mm$ and $800mm$. The actual porous test area is centered on the disc mounted at $x = 400mm$; a blank disc is placed in the other location.

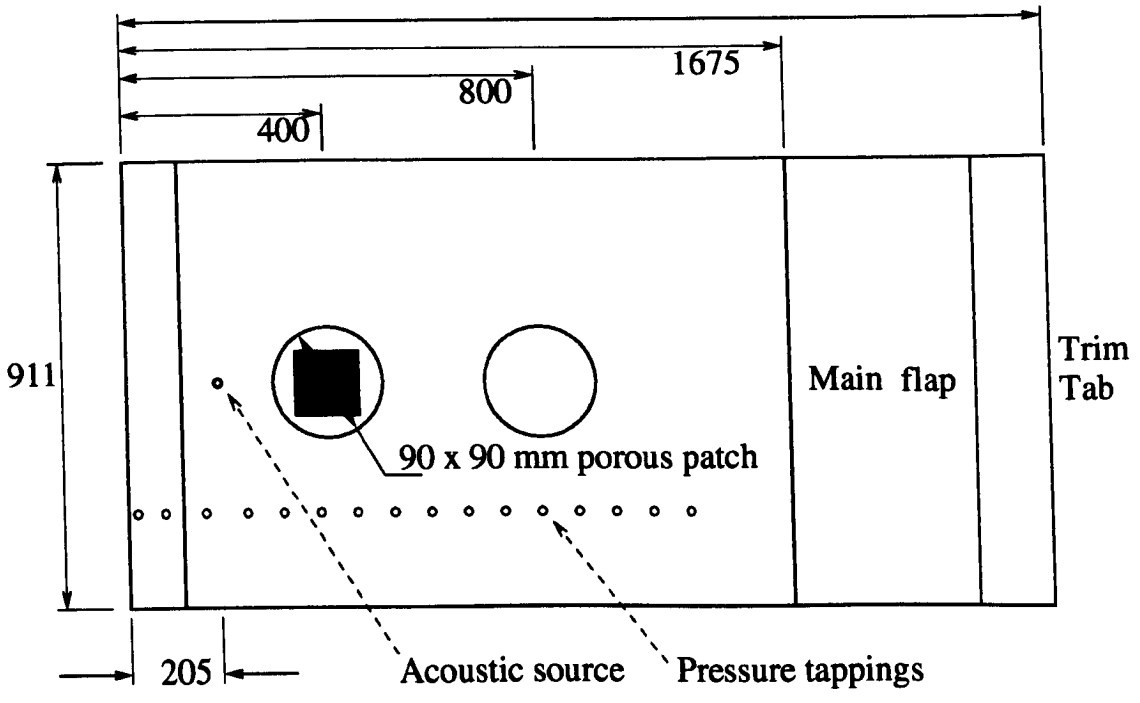

Figure 6.4: The flat plate and disc insert.

6.2.1 Hardware for T-S wave generation

The T-S waves must be generated artificially such that they are of known frequency and intensity. A small speaker, excited with a sinusoidal signal of less than 2 volts r.m.s., is adequate for this purpose. It is recessed into the plate $205mm$ downstream from the leading edge. These acoustic waves are propelled out into the boundary layer, through a $0.5mm$ hole in the plate, where they are convected downstream. They behave exactly as T-S waves except that the spectra of waves is confined to frequencies around that of the sinusoidal supply to the speakers.

The benefits of forced acoustic wave generation are considerable. The technique ensures that the dominant mode (one with largest growth rate) is that whose frequency is the same as the forcing frequency, thus allowing the use of electronic filtering of the hot-wire signal to remove any noise caused by background acoustics and vibration. Furthermore, the frequency of the supply can be controlled such that the response to a range of frequencies can be determined in a systematic manner.

The forcing signal supplied to the speaker is generated from software and stored in a hardware buffer (the SY12 shown in fig.6.6) via an IEEE interface. Essentially the computer generates a series of integers which determine the successive amplitude levels of the speaker signal. These integers correspond to voltage levels which, when released in sequence, form a sinusoid. The frequency at which these integers are released determines the overall frequency of the sinusoidal signal. Therefore, the frequency of the forcing can be set by the computer simply by adjusting the clock speed on the relevant IEEE module.

Every characteristic of the boundary layer forcing can be changed with software via the IEEE interface. The advantages of this are outlined below.

One of the requirements of the linear experiment is that the non-dimensional frequency should be kept constant throughout. Clearly, changes in tunnel temperature or barometric pressure will cause the value of F to vary continuously. For experiments of more that a few hours in duration, this can cause significant experimental error. However, to combat such a problem, tunnel codes can be designed to take environmental measurements at regular intervals; the computer then adjusts the clock speed to automatically compensate for such fluctuations.

6.2.2 Checking the expected behavior of T-S waves in region of interest

So that reliable comparisons can be made between theory and experiment, it is vital that the tunnel conditions are as close as possible to that which is required by the linear theory. In particular, care must be taken to ensure that there is no pressure gradient down the length or breadth of the plate. Furthermore, throughout the duration of the experimentation it is vital that parameters such as barometric pressure, temperature, and mean flow velocity are constantly updated so that parameters such as unit Reynolds number and F can be kept constant.

Once a nominal tunnel velocity is chosen, the frequency of the speaker supply must be set such that the T-S waves produced are unstable in the region of inter-

est. Consider the region of the porous wall insert, at between $300mm$ and $400mm$ downstream of the leading edge. At such a location, the displacement thickness is given as:

$$\delta^* = 1.72(\frac{\nu x}{U_\infty})^{\frac{1}{2}} \approx 0.91mm \tag{6.1}$$

The non-dimensional frequency at 20 m/s and 250 Hz is:

$$\omega = \frac{\overline{\omega} U_\infty}{\delta^*} \qquad F = \frac{\overline{\omega}}{Re_{\delta^*}} = \frac{\omega \delta^*}{U_\infty Re_{\delta^*}} = \frac{\omega \nu}{U_\infty^2} \tag{6.2}$$

$$F = \frac{\omega \nu}{U_\infty^2} = \frac{2 \cdot \pi \cdot 250 \cdot 1.533 \times 10^{-5}}{20.0^2} = 75 \times 10^{-6} \tag{6.3}$$

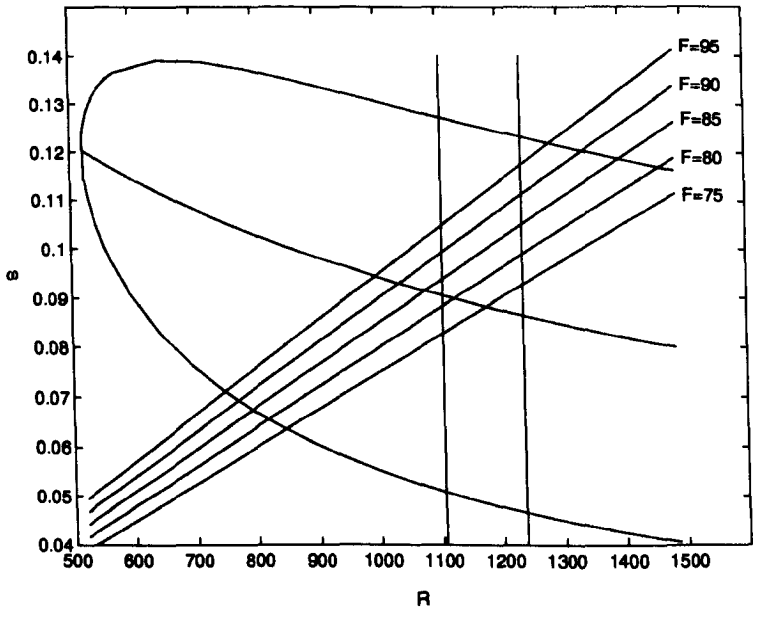

Figure 6.5: Neutral curve for the Blasius boundary layer. The parallel lines enclose porous region; diagonal lines indicate projections of constant frequency. The most unstable frequency line also shown.

The non-dimensional Reynolds number, based upon plate length, at say $350mm$ downstream of the leading edge, is approximately 1200. Inspection of the neutral stability curve shown in figure (6.5) illustrates that for this flow regime, one can expect the boundary layer to have a large response provided it is forced at

around the non-dimensional frequencies indicated by the diagonal lines. Indeed, the boundary layer over the porous patch of the plate is most unstable to a non-dimensional forcing frequency of around $\mathbf{92 \times 10^{-6}}$.

For reasons of safety, the actually experiments were run at a tunnel speed of $18\ \mathrm{m\,s^{-1}}$ for the range of forcing frequencies shown in figure (6.5). Speeds in excess of this caused serious blade vibrations on the propeller.

6.3 Data acquisition

6.3.1 Perturbation velocity measurements using the hot-wire

Streamwise velocity perturbations were measured using a Dantec^{TM} **55M01** constant-temperature hot-wire anemometer along with a single-wire probe constructed of $5\mu m$ platinum wire $1mm$ in length. The wire is fixed to a rod whose shaft is encased in an aerofoil to minimize the turbulent wake. This whole probe arm is then attached to the traverse gear such that it can move freely in x,y and z directions.

Equation (6.4) below defines the power law relating hot-wire voltage to the local flow velocity. The hot-wire voltage drifts over time owing to contamination of the hot-wire by dust particles or simply by changes in tunnel temperature. To maintain accuracy, a hot-wire re-calibration is generally done once every couple of hours. The value of the index parameter I is kept at 0.47 throughout while the values of the constants A and B are obtained by a least-squares curve fit to the calibration data.

$$E^2 = A + BU^I \tag{6.4}$$

For small perturbations, the following linearisation applies:

$$2E\delta E = IBU^{I-1}\delta U = \frac{IBU^I}{U}\delta U \tag{6.5}$$

Using eqn.(6.4) :

$$2E\delta E = \frac{I(E^2 - A)\delta U}{U} \tag{6.6}$$

Thus giving King's gradient as :

$$\frac{dU}{dE} = \frac{2EU}{I(E^2 - A)} \tag{6.7}$$

For small velocity perturbation, the following applies:

$$\delta U = \frac{dU}{dE}\delta E + O(dE^2) \tag{6.8}$$

Equation (6.8) therefore provides the magnitude of a velocity perturbation directly from the change in the wires a.c.coupled voltage. The dU/dE factor (King's gradient) is given from the calibration procedure and must be recalculated regularly to compensate for the voltage drift mentioned above.

6.3.2 Signal processing hardware

The experiment has been designed, by a number of previous researchers, such that every transducer (or actuator) can feed (or be fed) information directly into (or from) the computer. The IEEE interface provides the common bus system by which this integration can be achieved. Modular components of the system, such as filters, D/A converters and alike can simply be slotted into the bus thus allowing considerable flexibility of use. Figure (6.6) illustrates the particular setup used in the current experiment.

The hot-wire signal, in its raw form, is considerably noisy. However, since we are only concerned with the components of the signal which have frequencies around that of the forcing frequency, the signal-processing task is quite simple.

It is important to recognize that the use of analogue filters should ideally be

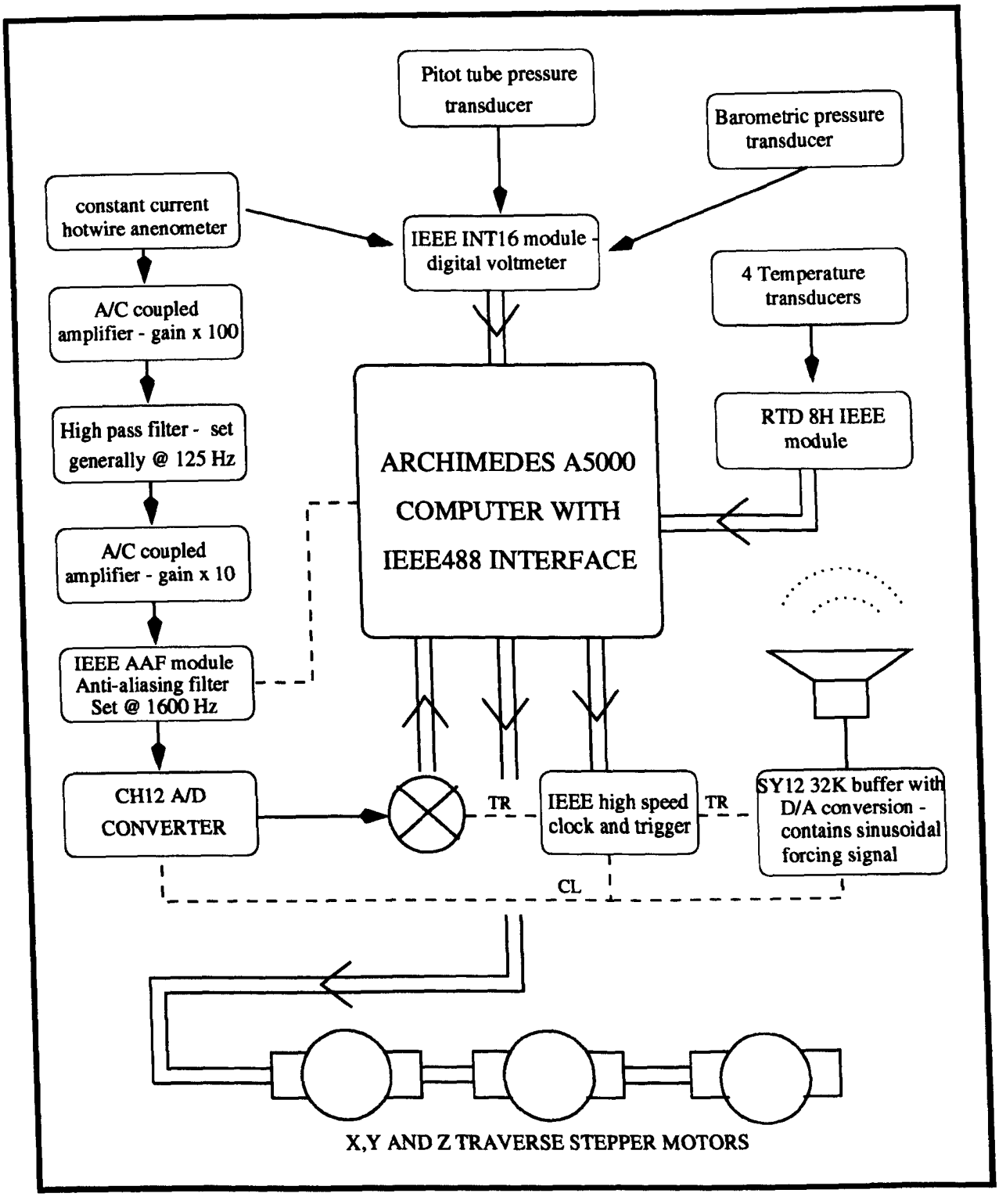

Figure 6.6: Flow chart for data collection system.

kept to a minimum. This is because such filters tend to alter the phase and gain of the signal they attempt to measure. The same is true for the use of analogue amplifiers; however, in this case, their use is unavoidable because the a.c. coupled

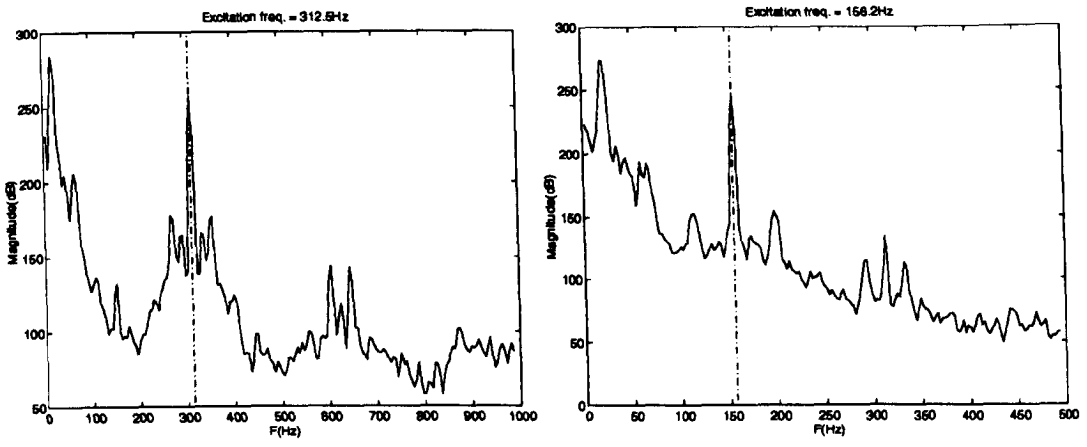

Figure 6.7: Power spectrum plots - for two forcing frequencies.

hot-wire signal is of the order of a few millivolts. An overall gain of 1000 was used in the growth experiments on the $50\mu m$ foil.

The inherent disadvantages of hardware filtering, as outlined above, have meant that the bulk of the signal processing has been done using software; ensemble averaging and Fourier analysis were both used for this purpose. However, a modicum of analogue filtering is required simply because the larger amplitudes of the signal power spectrum lie at very low frequencies. This can readily be seen in the spectral intensity plots of fig.(6.7). Essentially, when the raw hot-wire signal is viewed on the oscilloscope, the forcing frequency can be seen to ride on a very low frequency waveform of larger amplitude. This, in itself, should not be a problem, since the low-frequency noise would be filtered out in the ensemble-averaging process. However, the collection of such data would require a larger voltage range setting resulting in a loss of resolution when the noise is removed.

To enable smaller voltage collection ranges to be used, a high-pass analogue filter is used. This filter is inserted between the two a.c. coupled amplifier stages shown in fig.(6.6). This ensures the filter does not add any additional d.c. component to the signal. The settings for this filter depend on the type of experiment. For example, if the degree of tunnel turbulence is under consideration (no acoustic forcing applied) it is clear that the setting of the high pass filter is critical.

Indeed, any value of tunnel turbulence quoted should be accompanied by details of any filtering applied, otherwise the value is meaningless. For turbulence measurements it is critical that filtering only removes those disturbances whose length scales are too big to be considered turbulence, i.e.

$$L = \frac{U_\infty}{\omega}\frac{[\mathrm{m\,s^{-1}}]}{[\mathrm{s^{-1}}]} = \frac{20\ \mathrm{m\,s^{-1}}}{8\pi \mathrm{s^{-1}}} \approx 0.8\,\mathrm{m} \tag{6.9}$$

Equation 6.9 shows that at a tunnel speed of $20\ \mathrm{m\,s^{-1}}$, a disturbance of $4\,\mathrm{Hz}$ would have a length scale of around $0.8\,\mathrm{m}$. This scale is clearly much too large to be considered turbulence and it can therefore be deduced that filtering at 4 Hz should not effect the recorded value of true turbulence.

The collection of data in digital format requires the use of A/D converters (the CH12 modules). According to the Nyquist sampling theorem, if aliasing errors are to be avoided, the analogue data must be sampled at a minimum of twice the frequency of the wave to be recovered. For a more faithful digital reproduction, five times the analogue frequency is recommended. For this reason, it is necessary to band-limit the hot-wire signal such that frequencies above five times the forcing are removed. Devices constructed for this purpose are known as anti-aliasing filters (labeled AAF in fig.(6.6)).

The AAF filter, available as an IEEE module, is of the logic-controlled switched-capacitance type. This enables the filter to be programmed by the computer via the IEEE interface. Most of the experiments were done at forcing frequencies of between 200 Hz and 320 Hz. The AAF is therefore fixed at 1600 Hz throughout (roughly five times the forcing frequency).

6.3.3 Proposed type of transition experiment

Prior to a discussion of software signal processing it is important to establish what one would hope to achieve from the experiment. The main aim of the current research is to show that PPW's can be useful in attenuating the disturbance growth rates of forced acoustic waves. For this purpose, all that is required is a

comparative study using control experiments to compare with the results given using PPW's. The most critical aspect is therefore to ensure that the boundary layer characteristics and the tunnel environment are the same in both instances. Klingmann *et al.* (1993) outline what is required if one wants to do an experiment that will conform more closely to the linear theory. However, since the theory is widely accepted, there is little point in taking all of the exhaustive measures required to achieve such good agreement.

To reproduce the results predicted by the linear theory would require an enormous amount of attention to detail in setting up the experiment. The primary concern would be the attainment of a zero pressure gradient. In practice, it is extremely difficult to achieve such a pressure gradient. The finite plate thickness creates a suction peak near the elliptical leading-edge region which can extend up to $300mm$ downstream. The bulk of the pressure gradient must be set using the main flap. However, in the setup used at QMW college, the adjustment of this flap was very crude and could not be done while the tunnel was running.

For the above reasons, it was decided that only a comparative study was to be done. An emphasis was put upon ensuring that conditions were not changed from the control to the PPW experiment.

6.3.4 Signal processing software

Data sets of the $\hat{u}$ perturbation are required from within the boundary layer. The evolution of these perturbations can then be directly compared to that predicted by the linear theory (after suitable scaling). These readings are taken at many depths within the boundary layer (y co-ordinate) and at several streamwise locations (x - direction). At each hot-wire location (shown in figure (6.8)), a phase-locked data set is taken. These data can then be assembled into streamwise eigenfunction data sets and then compared directly to the results of the computational investigation. Section (6.5.1.3) explains in detail how the experimental results for

the growth experiment are compiled for comparison with theoretical e^n predictions.

Only the $2D$ components of the measured perturbations, u', are to be recorded as they evolve in the x dimension (down the length of the plate). However, the acoustic sources radiate their pressure waves in a three-dimensional manner. Inspection of fig.(6.8) illustrates the domain of influence of these pressure waves. Symmetry is assumed so that only half of the domain is shown. This information is used to ensure that during subsequent experiments, measurements are not wasted by moving the probe to locations where the source has no influence. In general, it is noticed that the domain of influence is narrowed as the excitation is moved to higher frequencies. This implies that lower frequency waves are more unstable in oblique directions. This means that experiments conducted at the higher frequencies can use a narrower experimental mesh. This could mean either fewer points (making data collection less time consuming) or a finer mesh and better resolution of flow features.

To recover only the 2D component of the forced wave, hot-wire traverses in the $\mathbf{z}$ direction (spanwise direction) are taken at both minimal extremes of the acoustic source's influence. These $\mathbf{z}$ - traverse data are then processed to remove the 3D components.

Figure (6.8) shows the 20 streamwise locations at which data is to be collected. In addition to this, 30 z locations are sampled at each streamwise position, so that the 3D components can be removed (using discrete Fourier transform techniques). Twenty-one data points are used in the $\mathbf{y}$ direction, through the boundary layer, so that disturbance profiles can be obtained. In fig.(6.8), only the magnitudes of the collected data corresponding to $\eta = \mathbf{6}^*$ are shown. The resultant experimental grid has 12600 nodes in total. Such large amounts of data mean that the typical duration of a single experiment is 16 hours.

*η is the wall normal co-ordinate used to define the boundary layer equation in Appendix A.3

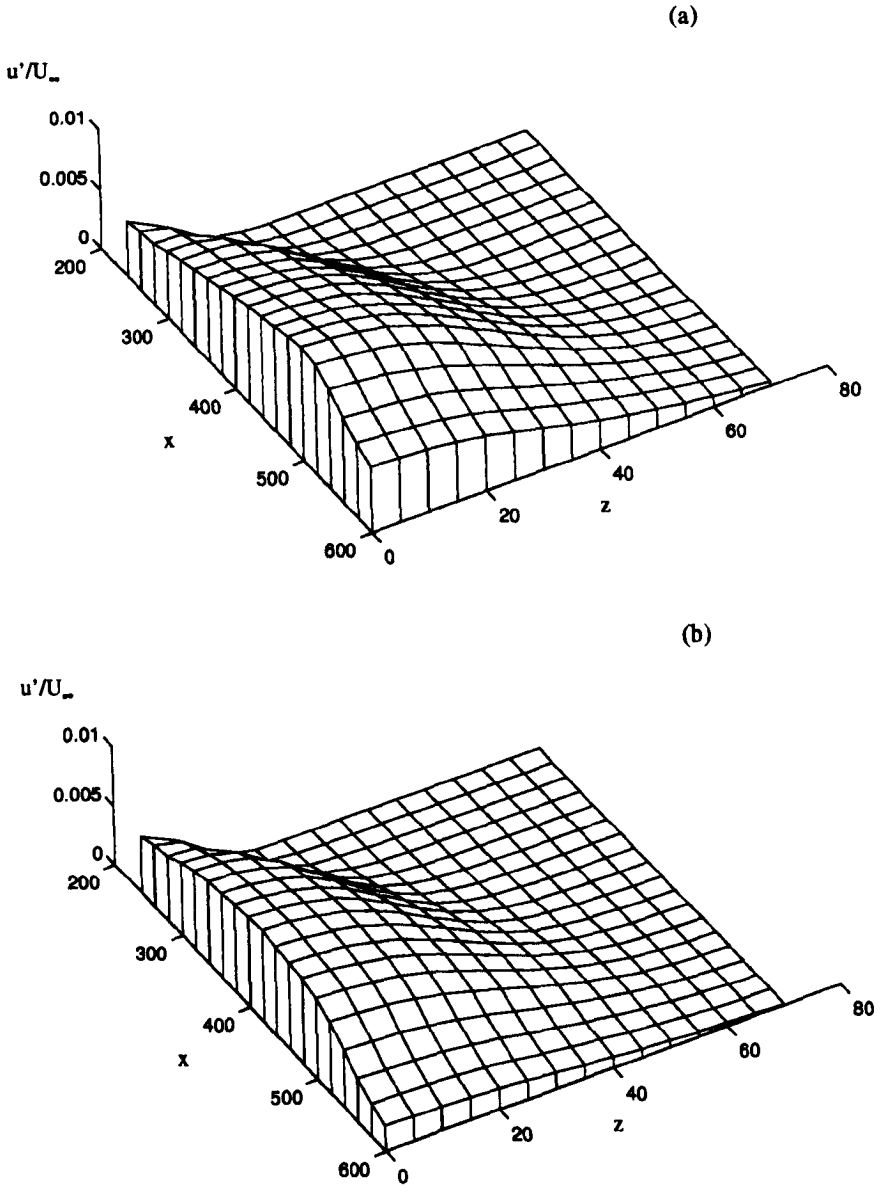

Figure 6.8: Plots of the domain of influence of the acoustic source, taken at $\eta = 6.0$ - (a) F=85, (b) F=92

Phase information is required so that the complete spatial evolution of the wave can be reconstructed. This phase information is achieved by *phase-locking*. This involves configuring the electronics such that the data set of each node is recorded at the same instant the acoustic sine wave is initiated. This requires the use of a high-precision internal clocking device. The sinusoidal signals received at each position are stored in a data file, in the form of complex numbers, ready

for further signal processing. At each location, 32 k bytes of data are collected. This amounts to 64 bytes of information per raw sinusoid. This data sample is then ensemble averaged (or folded) so that any non phase related background noise (usually acoustic in origin) can be averaged out. The averaging process is done during the experiment, using purpose written software, in real time on a Archimedes A5000 computer. This *on the fly* processing removes the need to store raw signal data.

To reduce the requirement for the storage of large amounts of data, only the first three Fourier components of the signal are stored at each measurement node. Equation (6.10) illustrates the discrete computation of the first Fourier component from the ensemble averaged signal;

$$C_1 = \frac{1}{N} \sum_{r=0}^{N-1} dE_r(x,y,z) e^{-i(2\pi r/N)} \tag{6.10}$$

where N is the total number of values contained in the ensembled dataset. In our case, the instrumentation was sampled at 64 points per cycle (of driver) until the 32k buffer was filled. This 32k buffer is then folded every 64 points to produce $dE_N(x,y,z)$; 64 values forming one sinusoid. $dE_r(x,y,z)$ is simply the r^{th} value of these 64 points. The second and third Fourier coefficients were computed in a similar manner

The CH12 module samples the hot-wire and assigns an integer from 1 - 4096 to each sample in the record. This integer corresponds to a measured instantaneous voltage for a given voltage range setting (CHVR - channel voltage range). If CHVR = 12, then integer 1 corresponds to -5 volts, 2048 is 0 volts and 4096 is +5 volts. Since the hot-wire signal was a.c. coupled, the mean of the integers collected in a given record should be 2048 - corresponding to 0 volts r.m.s. If the sampled voltages exceed the current voltage range, then the software will detect this, increase the range and re-sample that node. Similarly, if the voltage range is set too high, this is detected and reduced thereby increasing the resolution of the

sampled data. Equation 6.11 illustrates how the integer data are converted into hot-wire volts.

$$dE_r = \frac{(\mathrm{INT} - 2048)}{4096} * \mathrm{CHVR} \tag{6.11}$$

Equation (6.8) gives $du = du/dE \cdot dE_r$ where du/dE is the King's gradient as computed from the calibration procedure.

Ideally, data are also required from within (or beneath) an individual pore; characterizing the wall admittance. As shown in eqn.(3.55), this involves the measurement of wall pressure fluctuations, velocity perturbations through the wall and the phase relationship between these two quantities. Carpenter (1993) has shown that the theoretical performance of a PPW is very sensitive to the admittance phase angle (φ), so the measurement of this quantity is of critical importance . These magnitudes of $\hat{q}_W$ and $\hat{p}_{es}$ are expected to be minute. The normal velocity perturbations through the wall, for example, are expected to be of the order of 0.01 $\mathrm{m\,s^{-1}}$. It is not clear at this stage if the measurement of such a velocity is achievable. Laser Doppler techniques may be suitable for this purpose. With regard to the pressure measurement, this too is expected to present special difficulties. However, the measurement of both quantities is considered beyond the scope of the current research but are certainly challenging tasks worthy of future study.

6.4 Validating the experiment

6.4.1 Tunnel free-stream turbulence level

For comparison with results from the numerical investigation it is advantageous that the free-stream r.m.s. turbulence level should be as small as possible. The primary motivation for the achievement of minimal turbulence is the desire to maintain a laminar boundary layer throughout the full length of the plate. Free-stream disturbances are important in the initiation of natural transition due to the receptivity of the boundary layer. Not only would turbulence at the downstream portion of the plate actually shorten the domain over which experimental results can be collected, but intermittency of that turbulence would cause fluctuations in the upstream pressure gradients thereby invalidating the experiment.

Intermittency of turbulence can also be a problem on the non-working side of the plate. Here, pressure gradient fluctuations caused by intermittent turbulence may well cause the position of the stagnation point to vary. Such problems are avoided using a boundary layer trip wire, positioned close to the leading edge of the back of the plate. Trip wires are used for a similar reason just before the main flap on the working side of the plate.

Equation (6.12) defines the turbulence intensity as the RMS value of the $\hat{u}$ component.

$$Ti = \sqrt{\sum_{i=1}^{N} \frac{(x_i - \overline{x})^2}{N}} = \sqrt{\frac{\sum_{i=1}^{N} x_i^2}{N} - \left(\frac{\sum_{i=1}^{N} x_i}{N}\right)^2} \tag{6.12}$$

where x_i it the i^{th} sample out of N of the streamwise perturbation $\hat{u}/U_\infty$. The $\hat{v}$ and $\hat{w}$ components are not included because their magnitudes are much smaller.

Figure (6.9) illustrates how the free-stream turbulence fluctuates down the length of the tunnel working section. The two plots present data collected within half an hour of each other. Conditions were not precisely similar; the tunnel

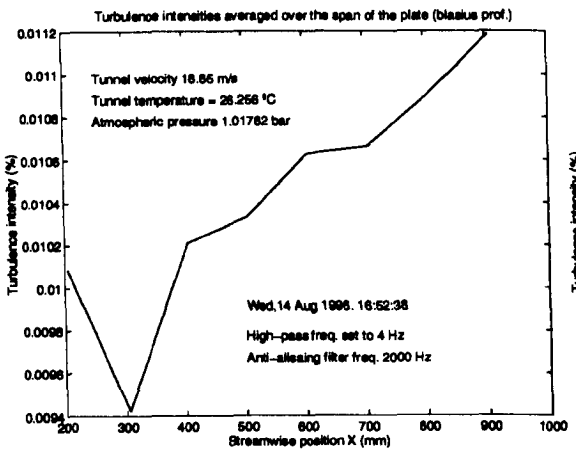

6.9.1: Ti, taken at 16:52

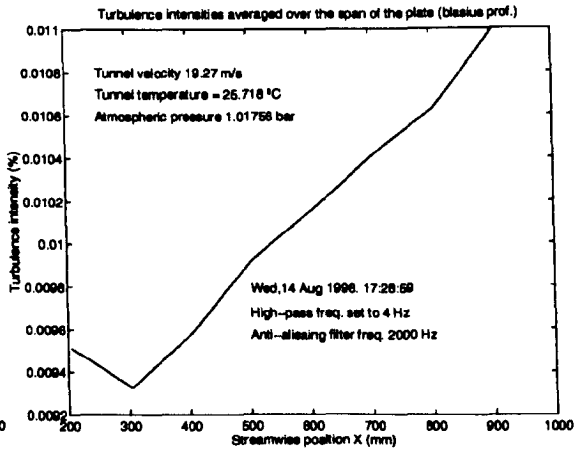

6.9.2: Ti, taken at 17:28

Figure 6.9: Two samples of mean turbulence measurements taken $60mm$ from the wall, in the free-stream, at various streamwise locations.

speeds differ slightly. However, the results show two distinct trends. The most obvious feature is the steady rise in the level of turbulence as one traverses down the length of the plate. This is, of course, to be expected. However, a more interesting observation is the apparent initial drop in turbulence intensity between $200mm$ and $300mm$. The cause of this is, as yet, unknown. Perhaps the advantageous pressure gradient caused as the flow accelerates around the elliptic nose of the plate may play a role.

Stability experiments of the type undertaken herein are extremely sensitive to deviations in both streamwise and spanwise pressure gradient. For ideal Blasius flow, a zero pressure gradient must exist all the way from the leading edge. However, this cannot be achieved in practice because the plate has finite thickness. The problem in compounded because the flat plate at QMW has some surface waviness.

It can be seen from the plate construction diagram fig.(6.4) that there are two flaps attached to the flat plate. The larger flap is used to set the overall pressure gradient while the smaller trim-tab is used to locate the position of the stagnation

point. The stagnation point should be adjusted such that the size of the leading edge suction peak is minimized. Figure (6.10) plots the readings taken from an alcohol manometer bank once the pressure gradient had been set. Each bar plotted corresponds to a reading taken from one of these tappings. Figure (6.10) clearly shows the suction peak formed by the elliptical nose. This region extends as far as $200mm$ downstream. Any T-S waves generated in this region will be attenuated by the accelerating flow. It is for this reason that the flat plate must have its acoustic exciter in a position far enough downstream to ensure that the pressure gradient has recovered to an acceptable level. It can clearly be seen, from the figure below, that the experimental setup at QMW does not provide sufficient data with which to accurately set the pressure gradient. The experiment requires a great many additional pressure tappings together with a high tapping concentration in the vicinity of the leading-edge.

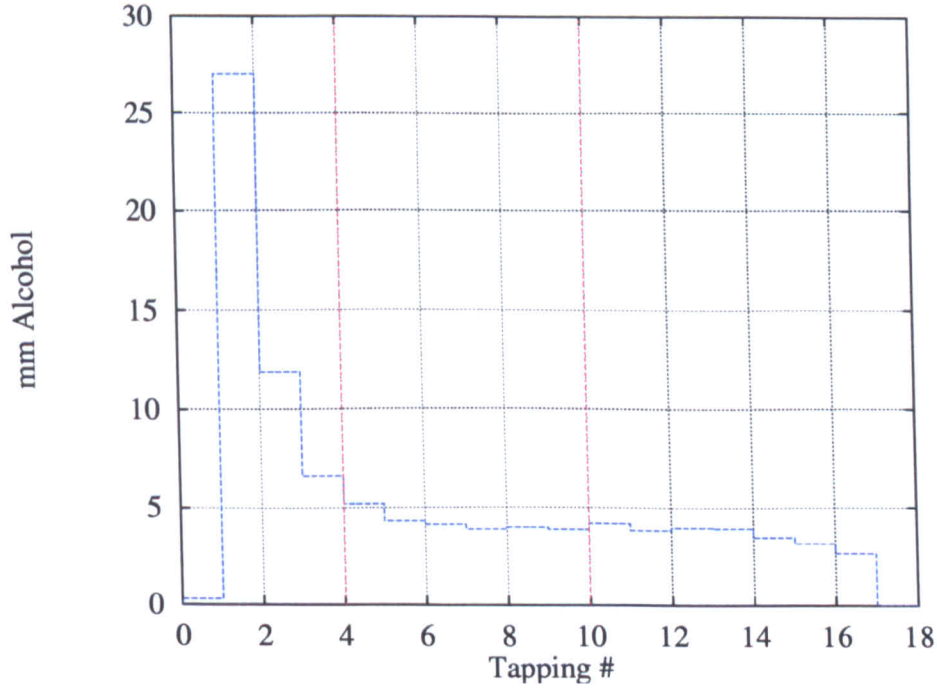

Figure 6.10: Manometer bank readings - from 16 static pressure tappings positioned down the length of the plate. Bank inclined at 1^o.

The parallel lines (in red) of fig.(6.10) define the domain over which T-S waves will be excited and measured. Within this region there is a pressure differential

corresponding to $\Delta h = 4mm$ of alcohol. The density of alcohol is $758\,\mathrm{kgm}^{-3}$, giving $\Delta P = \rho g h \theta = 0.52\mathrm{Pa}$ (for small θ). Here, θ is the inclined angle of the bank with respect to the horizontal; set at 1° in this case. Thus, the total pressure differential over the region of interest is very small. The results presented in § 6.5.2 will illustrate that even this small differential can be sufficient to cause major problems. Essentially a passive porous wall, with a continuous cavity, will prove useless in the presence of even a mild pressure gradient because such conditions would lead to gross inflows and outflows of fluid from the cavity. These larger scale fluid motions would essentially drown out the tiny fluid motions associated with the passive porous effect. Indeed, a reduced pressure over the aft region of the porous surface will cause a *blowing* effect at the downstream end. This would then lead to rapid destabilisation of the boundary layer.

There in one further complication worthy of consideration. The elliptical nose shape at the leading edge of the flat plate causes a large suction peak upstream of the measurement range. This will cause a discrepancy between the theoretical streamwise Reynolds number which applies to a infinitely thin flat plate, and that which exists in practice. Such effects are, however, fairly minor and could be easily compensated using a virtual origin. Such compensation was not used in the current study.

6.4.2 Ensuring the forced disturbances behave linearly

The question to be answered in this section is at what amplitudes should the acoustic waves be excited. The primary concern is to ensure that the forced disturbances within the boundary layer should remain sufficiently small that they can be said to behave linearly. In terms of the modal analysis, this amounts to there being a causal relationship between the input to the system (the acoustic signal) and its output (the T-S wave) with the boundary layer providing the system's response. As with any linear system, one would like the output of that system to be modified only in phase and amplitude from the input. If the system produces different modes or does not behave in a causal manner, then it is said to behave non-linearly.

As a general rule of thumb, according to Gaster (1997), any disturbance which exceeds 0.03% of the free stream velocity would tend to have a non-linear response within the boundary layer. However, this criterion must be applied to the appropriate portion of the disturbance profile. The inner maximum of the T-S disturbance profile is significantly larger than the outer and, although being harder to measure, is the real region of interest when considering linearity. More rigorous ways of ensuring a linear response are outlined as follows. In the first instance, one could use the signal processing methods presented earlier in § 6.3.4. After ensemble averaging of the signal , one could compare the relative magnitudes of the 1^{st}, 2^{nd} ...Fourier components. Essentially, a linear response would have a large 1^{st} component while all subsequence components would be negligible. This would have to be done over a range of positions since the boundary layer's response is dependent upon both the current x, y and z co-ordinates. Furthermore, such measurements should be taken on the centerline ($z = 0$) since all other z locations would measure oblique waves which are known to more stable for the frequencies used herein. Other methods include the measurement of disturbance profiles, using the signal processing of techniques of § 6.3.4, for incremental values of the forcing voltage to the acoustic source. These profiles

are then collapsed down upon each other by normalization such that the inner maximum is unity. Essentially, the forcing is too high and non-linear effects are apparent once the collapsed profiles do not fit closely upon one another. This was the technique used in the current study.

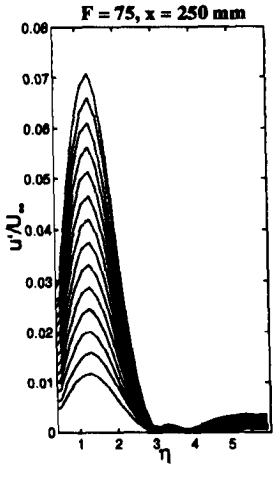

6.11.1: $F = 75$, $x = 250mm$ (near field)

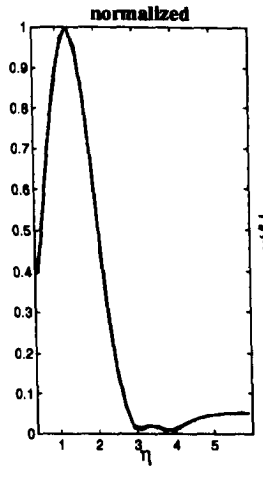

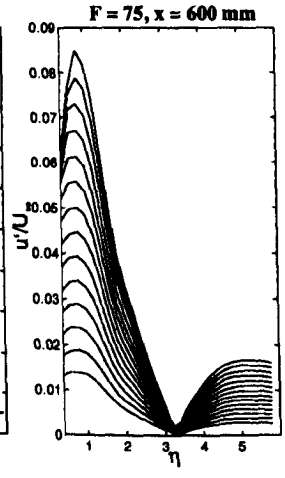

6.11.2: $F = 75$, $x = 600mm$ (far field)

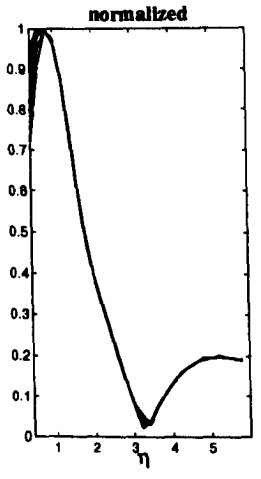

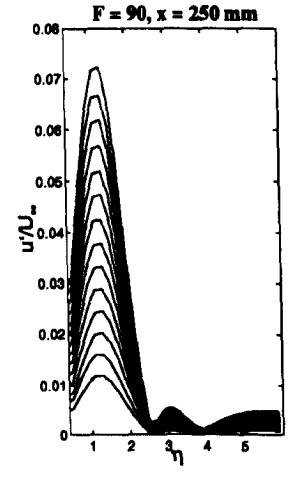

6.11.3: $F = 90$, $x = 250mm$ (near field)

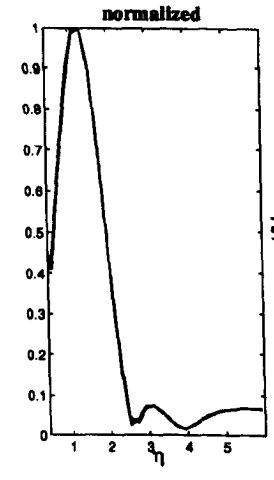

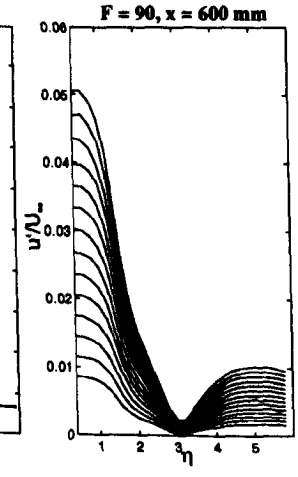

6.11.4: $F = 90$, $x = 600mm$ (far field)

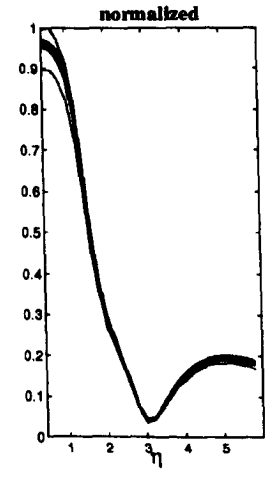

Figure 6.11: Boundary layer linearity tests - forced disturbance profiles - ramped voltage from 0.05 to 0.8 volts r.m.s.

Figure (6.11) shows some results in both the near and far field for exciter voltage increments of 0.054 volts over a range of 0.05 to 0.8 volts. The only plots which

do not collapse satisfactory are those of the last two voltage increments of the far field results for $F = 90$ (fig.6.11.4). This would suggest that a voltage of 0.78 volts would be suitable. This was the value used in all subsequent experimental work.

6.5 Experimental results

6.5.1 Preliminary results from the control experiment

6.5.1.1 Flow characteristics

Following the discussion of § 6.3.3, it is clear that the most critical aspect of the experiment is to ensure that the tunnel/flat plate configuration remains the same for both the control and the actual experiment. The required consistency can only be achieved by making the minimum of changes to the tunnel and plate once it is in situ. This was achieved most effectively by covering the porous insert with a sheet of adhesive acrylic sheet. The sheet was sufficiently thin so as not to cause any appreciable disturbances within the boundary layer. As such, the changeover from control experiment (no porosity) to the PPW experiment is a simple matter of removing the sheet covering the porous foil. This has many advantages. A major benefit is that the disk insert does not have to be removed, thus one is assured that the pressure gradient has not been altered between control and experiment. A further advantage is that one does not need to repeat the laborious task of installing the insert, ensuring it is level and filling-in any surface cavities around its edge.

Once the disk is installed and the pressure gradient and stagnation point have been set to produce the smallest and most even pressure gradient, one is then ready to proceed with hot-wire measurements. The usual starting point in such an investigation is to measure the mean velocity profiles, to ensure that the flow is indeed Blasius. Figure (6.12) plots the measured profiles obtained by taking the average of three sampled voltages at each grid node. These data are obtained by connecting the raw hotwire signal directly to the int16 IEEE digital voltmeter module. These voltages are then converted into velocities using the same techniques used to deduce u' as outlined in § 6.3. No amplification, a.c. coupling or any other signal processing is required for this measurement.

6.5.1.2 Post-processing raw profile data

The first problem encountered was the determination of the wall zero ordinate. The y-positioning system used in the tunnel is not sufficiently accurate for the raw data to be used without the redefinition of the y-ordinate origin. The distance from the wall and the first data point can deduced by simply fitting a polynomial to the 1^{st} few data points of the measured profile. In fact, a linear fit all that is required in this near-wall region. Only the 3^{rd},4^{th} and 5^{th} points were used in practice, since the points 1 and 2 were erroneous because of wall interference. This resultant linear equation is then used to extrapolate the data to the abscissa. The whole y-ordinate data set is then shifted by the value at the abscissa. The data are thus corrected for the no-slip condition.

The corrected data are then ready for processing. This includes the computation of parameters such as boundary layer displacement thickness δ^*, momentum thickness θ (or momentum loss thickness) and shape factor H, as shown in eqns.(6.13). These computation were done, using Simpson integration, within the MATLAB^{TM} software package.

$$\delta^* = \int_0^\infty (1 - \frac{u}{U_\infty})dy \qquad \theta = \int_0^\infty \frac{u}{U_\infty}(1 - \frac{u}{U_\infty})dy \qquad H = \frac{\delta^*}{\theta} \tag{6.13}$$

The boundary layer equations for Blasius flow have no preferred length scale. This means that velocity profiles are self similar. Hence, the profiles at varying streamwise locations, once normalised, should all look the same. Computations using the boundary layer equation for Blasius flow, Schlichting (1987), indicate that the theoretical ratio between δ^* and $(\nu/U_0)^{1/2}$ should be $\mathbf{1.72}$ with shape factor $H = \mathbf{2.59}$. Tables (6.3) and (6.4) summarise the characteristics of the measured boundary layer at various locations. Initial inspection of these tables reveals that the general trends are as expected. There is a thickening of the boundary layer from $\delta^* = 0.885$ to $\delta^* = 1.204$ as we move downstream from $x = 300$ to $x = 600$ at the centerline. However, at both x stations, it is interesting to note the

x (mm)	z (mm)	U_o (ms^{-1})	δ^* (mm)	$\delta^*/(\nu x/U_o)^{1/2}$	$\theta/(\nu x/U_o)^{1/2}$	Re_{δ^*}	$1.72Re_x^{1/2}$	H
300	-120	18.7	0.875	1.733	0.660	1029	1022	2.625
300	-80	18.7	0.890	1.761	0.662	1046	1021	2.660
300	-40	18.7	0.887	1.755	0.659	1042	1021	2.664
300	0	18.7	0.885	1.753	0.666	1041	1021	2.633
300	40	18.7	0.855	1.693	0.654	1005	1021	2.591
300	80	18.7	0.853	1.689	0.647	1002	1021	2.609
300	120	18.7	0.858	1.698	0.648	1008	1021	2.620

Table 6.3: Characteristics of the measured profiles at a streamwise location of $300mm$.

x (mm)	z (mm)	U_o (ms^{-1})	δ^* (mm)	$\delta^*/(\nu x/U_o)^{1/2}$	$\theta/(\nu x/U_o)^{1/2}$	Re_{δ^*}	$1.72Re_x^{1/2}$	H
600	-120	18.7	1.205	1.685	0.656	1414	1443	2.567
600	-80	18.7	1.196	1.672	0.650	1402	1443	2.573
600	-40	18.7	1.197	1.674	0.647	1404	1443	2.586
600	0	18.7	1.204	1.683	0.650	1412	1443	2.588
600	40	18.7	1.194	1.669	0.644	1400	1443	2.590
600	80	18.7	1.170	1.635	0.636	1372	1443	2.569
600	120	18.7	1.186	1.657	0.642	1390	1443	2.583

Table 6.4: Characteristics of the measured profiles at a streamwise location of $600mm$.

spanwise variation in displacement thickness. The boundary layer appears to be consistently thicker at the bottom of the plate.† This is not desirable and would in-

†Note the plate was mounted vertically in the tunnel working section.

dicate some asymmetry in the positioning or construction of the flat plate. However, most of the measured shape factors and ratios agree reasonably well with the predicted theory. The increased discrepancy at the downstream location is presumably due to the downstream flap and associated wake which create a non-zero pressure gradient upstream.

Figures (6.12) and (6.13) show the corrected data overlayed upon the theoretical profiles. Plots are also given showing the percentage deviation from the ideal for each profile measured. At $300mm$ the maximum deviation is 1% while at $600mm$ it is only 0.5%. This is probably only because the upstream profile is thinner and therefore cannot be measured with the same resolution as the downstream profile.

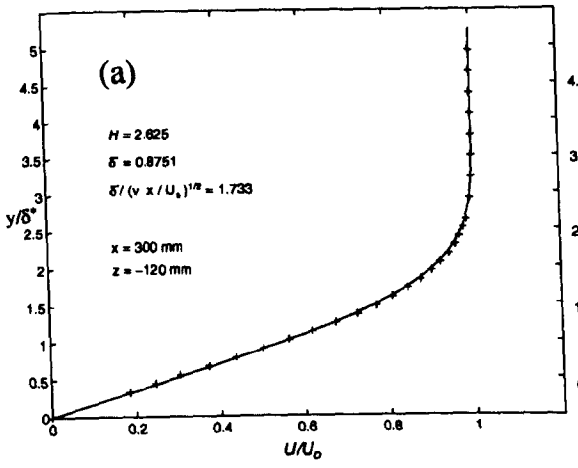

6.12.1: $x = 300mm$, $z = -120mm$

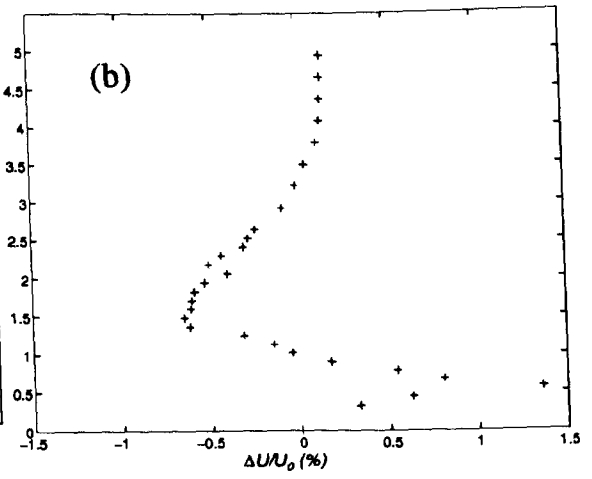

6.12.2:

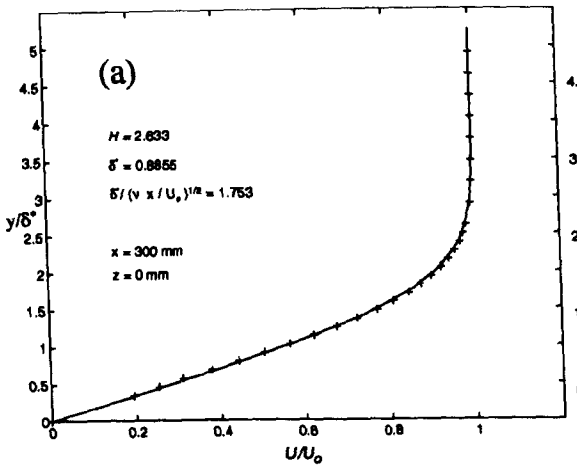

6.12.3: $x = 300mm$, $z = 0mm$

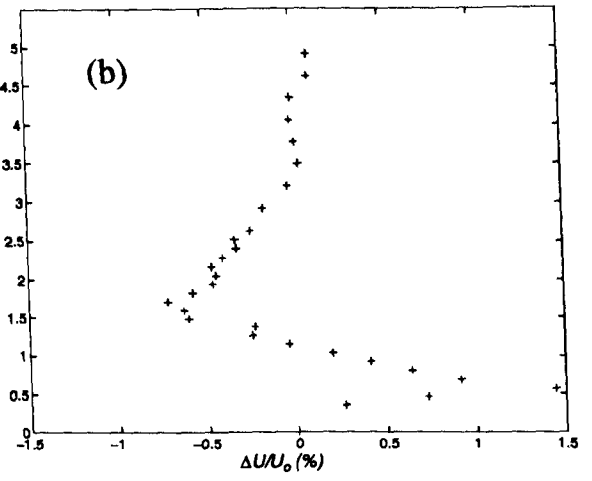

6.12.4:

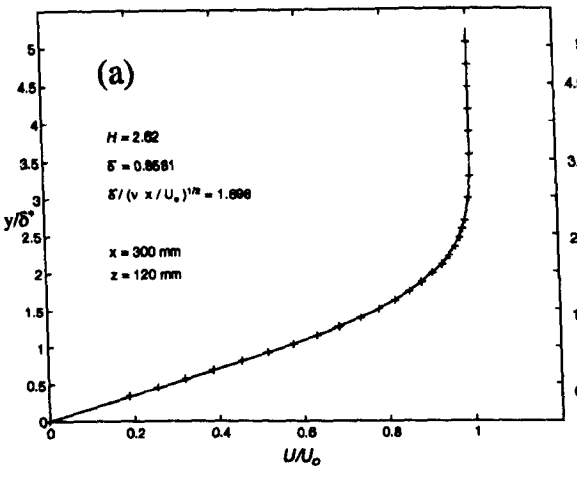

6.12.5: $x = 300mm$, $z = 120mm$

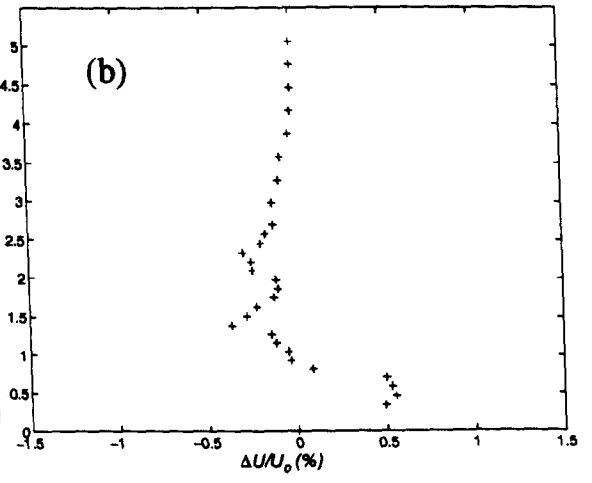

6.12.6:

Figure 6.12: (a) Mean velocity profiles at $x = 300mm$ for $U_o = 18.7\ \mathrm{m\,s^{-1}}$. —— computed Blasius profiles. '+' denotes experimental measurements. (b) Velocity discrepancy $\Delta U/U_o(\%)$ between measured and theoretical Blasius profiles.

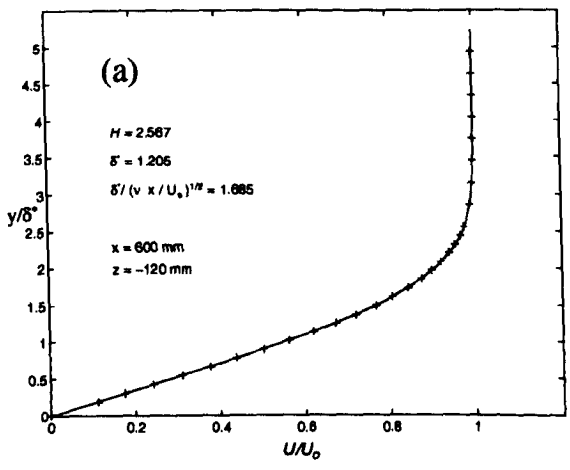

6.13.1: $x = 600mm$, $z = -120mm$

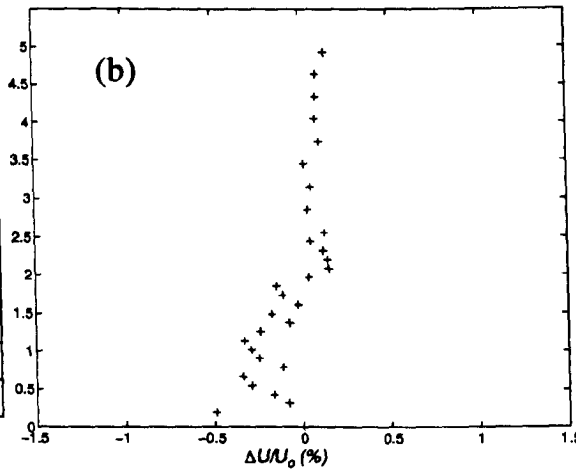

6.13.2:

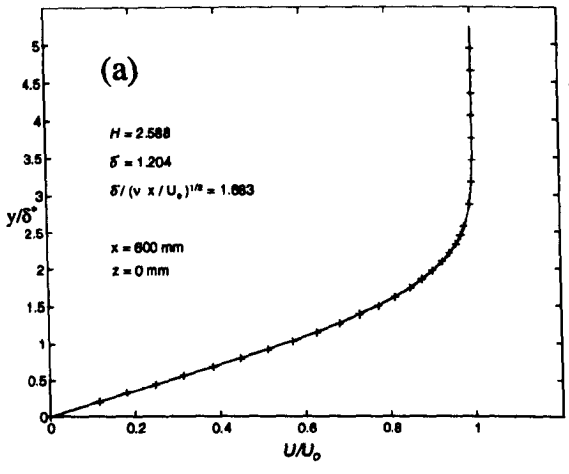

6.13.3: $x = 600mm$, $z = 0mm$

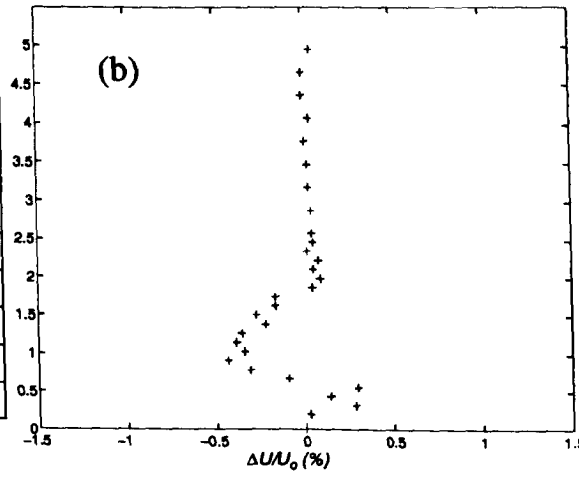

6.13.4:

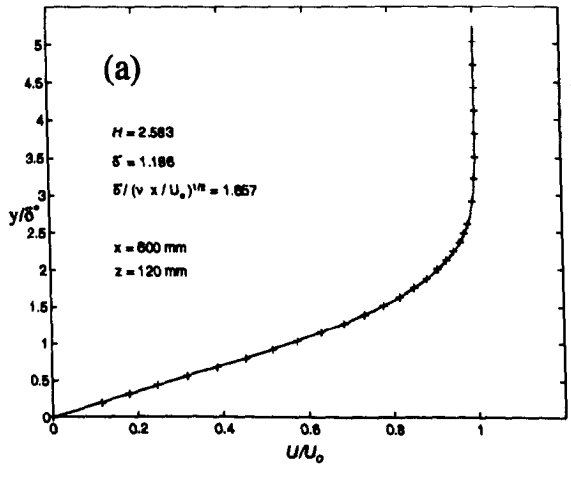

6.13.5: $x = 600mm$, $z = 120mm$

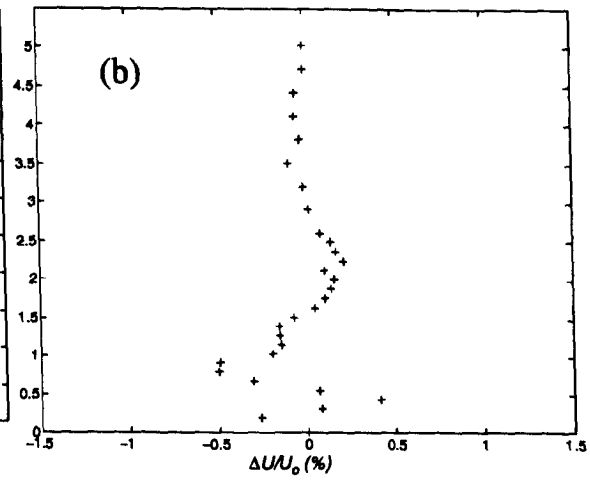

6.13.6:

Figure 6.13: (a) Mean velocity profiles at x=600mm for $U_o = 18.7$ m s^{-1}.—— computed Blasius profiles. '+' denotes experimental measurements. (b) Velocity discrepancy $\Delta U/U_o(\%)$ between measured and theoretical Blasius profile.

6.5.1.3 Processing of raw data for growth experiment

As outlined in § 4.4.3, engineering predictions of transition are generally given using the semi-empirical e^n method. A numerical prediction is possible using the linear theory provided data exists concerning the n factor at transition. Such data are obtained through experimentation. The n factor varies according to the geometry/pressure-gradient under consideration. For the Blasius boundary layer, an n factor of 9 is generally assumed (Smith and Gamberoni (1956)). According to eqn.(4.50) of § 4.4.3, the ratio of the disturbance magnitude at position x to its initial magnitude at x_i (i.e. $\hat{v_x}/\hat{v_i}$) is given by e^n where the n exponent is defined by:

$$n = -2/(1.7208)^2 \int_{Re_i}^{Re} \hat{\alpha_i^*} dRe \tag{6.14}$$

While the primary role of the experiment is to compare T-S growth rates with and without the PPW boundary condition, a further use is the comparison of measured $\hat{v_x}/\hat{v_i}$ values with the corresponding e^n value obtained by computation. This would enable us to calibrate the tunnel to determine an n factor at transition. This calibration is nevertheless only applicable to this specific tunnel configuration which, unfortunately, has all the imperfections associated with a practical experiment.

Section (6.3.4) explained how the hot-wire signal was ensemble averaged at each station with the first three Fourier components subsequently written to file. Since the frequency of the acoustic source is fixed, this 3D Fourier data can be processed further, using Fourier transform techniques, to extract the 2D wave components. Essentially, the 2-D wave fronts, located mid-channel, are expected to have a high 1st Fourier component and relatively small harmonic components. However, as one traverses (in z) outboard toward the top/bottom of the tunnel the wave fronts become more oblique. The oblique wavefronts would exhibit larger harmonic spectral content; increased 2nd and 3rd Fourier coefficients. Higher

second and third coefficients can also be expected when non-linearities start appearing in the flow.

The recovery of the 2-D spectral content is therefore a trivial computation. All that is required is the average of the 1st harmonic components at all the z locations for a given x, eqn.(6.15).

$$K_0(x,y) = \frac{1}{M}\sum_{k=1}^{M} C_1(x,y,z_k) \tag{6.15}$$

6.5.2 Results of 6% foil with pore diameter $50\mu m$

Figure (6.14) presents the growth data for the 6% porosity foil at a tunnel speed of $16.8\ \mathrm{m\,s^{-1}}$. Overlayed on each plot are the growth curves for the non- porous case.

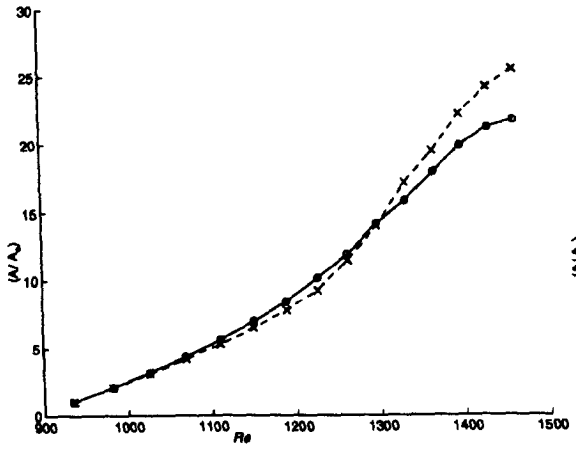

6.14.1: $F = 75$

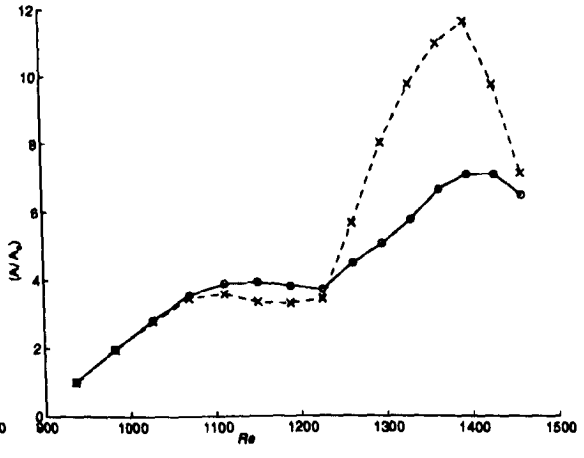

6.14.2: $F = 80$

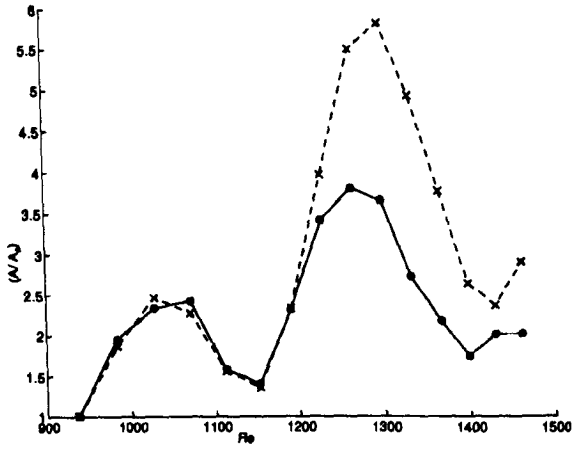

6.14.3: $F = 85$

Figure 6.14: Growth curves for the $50\mu m$ pore configuration at 6% porosity; —— non-porous control; – – – porous wall.

The most obvious result is that the downstream growth of disturbances are, without exception, larger for the porous surfaces in comparison with their control. It is also significant that there is a small region of suppression in the upstream

portion of the porous surface followed by a large amplification at the downstream end. Figure (6.14.3) illustrates that the final growth at $F = 85$ for the porous surface is nearly twice that for the control surface. This does not, however, indicate that the higher frequencies give the most unfavorable results, but rather that the higher frequencies have a lower overall growth thereby stretching the vertical scale on the plots. Indeed, the largest growth is attributed to the $F = 75$ experiment. This is in accordance with the predictions of the linear theory as shown in fig.(6.5).

6.5.2.1 Possible cause of unfavorable result for 6% foil

Kachanov (1997) has suggested that these results should not have been entirely unexpected. He performed a similar set of experiments on porous surfaces some years ago but was unable to achieve a beneficial result. He recalls similar growth features to those presented herein. Essentially, Kachanov proposed that the reason for the characteristic dip followed by rapid growth was a feature caused by suction over the leading portion of the foil and blowing at the downstream portion. This suction and blowing was simply caused by the existence of a finite, but small, pressure gradient in the streamwise direction. The volumes of fluid displaced and the perturbation magnitudes caused by such an effect need only be minute. The very existence of a bulk fluid movement will swamp out any effects due to passive porosity. Unfortunately Kachanov failed to publish any of these findings and hence our experimental program was unable to benefit from his experience.

It may indeed be possible to design an experiment where any bulk fluid displacement from within the cavity can be avoided. The passive porous effect could then be studied without hindrance. However, it was practically impossible to set the pressure gradient to the desired accuracy with the wind tunnel facilities available. Hence, the favorable properties of PPW's may yet be proven experimentally. It is however, more difficult to envisage how such a subtle and fragile phe-

nomenon will have a practical technological use.

6.5.3 Result for 10% foil with pore diameter 200μm

Figure (6.5.3) represents the captured time series of the raw hot-wire signal as seen on the oscilloscope. This signal has received no signal processing whatsoever. More importantly, this signal, which has a magnitude of the order of 25% of the freestream, has occurred naturally, i.e. without any forced excitation. In some instances, the magnitude of the instability was recorded to be as much as 40% of freestream velocity.

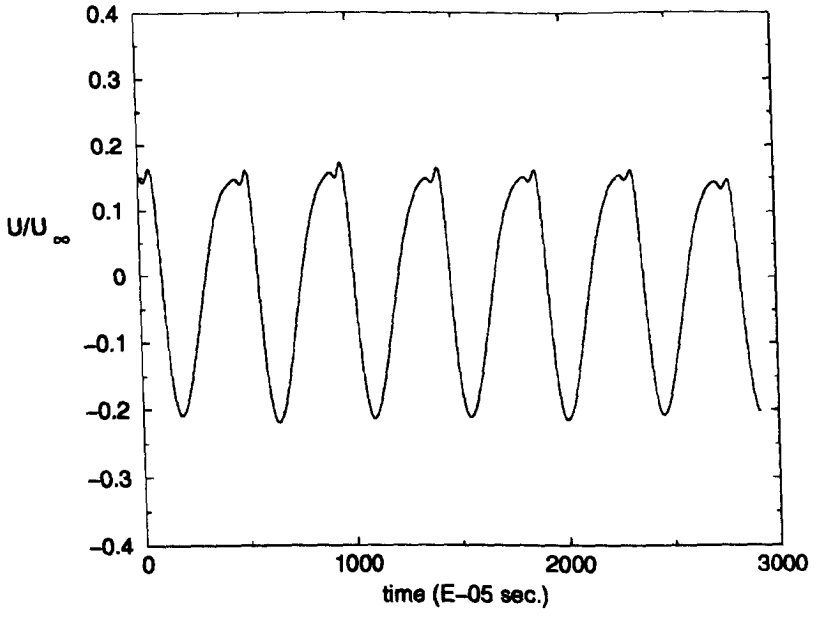

Figure 6.15: Resonant disturbance amplitude as as fraction of U_∞ at leading edge of cavity ($x = 430mm$, $y = 1mm$ and $z = 0mm$). $U_\infty = 16.5\ \mathrm{m\,s^{-1}}$.

Such a waveform was entirely unexpected and was initially thought to have been non-physical in origin. Exhaustive tests on the laboratory electronics were carried out to try and locate a possible source of interference. However, it was soon realised that this signal was in fact a true reflection of a physical phenomenon. A 3 $\mathrm{m\,s^{-1}}$ reduction in tunnel speed saw the signal return to the amplitudes given by the experiment of § 6.5.2. This feature proved the signal to be flow dependent

and therefore physical in origin. Other preliminary observations were that the onset speed and the switch-off speed were slightly different. Onset was around 13.5 $\mathrm{m\,s^{-1}}$ but, once unstable, the boundary layer could not be stabilised until 12 $\mathrm{m\,s^{-1}}$. Hysteresis was therefore a feature of the instability. Initial thoughts suggest that a waveform of the magnitude shown in fig.(6.5.3) could only be caused by some type of self-excited cavity resonance.

It was initially thought that the observed phenomenon was some type of acoustic resonance. The following paragraphs will rule out this possibility.

Assuming the wavenumber and growth rate of interest are those at the point of initiation of the disturbance, i.e. the upstream edge of the cavity, then if an acoustic resonance were responsible for the instability, one could get a first approximation to the length scale which is the source of the resonance using the following approximate formulae for an acoustic depth mode:

$$\omega_n = (n - \frac{1}{2})\pi c/l \qquad (n = 1, 2, \ldots) \tag{6.16}$$

where ω_n is the observed frequency and l is the cavity depth:

$$l = (n - \frac{1}{2})c/2f \qquad (n = 1, 2, \ldots) \tag{6.17}$$

The first mode to emerge from the unbaffled cavity was around 130 Hz, giving a length scale of:

$$l = (1 - \frac{1}{2})330/2.130 = 0.64\ \mathrm{m} \tag{6.18}$$

It can be clearly seen that the geometry of the cavity in no way presents a length scale of this magnitude. It can thus be concluded that either a different type of Kelvin-Helmholtz type acoustic resonance occurs or that the resonance is not acoustic in origin at all. It is certain, however, that the acoustic depth mode theory can be ruled out.

6.5.4 Explanation of cavity resonance - self-sustained oscillations

Preliminary measurement taken from the oscilloscope reveal that the approximate wavelength of the gross disturbance is $140mm$. This is ten times the cavity depth and 1.5 times its span. As shown in § 6.5.3, this instability is clearly not a Kelvin-Helmholtz type resonance (acoustic depth tone). The instability is much more likely to be a self-sustained transverse oscillation of the type described by Rockwell (1977). Indeed, this type of instability is more dependent upon cavity span rather than depth. Reviews of the the work of Rockwell (1977), Martin *et al.* (1975) and Sarohia (1977) confirm the type of instability observed; a shear-layer instability which is self excited by the feedback of disturbances caused by the shear layer's own impingement on the downstream cavity edge. Figure (6.16) illustrates this mechanism. Rockwell and Naudascher (1979) give an excellent review of previous work pertaining to self-sustained oscillations of impinging free shear layers.

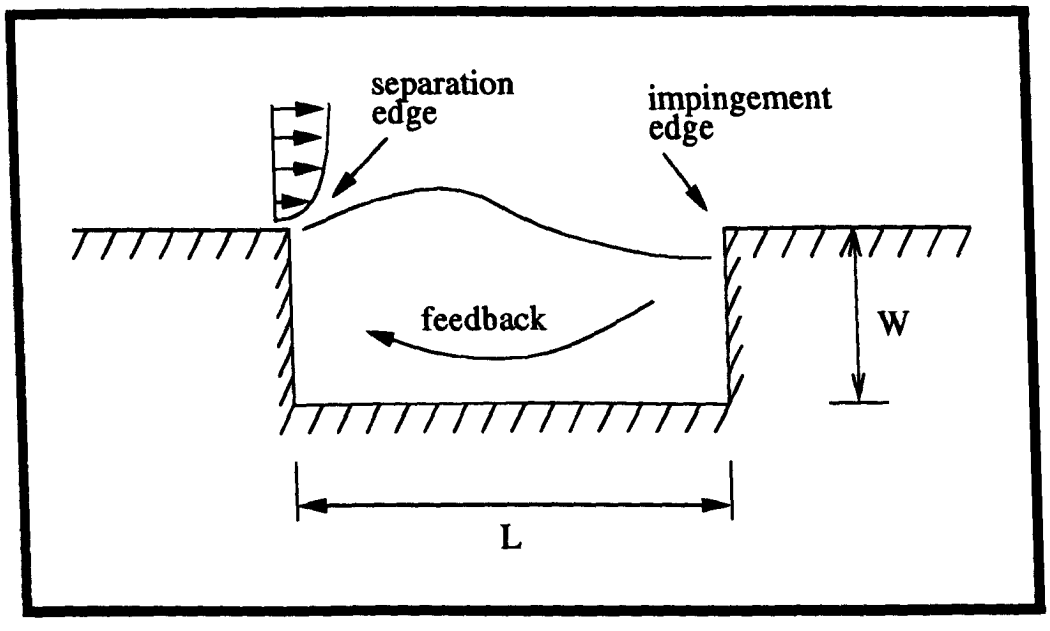

Figure 6.16: Shear-layer disturbance feedback and impingement-edge geometry

Theoretical predictions of the instability and possible ways of alleviating it are now discussed. Previous work on self-sustained transverse oscillations have all involved free shear layer flows. The effect of the porous surface covering the cav-

ity is less obvious. However, progress can be made by first checking which disturbance frequencies might be expected from a given geometry in the absence of the porous surface. A theoretical model is presented in § 6.5.5 for this purpose.

Cavity Depth	7 **mm (L/W = 12.86)**	14 **mm (L/W = 6.43)**
Onset speed	16.9 ms^{-1}	14.2 ms^{-1}
Fundamental frequency (n1)	190 Hz	109 Hz
Strouhal number (S_{n1})	1.012	0.691
Spectral power of n1	164,248	599,095
Second harmonic n2	379 Hz	216 Hz
Strouhal number (S_{n2})	2.018	1.369
Spectral power of n2	3,045	12,527

Table 6.5: Effect of variable cavity depth on self-sustained oscillations (L = 90 mm)

The mechanism for self-sustained oscillations requires two fundamental characteristics; upstream feedback of disturbances from a downstream impingement region and the subsequent streamwise amplification of those disturbances within the shear layer. The stability characteristics of the undisturbed shear layer have been well researched within the current text. As such, since disturbance growth is a necessary prerequisite, it can be inferred that those disturbances which have been fed back must have frequencies which lie within that narrow band defined by the neutral curve. Table (6.5) summarises some measurements taken of the oscillation for cavity depths of 7 and $14mm$. The measured non-dimensional frequencies of the instability (F) are 64 and 52 respectively. Inspection of fig.(6.5) illustrates that these frequencies do indeed correspond to unstable T-S modes. Although they are not the most unstable modes, the very fact that they are unstable is crucial to the existence of the cavity oscillation. The Strouhal number, S_n (Hzs^{-1}), is the dimensional parameter generally used to define such oscillations.

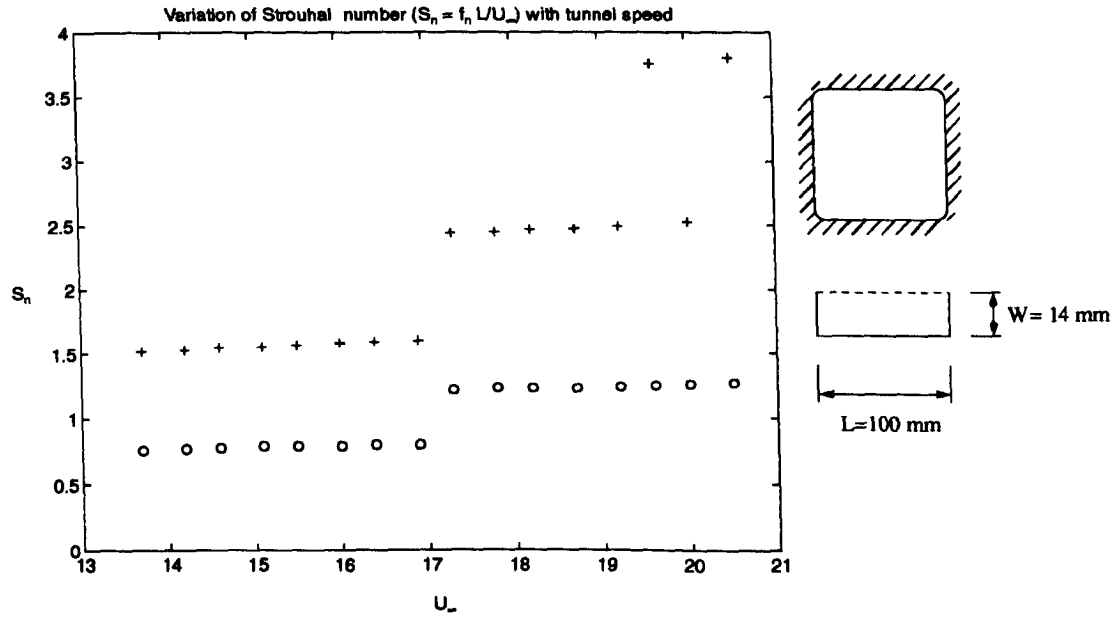

Figure 6.17: Strouhal number vs. tunnel velocity for the self-sustaining oscillations of a unbaffled cavity of depth $W = 14$ mm, o - Primary spectral component, + - Secondary component (overtone).

Cavity Depth	**7 mm (L/W = 12.86)**	**14 mm (L/W = 6.43)**
Onset velocity	16.9 $\mathrm{m\,s^{-1}}$	14.2 $\mathrm{m\,s^{-1}}$
Onset Re(@ $x = 365$ mm)	1092	1000
Apparent mode F (non-dimensional)	64	52
Theoretical most unstable mode	$\omega = 0.0905$ ($F = 82.9$)	$\omega = 0.0943$ ($F = 94.2$)
Wavenumber of most unstable mode	$\alpha_r = 0.2602$	$\alpha_r = 0.2661$
Growth rate of most unstable mode	$\alpha_i = -0.00823$	$\alpha_i = -0.00744$
$a = -\alpha_i/\alpha_r$	0.03163	0.02796

Table 6.6: Effect of variable cavity depth on self-sustained oscillations (L = 90 mm) - Some theoretical predictions of the most unstable modes.

Further measurements reveal some interesting features. Figure (6.17) plots the instability's response to a range of free-stream flow speeds. This figure plots the measured Strouhal numbers of the 1^{st} and 2^{nd} harmonics of the instability as

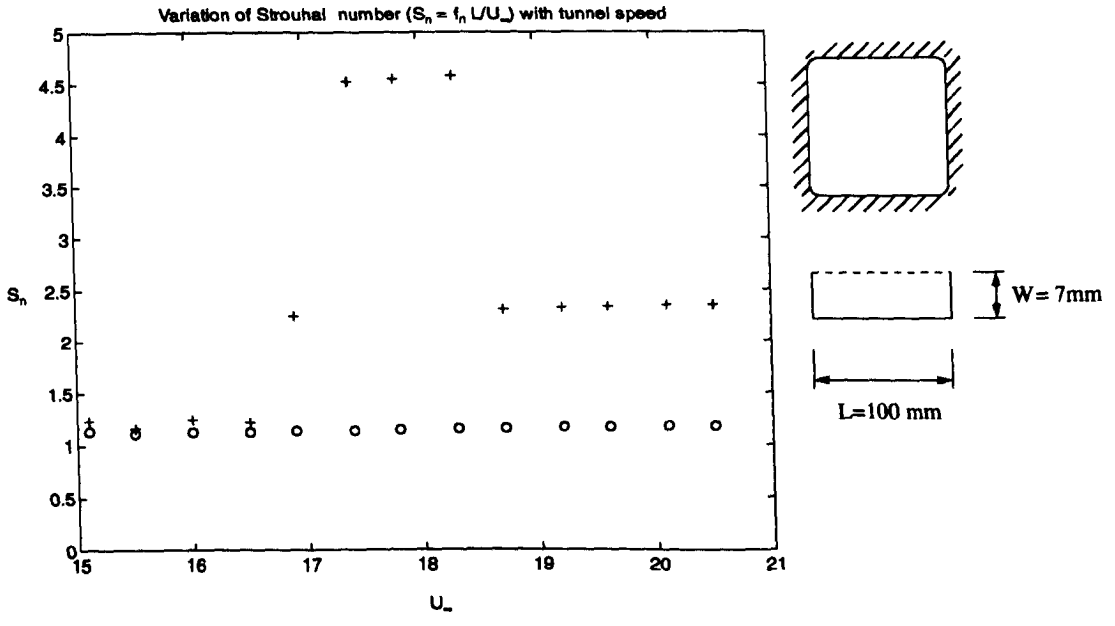

Figure 6.18: Strouhal number vs. tunnel velocity for the self-sustaining oscillations of a unbaffled cavity of depth $W = 7$ mm, **o** - Primary spectral component, + Secondary component (overtone).

a function of the U_∞ for a cavity depth of $14mm$. The discrete step up in S_n at $U_\infty = 17\ \mathrm{m\,s^{-1}}$ is of particular interest. This jump in Strouhal number indicates a rise in the frequency of the disturbance. The theory of § 6.5.5 can account for this feature.

Table (6.6) provides an insight into the wavenumbers and growth rates which may have existed at the instant the instability was initiated. These predictions are based upon the wavenumbers which would have existed at the leading edge of the cavity, and as such, relate to flows of the Blasius type. The upstream influence of the cavity flow cannot be accounted for in the present study.

Figure (6.18) illustrates the effect of a varied cavity depth on the instability. Half of the original cavity depth ($7mm$) was used in this case. This plots reveals two key features. The first is that the onset velocity of the instability occurs at $15.2\ \mathrm{m\,s^{-1}}$, nearly $2\ \mathrm{m\,s^{-1}}$ higher than for the $14mm$ cavity. It is also apparent that the discrete jump in the primary mode is not apparent for this configuration. Pre-

sumably, this bifurcation feature occurs an some higher velocity for which results are not available because they are in excess of the tunnel's maximum speed.

6.5.5 2D linear theoretical model for feedback generation of large scale coherent perturbations

Following the work of Carpenter (1998), the necessary conditions for self-sustained oscillation are as follows:

(1) Disturbances generated at the cavity leading edge must correspond to a strongly growing boundary layer instability;

(2) The fluctuation in cavity air mass $\dot{M}_c$ must be in phase with the instability at the cavity leading edge in order to generate the appropriate driving pressure.

These requirements are put in succinct mathematical form as follows. Consider a cavity inflow perturbation of the form:

$$v(x,t) = \hat{v}\cos(\alpha x - \omega t) \tag{6.19}$$

A simple two dimensional result can be obtained for the net mass flow-rate in-flow/outflow by integrating eqn.(6.19) in the streamwise direction:

$$\dot{M}_c = \rho\int_0^L v(x,t)dx = \rho\int_0^L \hat{v}\cos(\alpha x - \omega t)dx \tag{6.20}$$

$$= \underbrace{\rho\hat{v}\left[\int_0^L \exp(-\int \alpha_i)dx' \cos(\int \alpha_r dx')\cos\omega t dx\right]}_{\text{in phase with } v \text{ at } x=0} + \tag{6.21}$$

$$\underbrace{\rho\hat{v}\left[\int_0^L \exp(-\int \alpha_i)dx' \sin(\int \alpha_r dx')\sin\omega t dx\right]}_{\text{out of phase with } v \text{ at } x=0} \tag{6.22}$$

Requirement (2) requires the out-of-phase portion of eqn.(6.22) to be zero:

$$\int_0^L \exp(-\int \alpha_i)dx' \sin(\int \alpha_r dx')\sin\omega t dx \simeq 0 \tag{6.23}$$

It is reasonable to assume $-\alpha_i \ll 0$. Furthermore, let us assume α_r to be constant over the length of the cavity. These simplifications reduce eqn.(6.23) to:

$$\cos\alpha_r L \simeq 1 \qquad \Rightarrow \qquad \alpha_r L = n\pi: \quad n = 1,2,3 \tag{6.24}$$

Values of α_r, where $\alpha_r = \frac{n\pi\delta^*}{L}$, can therefore by computed for a range of Reynolds numbers for incremental values of n. Figure (6.19) illustrates these results. Permissible wavenumber lines are shown in their harmonic increments. Overlayed upon these results are the neutral curves expected for a cavity covered with a non-porous surface. Two cases are presented, fig.(6.19.1) presents results for a tunnel speed of $15\ \mathrm{m\,s^{-1}}$ while fig.(6.19.2) presents results for $20\ \mathrm{m\,s^{-1}}$.

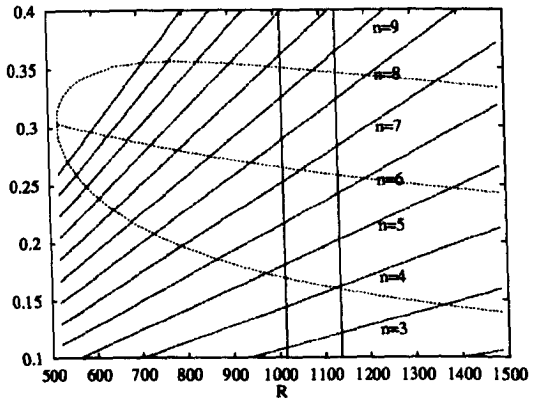

6.19.1: $U_\infty = 15\ \mathrm{m\,s^{-1}}$

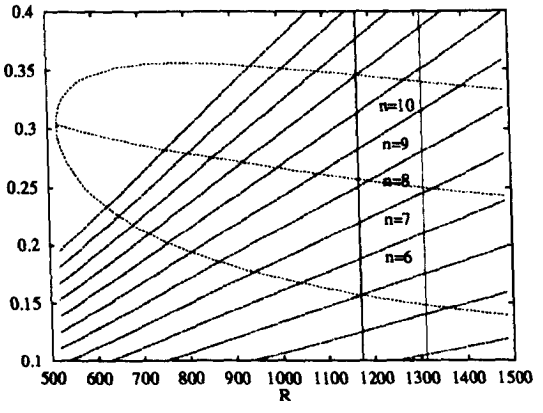

6.19.2: $U_\infty = 20\ \mathrm{m\,s^{-1}}$

Figure 6.19: Lines of harmonic increment in self-sustaining cavity oscillation (n), together with the neutral stability curves for a Blasius boundary layer.

If one assumes the wavenumber at the initiation of the instability to be that predicted by simple linear stability theory for a flat plate, then fig.(6.19.1) suggests that the $n = 7$ line (the 7_{th} harmonic) is one which might be expected to be the source of the instability at $15\ \mathrm{m\,s^{-1}}$. However, fig.(6.19.2) illustrates that at $20\ \mathrm{m\,s^{-1}}$, the $n = 8$ line intersects the line defining the most unstable modes. Hence, the theory would predict a discrete jump in the frequency of the measured instability to occur somewhere between $15\ \mathrm{m\,s^{-1}}$ and $20\ \mathrm{m\,s^{-1}}$

$$S_n = \frac{\omega L}{2\pi U_\infty} \tag{6.25}$$

As a first approximation, let us assume the phase speed of the disturbance to be equal to the speed of the freestream flow. As such, the observed frequency can be

given as:

$$\omega = \frac{\alpha U_\infty}{2\pi} \tag{6.26}$$

Hence, the Strouhal number simplifies to:

$$S_n = \frac{\alpha L}{4\pi^2} \tag{6.27}$$

This can be simplified further using eqn.(6.24) to give:

$$S_n = \frac{n}{4\pi} \tag{6.28}$$

In our case, as the flow speed increased from 15 $\mathrm{m\,s^{-1}}$ to 20 $\mathrm{m\,s^{-1}}$ the most unstable modes move from $n = 7$ to $n = 8$. The current model would thus predict the Strouhal number to change from $S_{n_{15ms^{-1}}} = 0.56$ to $S_{n_{20ms^{-1}}} = 0.64$. Furthermore, this rather crude theory suggests that the step rise in frequency will always be $1/4\pi$. It is also interesting to note that the magnitude of the step rise in Strouhal number is independent of both cavity dimension and U_∞.

The experimental results of fig.(6.17) show a change in the measured Strouhal numbers from 0.8 @ 16.9 $\mathrm{m\,s^{-1}}$ to 1.22 @ 17.3 $\mathrm{m\,s^{-1}}$. This is a 50% rise in Strouhal number. Using the simple 2D theory presented herein, this would correspond to a move from modes $n = 2$ to $n = 3$, but with very much higher Strouhal numbers. If one assumes the 2D theory to be correct, then the wavenumbers which initiated the instability must be much lower than those chosen based upon fig.(6.19). In summary, it can be seen by comparison with theory and experiment that either the theoretical model is not accurate or the wavenumbers used are wrong. In actual fact, the source of the error is likely to be a combination of these factors.

It is perhaps not surprising that there was a poor level of agreement for the current model. This is because the model is only two-dimensional, while the cavity dynamics are clearly three-dimensional. Furthermore, the most unstable modes were selected based upon computations of a linearly responding Blasius boundary layer. The theory, however, requires a free shear layer to be present. In practice, the conditions of the experiment were neither a free shear layer or

a Blasius boundary layer but rather a highly porous thin wall over which large non-linear disturbances develop. In such circumstances it is difficult to predict the frequencies of disturbance which initiated this instability and developed it to its final form, because the observed wavenumbers and stability characteristics would themselves have changed during its development. It may be true that the wavenumbers predicted by fig.(6.19) did indeed initiate the disturbance but this cannot be proven since the initiation of the disturbance is instantaneous. One fact that can be shown from table (6.5) is that once initiated, the disturbance wavenumbers seem to be driven down to the lower branch of the stability loop. These lower frequencies seem to produce the largest disturbance amplitudes.

A possible explanation for measured wavenumbers of the gross disturbance residing around the lower branch of the T-S stability loop is a frequency cascade effect. The most unstable T-S modes, in the middle of the loop in fig.(6.17) may initiate the feedback stability, but this frequency may then cascade down to frequencies at the lower branch simply because the self-sustaining oscillations are strongest at the lower frequencies.

The uncertainties and shortfalls outlined above indicate that the theoretical model can only be used to make qualitative predictions about the cavity feedback instability. The fact that the current model predicts the discrete change in instability frequency gives one confidence that the essential physics of the instability are well understood.

6.5.6 Boundary layer breakdown to turbulence (10% foil)

The experimental work of Kachanov (1994), on the physical mechanisms of laminar-boundary layer transition, identifies two distinct type of breakdown, known as K-type and N-type. The K-type boundary layer breakdown, so named after Klebanoff *et al.* (1961) who identified it, exhibits many of the characteristics seen in the current study. Kachanov describes the K-type breakdown, as observed in his

experiments, as the interaction of the stationary and traveling disturbances which results in the strong downstream amplification of spanwise modulated disturbances. Figure (6.20.1) illustrates the downstream growth of this spanwise modulation.

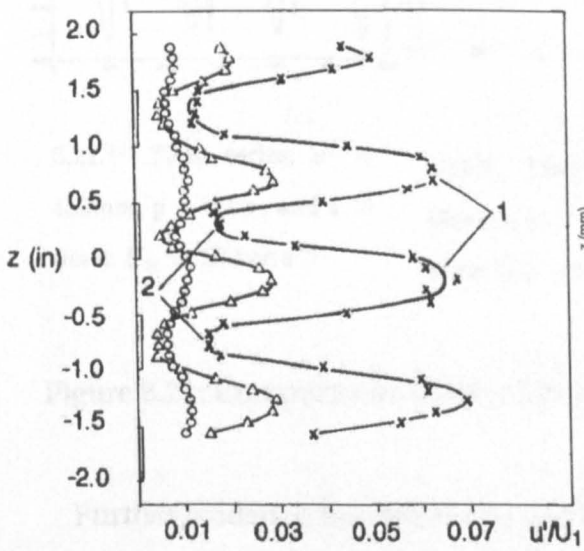

6.20.1: Results of Kachanov (1994), downstream growth and spanwise modulation of RMS amplitude of velocity disturbances in K-breakdown. 1: "peaks," 2: "valleys."

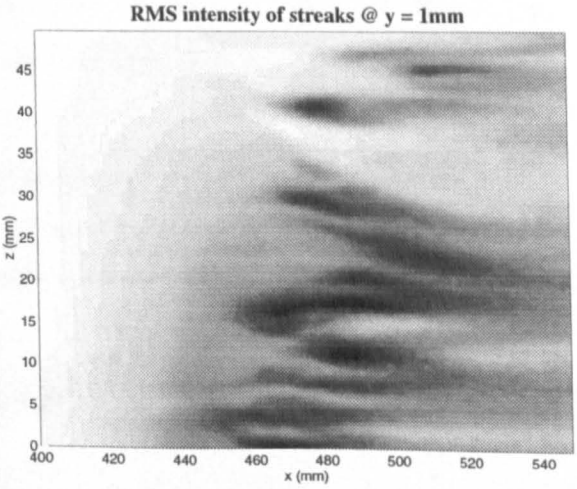

6.20.2: R.M.S. disturbance level for self sustained oscillation, $U_\infty = 16.2\,\mathrm{m\,s^{-1}}$. Slice taken $1mm$ above plate surface, for the plate half span at $x = 450mm$ (centre of insert) to $x = 550mm$ (well downstream of porous insert).

Figure 6.20: Comparisons of streamwise modulation for K-type transition.

Kachanov and Klebanoff *et al.* (1961) used strips of tape to initiate the spanwise modulation observed in natural transition. These strips can be seen adjacent to the vertical axis on the plot (6.20.1). The results for the PPW experiment on the 10% foil are shown in fig.(6.20.2) for comparison. This is a plot of the RMS disturbance level measured over a complete slice of the flow field taken $1mm$ from the surface of the plate. Although the clear modulation shown in Kachanov's results cannot be seen, it is clear from this figure that a degree of spanwise modulation has occurred. This is identified by the streaks which appear downstream of $x = 440mm$.

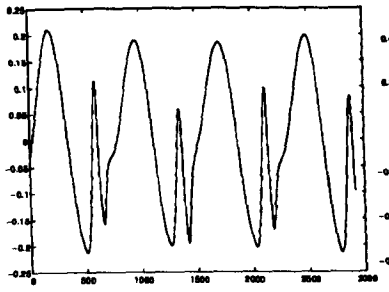

6.21.1: Time series, $x = 450mm$, $y = 1mm$ and $z = 0mm$. $U_\infty = 15.1\ \mathrm{m\,s^{-1}}$

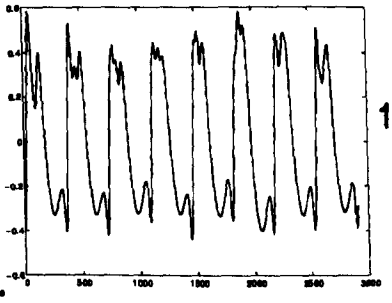

6.21.2: Time series, $x = 450mm$, $y = 1mm$ and $z = 0mm$. $U_\infty = 19.6\ \mathrm{m\,s^{-1}}$.

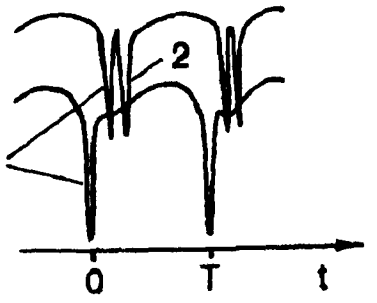

6.21.3: Typical single and double spikes (after Klebanoff *et al.* (1961)). 1: 1st Spike, 2:2nd spike, T: fundamental period

Figure 6.21: Comparisons of hot-wire traces to those of Klebanoff *et al.* (1961).

Further evidence that the cavity oscillation has indeed triggered K-type breakdown is given by inspection of the hot-wire signal, as seen on the oscilloscope. Kachanov draws attention to the fact that the observed instability can be as large as 40% of the free-steam velocity. Furthermore, high frequency flashes of disturbance (spikes) are observed in his experiments. Figs.(6.21.1) and (6.21.2) illustrates how the hot-wire traces taken from the current experiment, at two different tunnel speeds, compare to those of Klebanoff *et al.* (1961), fig.(6.21.3). The time series do indeed contain similar features and are of a similar magnitude. One can therefore speculate the self-sustained cavity oscillations have facilitated K-type breakdown. This, in itself, is remarkable when one considers the trouble Kachanov and others had in reproducing a stable lambda vortices for visualization purposes.

Kachanov observed the main spectral features of K-type transition to be as follows. Disturbances remain deterministic and almost completely periodic until very late in their development. The disturbance spectrum consists solely of the fundamental wave and its harmonics up until the appearance of spikes. Thus, all the main spectral characteristics of of K-breakdown are attributed to the ampli-

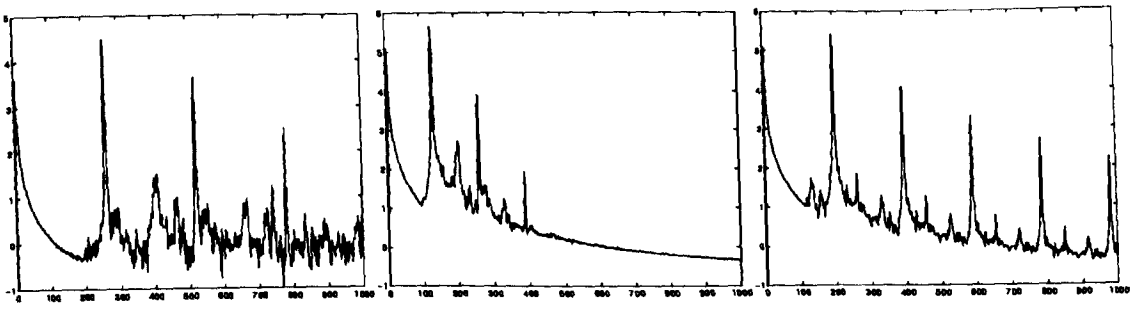

6.22.1: $x = 350mm$ 6.22.2: $x = 410mm$ 6.22.3: $x = 430mm$

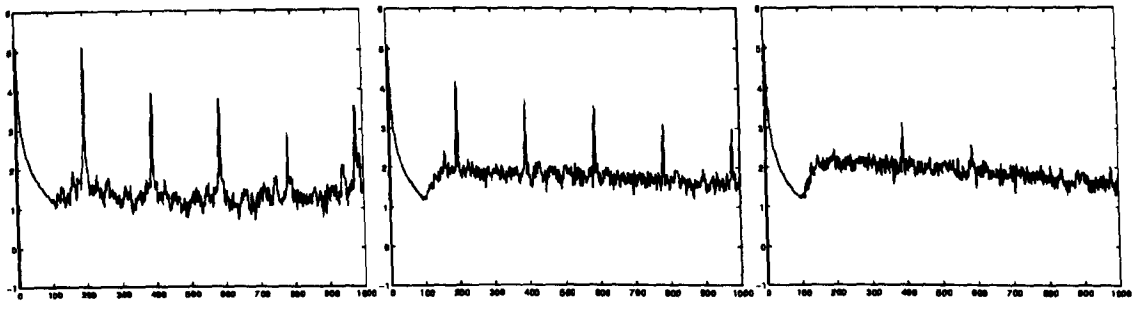

6.22.4: $x = 470mm$ 6.22.5: $x = 510mm$ 6.22.6: $x = 550mm$

Figure 6.22: Spectra of hot-wire signal for the breakdown of the laminar boundary caused by the cavity oscillation. Plotted as $\log_{10} P_h(f)$ **vs** f(Hz). $U_\infty = 16.5\ \mathrm{m\,s^{-1}}$.

tude and phase properties of the fundamental wave and its harmonics. The total disturbance intensity, in the peak position ($y = 1mm$ in his experiments), exhibits an explosive behavior shown as the probe traverses downstream at constant distance from the wall. A rapid jump in the disturbance amplitude is observed just at the moment of spike onset.

The spectral plots of fig.(6.22.1) to (6.22.6) exhibit most of the fundamental features outlined above. Here, $P_h(f)$ denotes the *one-sided power spectral density (PSD)* where $P_h(f) \equiv |H(f)|^2 + |H(-f)|^2$ for $0 \leq f \leq \infty$ (Parseval's theorem) and $|H(f)|$ is a discrete Fast Fourier Transform (DFFT) of the time series function $h(t)$. In this case, $h(t)$ is real, and therefore $P_h(f) = 2|H(f)|^2$. Of particular interest is the jump in the magnitude of the power spectrum (all frequencies) which has

occurred between $x = 430$ and $x = 470$. This quite considerable rise in total disturbance energy occurs over a traversed range of only $40mm$. If the breakdown observed in our experiment were K-type, then the observations of Kachanov should also be apparent here. In particular, the jump in magnitude observed between $x = 430$ and $x = 470$ should signal the appearance of the first spikes and their subsequent multiplication. It is the multiplication of these spikes which is likely to give this overall rise in spectral intensity (all frequencies). This is indeed verified by the time series of the signal taken at these stations, as shown in figs.(6.23.1) and (6.23.2).

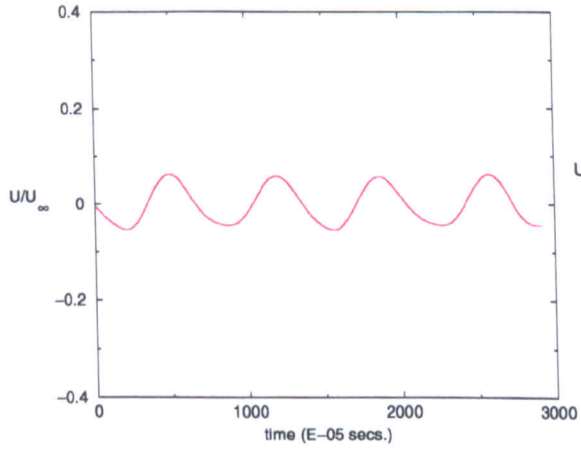

6.23.1: Time series, $y = 1mm$, $x = 430mm$ (no spikes).

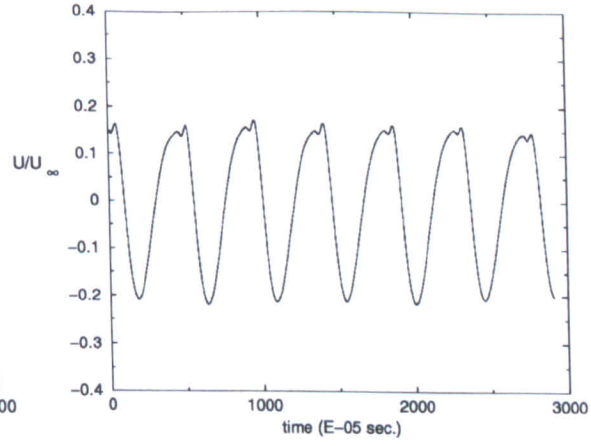

6.23.2: Time series, $y = 1mm$, $x = 470mm$ (with spikes).

Figure 6.23: Comparisons of time series as the probe traverses downstream through the self-sustained disturbance.

6.5.7 Effect of cavity baffles on gross instability

To ascertain the importance of both the streamwise and spanwise dimension of the cavity, various configurations of baffle were inserted into the cavity. Figures (6.24) and (6.25) illustrate the effect of a single spanwise baffle. Similar flow conditions and measurement locations are used in both cases. It can be seen that the

baffle has reduced the size of the instability to 25% of its unbaffled magnitude but has ultimately failed to remove the instability.

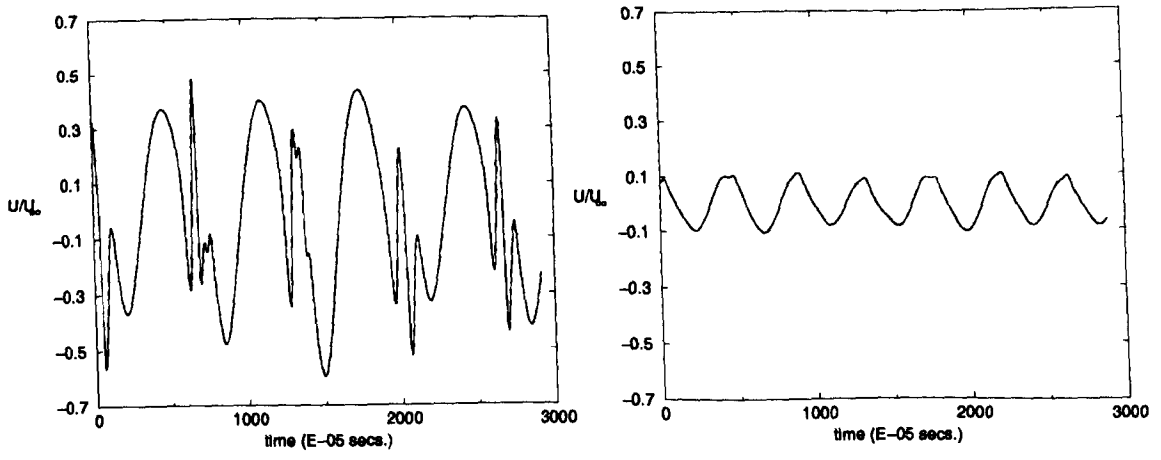

6.24.1: No baffle

6.24.2: Baffle config. 1

Figure 6.24: Comparison of disturbance amplitude time series U/U_∞ with and without a single cavity baffle. Measurements taken over centre of cavity ($x = 450mm$, $y = 1mm$ and $z = 0mm$). $U_\infty = 16.8\ \mathrm{m\,s^{-1}}$.

Figure (6.25) plots the evolution of the instability over a range of tunnel speeds. The trends exhibited for the baffled configuration, shown here, are less clear than those of the unbaffled cavity, fig.(6.17). A discrete jump from $S_n = 1.25$ to $S_n = 2.5$ appears at $17.6\ \mathrm{m\,s^{-1}}$. This is, however, only short-lived; the instability returns to its original mode at $20\ \mathrm{m\,s^{-1}}$. Many other baffle configurations were tried, as shown in fig.(6.26), and while some did make significant reductions in the magnitude of the observed instability, they all failed to remove it completely.

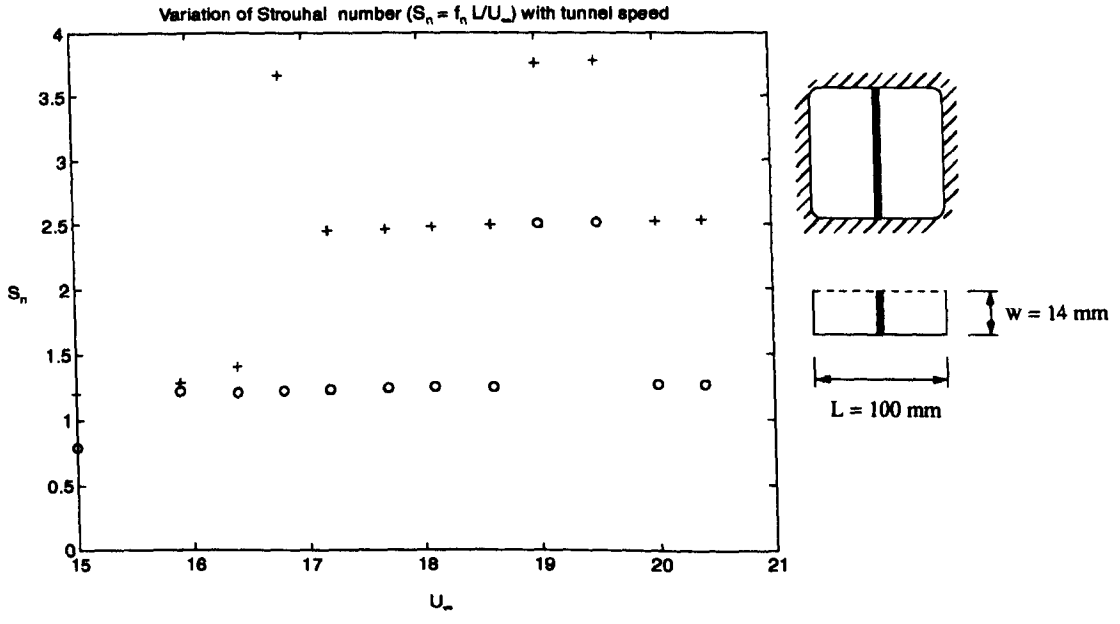

Figure 6.25: Strouhal number vs. tunnel velocity; cavity of depth $W = 14$mm with a single spanwise baffle, o - Primary spectral component, + - Secondary component (overtone).

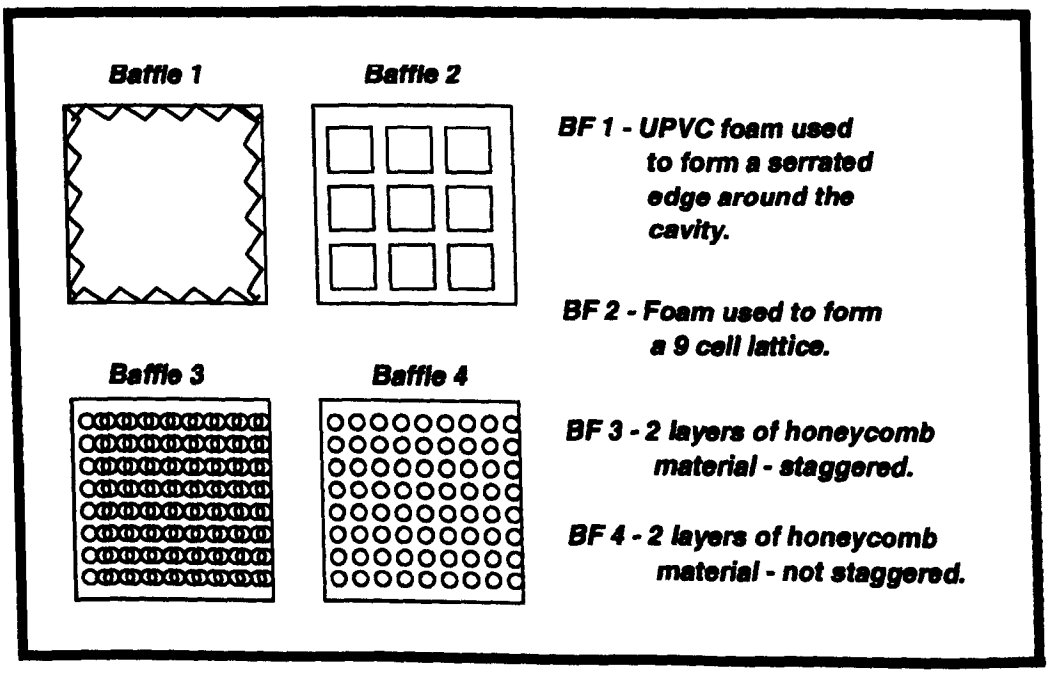

Figure 6.26: Baffle configurations used during experiment.

6.5.8 Flow visualization - slices through the vortex structure.

This section presents the data collected from a series of experiments designed to achieve a visualization of the cavity oscillation. The symmetry of the configuration only requires measurement over half of the porous surface..

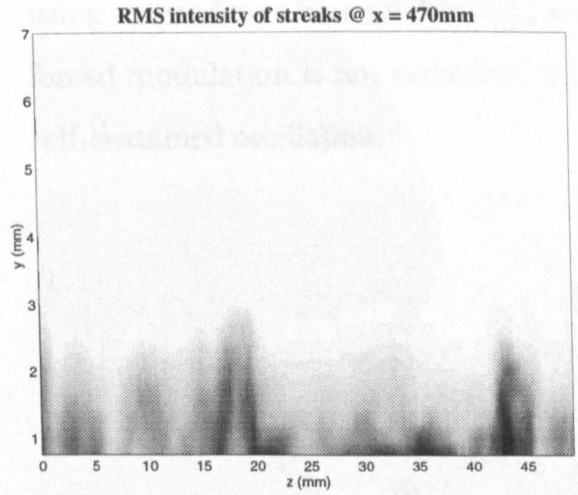

6.27.1: X - slice through vortex structure. $x = 470mm$ (single high-frequency spikes appear in time series)

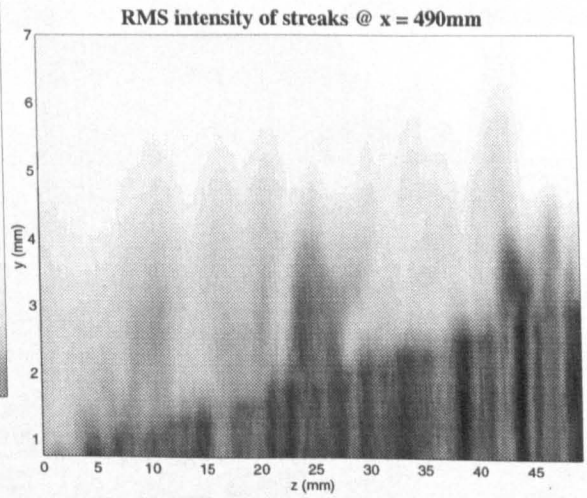

6.27.2: $x = 490mm$. Multiple high-frequency spikes appear in time series.

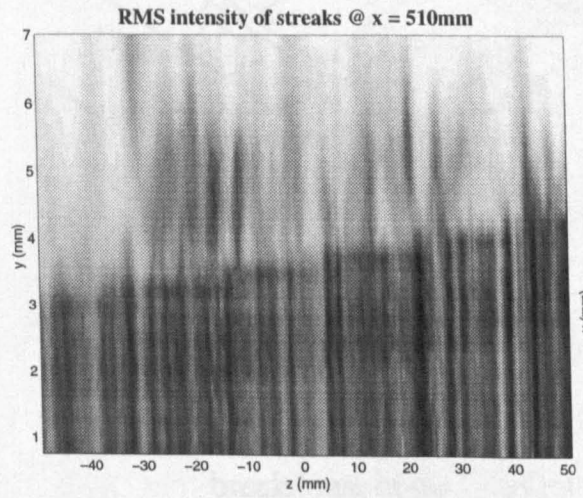

6.27.3: $x = 510mm$. No coherent structures - boundary layer fully turbulent.

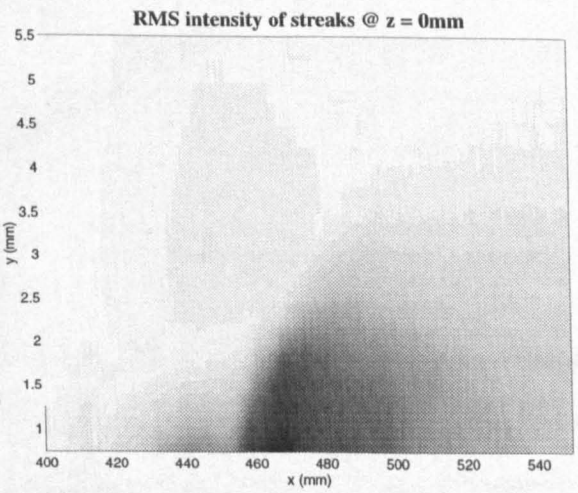

6.27.4: Const. Z - slice $z = 0mm$ (mid-span).

Figure 6.27: R.M.S. disturbance levels for self-sustained oscillation, $U_\infty = 16.2\ \mathrm{m\,s^{-1}}$. Deepest shade corresponds to a disturbance of $\approx 40\%$ freestream vel.

The results of figs.(6.27.1) and (6.27.2) illustrate a degree of spanwise vortex modulation. In particular, plot (6.27.1) exhibits two streaks distanced by $\approx 40mm$. However, the results here are not as convincing as those of Klebanoff *et al.* (1961) (fig.6.28). This may be because Klebanoff *et al.* forced this spanwise modulation using strips of tape beneath his vibrating wire actuator. In the current study, such forced modulation is not used, but is achieved rather by accident due to cavity self-sustained oscillation.

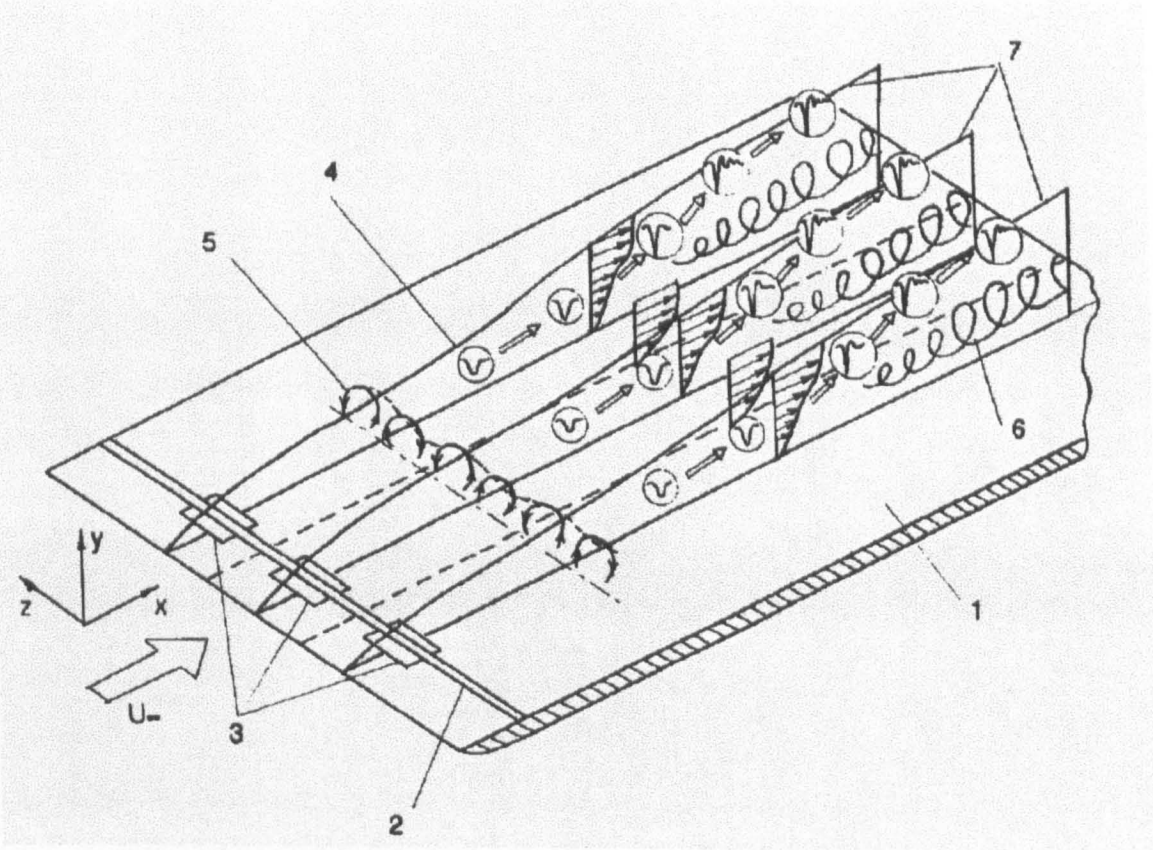

Figure 6.28: Sketch of experiments by Klebanoff et al (1962) on the nonlinear breakdown of the boundary layer in the K-regime. 1: plate, 2: vibrating ribbon, 3: spacers, 4: boundary layer edge, 5: pulsating streamwise vortices, 6: local flow randomization, 7: peaks. Diagram taken from Kachanov (1994).

The discovery of the self-sustained cavity oscillation marked the end of the experimental program in its original form. Although some additional effort and

tunnel time was spent trying to remove the cavity oscillation, it became clear that the QMW facilities were not capable of achieving a uniformly zero pressure gradient to the degree which the linear stability experiment required. This fact did not become apparent until the experimental program was well underway. This problem, together with constraints upon tunnel access, forced the termination of the experimental program. As such, the work contained in the chapters that follow will be entirely of an analytical nature.

Chapter 7

Instability in Three - Dimensional Boundary Layers

7.1 Introduction

The work that follows considers the stability of boundary layers subject to an imposed pressure gradient in the presence of a crossflow velocity component. These are the most common flow conditions experienced by aircraft. If a swept wing aerofoil is considered, then the leading-edge region experiences a negative pressure gradient (accelerated flow) which, when combined with wing sweep, deflects the external streamline inboard in a manner illustrated in fig. 7.1.1. The degree to which a streamline is deflected is proportional to the momentum of the fluid at that height in the boundary layer. As such, fluid towards the center of the boundary layer is deflected to a larger degree than that at the edge simply because it has less momentum. This variable streamline deflection, coupled with the 'no-slip' condition, explains why the mean profile is skewed by a velocity component which is perpendicular to the local inviscid flow vector (i.e. the crossflow component). Figure 7.1.2 is a schematic representation of such a mean profile. Notice that the span-wise component, known as the crossflow profile, is inflectional and

will therefore promote an inviscid (Rayleigh type) instability.

There are many surfaces on commercial aircraft were the crossflow is not of primary concern. For example, the surfaces of the nacells and fuselage make large contributions to the wetted area and are therefore worthy of consideration in the context of laminar flow control. As such, the work that follows will consider the general three-dimensional stability problem while treating the zero sweep configuration as a special case.

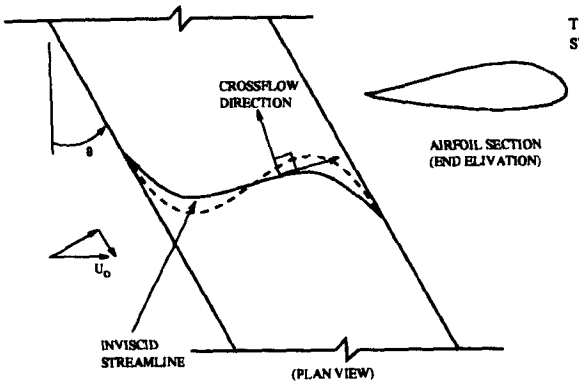

7.1.1: Streamline paths over a swept aerofoil

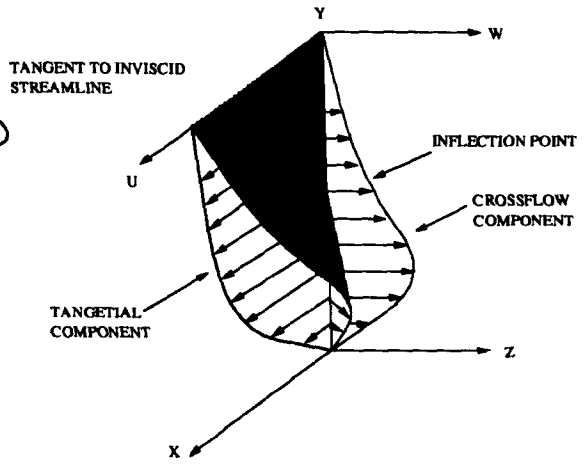

7.1.2: Boundary layer profile components

Figure 7.1: Schematic representation of a boundary layer with crossflow

Gray (1952) was the first to recognize that the transition processes on the swept wing were fundamentally different from those attributed to a streamwise instability or those due to curvature, such as the Görtler vortex. Gray reported that the so-called crossflow instability was particularly prone to development in regions of strong streamwise pressure gradients. The streamwise axial orientation of the 'cats eye' vortex structure was also very different, as was the fact that each of the vortices seem to roll in the same sense. The scale of these structures was deemed to be of the order of one boundary layer thickness. Gray also observed, in his flight tests, that transition occurred near the leading edge of an aerofoil at abnormally low Reynolds numbers in comparison to un-swept wings. Flow visualization revealed that prior to transition, the surface was covered with closely

spaced parallel streaks oriented close to the direction of the local potential flow.

Gregory *et al.* (1955) found similar streaks to those observed by Gray in their studies of the rotating disk configuration, although in this case a spiral pattern was apparent. Gregory *et al.* (1955) studied the physics of the crossflow instability and suggested a likely mechanism for its development. The streaks and spirals observed in this type of experiment are explained as manifestations of an inflectional (inviscid Rayleigh-type) instability caused by the inflectional crossflow profile. The whole phenomenon became known as the crossflow instability.

A similar situation to that explained above occurs towards the trailing edge of a wing. Here, the decelerating boundary layer together with the wing sweep deflects the streamline outboard, resulting in a reversal in the direction of the crossflow profile and a change in the sense of rotation of the corresponding vortex structure.

To avoid confusion, terms such as adverse and advantageous pressure gradient will no longer be used. Such expressions are only of use when describing the effect of pressure gradient on boundary-layer separation. It is merely coincidental that a pressure gradient which is considered adverse in that it leads to separation is also adverse in that it leads to instability growth for T-S modes. Indeed, such expressions are meaningless for flows with a crossflow component simply because any combination of pressure gradient and wing sweep can be considered adverse (or destabilizing).

The question of whether the crossflow instability will dominate is determined by the degree of sweep and the severity of the imposed pressure gradient. However, the fact that it is dynamically unstable in regions of accelerated flow has particular practical significance. The likely dominance and power of the crossflow instability in the leading-edge region leads one to believe that it will be the major contributor to transition in the e^N sense. Thus, study of the crossflow instability, rather than streamwise instability, is perhaps more relevant to the design of practical porous surfaces for aircraft.

7.2 Review of work on the three-dimensional stability problem

There are three basic flow configurations available for the theoretical study of the crossflow instability. These include the rotating disk, the infinite swept wedge and the infinite swept cylinder. Hybrid combinations of flows solutions around the latter two configurations can be used to perform stability calculations over infinite swept wings with common aerofoil sections.

A survey of the literature reveals that the most prolific theoretical studies have been done on the rotating disk. This is presumably because the transition mechanisms exhibited at the leading-edge region of swept-wings are similar to those found on a rotating disk (see Malik *et al.* (1981)). Indeed, work on the rotating-disk problem has been advanced to a stage whereby many of the additional complications such as Coriolis acceleration and non-parallel effects have now been resolved. Carpenter *et al.* (1995) provides a excellent review of the current status of research on the rotating disk. However, the rotating-disk problem can only be of limited use when extended to practical transition prediction on aircraft. For a complete understanding of the mechanisms involved one must include the effects of variable crossflow component, variable imposed pressure gradient and of streamline curvature. The Falkner-Skan-Cooke series of profiles, which represent infinite swept-wedge flows, are convenient for the study of such effects.

Prior to a review of previous work on the stability of flows over swept wings (or wedges) it is useful to state the problem clearly. The most fundamental difference between these flows and those over flat plates, are that two types of instability can coexist. Indeed, over the mid-chord regions of practical wings there is a fight for dominance between the viscous Tollmien-Schlichting (T-S) instability and the inviscid crossflow (CF) instability. Hence, waves will exist which are oblique to the stream direction. This causes particular problems when one attempts to extend the e^N computation to such flows. Such computations must seek to find

maximum growth rates which will depend on disturbance orientation, disturbance wavelength and disturbance frequency. The spatial stability problem for monochromatic waves is defined by the fixed real frequency ω_r and four arbitrary parameters, α_r, α_i, β_r and β_i. Two of the arbitrary parameters can be determined from the eigenvalue problem. The other two parameters must be either prescribed or computed, based on the type of instability one wishes to study. By contrast, the temporal problem is defined by two real wavenumbers (α, β) and a complex frequency ω, where ω_i accounts for the temporal growth of the wave. It can therefore be seen that the temporal eigenvalue problem has the advantage that one only need prescribe the value of the real spanwise wavenumber. The spanwise wave growth need only come into play when transforming the resultant eigenvalues into spatial modes (using a Gaster-type transformation). For the case where the wave is assumed to growth only in a direction normal to the crossflow direction, as with an infinite wedge or wing, the two methods are equivalent since $\beta_i = 0$.

The work of Srokowski and Orszag (1977) was significant in that it was among the first to apply a temporal linear stability theory to form an e^n method which was calibrated directly using the results from experiments on practical swept wings. This resulted in a rudimentary tool which could be used for the optimization of the transition properties of wings. The tool was put to good use in this case because it helped determine an appropriate level of suction necessary to achieve laminar flow over a particular aerofoil. Srokowski and Orszag (1977) calculated the maximum temporal amplification rate for a given dimensional frequency from the parallel incompressible stability equations (this is the so-called envelope method). They then use the real part of the group velocity to convert the temporal amplification rate into a spatial one (Gaster 1962) and integrate along the path defined by the real part of the group velocity.

Work by Cebeci and Stewartson (1979), using their saddle point method, compare the results from their rotating disk simulations with those from the experi-

ments of Cham and Head (1969). If an $n = 9$ transition criterion is applied to their simulations then the transitional Reynolds number is $R_T = 400$ rather that the value of $R_T = 530$ given by experiment. Cebeci *et al.* argue that there is no reason why $n = 9$ should be taken as a blanket assumption, but do concede that their method requires further investigation. The n-factor issue was largely resolved for the rotating disc problem following the work of Malik *et al.* (1981). Here, Coriolis acceleration and other effects are included in their 6th-order stability equations. Malik *et al.* (1981) include the effects of curvature and Coriolis acceleration in their formulation and derive a sixth order system of equations. Using the envelope method and a temporal formulation they achieve e^n predictions which compare extremely well with experimental results. This paper was significant because the majority of the previous work (Cebeci and Stewartson (1979) for example) used the Orr-Sommerfeld equation. Indeed, Malik *et al.* (1981) found that the inclusion of these additional effects predicted $n \approx 9$ to 10 for transition, which is in accordance with the experimental results. Carpenter and Cooper (1996) provide a excellent review of the more recent advances in the understanding of the rotating disk problem together with a complete summary of the various mechanisms which lead to transition.

The clarification of the rotating disk problem led many researchers to seek different configurations upon which to perform stability calculations. The swept-wing has become a particular focus of attention. Much of the pioneering work which paved the way for stability studies on swept-wing configurations was done by Mack (1978). He focused upon configurations for which the Falkner-Skan-Cooke series of similarity boundary-layer profiles were applicable. These include flows around swept wedges or swept cylinders (attachment line stability). Mack focused upon the solution of the temporal form of Orr-Sommerfeld equation but also developed many of the ideas which led to the solution of the spatial problem. His work will be reviewed in greater detail in § 7.3

The work of Itoh (1989) is of interest because he is one of the few people to

have investigated the effects of an imposed spanwise pressure gradient on the crossflow stability. He chose a swept flat plate configuration in conjunction with a displacement body to provide the required pressure gradient. Itoh (1989) has only considered the theoretical stability problem for such a configuration; experiments have yet to be conducted. Using the temporal linear stability theory, Itoh has shown that the application of an appropriate spanwise pressure gradient can provide a crossflow component which is equal and opposite to the crossflow component given by the accelerated flow over the leading edge of a typical wing. Hence, a spanwise pressure gradient can remove any inviscid crossflow instability and leave only the beneficial effects of accelerated flows on the traveling modes (T-S wave suppression). Itoh's work is in need of some further development. In particular, effects such as surface curvature should be considered. Furthermore, it would be interesting to discover what spanwise wing-section shapes can achieve the desired effect. It may indeed be the case that to mimic these results one must create wing section which would look ridiculous. In addition to this, the use of spanwise curvature might create additional problems such as the Görtler instability.

Cebeci *et al.* (1991) extend the work of Cebeci and Stewartson (1979) by applying their methods to flows around an infinite swept aerofoil (ONERA-D) attached to a half-fuselage. This work outlines a very different approach to the calculation of the linear growth exponent to that taken by Mack (1985). Whereas Mack used an assumed wavenumber relationship, Cebeci *et al.* (1991) presents a theory for the computation of a complex spanwise wavenumber based on the saddle point method previously applied to the rotating disk problem by Cebeci and Stewartson (1979) and Nayfeh (1980). This saddle point method makes no assumptions about the growth of the disturbance, but uses a simple asymptotic analysis to determine an approximation to the integral given in eqn.(7.2) below for a simple monochromatic wave. Consider a pressure perturbation within a three-dimensional bound-

ary layer:

$$p = \zeta(y,\beta)\exp[i(\alpha x + \beta z - \omega t)] \tag{7.1}$$

Summing the pressure components over all possible values of β gives the following expression for the magnitude of a monochromatic pressure perturbation:

$$p(x,y,z,t) = \exp(-i\omega t)\int \zeta(y,\beta)\exp[i\alpha(\beta)x - i\beta z]d\beta \tag{7.2}$$

where $\alpha = \alpha(\beta)$. Previous methods have avoided this integration by using the assumption that β is both real and constant. However, if no such assumptions are made, the evaluation of eqn.(7.2) requires the solution of the eigenvalue problem for all possible values of β followed by their subsequent integration. This rather laborious method creates significant computational overhead. For this reason more practical approaches are generally used.

Malik *et al.* (1994) sought answers of a more fundamental nature with respect to transition within three-dimensional boundary layers. They gave particular attention to the later stages of transition and a study of the non-linear processes which occur. The question as to how stationary crossflow vortices lead to turbulence is addressed along with studies into the nature of the interaction between traveling crossflow modes and stationary modes. Consideration was also given to the interaction of viscous T-S modes and the inviscid crossflow modes. Malik *et al.* (1994) use the framework of the non-linear parabolized stability equations (PSE) for their computations. This methods allows the full range of non-linear flow features to be captured without the unreasonable computational overheads required of direct numerical simulation. These include the resolution of streamwise vortex streaks as seen in flow visualizations. Additional flow features are also reproduced such as half-mushroom structures, inflected profiles and vortex doubling, all of which can be seen in actual flows just prior to transition. This paper is important because it is one of the first to numerically reproduce some of the flow features seen in three-dimensional transition over practical configurations. Indeed, Malik *et al.* (1994) were even able to predict the secondary instability iden-

tified as high-frequency bursts. This was a feature frequently shown in much of the experimental work of § 6.5.5.

Bippes *et al.* (1991) focus upon an experimental investigation into the natural transition of an unstable three-dimensional boundary layer. Their specific aim is to identify the most unstable modes and determine their growth rates. Bippes *et al.* argue in favor of a natural transition type experiment for the following reasons. Firstly, because there are so many additional modes of instability in three-dimensional flows, there is some uncertainty in the selection of an appropriate forced frequency. Therefore, in spite of the dominating nonlinear disturbance development, they make use of the natural filtering qualities of the boundary layer and can therefore be sure that they are measuring the most unstable modes. Obviously this type of experiment has its limitations. The use of simple hot-wire equipment can only facilitate the measurements of r.m.s. disturbance levels and frequencies. No phase information can be recovered. Bippes *et al.* find the initial amplification rates of non-stationary instability modes are fairly well predicted. However, the the amplification rates of the non-stationary modes were consistently overestimated. Furthermore, they draw attention to a remarkable feature: disturbances with the largest amplitudes are not, in every case, the most amplified ones. This is shown to be the case in both theory and experiment. Comparing their experimental results with the linear stability analysis of Dallmann and Bieler (1987), Bippes *et al.* show that stationary vortices, as well as traveling waves, are amplified and that the wavelengths of the stationary modes and the frequencies of the non-stationary modes are in good agreement.

The 0Hz stationary modes show some unexpected features also. With decreasing free-stream turbulence, the stationary mode becomes more and more dominant and have higher growths than the traveling modes. This is at odds with the predictions of the linear theory, which suggest a dominant traveling mode. All these observations lead to the conclusion that the disturbance development in accelerated three-dimensional boundary-layer flows depend on the disturbance

environment in a much more complex way than for the Blasius case.

Deyhle *et al.* (1993) made significant experimental advances in the understanding of the crossflow instability. Their experimental setup consisted of an aerofoil type displacement body above a swept flat plate. Natural transition was studied here also. An ingenious hot film arrangement and some sophisticated data processing techniques enabled them to retrieve detailed amplitude, frequency and phase information from natural T-S wave evolution. Contoured end plates were used on their configuration to insure infinite swept-wing conditions. They used a 10-element hot-film sensor which was flush mounted on a rotatable insert within the swept plate. A cross-spectral analysis was used to obtain growth direction, phase velocity and group velocity data for traveling crossflow disturbances. This paper is important because it uses pioneering experimental techniques to perform a thorough investigation into traveling disturbances. Deyhle *et al.* (1993) point out that while previous researchers have provided detailed descriptions of wavelength and amplification rates for both stationary and traveling vortices, the much needed phase and group velocity data was unavailable.

Deyhle *et al.* identify a discrepancy in the predictions of the linear theory and the experimental results. As mentioned above, the wavelengths and frequencies of the traveling waves agree quite well, but there is a consistent over-prediction in the growth of such wave by the local linear theory (quasi-parallel). The linear theory suggest that the most amplified waves propagate in a direction which is approximately normal to the potential streamline direction. Deyhle *et al.* (1993) seek verification of this prediction along with an explanation of why, given the over-prediction of growth, the frequencies and wavenumbers appear to be correctly predicted by the theory. They draw the following conclusions. The method they used to determine the direction of the wave propagation vector provided satisfactory results, although an interaction between stationary CF vortices and traveling waves occurred. The propagation directions agree very well with the results for the linear theory. Also, phase velocities and wavelengths of stability calculations

fitted well with the experimental results. With regard to the group velocity, significant differences appeared in direction and magnitude. These difference could not be adequately explained by the current setup. However, wave-front curvature was cited as a possible cause since it was not accounted for in either theory or experiment.

There are a few more examples of work of this type which appeared around the same time. All of them investigate the effects of the primary (or stationary instability) and its interaction with the traveling modes. Fischer and Dallmann (1991) are notable researchers in this area. Their work, while being important in the understanding of three-dimensional boundary layer transition, is too specialist to be considered in the current study.

7.3 Practical approaches to the general 3D stability problem

In the case of the swept wing, the root of the problem lies in the prediction of stability characteristics as the instability moves from the crossflow direction to the streamwise one. This is the situation as the wave approaches the mid-chord region where the T-S mode becomes dominant.

The discussion in the previous section highlights the fact that the application of the e^n method to three-dimensional boundary layers is a matter of some contention. What is clear is that effects such as streamline curvature and Coriolis acceleration complicate the problem. Furthermore, as pointed out by Mack (1984), if you consistently use the envelope method and compare results from the 4th order Orr-Sommerfeld calculation of Brown (1960) with those of the sixth order equation of Malik *et al.* , the results appear drastically different. Mack implies that this discrepancy means that the rotating-disk configuration is not well suited to the study of the crossflow instability.

Arnal *et al.* (1989) point out that, when comparing the various forms of e^N method, provided the external flow is accelerated along the whole region of interest, transition is mainly governed by the crossflow instability and the different e^n prediction methods all give very similar results. However, it is by no means certain that the e^n method is the best way to proceed. The essential dilemma is that there is no solid evidence which tells us which method to use, ie. the envelope method, the zero spanwise growth method of Mack or the saddle point method of Cebeci *et al.*. This is, perhaps, to be expected from an semi-empirical method such as the e^N method. However, for the purposes of the current research, the method chosen is purely academic since the primary objective is to assess the performance of passive porous walls, rather than the accurate prediction of transition.

Perhaps the simplest way to proceed is to select the simplest flow configuration which exhibit the crossflow instability without the complication of streamline curvature or Coriolis acceleration. The methodology used by Mack (1984) is particularly useful in this respect. According to Mack, the spatial stability problem can be simplified in the case of a infinite-span wing (or wedge) if there is assumed to be no disturbance growth in the spanwise direction. Setting $\beta_i = 0$ reduces the number of variables in the spatial problem from six to five. The second constraint that Mack imposed was the irrotationality (or constant-direction) condition applied to the wavenumber vector.

The selection of β_i warrants further discussion. Carpenter (1998) makes the point that the choice for β_i is determined by the physical experiment or phenomenon one chooses to represent by the theoretical model. For example, if one models the growth of disturbances from an impulsive point source on a rotating disc, then this is modeled by a superposition of all the axisymmetric eigenmodes. Thus, one can argue from symmetry that $\beta_i = 0$ for each eigenmode separately. After superposition, though, the resulting wave-packet grows along a spiral path. The resultant spiral band is approximately centered on a spiral trajectory that is everywhere tangent to the group velocity of the most rapidly amplified normal

mode. The infinite wing has a symmetry which should enforce vortex trajectories of a similar type. This argument is given a formal mathematical treatment by Mack (1984) - details of which can be found in § 7.3.1.

The above arguments are perfectly reasonable when one considers normal modes. They will therefore be used in much of the work that follows. However, they cannot, for example, explain the observed steady patterns which originate from randomly placed roughness elements on a rotating disk. These features would produce a jumble of waves with many different phase relationships. The dominant structure can only be deduced from an understanding of the nonlinear interaction and competition of many disturbances all with differing phases.

The work contained within the following sections focuses upon the boundary layers formed on an infinite swept wedge. Cooke (1950) was the first to successfully solve the boundary-layer equations for flows of this type. His solutions, known as the Falkner-Skan-Cooke set of similarity solutions, can be used to represent the velocity profiles of flows found on swept cylinders, swept plates and swept wedges

7.3.1 Details of the approximations of Mack

The work of Mack (1984) represents a significant simplification to the three-dimensional stability problem. For this reason, the current section will describe his method in some detail.

For a quasi-parallel boundary layer, the normal mode solutions are of the form:

$$u(x,y,z,t) = A_0\hat{u}(y;x)\exp^{i\theta(x,z,t)} \tag{7.3}$$

where the slowly varying amplitude $A(x)$ has been set to a constant A_0 and

$$\theta(x,z,t) = \int[\alpha(x)dx + \beta(x_1) - \omega(x_1)t]dx_1 \tag{7.4}$$

x_1 is used to indicate that β and ω are slow functions of x thereby making $\partial\theta/\partial x = \alpha$. $\hat{u}$ is also a slowly varying function of x. Consequently, the problem is reduced,

using these quasi-parallel approximations, to the solution of the eigenvalue problem at each value of x to account for changes in boundary layer thickness and profile shape. The e^N method is then used to resolve how to connect the possible eigenvalues at each x so that they represent a continuous wave train propagating through the growing (quasi-parallel) boundary layer.

In the spatial representation of the three-dimensional Orr-Sommerfeld equation, the dispersion relationship is represented by:

$$\omega = \Omega(\vec{k}, \vec{\sigma}, x, z) \tag{7.5}$$

where $\vec{k}$ and $\vec{\sigma}$ are complex. Fixing the values of ω, x and z still leaves 2 complex wave parameters remaining (or 4 unknowns in all). Two of these can be determined from a single complex eigenvalue equation (i.e. α_r and α_i) but the 2 values represented by the complex spanwise wavenumber ($\beta = \beta_r + i\beta_i$) remain unresolved.

Let the real wavenumber vector be given by eqn.(7.6) while the associated spatial amplification vector is given by eqn.(7.7).

$$\vec{k} = (\alpha_r, \beta_r) \tag{7.6}$$

$$\vec{\sigma} = (\alpha_i, \beta_i) \tag{7.7}$$

The respective directions of the above vectors are given by:

$$\psi = \arctan \frac{\beta_r}{\alpha_r} \tag{7.8}$$

$$\overline{\psi} = \arctan \frac{\beta_i}{\alpha_i} \tag{7.9}$$

Naturally occurring wave packets will consist of combinations of inhomogeneous waves, that is $\psi \neq \overline{\psi}$. However, it is worth considering two possible exceptions to this rule. The first is the case were $\psi = \overline{\psi}$ (termed a homogeneous wave) and the second is the case where $\overline{\psi} = 0$ (termed an irrotational wave). The distinction in these various types is made by the specification of the spanwise wavenumber. Recalling the phase function for three-dimensional parallel linear

disturbances is given as;

$$\theta = \alpha x + \beta z - \omega t \tag{7.10}$$

The differentiation of the above with respect to x (not x_1) and z yield the following:

$$\partial\theta/\partial x = \alpha \tag{7.11}$$

$$\partial\theta/\partial z = \beta \tag{7.12}$$

The gradient of the phase function yields the complex wavenumber vector k_c

$$\nabla\theta = \frac{\partial\theta}{\partial x}\vec{i} + \frac{\partial\theta}{\partial z}\vec{k} = \vec{k_c} \tag{7.13}$$

Using the identity, $\nabla \times (\nabla\phi) = 0$, it follows that the curl of $\vec{k}$ is given as:

$$\vec{\nabla} \times \vec{\nabla}\theta = \vec{\nabla} \times \vec{k_c} = 0 \tag{7.14}$$

Expanding the vector cross-product gives:

$$\frac{\partial\beta}{\partial y}\vec{i} + \left(\frac{\partial\alpha}{\partial z} - \frac{\partial\beta}{\partial x}\right)\vec{j} - \frac{\partial\alpha}{\partial y}\vec{k} \tag{7.15}$$

However, the assumptions given above assume β to vary with the slow scale x_1, hence the final result is:

$$\beta = \text{ const.} \tag{7.16}$$

for any given normal mode. The value of β is, however, still complex, and the solution to spatial dispersion problem of eqn.(7.5) cannot be achieved without the specification of the constant β. Fortunately, a major simplification applies to swept wings of infinite span. The infinite span assumption means that there cannot be any instability growth in the spanwise direction. As such, the following result is obtained:

$$\beta_i = 0 \qquad \text{for infinite swept wings} \tag{7.17}$$

The eigenvalue can therefore be solved simply by specifying the values of the real part of the spanwise wavenumber (β_r), which will be a constant for any given normal mode.

The following expressions will also be of use in the work contained in the remaining parts of this chapter.

$$\text{Magnitude of group velocity vector} : = \sqrt{\left(\frac{\partial \omega}{\partial \alpha}\right)_r^2 + \left(\frac{\partial \omega}{\partial \beta}\right)_r^2} \tag{7.18}$$

$$\text{Group velocity angle} : = \tan^{-1}\left(\left(\frac{\partial \beta}{\partial \alpha}\right)_r\right) \tag{7.19}$$

the r subscripts denote the real parts of the respective variables.

7.4 Mean flow field - FSC equations

Let us consider a body of constant cross-section which has an infinite span and a sweep angle φ. Figure (7.2) outlines the relevant notation and coordinate system. The external streamline velocity (or inviscid velocity) is taken to be Q_∞ with components U_∞ normal to the leading edge and W_∞ parallel to it. Two coordinate systems are applicable: the first (X, Z, y) is relative to the wedge while the other (x, z, y) is relative to the external streamline. Obviously the vertical y coordinate is common to both systems. U and W are defined as the projections of the free-stream velocity Q along X and Z respectively and therefore have values of U_∞ and W_∞ at the edge of the boundary layer.

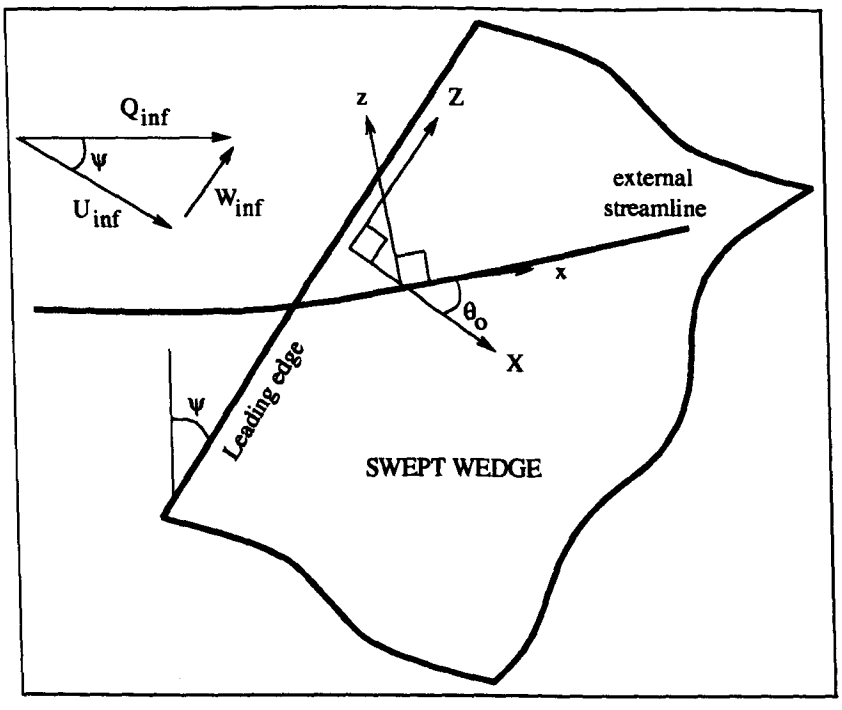

Figure 7.2: Coordinate system and notation for the swept wedge flow.

The Falkner-Skan-Cooke family of similarity solutions describe the three-dimensional flow over an infinite yawed wedge at zero angle of attack. This flow can be characterized by two parameters: the Hartree dimensionless pressure-gradient parameter β_h and the local sweep angle θ. Note that the wedge angle is given by $\pi \cdot \beta_h$ and the *local* sweep angle is given by: $\theta = \tan^{-1} \frac{W_e}{U_e}$. The e subscripts refer to values

evaluated at the outer edge of the boundary layer.

Using the similarity variables :

$$\bar{f}(\eta) = \frac{U}{U_e}, \quad \bar{g}(\eta) = \frac{W}{W_e} \quad \text{where} \quad \eta = y\left[\frac{U_e}{\nu X}\right]^{1/2} \tag{7.20}$$

the Navier-Stokes equations give the following governing equation.

$$(2-\beta_h)f''' + ff'' + \beta_h(1-f'^2) = 0 \tag{7.21}$$

$$(2-\beta_h)g'' + fg' = 0 \tag{7.22}$$

It is apparent that the FSC equations lend themselves to the (X,Z,y) coordinate system. Hence, the projections u and w are defined in terms of U and W as follows:

$$u = U\cos\theta + W\sin\theta \qquad w = -U\sin\theta + W\cos\theta \tag{7.23}$$

But:

$$q_e = \frac{U_e}{\cos\theta} = \frac{W_e}{\sin\theta} \tag{7.24}$$

Therefore:

$$\frac{u}{q_e} = \frac{U\cos\theta}{q_e} + \frac{W\sin\theta}{q_e} = \frac{U\cos^2\theta}{U_e} + \frac{W\sin^2\theta}{W_e} \tag{7.25}$$

and,

$$\frac{w}{q_e} = \frac{-U\sin\theta}{q_e} + \frac{W\cos\theta}{q_e} = \frac{-U\sin\theta\cos\theta}{U_e} + \frac{W\cos\theta\sin\theta}{W_e} \tag{7.26}$$

Using eqn.(7.20), the final expressions for the streamwise and crossflow profiles are given as:

$$\frac{u}{q_e} = \bar{f}'(\eta)\cos^2\theta + \bar{g}(\eta)\sin^2\theta \tag{7.27}$$

$$\frac{w}{q_e} = [\bar{g}(\eta) - \bar{f}'(\eta)]\sin\theta\cos\theta \tag{7.28}$$

The values of $f'(\eta)$, $g(\eta)$ are given from the solutions to eqns.(7.22). Appendix (A.3) details how these equations are broken down into a series of five first-order equations ready for solution using a Runge-Kutta technique.

Figure (7.3) illustrates the computed F-S-C profiles for the same parameter range used by Taylor and Peake (1998). The results of Taylor and Peake (1998) are

also presented for validation purposes in fig. (7.3.3) and fig. (7.3.4). No discrepancy is apparent and one can thus conclude that the computation of the F-S-C profiles is free from error. Table (7.1) gives the actual values which were computed using the Runge-Kutta technique for the F-S-C equations.

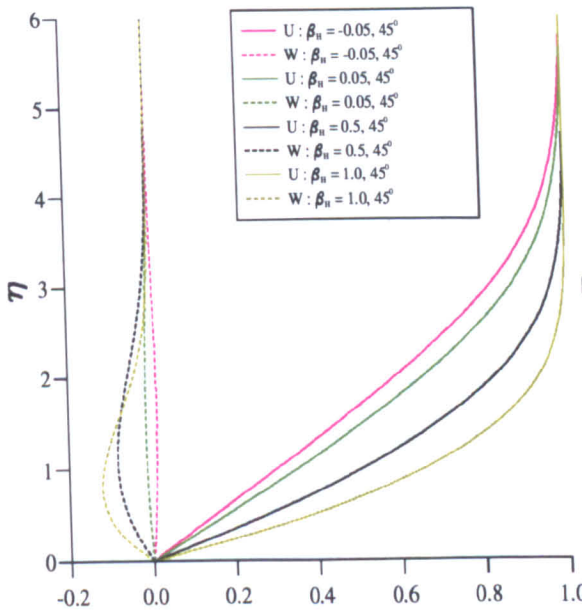

7.3.1: The FSC velocity profiles for $\beta_H = -0.05, 0.05, 0.5, 1.0$ at $\theta = 45^o$

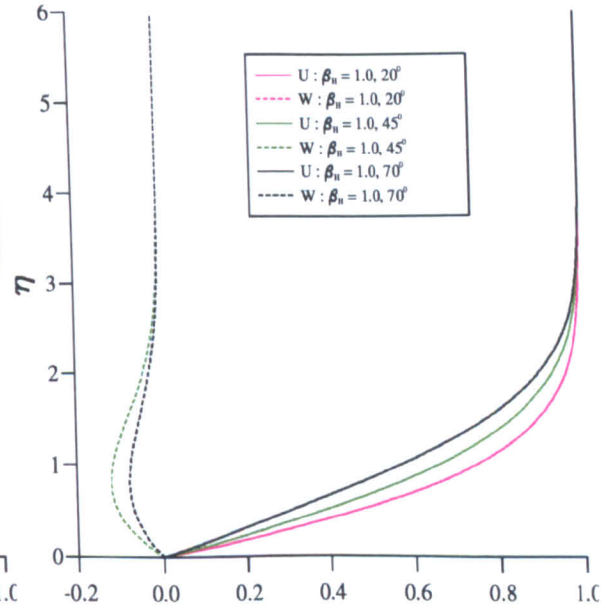

7.3.2: The FSC velocity profiles for $\theta = 20^o$,45^o,70^o at $\beta_H = 1.0$

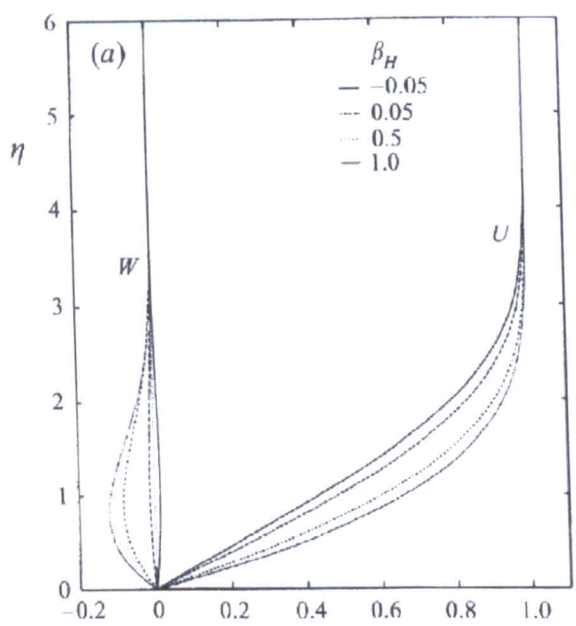

7.3.3: Results for Taylor and Peake (1998) (same parameters as above)

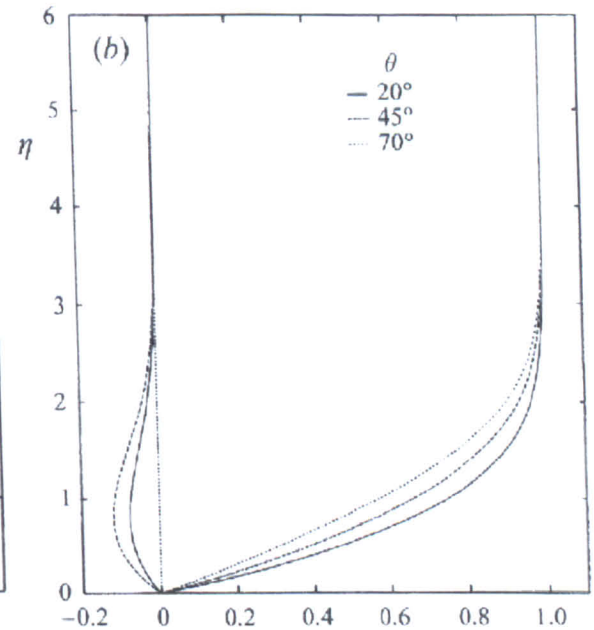

7.3.4: Results of Taylor and Peake (1998) (same parameters as above)

Figure 7.3: Validation of the computation of crossflow profiles

7.5 Formulation and solution of the swept-wing problem for spatially varying modes

Prior to using equations (7.27) and (7.28) in the stability equation it is vital that we make all the non-dimensional variables consistent with the two sets of equations. Note, in the F-S-C system of equations the similarity variable is $\eta = y\left[\frac{U_e}{\nu X}\right]^{1/2}$. If the length scale used to non-dimensionalise the stability equation is $L^* = \left[\frac{\nu x}{U_e}\right]^{1/2}$, then non-dimensional y coordinate would be $y_{L^*} = y/L^* = \eta$.
This leads to the convenient result that $u(y_{L^*}) = u(\eta)$ and $w(y_{L^*}) = w(\eta)$. That is, the similarity variable used in the F-S-C equations can be used directly as the non-dimensional variable in the stability equation without the need for scaling.

The appropriate velocity scale is the external streamline $q_e = (U_e^2 + W_e^2)^{1/2}$ and the length scale as $L^* = \left[\frac{\nu x}{U_e}\right]^{1/2}$ and finally the Reynolds number as $Re = q_e L^*/\nu$

The chord-wise Reynolds number is given as $Re_c = U_e L^*/\nu$. Hence, the stream-wise Reynolds number is related to the chordwise number by the following:

$$Re = Re_c/\cos\theta \tag{7.29}$$

and the perturbations are expressed in the form:

$$[u'(x,y,z,t), v'(x,y,z,t), w'(x,y,z,t), p'(x,y,z,t)]^T = [\hat{u}(y), \hat{v}(y), \hat{w}(y), \hat{p}(y)]^T \exp[i(\alpha x + \beta z - \omega t)] \tag{7.30}$$

$$\hat{v}^{IV} - 2(\alpha^2+\beta^2)\hat{v}'' + (\alpha^2+\beta^2)^2\hat{v} = iRe\left\{(\alpha\overline{U} - \beta\overline{W})(\hat{v}'' - (\alpha^2+\beta^2)\hat{v}) - \left(\alpha\frac{d^2\overline{U}}{dy^2} + \beta\frac{d^2\overline{W}}{dy^2}\right)\hat{v}\right\} \tag{7.31}$$

$$i(\alpha\overline{U}\hat{u} + \beta\overline{W}\hat{u} - \omega\hat{u}) + \hat{v}D\overline{U} = -i\alpha\hat{p} + \frac{1}{Re}(D^2\hat{u} - (\alpha^2+\beta^2)\hat{u}) \tag{7.32}$$

$$i(\alpha\overline{U}\hat{w} + \beta\overline{W}\hat{w} - \omega\hat{w}) + \hat{v}D\overline{W} = -i\beta\hat{p} + \frac{1}{Re}(D^2\hat{w} - (\alpha^2+\beta^2)\hat{w}) \tag{7.33}$$

β_h	DU_w	DW_w	$\delta^*{}_1 = \delta^*(U_o/\nu x)^{1/2}$	$\theta_1 = \theta(U_o/\nu x)^{1/2}$	H
-0.10000	0.26088	0.04055	1.98482	0.73576	2.69766
-0.08000	0.27682	0.03169	1.91869	0.71855	2.67024
-0.06000	0.29170	0.02329	1.86089	0.70310	2.64668
-0.04000	0.30577	0.01524	1.80946	0.68904	2.62604
-0.02000	0.31918	0.00750	1.76306	0.67610	2.60768
0.00000	0.33206	0.00000	1.72076	0.66409	2.59114
0.04000	0.35656	-0.01439	1.64578	0.64231	2.56230
0.08000	0.37978	-0.02816	1.58062	0.62285	2.53772
0.12000	0.40208	-0.04145	1.52284	0.60519	2.51629
0.16000	0.42369	-0.05438	1.47079	0.58895	2.49729
0.20000	0.44481	-0.06703	1.42332	0.57387	2.48021
0.24000	0.46558	-0.07947	1.37959	0.55974	2.46469
0.28000	0.48612	-0.09177	1.33894	0.54641	2.45044
0.32000	0.50652	-0.10397	1.30089	0.53375	2.43728
0.36000	0.52687	-0.11611	1.26504	0.52166	2.42504
0.40000	0.54725	-0.12823	1.23107	0.51006	2.41358
0.44000	0.56772	-0.14037	1.19872	0.49888	2.40282
0.48000	0.58836	-0.15256	1.16779	0.48807	2.39266
0.52000	0.60922	-0.16484	1.13809	0.47758	2.38303
0.56000	0.63037	-0.17723	1.10946	0.46736	2.37388
0.60000	0.65187	-0.18976	1.08178	0.45738	2.36516
0.64000	0.67378	-0.20248	1.05492	0.44760	2.35683
0.68000	0.69616	-0.21541	1.02880	0.43800	2.34884
0.72000	0.71909	-0.22858	1.00332	0.42855	2.34118
0.76000	0.74263	-0.24203	0.97840	0.41923	2.33381
0.80000	0.76685	-0.25581	0.95396	0.41000	2.32672
0.84000	0.79185	-0.26994	0.92996	0.40087	2.31986
0.88000	0.81771	-0.28448	0.90632	0.39180	2.31325
0.92000	0.84454	-0.29948	0.88299	0.38277	2.30684
0.96000	0.87243	-0.31498	0.85992	0.37378	2.30064
1.00000	0.90153	-0.33106	0.83706	0.36479	2.29462

Table 7.1: Properties of the Falkner-Skan-Cooke group of boundary layers - 45° sweep, various pressure gradients

$$i(\alpha\hat{u} + \beta\hat{w}) + D\hat{v} = 0 \tag{7.34}$$

Multiply eqn.(7.32) by $i\alpha$ and eqn.(7.33) by $i\beta$ and add to give :

$$\begin{aligned}\omega(\alpha\hat{u} + \beta\hat{w}) - \beta(\alpha\overline{W}\hat{u} + \beta\overline{W}\hat{w}) - \alpha(\alpha\overline{U}\hat{u} + \beta\overline{U}\hat{w}) \\ +i\hat{v}(\alpha D\overline{U} + \beta\overline{W}) = (\alpha^2 + \beta^2)\hat{p} + \frac{i\alpha}{Re}(\ldots) + \frac{i\beta}{Re}(\ldots)\end{aligned} \tag{7.35}$$

Substitute eqn.(7.34) and its 1^{st} and 2^{nd} derivatives into eqn.(7.35) to give :

$$\begin{aligned}iD\hat{v}\left[\omega - (\alpha\overline{U} + \beta\overline{W})\right] + i\hat{v}(\alpha D\overline{U} + \beta D\overline{W}) = (\alpha^2 + \beta^2)\hat{p} \\ +\frac{1}{Re}\left[(\alpha^2 + \beta^2)D\hat{v} - D^3\hat{v}\right]\end{aligned} \tag{7.36}$$

To evaluate the pressure at the wall, in the three-dimensional boundary layer, it is important to remember that the no-slip condition still applies even for the porous boundary condition.

Since $\hat{u}_{wall} = \hat{w}_{wall} = 0$ we can immediately see from eqn.(7.34) that $D\hat{v}_{wall} = 0$. This observation leads to the following expression for the pressure evaluated at the wall.

$$\hat{p}_w = \frac{1}{Re(\alpha^2 + \beta^2)}[D^3\hat{v}_w + iRe(\alpha D\overline{U}_w + \beta D\overline{W}_w)\hat{v}_w] \tag{7.37}$$

The admittance from the boundary-layer side of the PPW must be equal in magnitude to that from the cavity side.

$$|Y_b| = |Y_c| = \frac{\hat{q}_w}{\hat{p}_w} \tag{7.38}$$

But $\hat{v}_w = -\hat{q}_w$, so eqn.(7.37) and eqn.(7.38) lead to:

$$Y_w\hat{p}_w + \hat{v}_w = 0 \tag{7.39}$$

$$\frac{Y_w D^3\hat{v}}{Re} + Y_w i(\alpha D\overline{U} + \beta D\overline{W})\hat{v} + (\alpha^2 + \beta^2)\hat{v} = 0 \tag{7.40}$$

$$\alpha^2 \text{ coeffs.} \ldots \hat{v}$$

$$\alpha \text{ coeffs.} \ldots Y_w i D\overline{U}\hat{v}$$

$$\text{Non } \alpha \text{ coeffs.} \ldots \frac{Y_w D^3\hat{v}}{Re} + (Y_w i\beta D\overline{W} + \beta^2)\hat{v} \tag{7.41}$$

The following expressions relating to three-dimensional stability, will be used in much of the work to follow:

$$k = (\alpha_r + \beta_r)^{1/2} \tag{7.42}$$

$$\psi = \tan^{-1}(\beta_r/\alpha_r) \tag{7.43}$$

$$|\sigma| = (\alpha_i^2 + \beta_i^2)^{1/2} \tag{7.44}$$

$$c = \omega/k \tag{7.45}$$

$$\alpha_r = \left[\frac{k^2}{(1 + \tan^2\psi)}\right]^{1/2} \tag{7.46}$$

where k is the overall wavenumber, ψ is the waveangle, $|\sigma|$ is the overall growth rate and c the group velocity.

The application of the three-dimensional passive porous boundary condition is complicated slightly because the values of the derivatives of the mean profiles ($D\overline{U}$ and $D\overline{W}$) will vary depending upon what sweep angle is used and the value of the pressure gradient parameter. The values of these derivatives can be computed from the F-S-C equation using the following expressions.

$$\overline{U}'_w = f''_w \cos^2\theta + g'_w \sin^2\theta \tag{7.47}$$

$$\overline{W}'_w = (g'_w - f''_w)\sin\theta\cos\theta \tag{7.48}$$

7.5.1 Validation of the Spectral code for three-dimensional boundary layers

Following the methods of Mack (1978), the spectral code is validated, for the case where ($\beta_i = 0$), by direct comparison with Mack's results. Direct comparison is possible, despite the fact that the current code uses a spatial formulation while Mack uses a temporal one, because the two formulations are identical when comparing zarfs of neutral stability.

Figures (7.4.1) to (7.4.3) were computed using the spectral code for a rigid wall configuration at a Reynolds number of 400 for a wedge of 45^o sweep and a pressure gradient characterized by $\beta_h = 1.0$. This relates to a boundary layer which is approaching stagnation. Comparing these plots with those of Mack (fig. 7.4.4) illustrates that the spectral code has captured the essential features of Mack's zarf. There is an apparent discrepancy in the values of wavenumber K as a function of frequency. These discrepancies are not due to errors in the code. They are merely a consequence of the fact that zarfs illustrate the $K - F$ range of instability, whereas the author's computed results represent neutral curves. Zarfs are really plan-form projections of the whole three-dimensional instability space. In most instances there is no difference between zarfs and neutral curves; as in Blasius flows. However, the flow represented here has a neutral surface which is balloon shaped. Hence, the zarf computed by Mack is slightly larger than the neutral curves shown here.

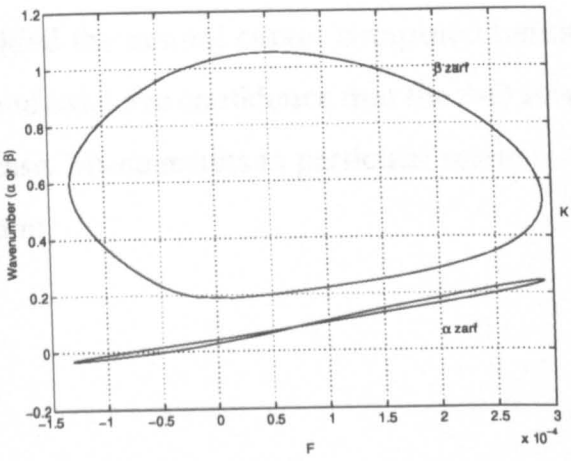

7.4.1: Zarfs for streamwise (α) and spanwise (β) wavenumber for $Re = 400$, 0% porosity @ $\beta_h = 1.0$ and $\theta = 45^o$

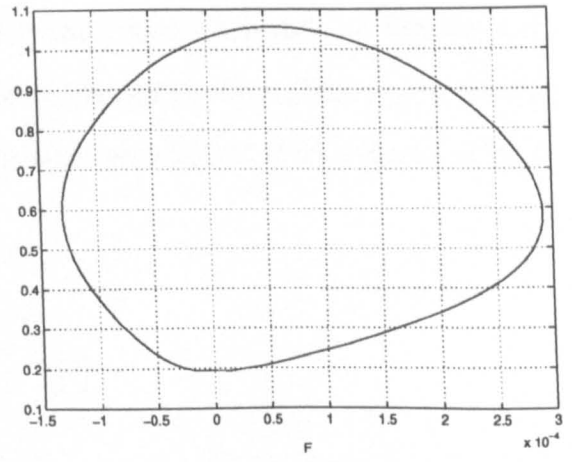

7.4.2: Zarfs of total wavenumber magnitude (K), same conditions as fig. (7.4.1)

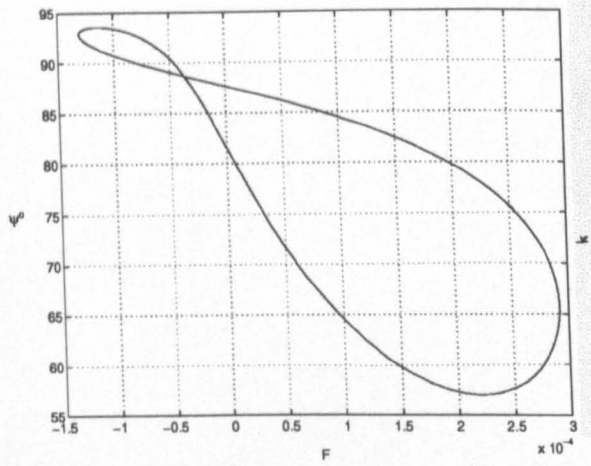

7.4.3: Zarfs of total wavenumber phase (Ψ), same conditions as fig. (7.4.3)

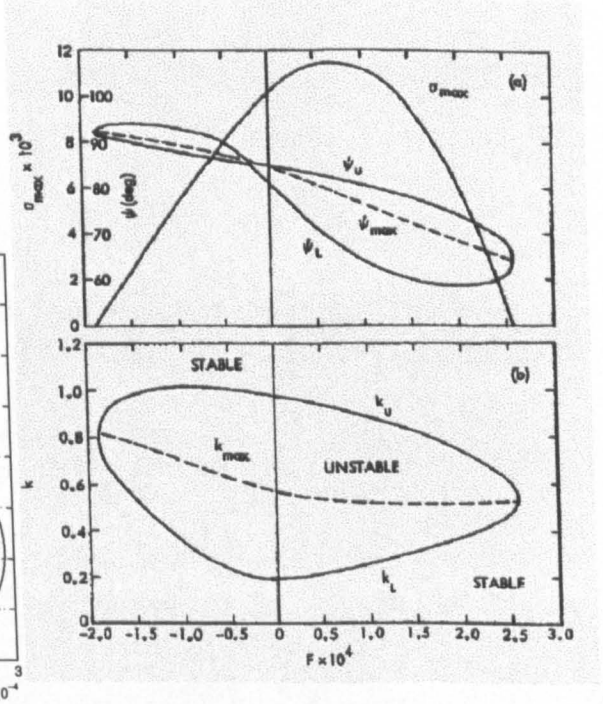

7.4.4: Results of Mack (1978), $Re = 400$, $\beta_h = 1.0$ and $\theta = 45^o$

Figure 7.4: Zarfs for the stability of F-S-C boundary layer. Validation of three dimensional spectral code using the results of Mack (1978).

The results of fig.(7.5.1) to (7.5.1) are again used for comparison with Mack's

Zarfs (fig.7.5.4). Here also, the essential features are accurately reproduced. Provided the neutral curves computed herein lie within the bounds of Mack's zarf, one can have confidence that the 3-D solver is free from error. This is indeed the case. These results in particular relate to flows which are on the verge of separation.

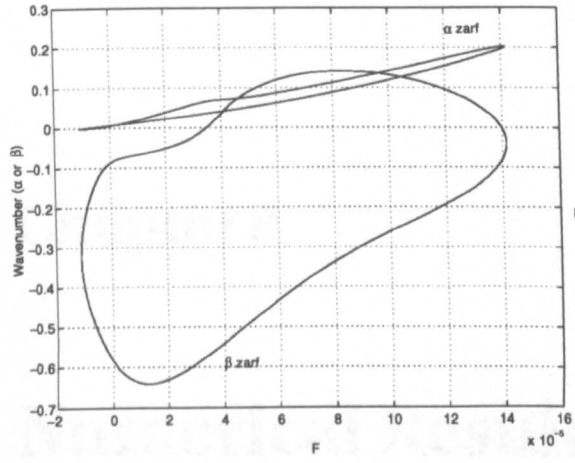

7.5.1: Zarfs for streamwise (α) and spanwise (β) wavenumber for $Re = 555$, 0% porosity @ $\beta_h = -0.1$ and $\theta = 45^o$

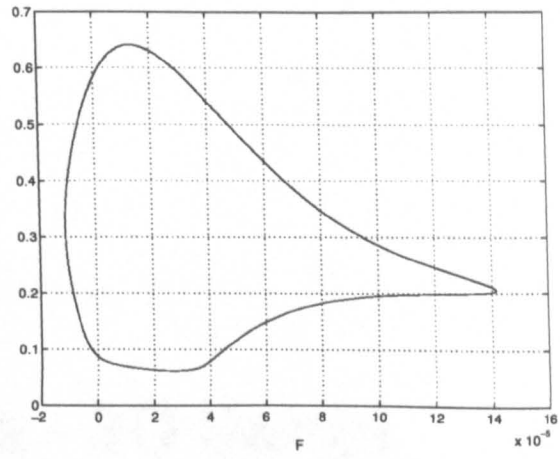

7.5.2: Zarfs of total wavenumber magnitude (K), same conditions as fig. (7.5.1)

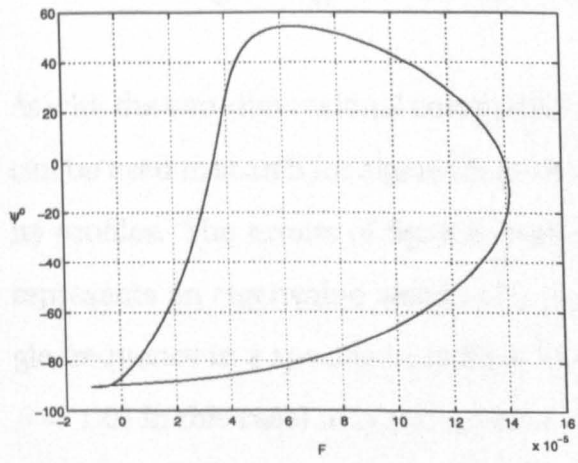

7.5.3: Zarfs of total wavenumber phase (Ψ), same conditions as fig. (7.5.1)

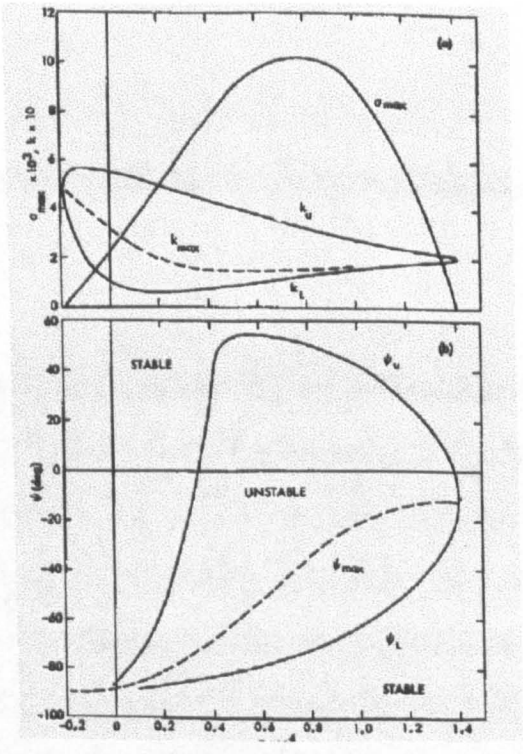

7.5.4: Results of Mack (1978), $Re = 555$, $\beta_h = -0.1$ and $\theta = 45^o$

Figure 7.5: Zarfs for the stability of F-S-C boundary layer. Validation of three dimensional spectral code using the results of Mack (1978).

Chapter 8

Numerical Results - 3D Swept Wedge Flows

8.1 Identification of physical modes & any unexpected modes - using the global scheme

As with the two-dimensional computations of § 4.2, the global eigenvalue scheme can be used to search for eigenvalues of the Falkner-Skan-Cooke series of similarity profiles. The results of fig.(8.1) represent one such computation. This figure represents an eigenvalue search of a flow which is nearing stagnation at a single frequency in a specified ray direction. The chosen ray direction (depicted by $\beta = 1.05$ in this case) may not represent the most unstable direction and indeed the chosen mode may not correspond to the most unstable frequency. However, a large number of such computations were made and, without exception, only one physical mode was discovered. It is thus concluded that there are no additional instability modes for swept wedge flows which have resulted from the addition of the porous boundary condition.

Prior to any computations which involve the application of porosity, it would be useful to ensure that the codes used here are able to reproduce the essential

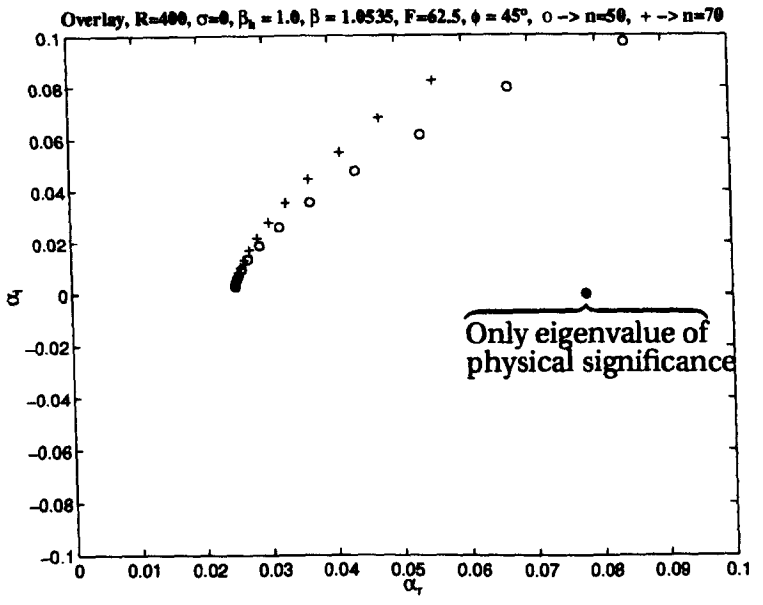

Figure 8.1: Global eigenvalue plots for $Re = 400$, $F = 62.5$, $\beta_h = 1.0$, $\beta = 1.0535$ and $\phi = 45^o$. o - Chebyshev. order $n = 50$. + - Chebyshev. order $n = 70$.

stability features of the Falkner-Skan boundary layer. Inspection of fig.(8.2) reveals the trends one might expect. That is, the accelerated flow given by $\beta = 0.04$ exhibits a higher critical Reynolds number ($Re_{cr} = 480$) and a narrower band of unstable frequencies. This is perhaps what you would expect to see over the leading-edge regions of un-swept airfoils. Conversely, the $\beta = -0.04$ neutral curve reveals a reduction in the critical Reynolds number ($Re_{cr} = 195$) together with a broadening of the range of unstable frequencies. These effects would be seen in mid-chord regions of un-swept airfoils. The neutral curve for zero pressure gradient gives ($Re_{cr} = 300$). When multiplied by the Blasius scaler 1.7208, this gives ($Re_{cr_{bl}} = 520$) which is a commonly agreed result (see Schlichting (1987)).

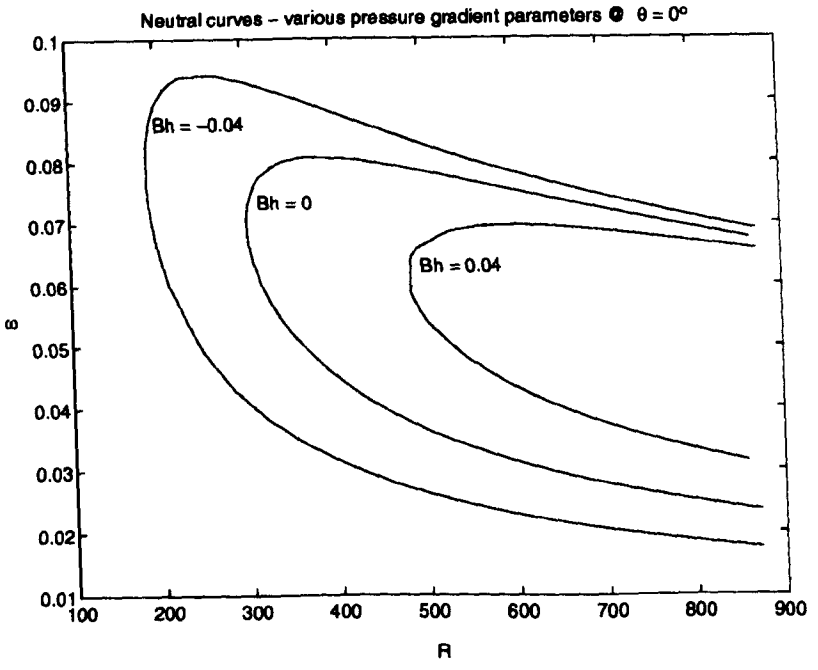

Figure 8.2: Effect of streamwise pressure gradients on the neutral-stability curve. Non-porous surface. (Coordinates can be scaled to the Blasius variable η by multiplying by 1.7208.)

8.2 F-S-C flow stability results - effect of pressure gradient on TS wave stability (no sweep)

All of the results in the following section use the coupled boundary condition in their application of the passive porous boundary condition. Section (4.3.1) gives a more complete description of this technique. The results concern the effects of streamwise pressure gradient and passive porosity upon boundary layer stability. No sweep has been applied in these cases. As such, only streamwise viscous instability is considered. The framework of the three-dimensional stability equations can still be used for these computations, all that is required is that the spanwise wavenumber (β_r) be set to zero. The F-S-C family of profiles can represent 2-D planer flow with an imposed pressure gradient provided the sweep angle θ is set to zero This is equivalent to the commonly known Falkner-Skan set of similarity solutions. There is, however, one important difference. For zero sweep, the solu-

tion for $\beta_h = 1.0$ corresponds to a stagnation point and thus the Reynolds number is zero. However, for non-zero sweep angles, $\beta_h = 1.0$ corresponds to attachment line flow and therefore does have a non-zero Reynolds number.

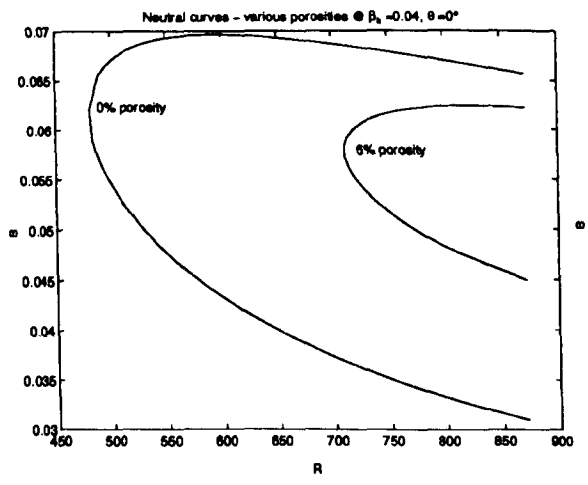

8.3.1: 6% porosity, $\beta_h = 0.04$ and $\beta = 0$

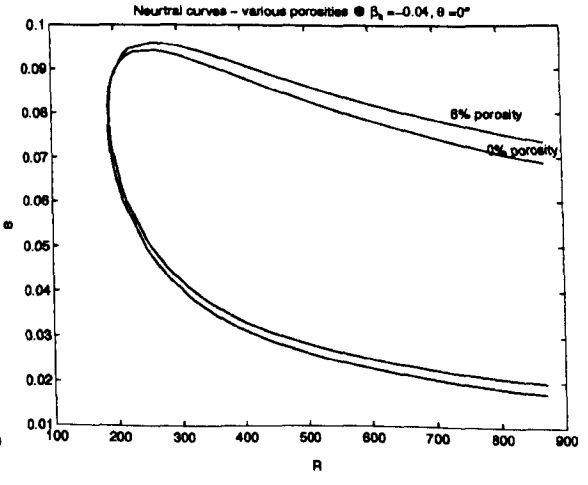

8.3.2: 6% porosity, $\beta_h = -0.04$ and $\beta = 0$

Figure 8.3: Effect of a 6% porous surface on the neutral stability of boundary layers with a streamwise pressure gradient.

The results of fig.(8.3.1) and fig.(8.3.2) represent the stability curves which result from the application of a 6% porous surface to mildly favourable and a mildly adverse pressure gradient respectively. The admittance magnitudes and phases used in both cases were computed iteratively based upon the wavenumbers applicable to a neutral wave at a particular Reynolds number with porosity.

The above plots are important because they give the first insight into the sensitivity of the PPW effect to an imposed pressure gradient. The experimental results of § 6.5.2.1 have already illustrated that there are also more fundamental reasons why pressure gradients can negate any positive effects from porosity. In particular, finite pressure gradients tend to cause gross inflows/outflows into the cavity, thus causing the boundary layer to trip. However, even if this were not the case, it is noticed from fig.(8.3.2) that even a mildly adverse pressure gradient can cause a total loss in any reduction in critical Reynolds number resulting from porosity.

However, the results for neutral curves cannot be used to predict how the growth of a T-S wave is affected by the PPW boundary condition. For this reason, further research is warranted.

8.2.1 Accelerating flows - favourable negative pressure gradients (uncoupled B.C.)

The solution of the un-coupled boundary condition problem is useful when one wishes to identify possible regions of parameter space where wall porosity may offer some benefit. To this end, the results of figs.(8.4.1) to (8.4.4) plot contours of constant α_i for the complete range of admittance magnitudes and phases.

For accelerated flows, comparing figs.(8.4.2), (8.4.3) and (8.4.4) with figure (8.4.1) one can see that as the pressure gradient becomes more favourable, so the comparative favourable effect of PPWs increases. However, for the most favourable pressure gradient, where the boundary layer is naturally stable anyway, the PPW effect merely serves to damp out the disturbances at a faster rate. For marginally unstable accelerated flows, such as those for $\beta = 0.04$ in fig.(8.4.2), the range of useful phase angles for T-S suppression is increased down to levels of admittance phase angles of $\varphi = 86.5^o$. This increased range may simply have resulted from the fact that the boundary layer was only marginally unstable in the first place. However, the theory of § 3.3 suggests that lower phase values such as these may be more realizable in practice given the PPW must have a finite thickness.

8.2.2 Decelerating flows - adverse pressure gradients (uncoupled B.C.)

The results of figs.(8.5.1), (8.5.2), (8.5.3) and (8.5.4) represent the full range of admittances values applied to boundary layers of progressively increasing adverse streamwise pressure gradient. Figure (8.5.2) plots the results of a mildly adverse pressure gradient corresponding to $\beta_h = -0.02$. When comparison is made between this plot and that of Blasius boundary layer of fig.(8.5.1), it can be seen that

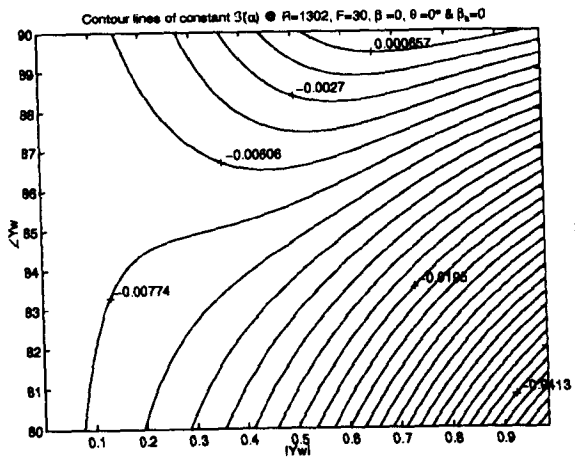

8.4.1: Wedge with zero sweep, pressure gradient $\beta_h = 0.0$ (Blasius flow).

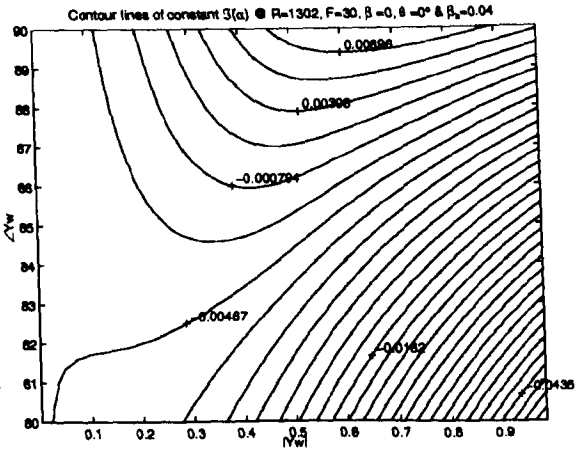

8.4.2: Wedge, zero sweep $\beta_h = 0.04$ (accelerating flow).

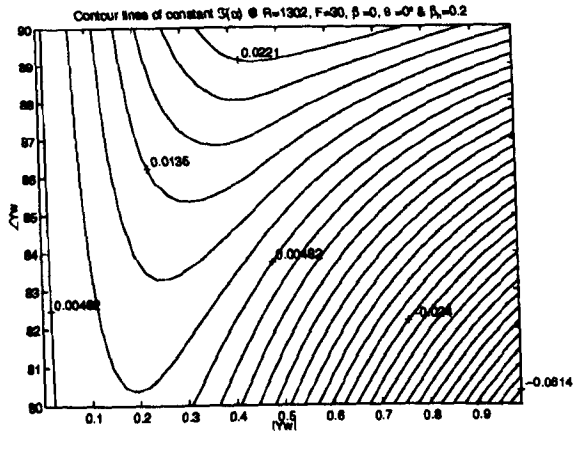

8.4.3: Wedge with zero sweep, pressure gradient $\beta_h = 0.2$ (Strong advantageous pressure gradient).

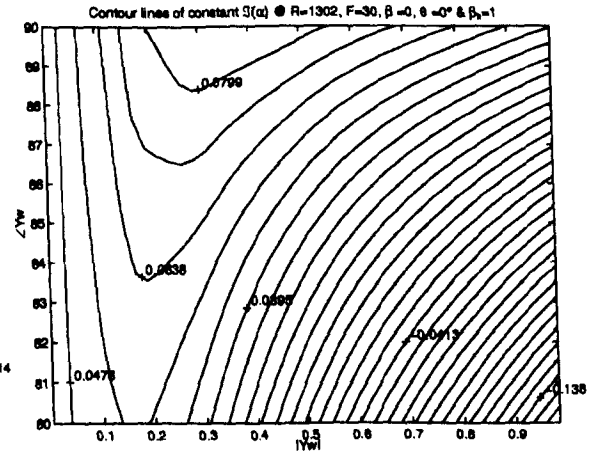

8.4.4: Wedge, zero sweep $\beta_h = 1.0$ (stagnation point flow).

Figure 8.4: Contours of constant growth exponent α_i for full range of admittance values Y_w and phases ϕ.

the range of useful admittances has shrunk appreciably. This feature is seen to worsen with increased flow deceleration until, at $\beta_h = -0.1$ (fig.(8.5.4)), the addition of the PPW boundary condition serves only to cause increased instability. It can therefore be predicted that PPW's will be wholly ineffective at delaying tran-

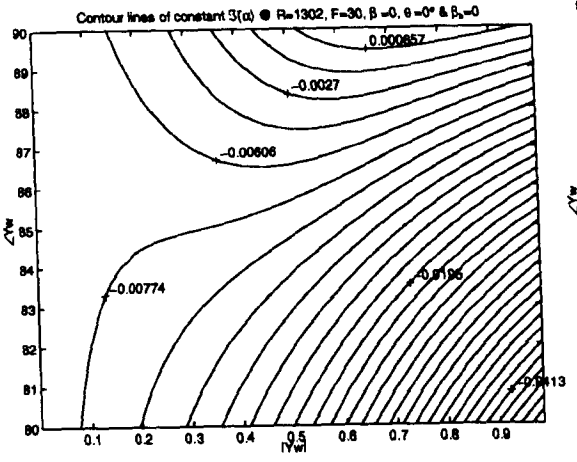

8.5.1: Wedge with zero sweep, pressure gradient $\beta_h = 0.0$ (Blasius flow).

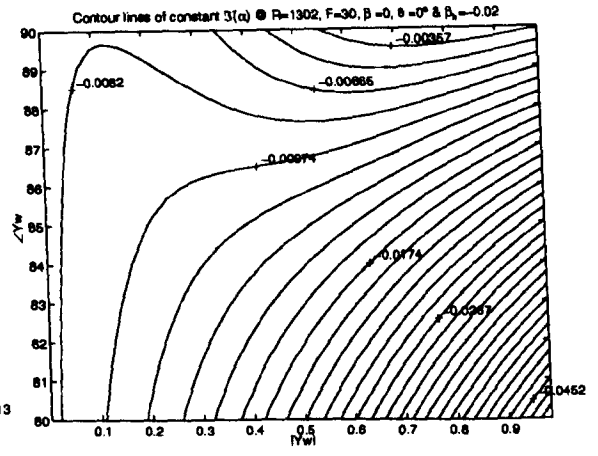

8.5.2: Wedge with zero sweep, pressure gradient $\beta_h = -0.02$ (Adverse pressure gradient).

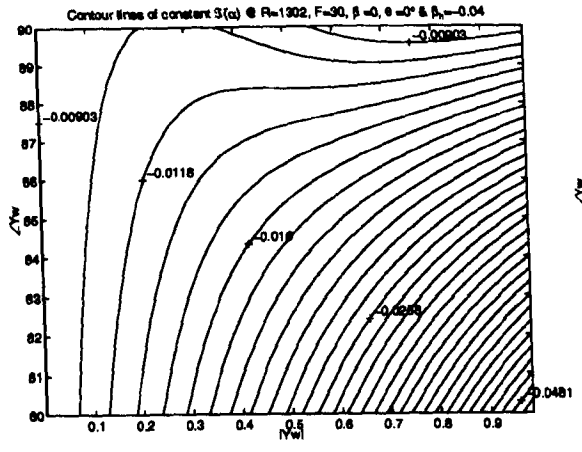

8.5.3: Wedge, zero sweep $\beta_h = -0.04$ (strongly adverse in the T-S sense).

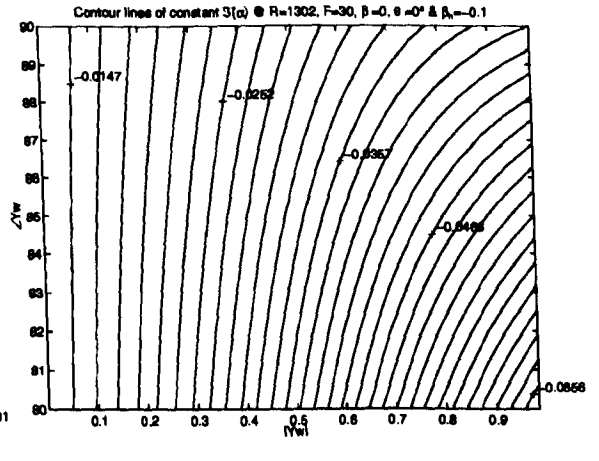

8.5.4: Wedge, zero sweep $\beta_h = -0.1$.(Boundary layer approaching separation)

Figure 8.5: Contours of constant growth exponent α_i for full range of admittance values Y_w and phases ϕ.

sition for flows with significant deceleration.

8.3 Stationary crossflow vortices - various pressure gradients *with sweep* (uncoupled B.C.)

The results of this section relate to the stability of the F-S-C boundary layer profiles which results from the combined effect of sweep and streamwise pressure gradient. The results presented below apply to wedges of 45^o sweep and a variety of imposed pressure gradients. The spanwise wavenumbers have been specially selected so that stationary monochromatic crossflow modes (zero-frequency waves) will result. The global eigenvalue scheme of § 4.2 helps identify such modes. Oblique stationary waves of this type could be reproduced by timed arrays of point sources in a practical stability experiment. Bakchinov *et al.* (1995) have succeeded in doing this in experiments over a flat plate. Such modes are of particular use because they can be identified easily using oil-film flow-visualization techniques.

All plots in figs.(8.6.1) -(8.6.4) suggest that the application of the PPW boundary condition tends to increase the rate of growth of disturbances of this type.

A common pattern can now be seen in the theoretical calculations which predict the failure of the PPW effect. In all cases where performance has been poor, the source of the instability is inviscid rather than viscous. In the above cases, the crossflow instability is dominant. The crossflow profile, being inflectional, will promote inviscid instability. The same is true for decelerated boundary layers without sweep as shown in § 8.2.2. Again, such boundary layers will be inflectional.

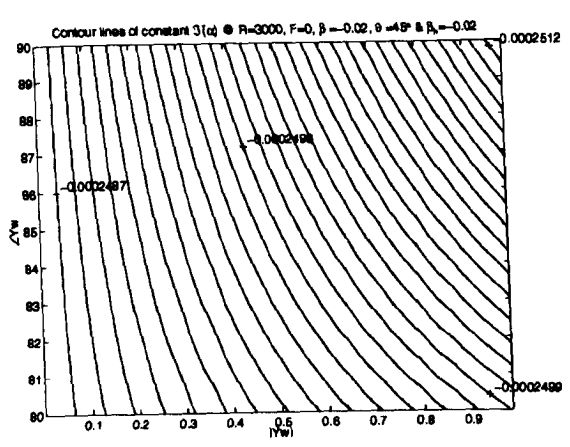

8.6.1: Stationary vortices ($F = 0$), $Re = 3000$, $\beta = -0.02$, $\theta = 45^o$ and $\beta_h = -0.02$

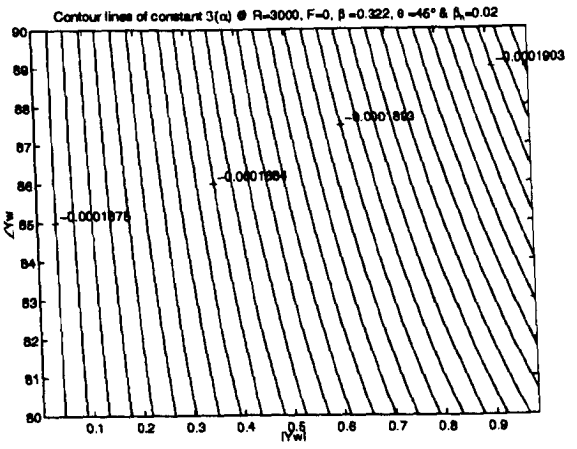

8.6.2: Stationary vortices ($F = 0$), $Re = 3000$, $\beta = 0.322$, $\theta = 45^o$ and $\beta_h = 0.02$

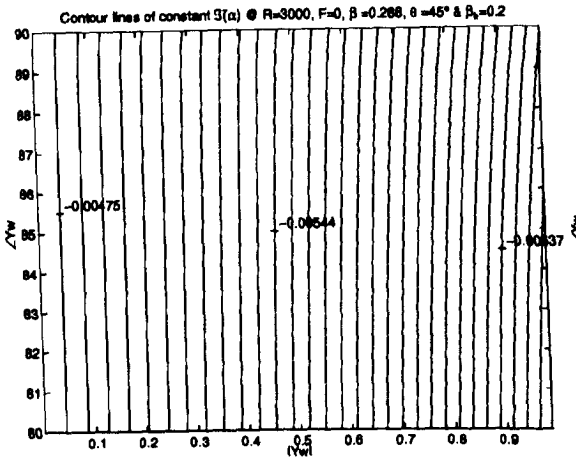

8.6.3: Stationary vortices ($F = 0$), $Re = 3000$, $\beta = 0.288$, $\theta = 45^o$ and $\beta_h = 0.2$

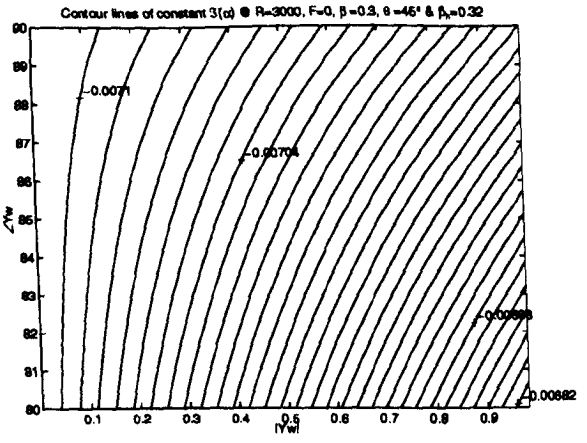

8.6.4: Stationary vortices ($F = 0$), $Re = 3000$, $\beta = 0.3$, $\theta = 45^o$ and $\beta_h = 0.32$

Figure 8.6: Contours of constant growth exponent α_i for full range of admittance values Y_w and phases ϕ. Stationary vortices only.

8.4 Effect of wall porosity on boundary layers with both streamwise and crossflow instability - boundary conditions fully coupled

The plots shown in figs.(8.7.1) and (8.7.2) represent the magnitudes and phases of the real spatial amplification rate vector (i.e. $\vec{\sigma} = (\alpha_i, \beta_i)$) and the real wavenumber vector ($\vec{k} = (\alpha_r, \beta_r)$). As discussed in § 7.3.1, the use of the irrotational condi-

tion of Mack (1984) allows us to set the spanwise component of the spatial amplification factor to zero ($\beta_i = 0$). As such, the computations that follow all assume $\vec{\sigma} = \alpha_i$.

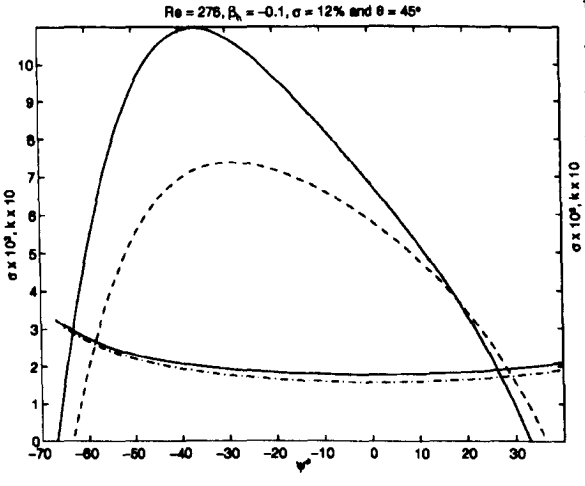

8.7.1: $\beta_h = -0.1$, $\theta = 45°$, $R = 276$ and $F = 2.2 \times 10^{-4}$. - - - - Results for 0% porosity (same as Mack's results). —— Results for 12% porosity.

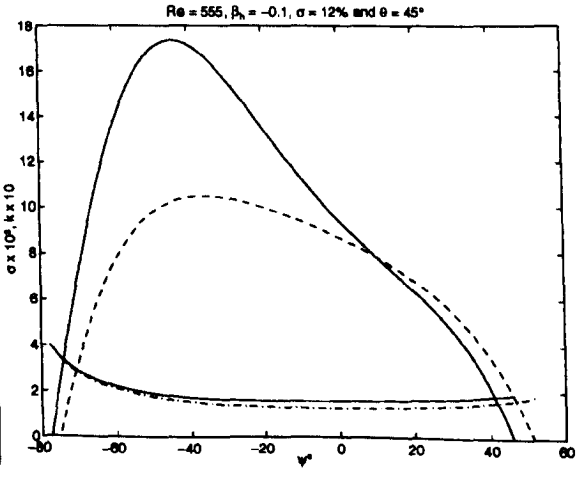

8.7.2: Parameters typical of a swept wedge experiment - traveling disturbances within a profile with a moderate crossflow component. $\beta_h = -0.1$, $\theta = 45°$, $R = 555$ and $F = 2.2 \times 10^{-4}$. - - - - Results for 0% porosity (same as Mack's results). —— Results for 12% porosity

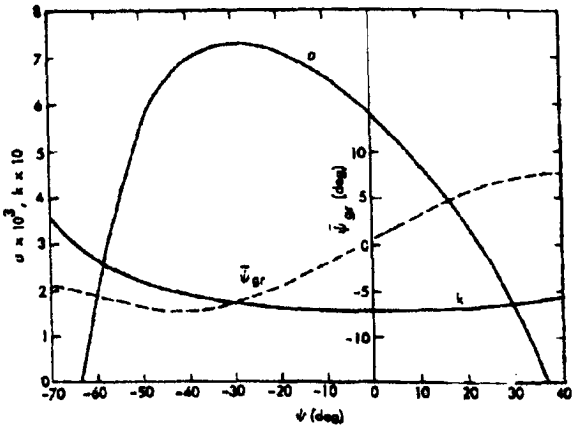

8.7.3: Results of Mack (1978)

Figure 8.7: Effect of wavenumber angle on the spatial growth exponent σ and wavenumber magnitude k. Using the parameters of Mack (1978).

Plot (8.7.1) shows the stability results for a boundary layer which displays both crossflow and streamwise T-S instability. The distribution of $\vec{\sigma}$ with ψ is shown for

$F = 2.2 \times 10^{-4}$. This frequency has been specifically selected, in accordance with the results of Mack (1978), because it represents the most unstable frequency at the given Reynolds number. Furthermore, the pressure gradient parameter (β_h) has been selected such that the maximum crossflow component is attained ($\overline{W} = 0.00349$). The results for 0% porosity are shown in dotted lines for comparison. Comparing the 0% results with the original results of Mack (1978), fig.(8.7.3), it is clear that there is excellent agreement. These results indicate that this type of boundary layer exhibits an asymmetric distribution of amplification factor with respect to wavenumber angle (ψ). This provides further evidence against the use of Squire's theorem for forced monochromatic waves.

The solid lines in figure (8.7.1) indicate the results for a 6% porous foil. The application of the PPW boundary condition seems to worsen the observed asymmetry and, more importantly, increases the maximum growth rate to $\vec{\sigma} = 11 \times 10^{-3}$, at $\psi = 37^o$. This amounts to a 50% increase in the maximum growth factor.

The results of fig.(8.7.2) illustrate a similar pattern of behaviour to that outlined above. Again, the instability waves subject to the PPW boundary condition illustrate a further shift away from the potential flow direction. At this higher Reynolds number, however, the increase in the maximum growth factor nears 70%.

The plots of fig.(8.8.1) and fig.(8.8.2) are zarfs intended to illustrate the effect of porosity on a boundary layer profile nearing separation ($\beta_h = -0.1$) with a 45^o sweep. The results displayed as dotted lines apply to the 0% porosity case. These compare favorably with the results of Mack (1984), fig.(7.5.4). Again the results for the 6% foil are unremarkable. The parameter space relating to instability has a similar area to that of the non-porous wall. The only feature worthy of comment is the shift in the range of unstable frequencies.

The results of fig.(8.9.1) and (8.9.1) relate to a wall of 12%. Here, the pattern remains the same, with a further shift in the range of unstable frequencies.

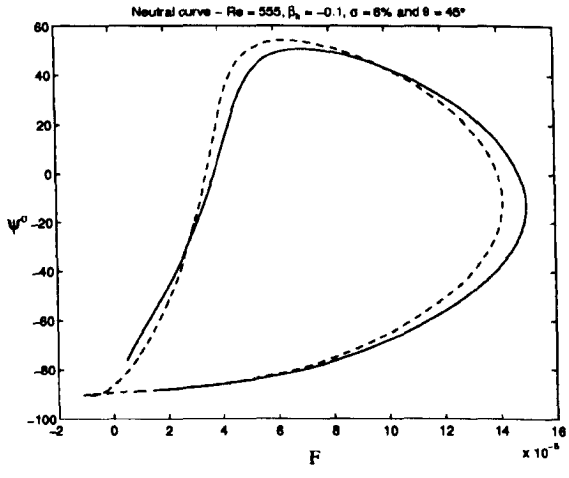

8.8.1: $\beta_h = -0.1$, $\theta = 45^o$, $R = 555$. Wavenumber direction (ψ) *vs.* frequency (F).

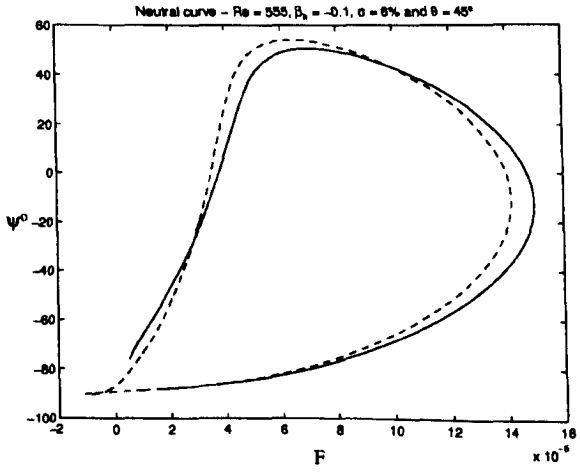

8.8.2: Wavenumber vector magnitude ($\vec{k}$) *vs.* frequency (F), same parameters as fig.(8.8.1).

Figure 8.8: Zarfs of spatial growth exponent $\vec{\sigma}$ and wavenumber phase angle ψ as a function of frequency (F). Using the parameters of Mack (1978). - - - - Results for 0% porosity. — Results for 6% porosity.

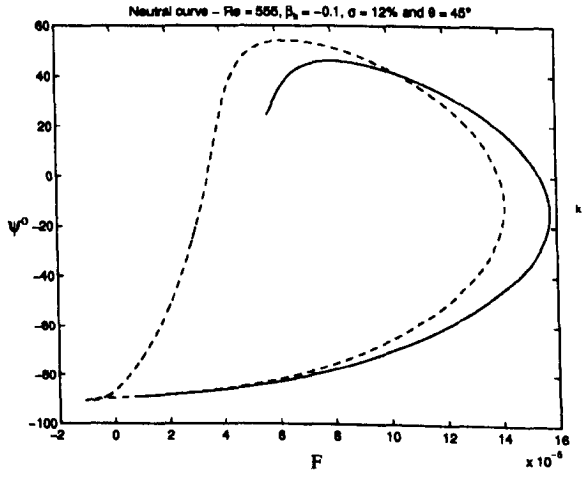

8.9.1: Unstable $\psi - F$ region.

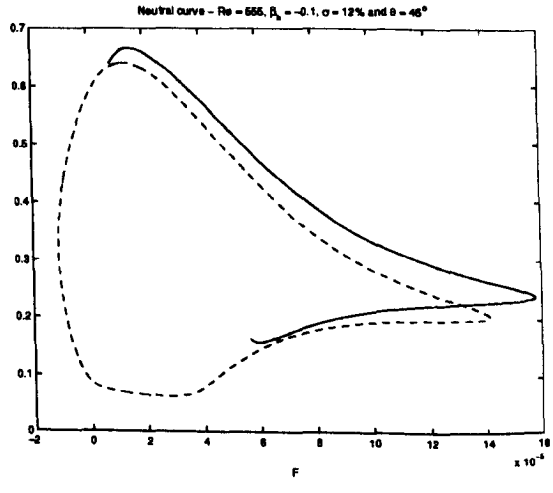

8.9.2: Unstable $k - F$ region. Same parameters as fig.(8.9.1).

Figure 8.9: Zarfs - using the parameters of Mack (1978). $Re = 555$, $\beta_h = -0.1$, $\theta = 45^o$ - - - - - 0% porosity. —12% porosity.

Chapter 9

Conclusions

The current work has considered the stability characteristics of a passive porous surface with air as the working fluid. The chosen configuration consists of a continuous distribution of holes made though a thin metal foil beneath which lies a sealed cavity, or plenum chamber, containing air as its quiescent fluid.

The stability characteristics of the above configuration were analyzed theoretically under the influence of a variety of boundary-layer flows. A highly accurate spectral technique was used to integrate the Orr-Sommerfeld equation for the cases of zero pressure gradient (Blasius flow) and flows with both streamwise pressure gradient and sweep. The Falkner-Skan-Cooke series of similarity profiles were used to represent the mean flow. These equations accurately represent the flow over an infinite swept wedge. As such, no account is taken of the effects of curvature or Coriolis acceleration.

The formation of the admittance boundary condition relies on two principal assumptions: the foil surface has a continuous distribution of porosity and that the foil itself is infinitely thin. It has been shown that the assumption of continuous porosity distribution is valid in this instance. However, the assumption of an infinitely thin foil is not satisfactory as it implies that the pores themselves offer no additional resistance to flow perturbations. The admittance is therefore

attributed to the exposed area of quiescent fluid alone. However, the use of the infinitely thin membrane approximation provides a good starting point for the study of these surfaces.

The theoretical model, using the admittance boundary condition, predicts a beneficial effect on the stability of boundary layers which exhibit viscous instability only. In particular, the PPW boundary condition led to reduced growth rates for both Blasius boundary layers and marginally unstable accelerated boundary layers. Simulation indicates that a 12% porous foil may reduce overall growth rates by up to 100% in the Blasius case.

Passive porosity seems to provide three principal effects which lead to an overall drop in the total mechanical energy of a disturbance. The first effect is a significant drop in the energy production term due to Reynolds stresses. This is particularly noticeable adjacent to the wall, where the sign of the Reynolds stress term can be reversed. The second effect, which is destabilizing, is a drop in the energy removal term attributed to viscous dissipation. However, this reduction in dissipation is almost wholly compensated by the third effect, the removal of energy due to a new pressure work term effective at the wall.

Effect of variable cavity depth has also be studied using the present theory. The results suggest a optimum cavity depth equivalent to ten boundary layer displacement thicknesses. Cavity depths in excess of this were seen to offer no additional benefit.

A global eigenvalue scheme has been used to search for any additional modes which have resulted from the application of porosity. The search covered the whole parameter space. All the expected modes associated with streamwise (Tollmien-Schlichting) waves and crossflow instability were observed but there were, however, no additional modes resulting from the PPW boundary condition.

The model predicts that boundary layers which have either decelerated flow or a crossflow component will respond poorly to the PPW boundary condition. The

stability theory predicts increased growth rates for such flows which implies that passive porosity would lead to premature transition. It is noted that the poor performance was observed only on those boundary layers which exhibit an inviscid instability mode, caused by inflectional boundary layers. An argument has been formed to explain this observation in terms of the physics of viscous instability. Essentially, it is thought that wall porosity interferes with the production of vorticity at the wall. This might involve the dissipation of incoming vorticity packets within the plenum chamber or a modification of the phase modulation of such incoming and induced packets. Both of these mechanisms relate to vorticity interactions at the wall. It is therefore to be expected that such a wall would have no effect upon inviscid instability because this mechanism results from the fluid shear which occurs further out in the boundary layer, around a point of inflection in the profile.

The results from the experimental studies did not, in general, exhibit any of the features predicted by the theory. The reasons for this were largely due to fundamental experimental difficulties resulting from the proposed configuration. The PPW effect relies on the interactions of tiny flow perturbations through the porous surface. The existence of any bulk fluid movement into the cavity would clearly negate the PPW effect. There is, therefore, a real practical difficulty in designing an experiment to illustrate the proposed effect because of the reliance upon a zero pressure gradient (to a very high tolerance). The experimental results herein have indicated that pressure differentials of only a few Pascals can produce bulk flows into the cavity which are sufficient to induce large disturbance growth rates or even trip the boundary layer.

The higher porosity surfaces produced some particularly interesting flow phenomena. In one instance, what appeared to be a self-sustained cavity oscillation was observed, which produced mean flow distortions of up to 40%. A two-dimensional theoretical model for the cavity resonance has been developed which is able to qualitatively explain the essential features of the instability. This self-

sustained cavity oscillation was sufficiently violent to cause transition. Various cavity baffle configuration were attempted with the aim of suppressing the oscillations. However, none of the baffle designs were able to remove the instability to a level where a linear experiment could proceed. Flow visualization of the gross flow distortions indicate the existence of large streamwise streaks. It has been proposed that the cavity oscillation has somehow provided the spanwise vortex modulation indicative of K-type transition.

9.1 Future work

9.1.1 Modifications to the standard transition experiment

It is the authors opinion that the most fruitful areas of future work will involve the pursuit of an experimental design which can prove the benefits, or otherwise, of wall porosity in transition delay. Perhaps the most important conclusion from this work is that the techniques and tunnel apparatus used in standard transition experiments are not of sufficient precision for this purpose. PPWs require experimental apparatus which have been tailored to have the following qualities:

- A flat plate with minimal surface waviness. A high fineness ratio is also desirable, thereby reducing the pressure peak at the leading edge.
- A compliant displacement body, with many degrees of freedom, which will allow fine adjustments to be made to the pressure gradient in both streamwise and spanwise directions.
- A non-invasive disturbance measurement system. It is thought that the proximity of instruments such as hot-wire probes can create local pressure gradients which are sufficient to negate the PPW effect.
- A non-invasive pressure gradient measurement system is required. PPW experiments can only be conducted successfully if a complete 2-D picture of

surface pressure is available. Such information could then be used in conjunction with the compliant displacement body to ensure the pressure gradient is zero over the complete surface. The traditional pressure tapping techniques are not of sufficient accuracy and it is impractical to use them in the numbers required to cover the whole surface.

With reference to the final item outlined above, perhaps the recent developments in pressure sensitive paint (PSP) technology may present some opportunities. These paints emit photons when exposed to UV light in the presence of oxygen. The intensity of photon emission is proportional to the local concentration of oxygen which is, in turn, dependent upon the flow. Laser scanning PSP systems are currently under development. These systems are able to scan large areas of the painted surface, from a remote tunnel location, and can produce and image process pressure measurements in real time. Preliminary tests indicate that PSP's can be developed which are sensitive to very small pressure gradients (only a few Pascals) while retaining a reasonable frequency response.

The production of porous surfaces is another area in need of further development. The surfaces used in the current study were produced by laser drilling a stainless-steel alloy foil. This process requires expensive equipment and is rather laborious. Furthermore, the quality of the finished surfaces was often poor. Research should be focused upon the search for different materials and processes. Perhaps some sort of etching technique would be appropriate?

Improvements in the disturbance measurement system will be a challenging task when considering the redesign of the experiment. It is unlikely that any technologies will become available in the near future which will improve upon the sensitivity and accuracy of a hot-wire system. Indeed, hot-wire systems produce very good results. Perhaps future work should therefore focus upon the design of a probe mounting arm which produces a minimal disturbance to the pressure field.

9.1.2 An additional admittance measurement experiment

The theory presented in the current work outlines the admittance phase angles which are likely to produce a beneficial result. However, the current work has been unable to make practical use of this information. Experimental measurements of the flow through individual pores is crucial to the understanding of PPWs. An experiment should therefore be devised which attempts to measure the admittance of a single pore. This experiment could then be used to optimize parameters such as pore diameter, depth, aspect ratio or shape. An experiment of this type should precede the complete transition experiment presented here. It is likely that the small scale of the experiment will present many technical difficulties (with pore sizes as small as $50\mu m$). Perhaps a larger scale experiment could be carried out at Reynolds numbers which produce dynamically similar conditions to those used here?

9.1.3 Additions to the PPW theory

The key area of PPW theory in need of further development is in the definition of the wall's admittance function. In particular, the current model takes no account of the admittance of the wall by virtue of its finite thickness. Early efforts, using an assumed fully developed pipe flow, do not model the physics of the flow particularly well. Efforts should therefore be made towards the definition of an additional admittance term which can account for the aperture type flow which exists within discrete pores. Inclusion of such a term may provide additional information on whether the required admittance phases, for T-S wave suppression, can be achieved by a practical porous surface.

Aside from the additions required by the admittance theory, there are also the usual refinements which can be made to the standard linear stability theory within which the PPW theory resides. These include effects of non-parallelism, curvature and alike. These areas are all well researched, all that is required is the

inclusion of the various improvements into the existing theory.

It is the author's opinion that in the immediate future, research effort should focus upon the design of an appropriate PPW experiment. There is little point in the pursuit of an accurate PPW theory when there is, as yet, no experimental evidence that PPWs can indeed delay transition.

Bibliography

Arnal D., Casalis G. and Juillen J.C., (1989). Experimental and Theoretical Analysis of Natural Transition on "Infinite" Swept Wings. In D. R.Michel, ed., *Laminar-Turbulent Transition*, pages 311-325. IUTAM Symposium, Springer-Verlag, Toulouse/France.

Bakchinov A.A., Grek G.R., Klingmann B.G.B. and Kozlov V.V., (1995). Transition experiments in a spanwise-modulated boundary layer. *Phys. Fluids*, 7(4):820-832.

Bippes H., Muller B. and Wagner M., (1991). Measurements and stability calculations of the disturbance growth in an unstable three-dimensional Boundary-Layer. *AIAA journal*, 3(10):2371-2377.

Bridges T.J. and Morris P.J., (1984). Differential eigenvalue problems in which the parameter appears nonlinearly. *J. Computational Physis*, 55:437-460.

Brown W., (1960). Exact numericalsolution of the stability equations of the laminar boundary layer. In *International Congress of Applied Mechanics*. Stresa, Italy.

Carpenter P.W., (1993). The feasibility of using Passive Porous Walls for drag reduction. Technical Report 13, Control and Instruments Systems Centre, University of Warwick.

Carpenter P.W., (1996). Feasibility of using passive porous walls for drag reduction. In T.V. Choi K S. Truong and K.K. Prasad, eds., *Emerging Techniques for Drag Reduction*, pages 221-242. Mechanical Engineering Pub. Ltd., UK.

Carpenter P.W., (1998). *Private communication - April '98.*. 2. Dept. of Engineering, University of Warwick, Coventry, CV4 7AL.

Carpenter P.W. and Cooper A.J., (1996). Effect of Wall Compliance on Ratating-Disc Boundary-Layer Stability. In P.W. Duck and P. Hall, eds., *IUTAM Symposium on Nonlinear Instability and Transition in Three-Dimensional Boundary Layers*. Kluwer Academic Publishers.

Carpenter P.W., Cooper A.J. and Davies C., (1995). Laminar-turbulent transition in the three-dimensional boundary layer over a rotating disc. In *Proceedings of the* 40^{th} *Annual Congress of Indian Society of Theoretical and Applied Mechanics*. Bhopal,India. The Taylor Memorial Lecture.

Carpenter P.W. and Garrad A.D., (1985). The hydrodynamic stability of flow over Kramer-type compliant surfaces. Part 1. Tollmien-Schlichting instabilities. *J. Fluid Mech.*, 155:465-510.

Carpenter P.W. and Morris P.J., (1990). The effect of Anisotropic Wall Compliance on Boundary-Layer Stability and Transition. *J. Fluid Mech.*, 218:171-223.

Cebeci T., Chen K., Arnal D. and Huang T.T., (1991). Three-Dimensional Linear Stability Approach to Transition on Wings and Bodies of Revolution at Incidence. *AIAA journal*, 29(12):2077-2085.

Cebeci T. and Stewartson K., (1979). On Stability and Transition in Three-Dimensional Flows. *AIAA journal*, 18(4):398-405.

Cham T.S. and Head M.R., (1969). Turbulent boundary-layer flows on a rotating disk. *J. Fluid Mech.*, 37:429.

Collier F.S. and Schetz J.A., (1983). Injection into a turbulent Boundary-Layer through porous surfaces with different surface geometries. *AIAA journal*, 83(0295).

Cooke J.C., (1950). The Boundary-Layer of a Class of Infinite Yawed cylinders. In *Proc. Cambridge Phil. Soc.*, volume 46, pages 645-648.

Dallmann U. and Bieler H., (1987). Analysis and Simplified Prediction of Primary Instability of Tree-Dimensional Boundary-Layer Flows. In *AIAA 19th Fluid Dynamics, Plasma Dynamics and Lasers Conference*, volume AIAA-87-1337. Honolulu, Hawaii.

Davies C. and Carpenter P.W., (1997). Numerical simulation of the evolution of Tollmien-Schlichting waves over a finite compliant panel. *J. Fluid Mech.*.

Deyhle H., Hohler G. and Bippes H., (1993). Experimental Investigation of Instability Wave Propagation in a Three-Dimensional Boundary-Layer Flow. *AIAA journal*, 31(4):637-645.

Fischer T.M. and Dallmann U., (1991). Primary and secondary stability analysis of a three-dimensional boundary-layer. *Phys. Fluids*, 3(10):2378-2391.

Fox L. and Parker I.B., (1968). *Chebyshev Polynomials in Numerical Analysis*. Oxford University Press, London.

Gaponov S.A., (1971). Influence of porous wall properties on boundary-layer stability (in Russian). *Izv. Sibirsk. Otdeleniya Akad. Nauk SSSR*, 3(1):21-23.

Gaponov S.A., (1975a). Stability of a Boundary-Layer of incompressible fluid over a slotted surface (in Russian). *Izv. Sibirsk. Otdeleniya Akad. Nauk SSSR*, 8(2):37-42.

Gaponov S.A., (1975b). The influence of gas compressibility on Boundary-Layer stability over a permeable surface with a subsonic velocity (in Russian). *Prikl. Mat. Tekh. Fiz.*,, 1:121-125.

Gaster M., (1962). A Note on the Relation Between Temporally Increasing and Spatially Increasing Disturbances in Hydrodynamic Stability. *J. Fluid Mech.*, 14:222-224.

Gaster M., (1965). The role of spatially growing waves in the theory of hydrodynamic stability. *Progress in Aeronautical Sciences*, pages 251-270.

Gaster M., (1997). *Private communication - July '97.*. Aeronautical Engineering Dept., Queen Mary & Westfield College, London.

Gray W.E., (1952). The Nature of the Boundary-Layer Flow at the Nose of a Swept Wing. RAE TM Aero 256, Royal Aircraft Establishment, Farnborough, England, UK.

Gregory N., Stuart J.T. and Walker W.S., (1955). On the Stability of Three-Dimensional Boundary Layers with Application to the Flow Due to a Rotating Disk. *Philosophical Transactions of the Royal Society, London*, 248:155-199.

Itoh N., (1989). Crossflow Instability of 3D Boundary Layers on a Flat Plate. In D. R.Michel, ed., *Laminar-Turbulent Transition*, pages 359-368. IUTAM Symposium, Springer-Verlag, Toulouse/France.

Jordinson R., (1970). The Flat Plate Boundary-Layer. *J. Fluid Mech.*, 43:801-811.

Jordinson R., (1971). Spectrum of Eigenvalues of the Orr-Sommerfeld Equation for Blasius Flow. *Phys. Fluids*, 14:2535-2537.

Kachanov Y.S., (1994). Physical Mechanisms of Laminar Boundary-Layer Transition. *Ann. Rev. Fl. Mech.*, 26:411-482.

Kachanov Y.S., (1997). *Private communication - March '97.*. 3. EUROMECH conference , University of Stuttgart, Stuttgart, Germany.

Klebanoff P.S., Tidstrom K.D. and Sargent L.M., (1961). The three-dimensional nature of boundary-layer instability. Technical report, National Bureau of Standards, Washington, D.C.

Klingmann B.G.B., Boiko A.V., Westin K.J.A., Kozlov V.V. and Alfredsson P.H., (1993). Experiments on the stability of Tollmien-Schlichting waves. *Eur. J. Mech., B/Fluids*, 12(4):493-514.

Lancaster P., (1964). Lambda matrices and vibrating systems. *Int. J. Num. Meth. Eng.*, 6:388-394.

Lanczos C., (1956). *Applied Analysis*. Prentic-Hall.

Landahl M.T., (1962). On the stability of a laminar incompressible Boundary-Layer over a flexible surface. *J. Fluid Mech.*, 13:609-632.

Lekoudis S.G., (1978). Stability of Boundary-Layers over permeable surfaces. In *AIAA*, volume 78 of *203*.

Lighthill M.J., (1963). *Introduction. Boundary Layer theory.*

Lin C.C., (1945). On the stability of two dimensional parallel flows. *Quart. Appl. Math.*,, 117-42, 218-34, 277-301.

Lucey A.D. and Carpenter P.W., (1995). Boundary layer instability over compliant walls: Comparison between theory and experiment. *Phys. Fluids*, 7:2355-2363.

Mack L., (1985). The wave pattern produced by a point source on a rotation disk. In *AIAA paper*, volume 850490.

Mack L.M., (1978). Three-Dimensional Effects in Boundary Layer Stability. In *Proc. of 12th symposium on naval hydrodynamics*, volume 6376. Nat. academy of sciences, Washington DC.

Mack L.M., (1984). Boundary-layer linear stability theory. Technical Report 709, AGARD. Special Course on Stability and Transition of Laminar Flows.

Malik M.R., Li F. and Chang C.L., (1994). Crossflow disturbances in Three-Dimensional Boundary-Layers: nonlinear development, wave interaction and secondary instability. *J. Fluid Mech.*, 268:1-36.

Malik M.R., Wilkinson S.P. and Orszag S.A., (1981). Instability and Transition in Rotating Disk Flow. *AIAA journal*, 19(9):1131-1138.

Marsdon P., (1996). *Private communication - May '96.*. 1. British Aerospace (Operations) Limited, Sowerby Research Centre, P.O.Box 5, Filton, Bristol, BS12 7QW.

Martin W.W., Naudascher E.N. and Padmanabhan M., (1975). Fluid-Dynamic Excitation Involving Flow Instability. In *Journal of the Hydraulic Division, Proceedings of the American Society of civil Engineers*, number 101 in HY6, pages 681-698. ASCE.

Morris P.J., (1976). The Spatial Viscous Instability of Axisymmetric Jets. *J. Fluid Mech.*, 77:511-529.

Morris P.J., (1987). Applications of Matrix Factorization in Hydrodynamic Stability. Technical report, Dept. of Aerospace Engineering.

Nayfeh A.H., (1980). Stability of Three-Dimensional Boundary-Layers. *AIAA journal*, 18(4).

Orszag S.A., (1971). Accurate solution of the Orr-Sommerfeld stability equation. *J. Fluid Mech.*, 50:689-703.

Press W.H., Teukolsky S.A., Vetterling W.T. and Flannery B.P., (1992). *Numerical Recipes in Fortran.* Cambridge University Press, 2^{nd} edition.

Pretsch J., (1941). Die Stabilitat einer ebenen Laminarstöming bei Druckgefälle und Druckanstieg. *Jahrbuch d. Deutschen Luftfahrtforschung*, 1.

Rockwell D., (1977). Prediction of Oscillation Frequencies for Unstable Flow Past Cavities. In *Transactions of the ASME*, pages 294-300. ASME Fluids Engineering Division.

Rockwell D. and Naudascher E., (1979). Self-Sustained Oscillations of Impinging Free Shear-Layers. *Ann. Rev. Fl. Mech.*, 11:67-94.

Sarohia V., (1977). Experimental Investigation of Oscillations in Flows Over Shallow Cavities. *AIAA journal*, 15(7):984-991.

Schetz J.A. and Kong F., (1981). Turbulent Boundary-Layers over solid and porous surfaces with small roughness. *AIAA journal*, 81(0418).

Schlichting H., (1987). *Boundary-Layer Theory.* McGraw-Hill, Inc., New York, 7^{th} edition.

Schubauer G.B. and Skramstad H.K., (1949). Laminar Boundary-Layer oscillations and transition on a flat plate. *NACA*, 909.

Smith A.M.O. and Gamberoni N., (1956). Transition, Pressure Gradient, and Stability Theory. Technical Report ES 26388, Douglas Aircraft Co., El Segundo, CA.

Squire H.B., (1933). On the Stability of Three-Dimensional Disturbances of Viscous Fluid between Parallel Walls. In *Proc. Roy. Soc. London*, volume A142, pages 621-628.

Srokowski A. and Orszag S.A., (1977). Mass Flow Requirements for LFC Wing Design. *AIAA Paper*, 77(1222).

Taylor M.J. and Peake N., (1998). The long-time behaviour of incompressible swept-wing boundary layers subject to impulsive forcing. *J. Fluid Mech.*, 355:359-381.

Thomas A.S.W., (1985). Aircraft Drag Reduction Technology - A summary,. *AGARD Report*, 723(1).

Ulrich A., (1944). *Acad. d Luftfarhrforchung*, 8B.

Wilkinson J.H., (1965). *The Algebraic Eigenvalue Problem.*. Oxford University Press, London.

Wilkinson S.P., (1983). Influence of wall permeability on turbulent Boundary-Layer properties. *AIAA journal*, 83(0294).

Yeo K.S., (1986). *The stability of flow over flexible surfaces.* Ph.D. thesis, Cambridge University.

Appendix A

A.1 Derivation of the 3D Orr-Sommerfeld equation

$$\frac{\partial u}{\partial X} + \frac{\partial w}{\partial Z} + \frac{\partial v}{\partial y} = 0 \tag{A.1}$$

$$\frac{\partial u}{\partial t} + U\frac{\partial u}{\partial X} + W\frac{\partial u}{\partial Z} + v\frac{\partial U}{\partial y} = -\frac{\partial p}{\partial X} + D_X \tag{A.2}$$

$$\frac{\partial w}{\partial t} + U\frac{\partial w}{\partial X} + W\frac{\partial w}{\partial Z} + v\frac{\partial W}{\partial y} = -\frac{\partial p}{\partial Z} + D_Z \tag{A.3}$$

$$\frac{\partial v}{\partial t} + U\frac{\partial v}{\partial X} + W\frac{\partial v}{\partial Z} = -\frac{\partial p}{\partial y} + D_y \tag{A.4}$$

where $D = \frac{\partial^2}{\partial X^2} + \frac{\partial^2}{\partial y^2} + \frac{\partial^2}{\partial Z^2}$

The velocity and pressure fluctuations are assumed to take the following form:

$$(u, w, v, p) = Re\{(f, h, \phi, \pi)\exp[i(\alpha X + \beta Z - \omega t)]\} \tag{A.5}$$

Substitution of this form of disturbance into eqns.(A.1), (A.2), (A.3) and (A.4) yields the following set of equations:

$$i(\alpha f + \beta h) + \phi' = 0 \tag{A.6}$$

$$i(\alpha\overline{U} + \beta\overline{W} - \omega)f + D\overline{U}\phi = -i\alpha\pi + \frac{1}{Re}(f'' - (\alpha^2 + \beta^2)f) \tag{A.7}$$

$$i(\alpha\overline{U} + \beta\overline{W} - \omega)h + D\overline{W}\phi = -i\beta\pi + \frac{1}{Re}(h'' - (\alpha^2 + \beta^2)h) \tag{A.8}$$

$$i(\alpha\overline{U} + \beta\overline{W} - \omega)\phi = -\pi' + \frac{1}{Re}(\phi'' - (\alpha^2 + \beta^2)\phi) \tag{A.9}$$

Multiplying eqn.(A.7) and (A.8) by $i\alpha$ and $i\beta$ respectively and adding the result

gives:

$$-(\alpha^2+\beta^2)\pi = \frac{i}{Re}(\alpha f''-\alpha(\alpha^2+\beta^2)f+\beta h''-\beta(\alpha^2+\beta^2)h)+\overline{Q}(\alpha f+\beta h)-i\phi(\alpha D\overline{U}+\beta D\overline{W}) \tag{A.10}$$

where $\overline{Q} = \alpha\overline{U} + \beta\overline{W} - \omega$.

Differentiating eqn.(A.10) once with respect to y gives:

$$-(\alpha^2+\beta^2)\pi' = \frac{i}{Re}\left[\alpha f''' + \beta h''' - (\alpha^2+\beta^2)(\alpha f' + \beta h')\right]$$
$$+\overline{Q'}(\alpha f+\beta h) + \overline{Q}(\alpha f' + \beta h') - i\left[\phi(\alpha D^2\overline{U} + \beta D^2\overline{W}) + \phi'(\alpha D\overline{U} + \beta D\overline{W})\right] \tag{A.11}$$

But from eqn.(A.6):

$$\alpha f + \beta h = i\phi'$$
$$\alpha f'' + \beta h'' = i\phi'''$$
$$\alpha f''' + \beta h''' = i\phi''''$$

Therefore:

$$-(\alpha^2+\beta^2)\pi' = \frac{i}{Re}\left[i\phi'''' - (\alpha^2+\beta^2)i\phi''\right] + i\overline{Q'}\phi' + i\overline{Q}\phi''$$
$$-i\left[\phi(\alpha D^2\overline{U} + \beta D^2\overline{W}) + \phi'(\alpha D\overline{U} + \beta D\overline{W})\right] \tag{A.12}$$

Substituting in π' from eqn.(A.9) gives:

$$i\overline{Q}\phi(\alpha^2-\beta^2)-\frac{(\alpha^2+\beta^2)}{Re}\left[\phi'' - (\alpha^2+\beta^2)\phi\right] = \frac{1}{Re}\left[(\alpha^2+\beta^2)\phi'' - \phi''''\right]-i\left[\phi\overline{Q''} - \phi''\overline{Q}\right] \tag{A.13}$$

After some simplification, the full three-dimensional Orr-Sommerfeld equation results:

$$\phi'''' - 2\phi''(\alpha^2+\beta^2) + (\alpha^2+\beta^2)^2\phi = iRe\left[\overline{Q}(\phi'' - \phi(\alpha^2+\beta^2)) - \overline{Q''}\phi\right] \tag{A.14}$$

A.2 Spatial derivatives using the mapped variable

The derivatives with respect to the physical boundary layer normal ordinate $y \in [0, \infty]$, are related to the derivatives with respect to the mapped ordinate $z \in [-1, 1]$ by the matrix $m(z) = (1 - z^2)/4$. The following relations define the higher-order derivatives:

1^{st} derivative:

$$\hat{v}'(y) = m(z)\hat{v}'(z) \tag{A.15}$$

2^{nd} derivative:

$$\hat{v}'' = m(z)^2\hat{v}'' + m(z)m'(z)\hat{v}' \tag{A.16}$$

3^{rd} derivative:

$$\hat{v}''' = m(z)^3\hat{v}''' + 3m(z)^2m(z)'\hat{v}'' + (m(z)^2m(z)'' + m(z)m(z)'^2)\hat{v}' \tag{A.17}$$

4^{th} derivative:

$$\begin{aligned}\hat{v}'''' = 6m(z)^3m(z)'\hat{v}''' + 7m(z)^2m(z)'^2\hat{v}'' + 4m(z)^3m(z)''\hat{v}'' + \\ 4m(z)^2m(z)'m(z)''\hat{v}' + m(z)^3m(z)'''\hat{v}' + m(z)m(z)'^3\hat{v}' + m(z)^4\hat{v}''''\end{aligned} \tag{A.18}$$

A.3 Runge Kutta solution of Falkner-Skan-Cooke equations (and Blasius equation ($\beta_h = 0$))

The Falkner-Skan-Cooke equations take the following form:

$$(2-\beta_h)f''' + ff'' + \beta_h(1-f'^2) = 0 \tag{A.19}$$

$$(2-\beta_h)g'' + fg' = 0 \tag{A.20}$$

where primes indicate differentiation with respect to the similarity variable $\eta = y\left[\frac{U_e}{\nu X}\right]^{1/2}$.

Assign the following values for each variable and its derivatives:

$$\left\{\begin{array}{rcl} A_1 &=& f'' \\ A_2 &=& f' \\ A_3 &=& f \\ A_4 &=& g \\ A_5 &=& g' \end{array}\right\} \qquad \text{Therefore:} \quad \left\{\begin{array}{rcl} Z_1 &=& A_1' \\ Z_2 &=& A_2' \\ Z_3 &=& A_3' \\ Z_4 &=& A_4' \\ Z_5 &=& A_5' \end{array}\right\} \tag{A.21}$$

From eqn.(A.19):

$$(2-\beta_h)Z_1 + A_1A_3 + \beta_h(1-A_2^2) = 0, \qquad Z_1 = \frac{\beta_h(A_2^2-1) - A_1A_3}{(2-\beta_h)} \tag{A.22}$$

and from eqn.(A.20):

$$(2-\beta_h)Z_5 + A_3A_5 = 0 \qquad Z_5 = \frac{-A_3A_5}{(2-\beta_h)} \tag{A.23}$$

$$Z_2 = A_1 \quad Z_3 = A_2 \quad Z_4 = A_5 \tag{A.24}$$

Setting $\beta_h = 0$ reduces eqn.(A.20) to the Blasius equation. Hence, the Runge Kutta code used to produce swept wedge flows can also be used to compute the Blasius flow. Aside from setting β_h to zero, there is an additional scaling to be done because the similarity variable used in the Blasius computations has a coefficient of 1.7208. The FSC similarity variable is of the same form as the Blasius but without this constant coefficient.

A.4 Derivation of pressure term from the linearized Navier-Stokes equations with $U_\infty = 0$

The x-component of the linearized Navier-Stokes equation is given as:

$$\rho\frac{\partial u}{\partial t} = -\frac{\partial p}{\partial x} + \mu\nabla^2 u \tag{A.25}$$

For a spatially evolving disturbance, the following apply:

$$\hat{u} = iD\hat{v}/\alpha \qquad \frac{du}{dt} = \omega D\hat{v}/\alpha \qquad \frac{\partial^2\hat{u}}{\partial x^2} = -i\alpha D\hat{v} \qquad \frac{\partial^2\hat{u}}{\partial y^2} = iD^3\hat{v}/\alpha \qquad \frac{\partial\hat{p}}{\partial x} = i\alpha\hat{p}$$

Substitution of the above produces:

$$\hat{p} = -\frac{D\hat{v}}{\alpha^2}(\rho + \alpha^2\mu) + \frac{\mu D^3\hat{v}}{\alpha^2} \tag{A.26}$$

Evaluation at the wall means that the no-slip condition $D\hat{v}_w = 0$ applies. Hence:

$$\hat{p}_w = \frac{\mu D^3\hat{v}}{\alpha^2} \tag{A.27}$$

Appendix B

B.1 Disk insert working drawings

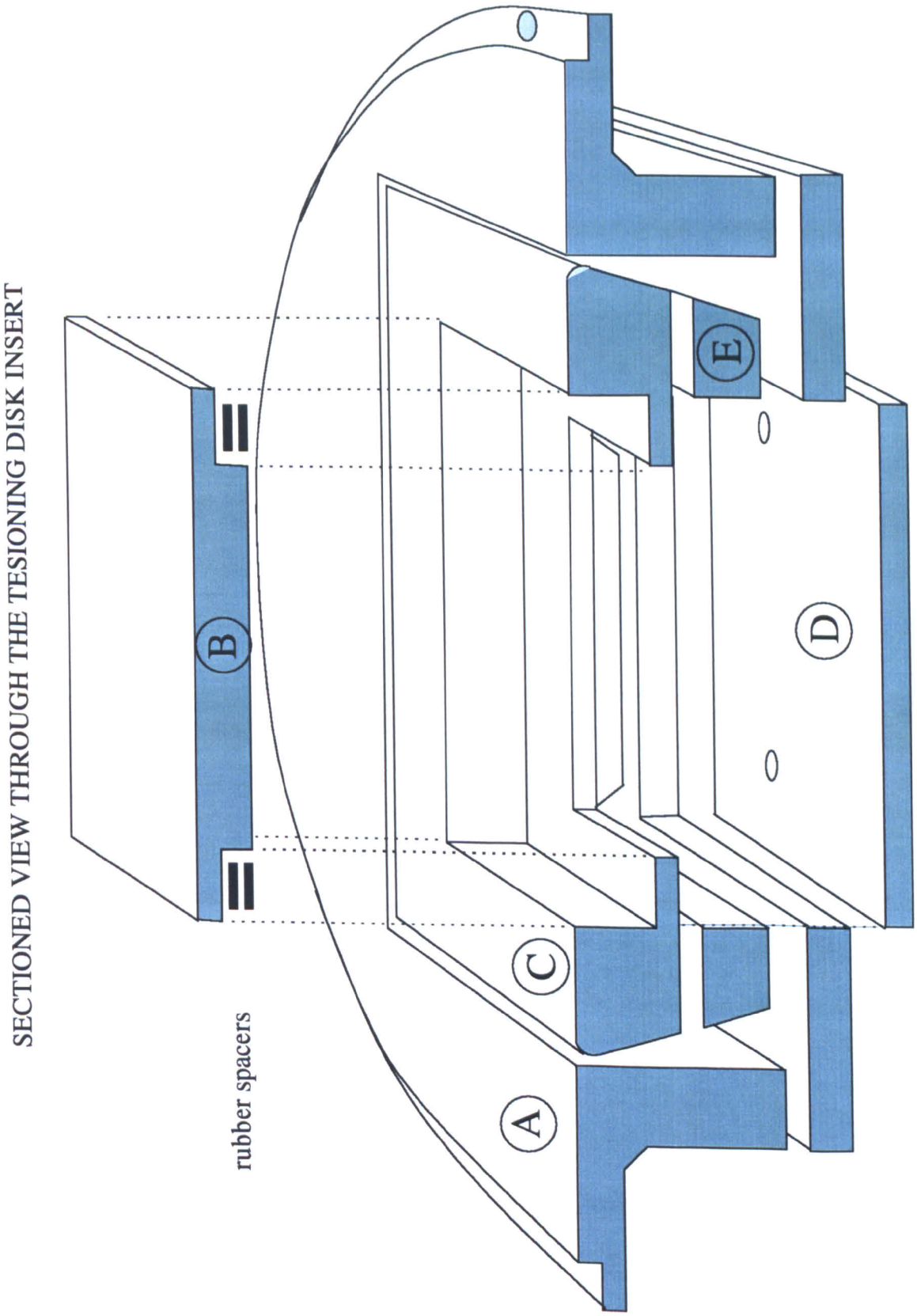

Figure B.1: Sectioned view of the general arrangement (G.A.) of disk insert tensioning mechanism, together with insert housing and cavity adjustment components.

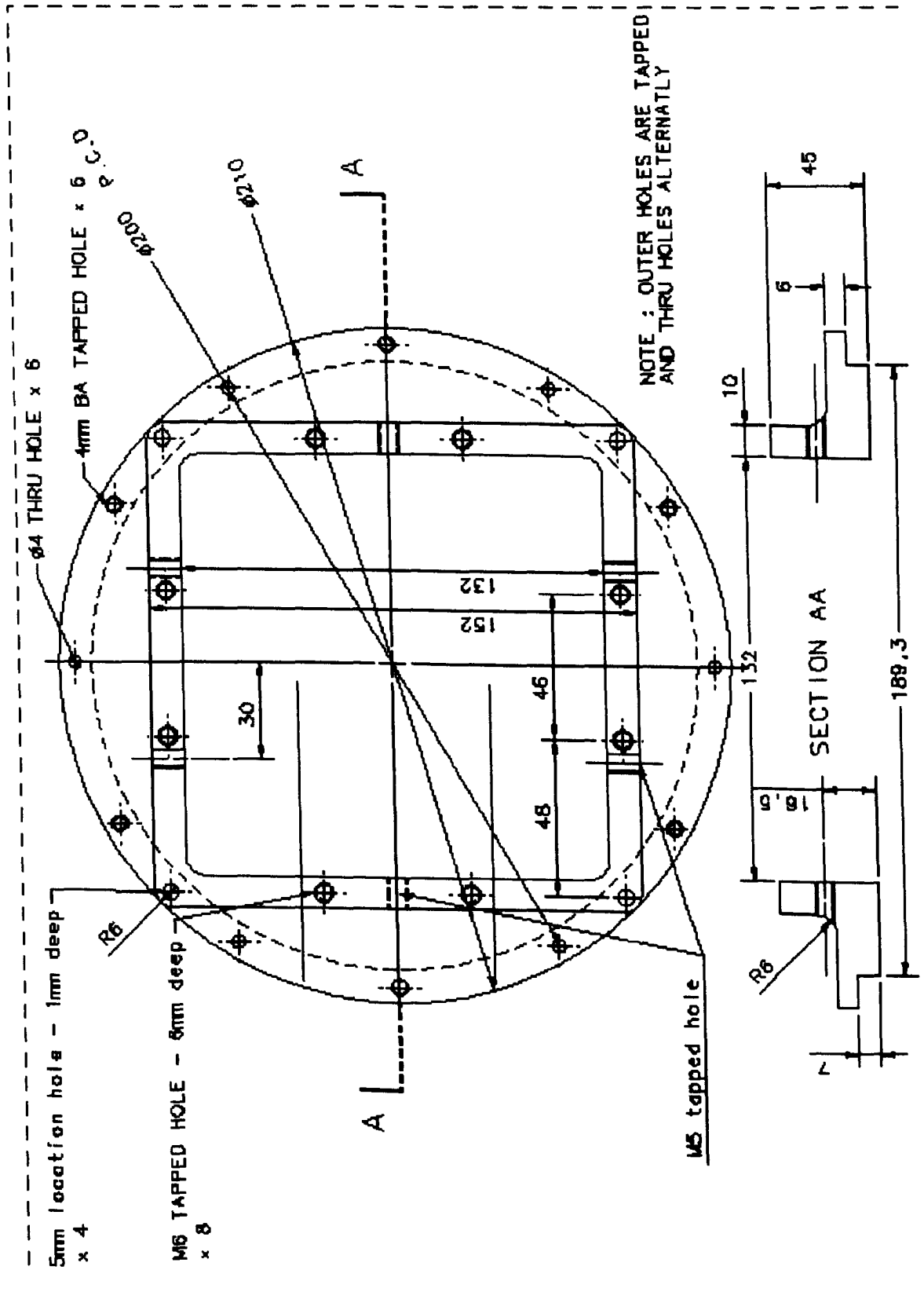

Figure B.2: Insert housing working drawing (to fit tunnel flat plate) - component 'A' on G.A. drawing B.1

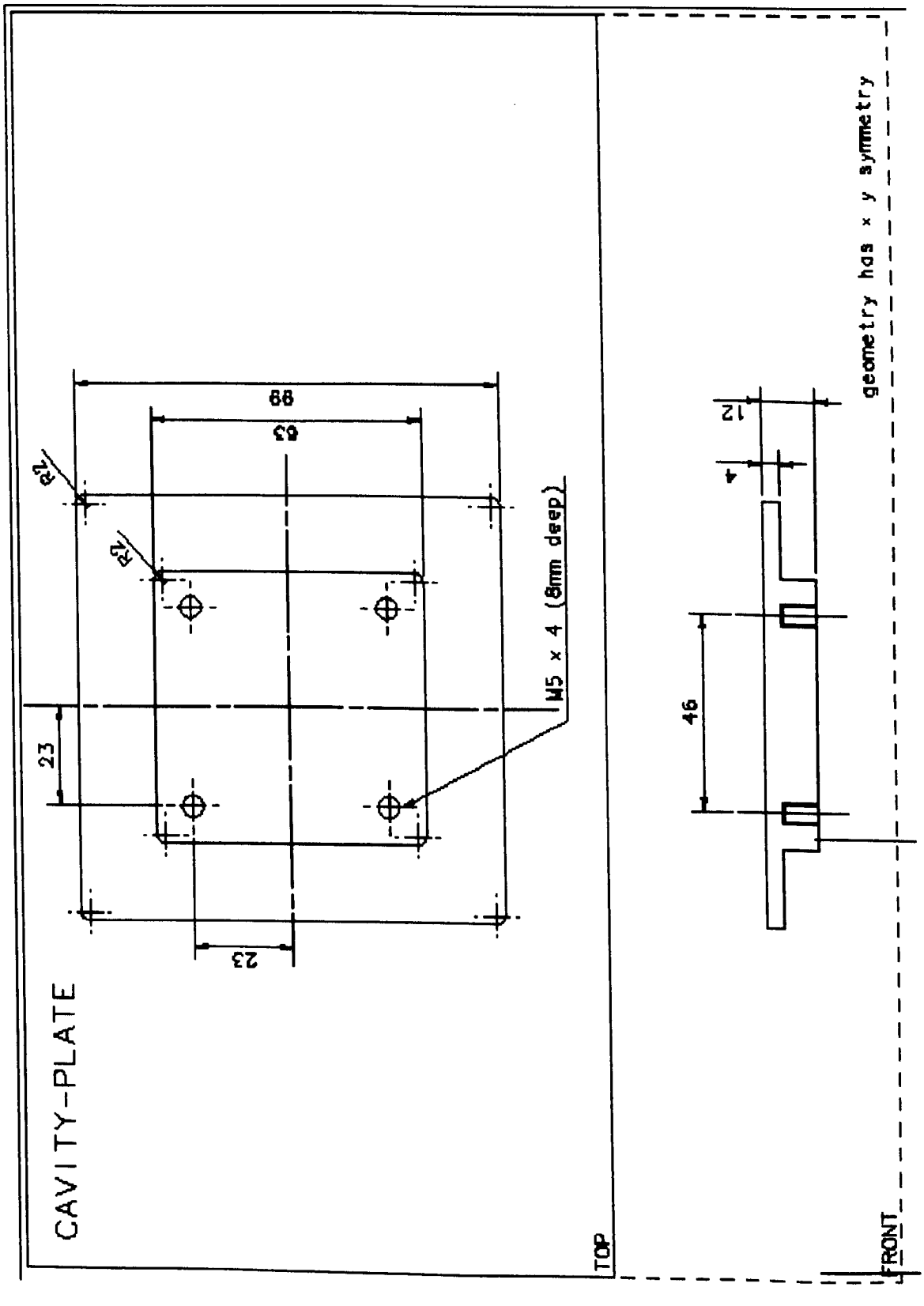

Figure B.3: Cavity flange working drawing - component 'B' on G.A. drawing B.1

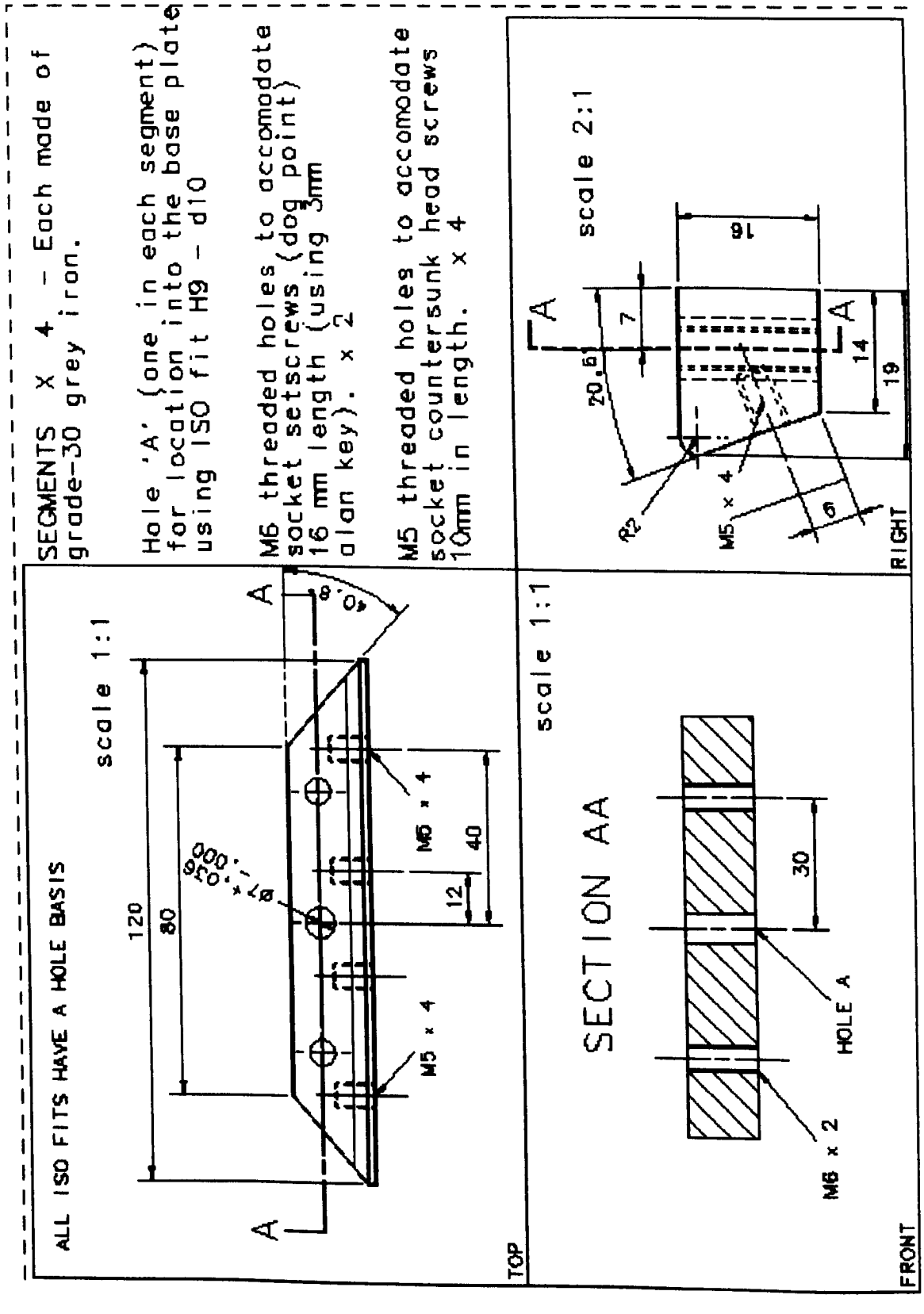

Figure B.4: Working drawing of floating tensioning segments ×4 - component 'E' on G.A.

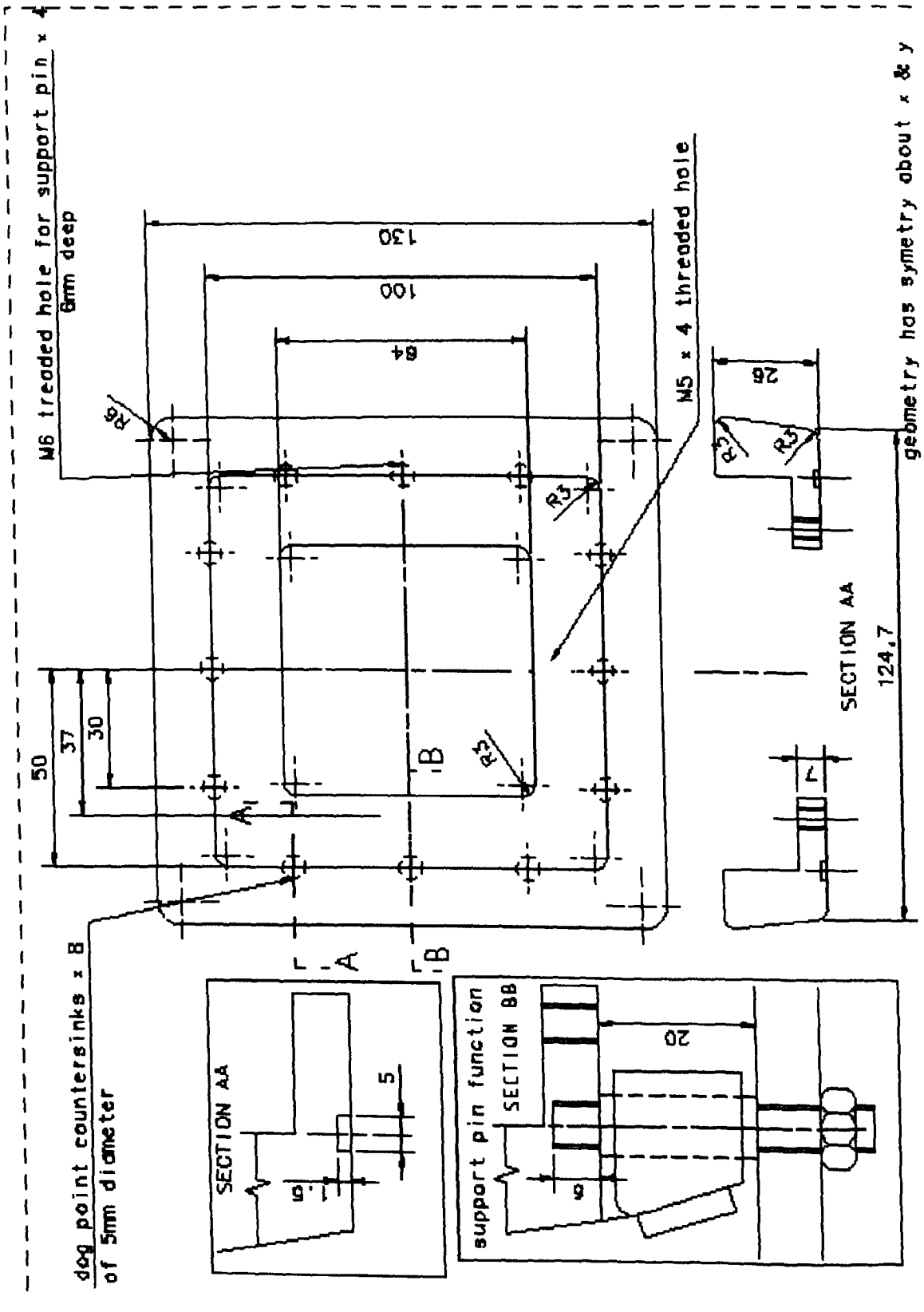

Figure B.5: Working drawing, with detailed views, of foil forming block and integral cavity - component 'C' on G.A.

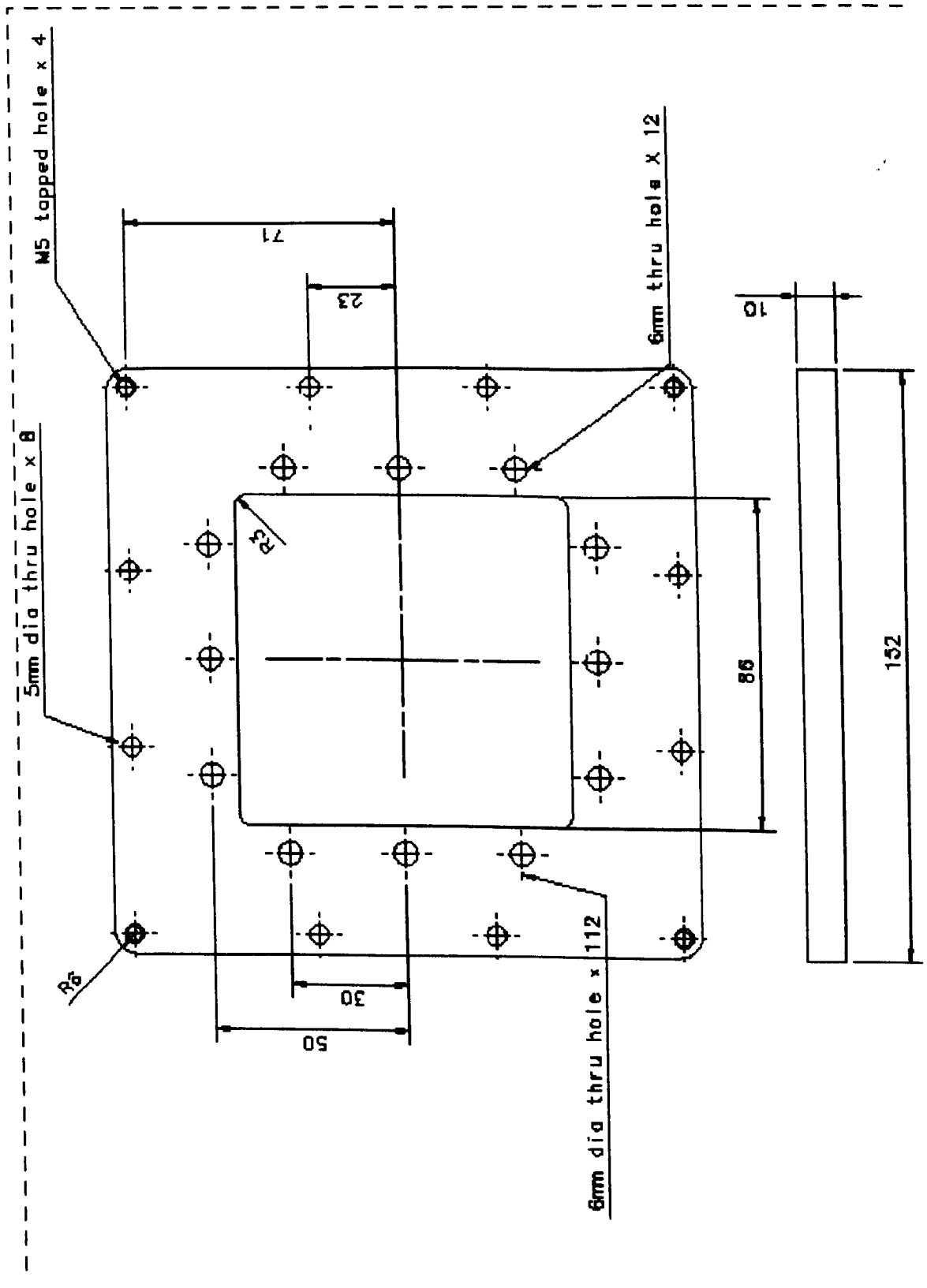

Figure B.6: Backplate (providing stiffness to pins for floating segments, cavity access and aspect adjustment for foil forming body) - component 'F' on G.A.

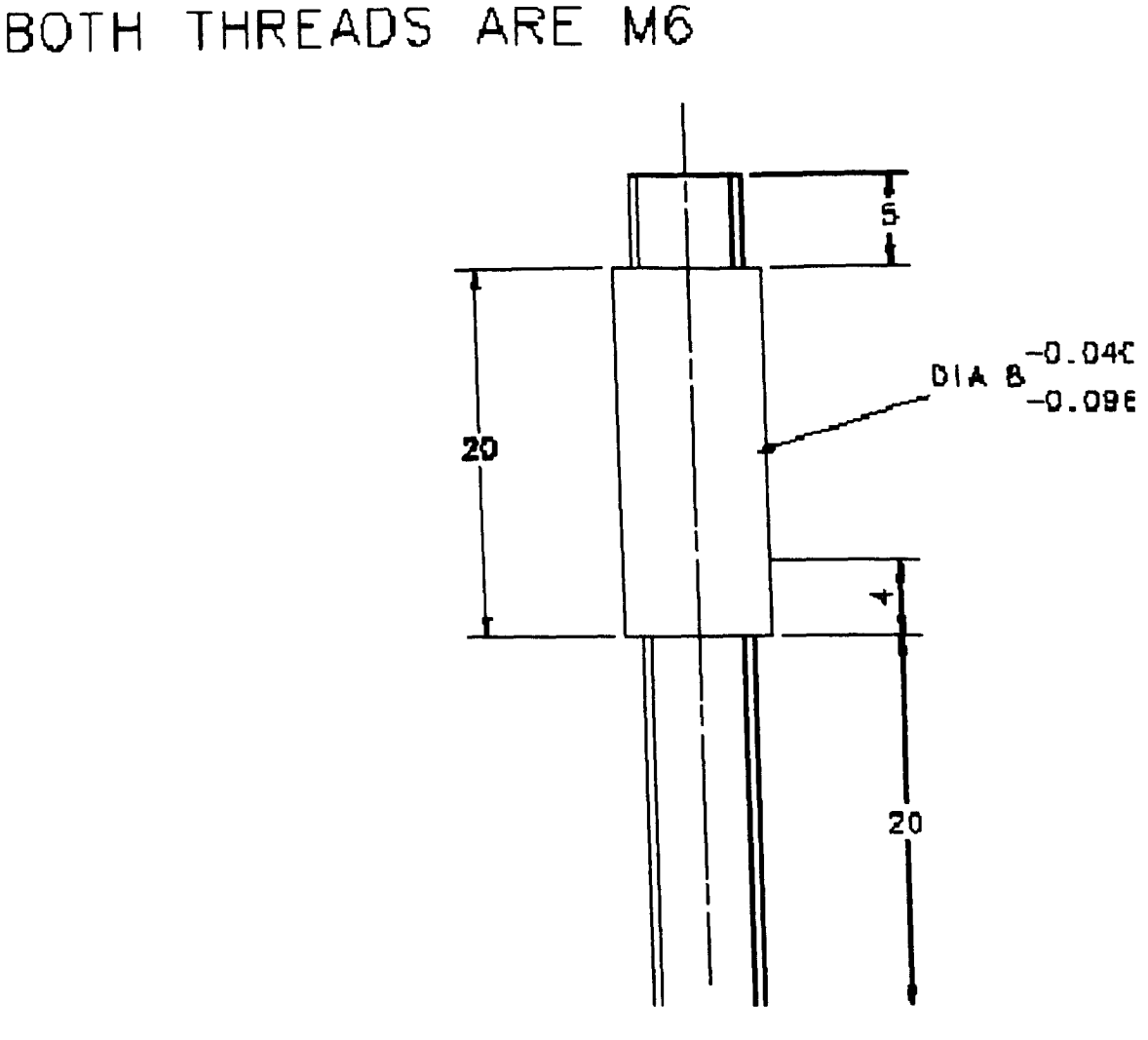

Figure B.7: Floating segment support pins. A clearance fit is provided between these pins and the clamping segments they pass through. This is to allow the segments to pivot slightly about the axis perpendicular to the longitudinal axis of the segment. This ensures that each clamping segment can adjust its aspect such that equal stress are applied to the foil. Pin not shown in G.A. (see detail of drawing B.5

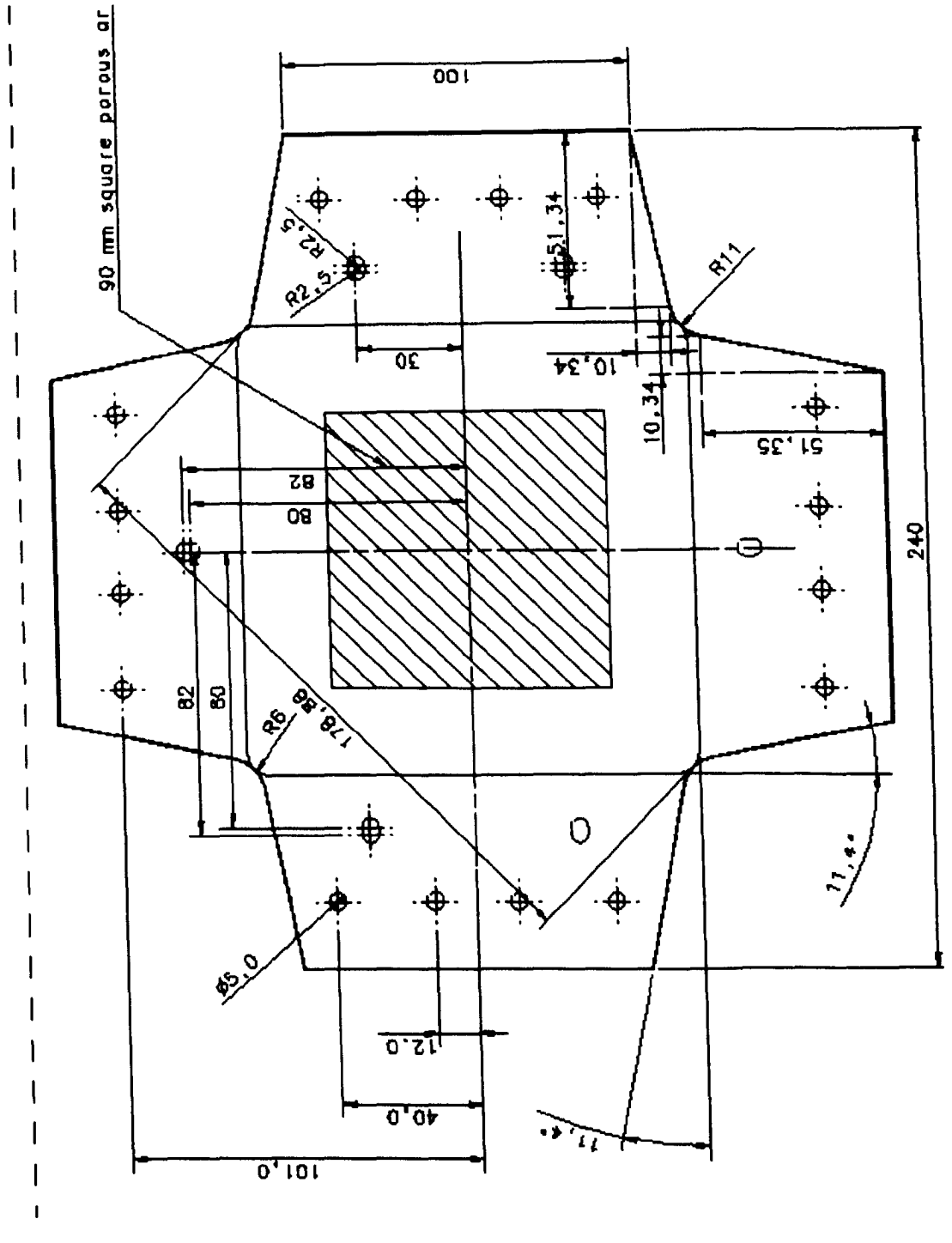

Figure B.8: Foil working drawing - for CNC laser cutting. Porous area (hatched) is laser drilled to either 6% or 12% porosity using $50\mu m$ or $200\mu m$ holes.

B.2 Tensioning insert photographs

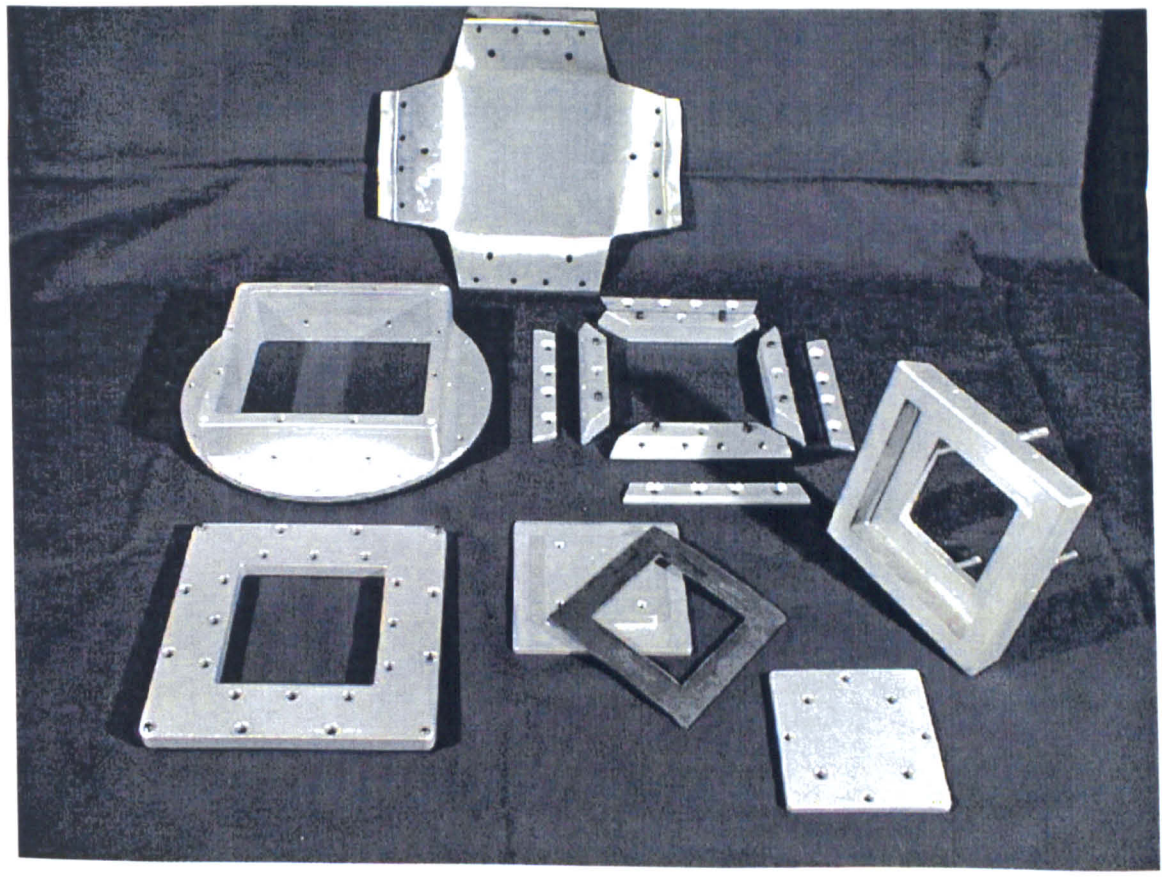

B.9.1: Components of Tensioning insert

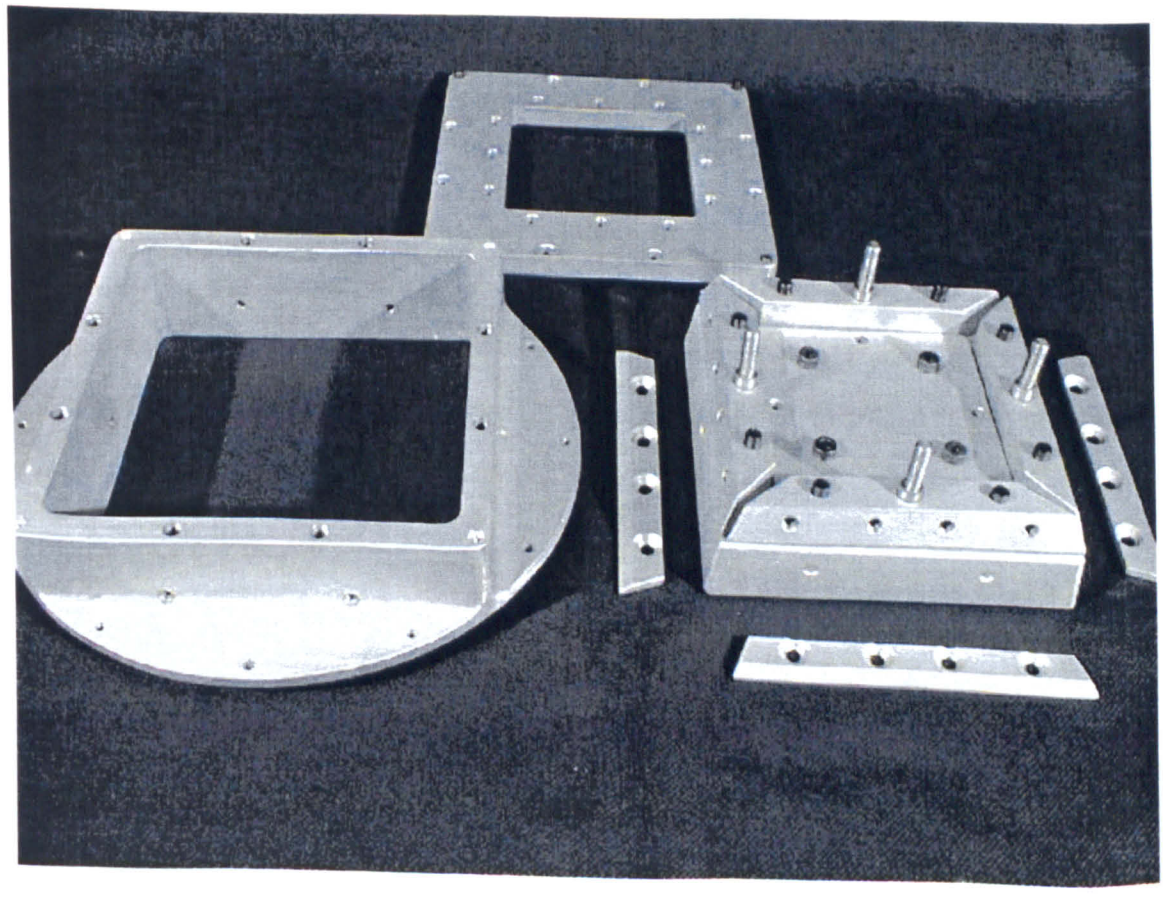

B.9.2: Insert casing (left), forming body with integral cavity (right) and stiffening plate (rear)

Figure B.9: Photographs of disassembled tensioning insert

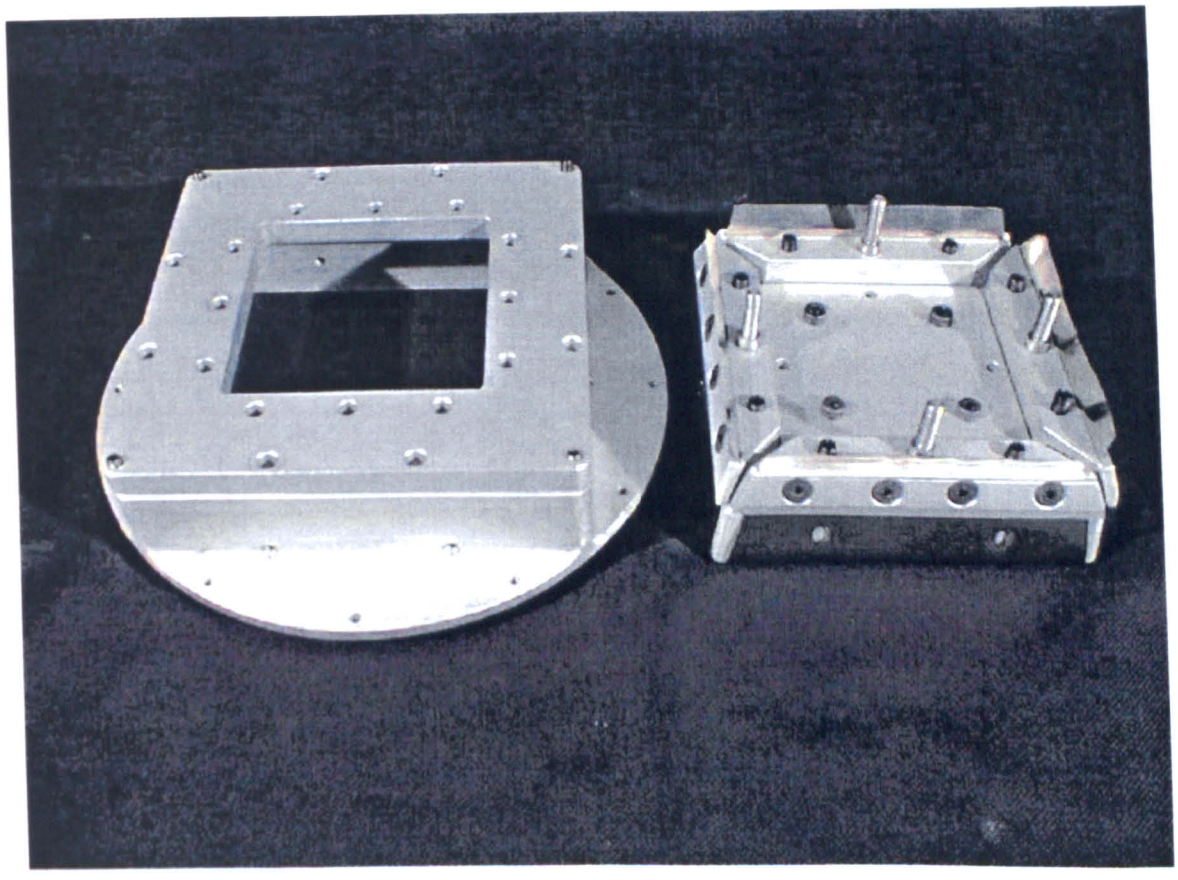

B.10.1: Insert casing (left) and the forming body with tensioned foil (right)

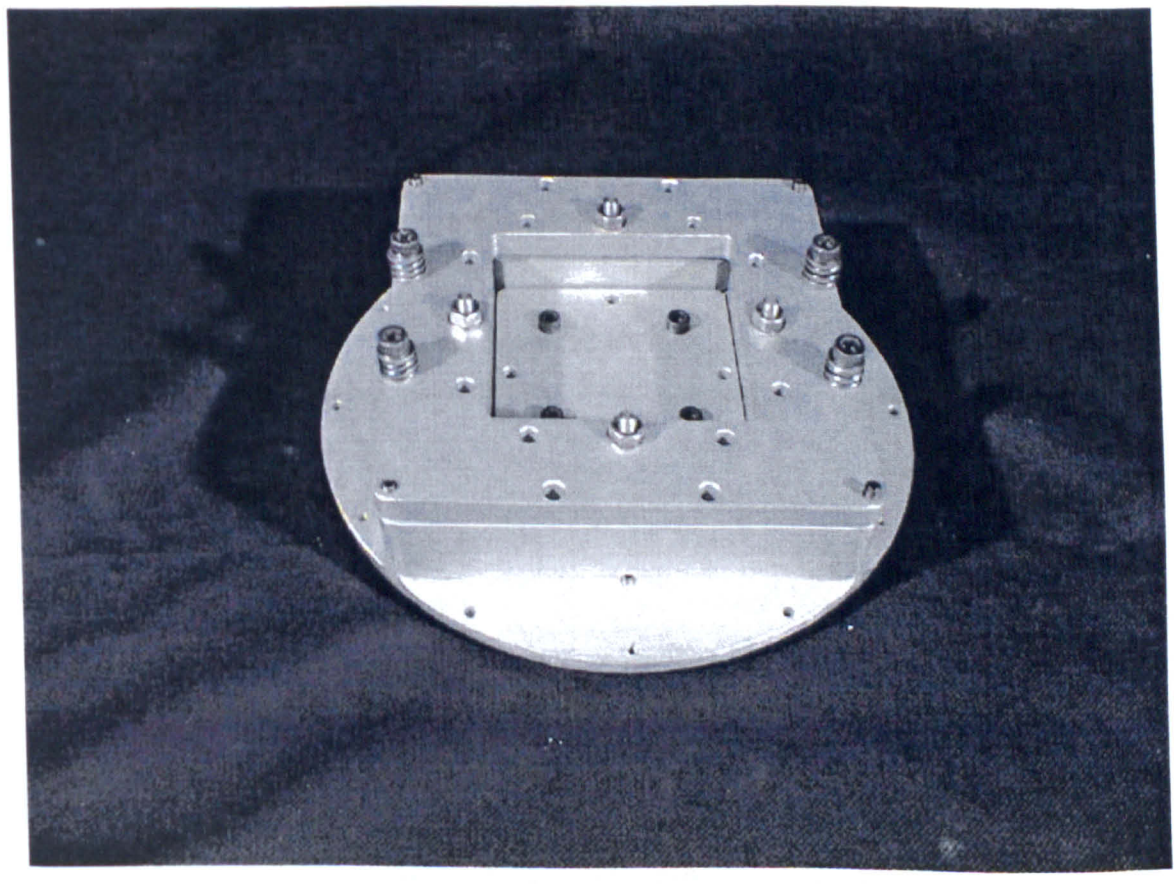

B.10.2: Rear view of assembled insert

Figure B.10: Photographs of assembled tensioning insert